eman ta zabal zazu

**Universidad
del País Vasco** **Euskal Herriko
Unibertsitatea**

ZIENTZIA
ETA TEKNOLOGIA
FAKULTATEA
FACULTAD
DE CIENCIA
Y TECNOLOGÍA

Improvements in MALDI-Imaging Mass Spectrometry to analyze the lipidome in different tissues. A step forward to clinical application.

Doctoral Thesis

Lucía Martín Saiz

Supervised by:

José Andrés Fernández González

2021

CONTENTS

Chapter 1

Introduction and scope of the thesis

1.1   Introduction

Since the process of mapping and sequencing the human genome was accomplished, new technologies have appeared that facilitate obtaining large sets of data from a tissue or cell1. These technologies enable to get a snapshot of the underlying molecular mechanisms in a biological system of interest at a resolution that has never been achievable before. Broadly speaking, the scientific domains connected with monitoring such biological molecules in a high-throughput manner are collectively referred to as "omics"2.

The term "omics" refers to a broad category of research. Genomics, transcriptomics, proteomics, metabolomics, lipidomics and glycomics are examples of global assessments of genes, mRNA, proteins, metabolites, lipids and glycans respectively. The study of an organism's whole genome was the first emerging field by the end of the twentieth century[3]. The Human Genome Project[1], which was completed in 2002, revolutionized medicine by providing new insight into biological processes that could aid in cancer and rare disease diagnosis. They are, however, only a part of the picture, as many diseases have been linked to post-translational changes or processes. Later on, the revolution of transcriptomics (total mRNA) and especially proteomics (the study of all expressed proteins)[4, 5] emerged. Nonetheless, because these three domains together do not provide a complete vision, metabolomics, the comprehensive investigation of low molecular weight compounds (less than 1.500 Da), is gaining momentum[6]. Certainly, enzymatic proteins, which are expressed by gene transcription, produce metabolites, the final stage in the "omics cascade". Thus, to establish the link between genotype and phenotype it is also necessary to have a deep knowledge of the metabolome (**Figure 1.1**).
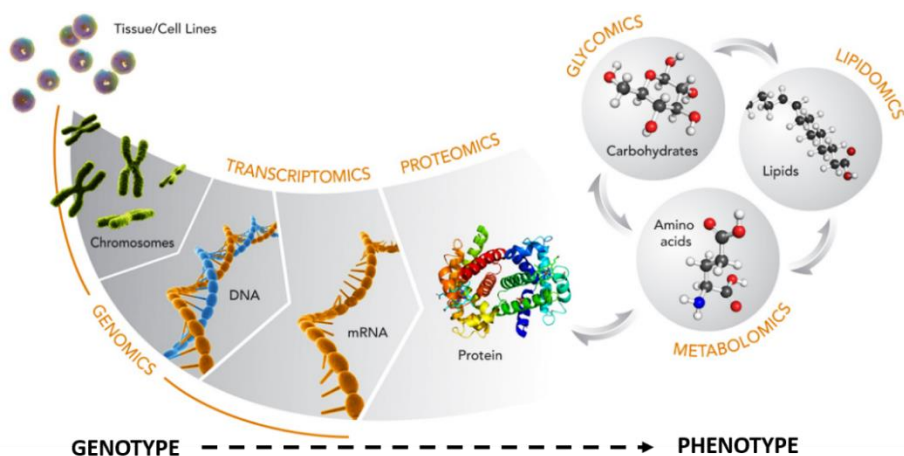
Figure 1.1. *Scheme of the omics science. Adapted from E De Hoffmann et al. [7]*

A multitude of variables may drive the omics research but the most prevalent reasons are to have a thorough grasp of the biological system under investigation and to associate the omics-based molecular measurements with a clinical outcome of interest. The rationale is that by exploiting the omics-based data, there is the potential to develop a more accurate predictive or prognostic model of a particular condition or disease, which can complement standard clinical approaches[2].

Mass spectrometry (MS) is one of the key analytical technologies on which the emerging ''-omics'' approaches are based. It may provide detection and quantization of thousands of proteins and biologically active metabolites from a tissue, body fluid or cell culture working in a ''global'' or ''targeted'' manner, down to ultra-trace levels. It can be expected that the high performance of MS technology, coupled to routine data handling, will soon fructify in the request for a better understanding of human diseases, leading to new molecular biomarkers, hence affecting drug targets and therapies.

MS was first developed by J.J. Thomson when, like in many great scientific discoveries in history, he was looking for something else, specifically the origin of the cathode rays[8]. Mass spectrometry was first employed in the field of physics to determine the mass of atoms, helping to establish the existence of stable isotopes of elements, but it took of as analytical technique in the petroleum industry to measure the abundance of small hydrocarbons and as a technique to assess the quality of the crude[9]. Great advancements propelled MS into new research domains, but it was not until the invention of soft ionization techniques that its application was brought into biology, primarily in the omics field.[8]

In the eighties, mass spectrometry was transformed by the invention of electrospray ionization (ESI)[10] and matrix assisted laser desorption ionization (MALDI)[11, 12]. These two techniques as well as nuclear magnetic resonance (NMR) changed the way in which biology was studied. In fact, Kurt Wüthrich (for NRM discoveries), J. Fenn and K. Tanaka (for MS approaches) were awarded the Nobel Prize in Chemistry in 2002 for "the development of methods for identification and structure analysis of biological macromolecules"[13].

ESI was developed by J.B. Fenn[10] and allowed for the detection of proteins in very low concentrations (ppm). It could be coupled to any mass spectrometer and used to measure directly from a liquid matrix, making it suitable for liquid chromatography systems (LC-MS) and other flow injection techniques. Furthermore, ESI was capable of producing ions with multiple charges, enabling the identification of large (bio)molecules.

In parallel, MALDI was introduced by M. Karas and F. Hillenkamp[11], and K. Tanaka[12] simultaneously, and allowed ionizing molecules up to 300,000 Da, without fragmenting

them. Within this new approach, analytes did not need to be dissolved in a liquid phase. Conversely, they could be measured directly from a solid sample. This fact opened the door to obtain the spatial distribution of the molecules in a tissue section. It was in this framework that imaging mass spectrometry (IMS) was developed[14]. IMS originated with secondary ion mass spectrometry (SIMS) over 50 years ago[15]. However, the analysis of biological samples only became possible once soft ionization techniques such as MALDI were introduced[14, 15]. IMS can identify and localize thousands of distinct compounds in tissue sections. In biochemistry, IMS is used to identify the tissue's molecular constituents, mainly metabolites and proteins, in order to better understand the relationships between genome, phenotype, and biological response in disease. In this context, IMS has proven to be a useful tool in cancer research for a variety of purposes, including biomarker discovery[16], understanding biological processes[17], and disease classification[18, 19], among others[20].

Since the beginning of the 21st century, after the development of the so-called techniques of soft ionization, the race for the evolution of mass spectrometers dedicated to the biomedicine has been inexorable. Both in the ionization stage, with new modifications of the ESI and MALDI ion sources[21, 22], and in the analysis stage, with increasingly precise spectrometers, with Fourier transform analyzers such as the Orbitrap (Thermo Scientific)[23] or the FT-ICR19 (Bruker)[24], capable of to achieve mass resolutions of more than 2,000,000 FWHM (width at half maximum). Every year new solutions to the problems arise, and each solution brings with it new problems to solve.

As the equipments are more accurate and faster, data production capacity is multiplies, so more powerful and complex statistical analysis programs are required. Some techniques with spatial resolution such as MALDI-IMS, or the data from ion mobility also require specific tools that allow converting spectra into images and extracting conclusions from the huge amount of data obtained[25]. All these recent advances have made mass spectrometry a precise, reliable and highly useful analysis technique in fields as diverse as biomedicine, forensic medicine or agriculture[26-29].

In the realms of biomedicine, lipidomics is a fast emerging analytical method in life and health sciences[30-32]. Lipids present some unique advantages for mass spectrometry analysis. The application of ESI to crude lipid extracts without prior fractionation resulting in lipid class specific fragments—the so called shotgun approach—is one such example, as it has perhaps been more successfully applied in lipidomics than in any other discipline[33].

Since the first lipid analysis by ESI developed by Han and Gross in 1994[34], a tremendous amount of qualitative and quantitative studies based on lipidomics have been performed[27, 35-38]. The most widely used MS instrument in the analysis of lipids is

MS coupled with liquid chromatography electrospray ionization (LC-ESI-MS). Many reports have shown that shot-gun lipidomics analyses are the most suitable analytical method to investigate the full range of lipid molecules in cells or tissues or to find molecular-level indications of diseases by comparison between the lipid distribution in diseased and control samples[39, 40]. However, this technique entails extraction and purification steps, leading to the loss of the spatial distribution over the biological tissue. Meanwhile, numerous techniques of chemical imaging enable the detection and the localization of lipids. Staining with Nile Red, Oil Red O[41], osmium tetroxide[42], or BODIPY[43] is a common method to localize the lipid fraction on frozen sections, whereas few specific lipid antibodies[44] are commercially available. These approaches target either the complete lipid fraction or only one specific family, but they are not able to label individual molecular species with a wide variety of fatty acid compositions. By contrast, IMS enables the visualization of the spatial distribution of biomolecules and specifically, the versatility of MALDI-IMS has opened a new frontier in several other fields, as well as lipidomics.

However, many concerns remain unresolved until lipid IMS reaches its full potential[45]. One of the primary themes of IMS is whether it can provide meaningful data to assist medical doctors in clinical decisions such as diagnoses, prognosis, therapy selection, and monitoring[46]. In this thesis, we demonstrate various enhancements to a MALDI-IMS system, as well as combinations with other orthogonal techniques, all with the goal of providing a more accurate description of alterations in the lipidome of cells and tissues in the context of disease. We have confronted complicated analytical problems thanks to collaboration with various research groups, each of which demanded special modifications to allow MALDI-IMS to answer relevant biological questions.

1.2   Scope of the thesis

Despite the important evolution experienced by the IMS technique since its appearance, it is a technique prone to experimental artifacts and still requires of technical improvements in several areas before taking off as a potent technology in clinical use. The goal of this thesis is to improve some aspects involved in the MALDI-IMS workflow and to focus on their implementation to bring IMS closer to its application in clinics. Such developments were always carried out in the context of a particular study; the methodological and technical problems faced during the studies were the stimulus required to accomplish such developments.

Following this reasoning, **Chapter 4** deals with technical improvements achieved during this thesis. In systems biology, It is of paramount importance to ensure good

data reproducibility among samples as well as to push the equipment to the limits in order to obtain the best spatial resolution. With this purpose, a new in-house designed sublimator was developed and, additionally, the original MALDI source of the mass spectrometer was modified to achieve higher spatial resolution without oversampling. Moreover, and making an effort to obtain and compile as much information as possible from the same sample, a new protocol for detecting lipids and protein by MALDI-IMS over the same section was carried out. The improvements in the spatial resolution achieved with the modification of the original MALDI source of our mass spectrometer, were carried out in collaboration with Dr. Raul Montero from the Laser Facility of SGIKER (UPV/EHU). The implementation of a bimodal protocol to analyze lipids and protein from the same tissue was part of a collaboration with the group of Dr. Felix Elortza from the proteomics platform in the Centro de investigación cooperativa (CIC-Biogune (Derio, Spain).

Chapter 5 presents the characterization of the differences in the lipid profile between normal mouse kidney, a Folic acid (FA)-induced acute kidney injury (AKI) model and ferrostatin (Fer-1)-treated AKI kidney. Fer-1 is a drug candidate to treat this disease. The main challenge of this project is to find the region-specific lipid variation over the three kidney models. This research was accomplished with the collaboration of the group of MD. Alberto Ortiz Arduan, head of the department of nephrology in the Fundación Jimenez Díaz universitary hospital (Madrid, Spain).

Chapter 6 introduces the first characterization of the different segments of the human nephron by MALDI-IMS of lipids combined with fluorescence staining protocols. This was carried out in collaboration with Prof. Gorka Larrinaga from Department of Nursing, Dr. Olatz Fresnedo and Dr. Yuri Rueda from the Department of Physiology both from the Faculty of Medicine and Nursing (University of the Basque Country, UPV/EHU). There are very few, if any, previous reports on these types of studies in which immunohistochemistry (IHC) techniques are combined, on the same tissue, with IMS. However, such combination required to precisely identify each tissue type, due to the complex histology of the kidney.

Once characterized the normal murine and human kidney, a comparison of the lipid profiles obtained from these two species was performed in Chapter 7 in order to evaluate the quality of the mouse as a good animal model for human diseases.

Chapter 8 focusses on the study of clear cell renal cell cancer (ccRCC) lipidome using MALDI-IMS and uHPLC techniques. This study served us to exploit the synergy between the two techniques. On the one hand, comparison between them showed that both techniques yield similar results. On the other hand, we demonstrate that it is possible to combine the spatial information obtained by IMS with the superior resolving power of the uHPLC to obtain more conclusive results. This work was accomplished

with the help of Prof. Gorka Larrinaga from the Department of Nursing, Dr. Olatz Fresnedo and Dr. Yuri Rueda from the Department of Physiology both from the Faculty of Medicine and Nursing (University of the Basque Country, UPV/EHU).

In **Chapter 9,** we present the results from a pilot study which examine the lipid changes occasioned in the context of glioblastoma as well as the effects of temozolomide treatment in both diseased and normal adjacent human brain tissue. This study was performed in collaboration with the group of Dr. Gwendolyn Barceló-Coblijn, Lipids in Human Pathology from Balearic Islands Health Research Institute (Son Espases University Hospital)

To conclude, some preliminary results were included in **Chapter 10,** regarding the characterization of the lipid profile of inflammatory bowel diseases (IBD) revealed by MALDI-IMS of lipids. This study is now in progress with the collaboration of the group of Dr. Gwendolyn Barceló-Coblijn and with the Kratos Analytical Ltd, a Shimadzu Group company (Manchester, UK).

1. International Human Genome Sequencing Consortium. Finishing the euchromatic sequence of the human genome. *Nature* **431**, 931 (2004).

2. Micheel, C. M., Nass, S. J. & Omenn, G. S. in *Evolution of Translational Omics: Lessons Learned and the Path Forward* (National Academies Press (US), 2012).

3. Baltimore, D. Our genome unveiled. *Nature* **409**, 815-816 (2001).

4. Petricoin, E. F., Zoon, K. C., Kohn, E. C., Barrett, J. C. & Liotta, L. A. Clinical proteomics: translating benchside promise into bedside reality. *Nature reviews Drug discovery* **1**, 683-695 (2002).

5. Vlahou, A. & Fountoulakis, M. Proteomic approaches in the search for disease biomarkers. *Journal of Chromatography B* **814**, 11-19 (2005).

6. Nicholson, J. K. & Lindon, J. C. Metabonomics. *Nature* **455**, 1054-1056 (2008).

7. De Hoffmann, E. Mass spectrometry. *Kirk-Othmer Encyclopedia of Chemical Technology* (2000).

8. Griffiths, J. A brief history of mass spectrometry. *Anal. Chem.* **80**, 5678-5683 (2008).

9. Hoover, H. & Washburn, H. A preliminary report on the application of the mass spectrometer to problems in the petroleum industry. *Transactions of the AIME* **142**, 100-106 (1941).

10. Fenn, J. B., Mann, M., Meng, C. K., Wong, S. F. & Whitehouse, C. M. Electrospray ionization for mass spectrometry of large biomolecules. *Science* **246**, 64-71 (1989).

11. Karas, M. & Hillenkamp, F. Laser desorption ionization of proteins with molecular masses exceeding 10,000 daltons. *Anal. Chem.* **60**, 2299-2301 (1988).

12. Tanaka, K. *et al*. Protein and polymer analyses up to m/z 100 000 by laser ionization time-of-flight mass spectrometry. *Rapid communications in mass spectrometry* **2**, 151-153 (1988).

13. Vairamani, M. Chemistry Nobel Prize 2002-Mass Spectrometry. *Resonance* **8**, 69-76 (2003).

14. Spengler, B., Hubert, M. & Kaufmann, R. *MALDI ion imaging and biological ion imaging with a new scanning UV-laser microprobe* (Proceedings of the 42nd Annual Conference on Mass Spectrometry and Allied Topics Ser. 1041, Chicago, 1994).

15. Castaing, R. & Slodzian, G. Optique corpusculaire-premiers essais de microanalyse par emission ionique secondaire. *Comptes Rendus Hebdomadaires Des Seances De L Academie Des Sciences* **255**, 1893-& (1962).

16. Cazares, L. H., Troyer, D. A., Wang, B., Drake, R. R. & Semmes, O. J. MALDI tissue imaging: from biomarker discovery to clinical applications. *Analytical and bioanalytical chemistry* **401**, 17-27 (2011).

17. Cornett, D. S., Reyzer, M. L., Chaurand, P. & Caprioli, R. M. MALDI imaging mass spectrometry: molecular snapshots of biochemical systems. *Nature methods* **4**, 828-833 (2007).

18. Rauser, S. *et al*. Classification of H&ER2 receptor status in breast cancer tissues by MALDI imaging mass spectrometry. *Journal of proteome research* **9**, 1854-1863 (2010).

19. Gustafsson, J. O., Oehler, M. K., Ruszkiewicz, A., McColl, S. R. & Hoffmann, P. MALDI imaging mass spectrometry (MALDI-IMS)—application of spatial proteomics for ovarian cancer classification and diagnosis. *International journal of molecular sciences* **12**, 773-794 (2011).

20. Bodzon-Kulakowska, A. & Suder, P. Imaging mass spectrometry: instrumentation, applications, and combination with other visualization techniques. *Mass Spectrom. Rev.* **35**, 147-169 (2016).

21. Bramwell, C. J., Colgrave, M. L., Creaser, C. S. & Dennis, R. Development and evaluation of a nano-electrospray ionisation source for atmospheric pressure ion mobility spectrometry. *Analyst* **127**, 1467-1470 (2002).

22. Laiko, V. V., Moyer, S. C. & Cotter, R. J. Atmospheric pressure MALDI/ion trap mass spectrometry. *Anal. Chem.* **72**, 5239-5243 (2000).

23. Hu, Q. *et al*. The Orbitrap: a new mass spectrometer. *Journal of mass spectrometry* **40**, 430-443 (2005).

24. Marshall, A. G., Hendrickson, C. L. & Jackson, G. S. Fourier transform ion cyclotron resonance mass spectrometry: a primer. *Mass Spectrom. Rev.* **17**, 1-35 (1998).

25. McCombie, G., Staab, D., Stoeckli, M. & Knochenmuss, R. Spatial and spectral correlations in MALDI mass spectrometry images by clustering and multivariate analysis. *Anal. Chem.* **77**, 6118-6124 (2005).

26. Brown, M. A. in *Liquid chromatography/mass spectrometry: applications in agricultural, pharmaceutical, and environmental chemistry.* (American Chemical Society, 1990).

27. Harkewicz, R. & Dennis, E. A. Applications of mass spectrometry to lipids and membranes. *Annu. Rev. Biochem.* **80**, 301-325 (2011).

28. Yinon, J. in *Forensic applications of mass spectrometry* (CRC press, 1994).

29. Siuzdak, G. The emergence of mass spectrometry in biochemical research. *Proc. Natl. Acad. Sci. U. S. A.* **91**, 11290-11297 (1994).

30. Burla, B. *et al*. MS-based lipidomics of human blood plasma: a community-initiated position paper to develop accepted guidelines. *J. Lipid Res.* **59**, 2001-2017 (2018).

31. Rinschen, M. M., Ivanisevic, J., Giera, M. & Siuzdak, G. Identification of bioactive metabolites using activity metabolomics. *Nature Reviews Molecular Cell Biology* **20**, 353-367 (2019).

32. Paglia, G., Smith, A. J. & Astarita, G. Ion mobility mass spectrometry in the omics era: Challenges and opportunities for metabolomics and lipidomics. *Mass Spectrom. Rev.* (2021).

33. Blanksby, S. J. & Mitchell, T. W. Advances in mass spectrometry for lipidomics. *Annual Review of Analytical Chemistry* **3**, 433-465 (2010).

34. Han, X. & Gross, R. W. Electrospray ionization mass spectroscopic analysis of human erythrocyte plasma membrane phospholipids. *Proc. Natl. Acad. Sci. U. S. A.* **91**, 10635-10639 (1994).

35. Hanson, V. L., Park, J. Y., Osborn, T. W. & Kiral, R. M. High-performance liquid chromatographic analysis of egg yolk phospholipids. *Journal of Chromatography A* **205**, 393-400 (1981).

36. Hutchins, P. M., Barkley, R. M. & Murphy, R. C. Separation of cellular nonpolar neutral lipids by normal-phase chromatography and analysis by electrospray ionization mass spectrometry. *J. Lipid Res.* **49**, 804-813 (2008).

37. Kim, H. & Salem Jr, N. Separation of lipid classes by solid phase extraction. *J. Lipid Res.* **31**, 2285-2289 (1990).

38. Nakanishi, H., Ogiso, H. & Taguchi, R. in *Lipidomics* 287-313 (Springer, 2009).

39. Han, X. & Gross, R. W. Shotgun lipidomics: electrospray ionization mass spectrometric analysis and quantitation of cellular lipidomes directly from crude extracts of biological samples. *Mass Spectrom. Rev.* **24**, 367-412 (2005).

40. Yang, K., Cheng, H., Gross, R. W. & Han, X. Automated lipid identification and quantification by multidimensional mass spectrometry-based shotgun lipidomics. *Anal. Chem.* **81**, 4356-4368 (2009).

41. Van Goor, H., Gerrits, P. & Grond, J. The application of lipid-soluble stains in plastic-embedded sections. *Histochemistry* **85**, 251-253 (1986).

42. Wigglesworth, V. Histological staining of lipids for the light and electron microscope. *Biological Reviews* **63**, 417-431 (1988).

43. Pagano, R. E. & CH&EN, C. Use of BODIPY-labeled Sphingolipids to Study Membrane Traffic along the Endocytic Pathway a. *Ann. N. Y. Acad. Sci.* **845**, 152-160 (1998).

44. Dani, F. R. *et al*. Exploring proteins in Anopheles gambiae male and female antennae through MALDI mass spectrometry profiling. *PLoS One* **3**, e2822 (2008).

45. Vaysse, P., Heeren, R. M., Porta, T. & Balluff, B. Mass spectrometry imaging for clinical research–latest developments, applications, and current limitations. *Analyst* **142**, 2690-2712 (2017).

46. Basu, S. S. & Agar, N. Y. Bringing Matrix-Assisted Laser Desorption/Ionization Mass Spectrometry Imaging to the Clinics. *Clin. Lab. Med.* **41**, 309-324 (2021).

Chapter 2

Mass Spectrometry and Lipidomics; Fundamentals

This chapter provides a detailed description of mass spectrometry fundamentals including the major techniques used in this thesis. Furthermore, a brief introduction to lipidomics is provided, as well as lipid classification according to the rules in LIPID MAPS1 and structure of the lipid classes involved in this thesis.

2.1   Mass Spectrometry

Mass spectrometry is an analytical technique that allows for the analysis of the molecular mass of countless compounds by converting them into ions. In the late nineteenth century, this technique began as a tool for cathode rays detection but nowadays, mass spectrometry plays a key role in a high number of scientific disciplines such as physics, chemistry, drug discovery or medical science. It consists of the ionization of the sample with the subsequent molecules conversion into gaseous ions and their characterization by their m/z using a combination of magnetic and electric fields. Therefore, a mass spectrum is obtained and displayed as a graphic representation of the relative abundance versus m/z of each ion[2].

A mass spectrometer mainly consists of four parts: The **ion source**, where the ions are generated and, eventually, fragmented, the **ion analyzer**, that allows obtaining the different ion mass-charge ratio, the **ion detector** and the **recording system** in order to get and visualize the spectrum[3] (**Figure 2.1**)
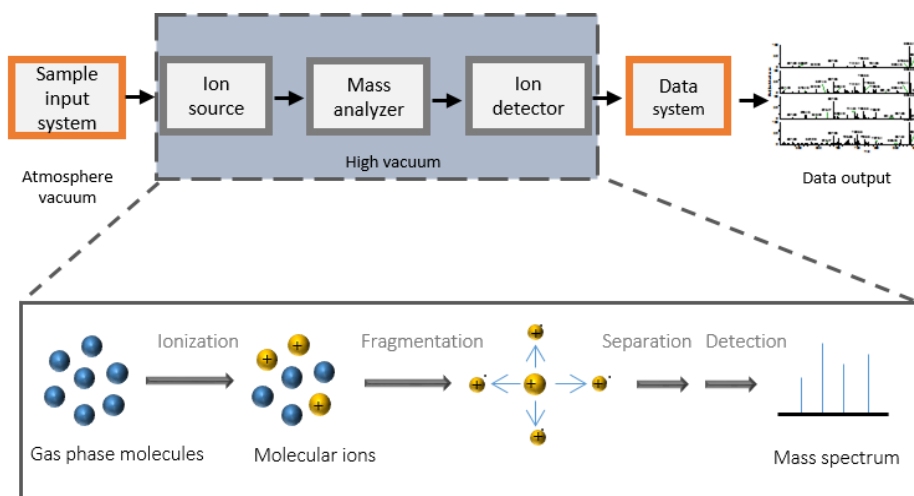
Figure 2.1. *Main components of a mass spectrometer and major steps in the mass spectrometry technique.*

Ion source

There is a large variety of ion sources available depending of the physico-chemical properties of the sample to be analyze. Ion sources can be classified in two groups based on the energy used to ionize the molecules: hard ionization and soft ionization sources.

In hard ionization sources, high energy is transferred into the formed ions and consequently, more complex spectra are obtained in comparison with those generated by soft ionization sources, where fragmentation process is scarce. Electron Impact ionization (EI)[4] is an example of hard ionization source while secondary ion mass spectrometry (SIMS)[5], electrospray Ionization (ESI)[6] and matrix assisted laser desorption/ionization (MALDI)[7] belong to the soft ionization techniques.

These soft ionization techniques were developed in the 80's and open the field to the analysis of large mass compounds such as peptides and proteins. These molecules fragment easily and therefore they suffered extensive degradations due to the excess of energy put on the molecules when using hard ionization techniques. ESI and MALDI were the revolutionary methods that caused the change in the way to approach the chemical study of biological compounds. Currently, they are still the most used techniques, although recent developments have led to incorporate other new ionization approaches such as (LAESI)[8].

As ESI and MALDI ionization techniques are the most widely used, a brief description of them is featured below.

Electrospray Ionization (ESI)

Electrospray ionization is an atmospheric pressure ionization technique that can be applied to a broad collection of liquid-phase samples. It was developed in 1989 by John Fenn, Nobel prize of 2002, together with Tanaka, who showed that multiply charged ions were obtained from the proteins [9, 10]. Nowadays, ESI is not only used to study proteins and biopolymers, but also to analyze small polar molecules. Besides, ESI provides high mass sensitivity and it is usually connected to high-performance liquid chromatography HPLC, µHPLC or capillary electrophoresis.

Electrospray ionization is produced by applying a strong electric field (3-6 kV) between a capillary tube which contains the sample and a counter-electrode. Due to the intense gradient generated, the emerging solution is dispersed into a fine mist of charged droplets. Then, the droplets are evaporated by a hot flow of nitrogen and finally, naked charged analyte arrives to the mass analyzer **(Figure 2.2)**.
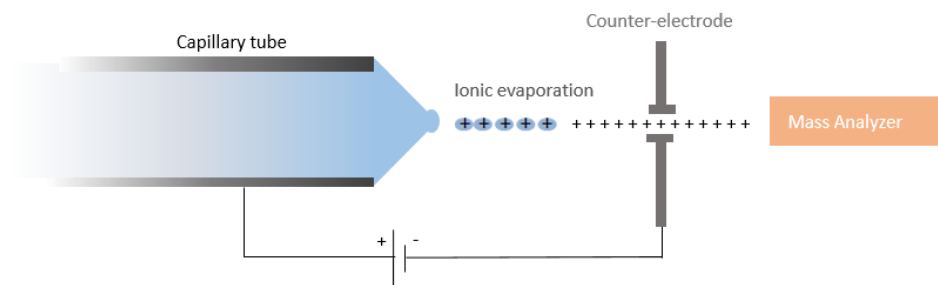
Figure 2.2. *ESI system scheme.*

There are some variation of ESI source which enable the ionization not only of liquid but also solid samples, such as desorption electrospray ionization (DESI)[11] and laser desorption electrospray ionization (LAESI)[8].

Laser desorption (LD)

Laser desorption is a method that produces gaseous ions from a sample solid surface by focusing laser pulses on it. The laser beam ablates material from the sample surface and crates a plume of ions and neutral molecules that usually interact among themselves. In order to improve the photons absorption, a substrate may be added which is going to determine the LD type; DIOS (Silicon is used)[12], NALDI (Nanostructures surfaces are required) [13] or MALDI (A matrix is employed)[14].

Because MALDI is the main ionization method used in this thesis, a brief description will be given.

Matrix assisted Laser Desorption Ionization (MALDI)

MALDI was developed by Karas and Hillenkamp in 1987[7, 15] and produced a revolution in the study of high mass biomolecules by mass spectrometry.

MALDI consists of two steps: firstly, the sample is co-crystalized with an organic matrix with absorption bands in the 300-400 nm region. Second, the sample is irradiated with a laser with emission in the region of the absorption bands of the organic matrix. The matrix and the analytes absorb then the laser energy and simultaneously are desorbed and ionized in gas phase form. **Figure 2.3** shows a schematic representation of MALDI desorption and ionization process.
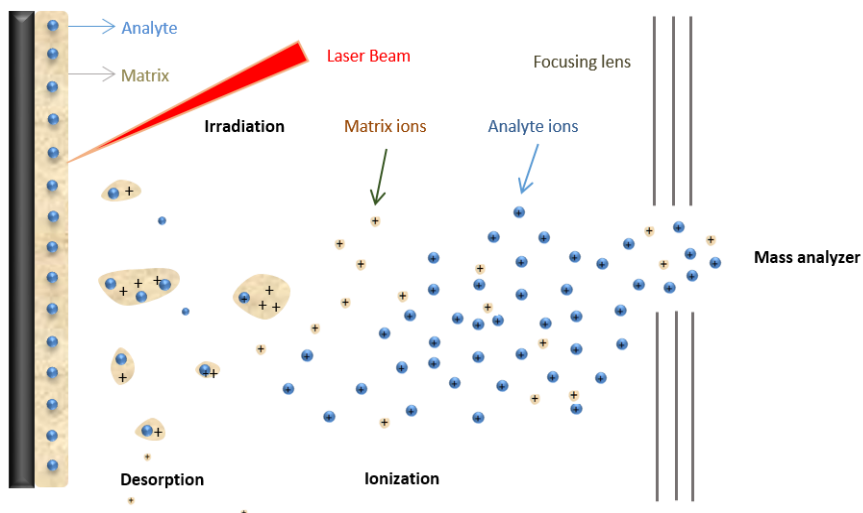
Figure 2.3. *MALDI system scheme.*

Mass analyzers

A mass analyzer is the component that enables the determination of the m/z of the analytes produced in the ion source. There is a wide variety of mass analyzers, differing in sensitivity, mass resolution and mass accuracy. A brief description of the most widely mass analyzers used will be given.

Quadrupole

The principle of the quadrupole was described by Paul and Steinwedel in 1953[16] and basically, it is formed by four metal parallel rods (electrodes). Each opposing rod pair is connected together electrically, and a radio frequency (RF) voltage with a DC offset is applied between them. In order for the ions to cross through the quadrupole and reach the detector, they must have a stable trajectory in the two planes formed by each pair of rods. Only ions with a certain mass-to-charge ratio will have stable trajectory; the rest of them will collide with the rods. In this way, this technique allows for the selection of particular m/z ions or the range of m/z-values by continuously varying the applied voltage.
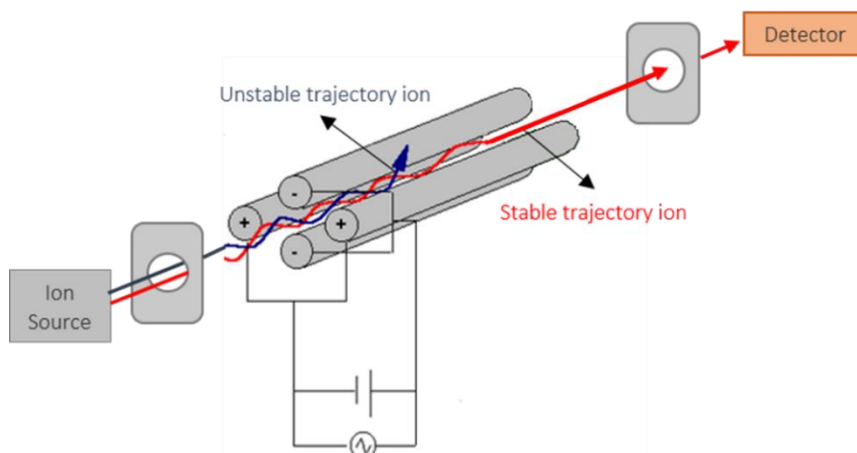
Figure 2.4. *Quadrupole mass analyzer scheme.*

Ion trap

Paul and Steinwedel also described an "ion trap" in 1960 but few years later, Stafford et al. modified and turned it into a "useful" mass spectrometer[17].

Conceptually, an ion trap can be visualized as a quadrupole bent in on itself in order to form a closed loop consisting on an annular central electrode with two electrode caps. Constant and variable RF potentials are applied to the caps and annular electrodes respectively. In this way, a quadrupolar magnetic field is generated, where the ions are trapped. By modifying the annular electrode radiofrequency signal, the trajectory of certain ions is destabilized, ejecting them out of the trap. Thus, the ion trap is emptied in m/z increasing order obtaining a mass spectrum[18].
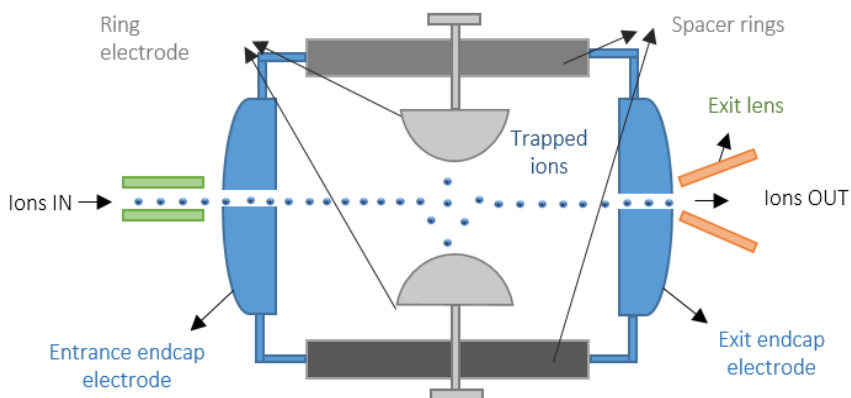
Figure 2.5. *Ion trap analyzer scheme.*

Orbitrap

The orbitrap is an electrostatic ion trap that uses the Fourier transform to obtain mass spectra. This system is based on the concept introduced by Makarov at the end of the 1990s, starting a sequence of technology improvements, which resulted in the commercial introduction of this analyzer by Thermo Fisher® as a part of the hybrid LTQ Orbitrap instrument in 2005[19]. As it is appreciated in **Figure 2.6**, the external part of the Orbitrap is a barril-shaped electrode cut into two parts separated by a small gap through which ions are injected tangentially. Inside, there is a second spindle-shaped electrode, around which ions rotate and oscillate along the z-axis due to the application of an electrostatic voltage. Using the Fourier transform, the spectrum of the frequencies of the ion orbits is obtained, and from it, the m/z of each ion.
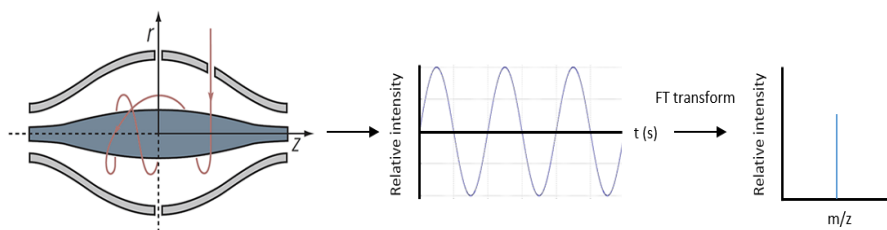
Figure 2.6. *Orbitrap system scheme.*

Time of flight (TOF)

The TOF analyzer uses an electrical field to accelerate the ions and send them flying through the drift tube and then, determines the time taken for them to get to the detector. This acceleration allows all ions with the same charge to have the same kinetic energy. Hoverer, not all the ions reach the detector at the same time; the velocity of the ion depends on the mass-to-charge ratio where the heavier ions reach the detector later than the lighter ones[20]. TOF mass analyzers have been broadly used for biomolecules analysis[21]. Although TOF systems have improved in terms of accuracy/resolution, high sensitivity, and high efficiency, it is common to find difficulty in performing MS/MS experiments for biomolecules analysis with this instrument. Therefore, hybrid instruments with quadrupoles (i.e., QqTOF) or liner trap (i.e., LIT-TOF) are used in these approaches.

2.2   Imaging mass spectrometry (IMS)

IMS is a variation of conventional mass spectrometry that enables the detection, the identification and the localization of a wide variety of molecules directly from tissue

sections[22, 23]. Against to other imaging techniques, such as immunohistochemistry (IHC), it is a label-free and non-invasive approach. It can map hundreds of biomolecules in one experiment, from sub-cellular to multi-cellular level. The combination of information gained from mass spectrometry and visualization of spatial distributions in thin sample sections makes this a valuable analytical tool for biological specimen characterization.

The three major ionization methods used in IMS are matrix-assisted laser desorption ionization (MALDI)[7,24-26], secondary ion mass spectrometry (SIMS)[5] and desorption electrospray ionization (DESI)[11]. More recently, improvements of the techniques have led to the development of other ionization techniques, such as laser ablation electrospray ionization (LAESI)[8]. The choice of the method has a large impact on the spatial resolution of the experiment, as well as on the biomolecules that can be identified. **Table 2.1** summarizes the spatial resolution achievable with each technique, as well as the molecules each technique is more suitable for.

Table 2.1. Most common ionization techniques used in imaging mass spectrometry with their main characteristics: need of a previous sample preparation requirements, resolution achievable and most common targeted biomolecules[27].

	Sample Preparation	Ionization source	Ionization type	Spatial resolution	Targeted biomolecules
MALDI	Matrix coating	Laser beam	Soft	1.4-200 μm	Lipids, peptides, proteins, metabolites
DESI	None	Solvent spray	Soft	>100 μm	Mostly lipids and metabolites
SIMS	None or matrix/metal coating	Ion gun	Hard	<1 μm dynamic mode, >1 μm static mode	Atoms, small molecular fragment, fatty acids and lipids
LAESI	None	Laser beam combined with electrospray	Soft	>200 μm	Lipids, peptides, proteins, metabolites

Regarding mass analyzers, collinear Time-of-flight (TOF) type were the first ones to be used for MALDI-IMS[7], and though it is still popular, the development of Fourier transform ion cyclotron resonance (FT-ICR) and Orbitrap has expanded the selection of analyzers. The main improvement of these devices is their extremely high mass resolving power, especially for small molecules such as lipids. Still, there is room for improvement, mainly regarding acquisition speed. **Table 2.2** summarizes the main characteristics of each mass analyzer type.

Table 2.2. Summary of mass analyzers used in imaging mass spectrometry, together with their main characteristics: mass resolving power, mass range, MS/MS capabilities and targeted biomolecules[28].

Mass analyzer	mass resolving power $(m/\Delta m)$	m/z range	pixels/s	Tandem MS capabilities	Application
Linear TOF	10^3	$0\text{-}10^6$	>10	no	peptides/proteins
Reflectron TOF	$10^3\text{-}10^4$	$0\text{-}10^5$	>10	MS^2	drug/metabolites/peptides/lipids
QqTOF	$10^3\text{-}10^4$	100-6k	>10	MS^2	drug/metabolites/peptides/lipids
Linear ion trap	$10^2\text{-}10^3$	50-3k	1	MS^n	drug/metabolites/peptides/lipids
Triple quadrupole	$10^2\text{-}10^3$	50-5k	>100	MS^2	drug/metabolites/peptides/lipids
FT-Orbitrap	$10^4\text{-}10^6$	50-10k	0.5-1.5	MS^n	drug/metabolites/peptides/lipids
FT-ICR	$10^4\text{-}10^5$	100-10k	1	MS^n	drug/metabolites/peptides/lipids

As MALDI-IMS is the imaging technique used in this thesis, a brief description of the experimental workflow is offered below.

During a MALDI-IMS experiment, the surface of the selected area in the study tissue is raster-scanned with a defined distance between laser pulses. Each beam will generate a spectrum with molecular information, providing a new dimension to the experiment: the spatial resolution. This enables the collection of distribution maps of all the molecules detected across the analyzed area. The next steps consist of performing statistical analysis to visualize histological regions of interests, as well as identification of biomolecules. **Figure 2.7** shows a scheme of a typical MALDI-IMS experiment.
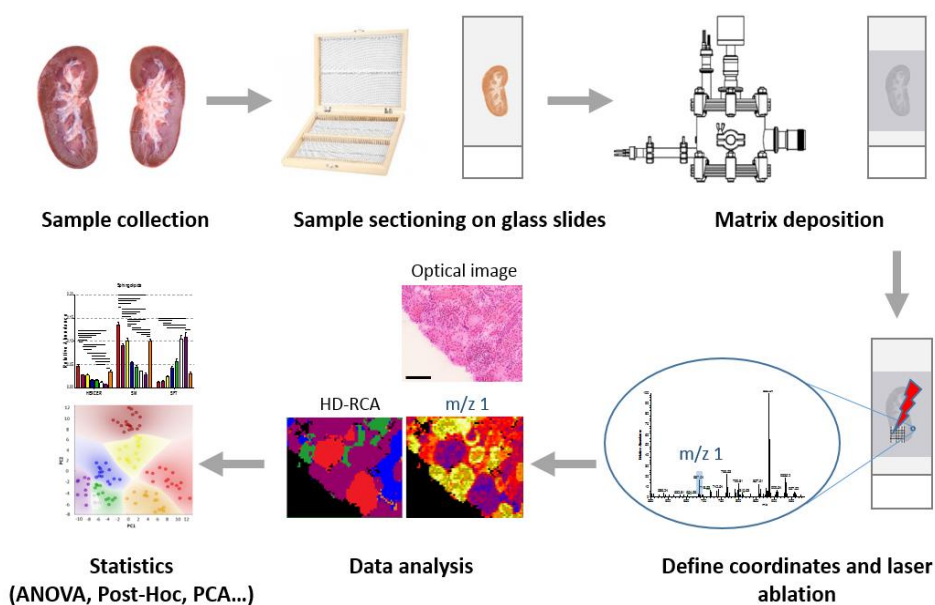
Figure 2.7. *Workflow of a typical MALDI-IMS experiment. Frozen samples are cryosectioned and thaw-mounted on glass slides. After the deposition of a thin coat of matrix, a virtual grid is defined, as well as the separation space between laser irradiations. Once the laser rasters the whole area selected, molecular images are reconstructed. Finally, the tissue section is stained and with the optical information and statistical analysis performed over the experiment, regions of interest or patterns are recognized. Further statistical analysis can be used to hunt for biomarkers or to build classification models.*

2.3 Liquid Chromatography

Liquid chromatography (LC) is a technique used to physically separate the different components of a solution, thanks to the selective adsorption of its constituents on a stationary phase. It consists of two phases: an immiscible stationary phase, which remains fixed in a column or chromatographic bed, and a mobile phase, which is a liquid or a mixture of liquids that flows through the stationary phase and it helps the analytes to flow through the column. The stationary phase is a solid adsorbent with a large surface area and is usually made of alumina, silica or ion-exchange resins. The active centers that are located on the surface of the stationary phase interact with the polar functional groups of our solution and separation occurs as a consequence of the different intensity of such interactions for the different compounds.

Depending on the polarity of the phases, two types of liquid chromatography can be distinguished: normal phase and reverse phase LC. In normal phase LC, relatively non-polar mobile phase (hexane, isopropyl ether, etc) and a very polar stationary phase is used, which makes the less polar analytes migrate faster and also by increasing the polarity of the mobile phase, the retention time is reduced. On the other hand, reverse phase LC employs a non-polar stationary phase and a relatively more polar mobile phase (H_2O, MeOH, AcN). In this case, more polar analytes will appear earlier and elution time will increase by increasing the polarity of the mobile phase[29].

High performance liquid chromatography (HPLC)

Although there are several types of liquid LC, HPLC is the most widely used, specially in the analysis of biomolecules. In high performance liquid chromatography, the stationary phase is confined within a cylindrical column, through which the mobile phase and the anlaytes flow. This configuration allows increasing the pressure of the eluent, thus increasing its linear speed, minimizing diffusion effects and increasing its chromatographic resolution.

In addition, this technique permits the modification of the mobile phase throughout the analysis, so that the time that takes to each compound to elute (retention time RT) is characteristic not only for the analyte's nature but also for the specific conditions of the analysis.

Although the most common detectors for the detection of eluted analytes in a HPLC system are UV / Vis or fluorescence, it is also possible to couple the column outlet directly to a mass spectrometer equipped with an ESI source and obtain the mass spectrum for each point (retention time) of the chromatogram. That is, using a coupled HPLC-MS system it is possible to first separate the compounds by their polarity in the chromatographic column and then obtain the spectrum for each of them. Consequently, it is possible to obtain the spectrum of compounds with the same mass

but different retention time and simplifying their identification and the selection of the parents for MS/MS or MS^E fragmentation studies[29].

An improved subtype of HPLC is ultra high performance liquid chromatography (uHPLC), which will be the one used in this thesis. The major difference between HPLC and uHPLC is that, due to particle size, uHPLC works at higher pressures, achieving reduced run time, lower solvent consumption, and better analysis separation and detection.

2.4   Lipids and Lipidomics

In accordance with the literature, Lipidomics is the study of the structure and function of the complete set of lipids produced in a given cell or organism, as well as their interactions with other lipids, proteins or metabolites[30, 31].

The general structure of the lipids is amphipathic, although some exceptions are also found, including triacylglycerols or triglycerides (TG), diacylglicerols or diglycerides (DG), ceramides (Cer), cholesteryl ester (ChE), and waxes, which are mainly hydrophobic. They contain essentially hydrocarbons, which compose the building blocks of the structure and function of living cells[30]. Genetics, cell biology and biochemistry have fundamentally advanced our understanding of the biology of lipids in recent years, revealing the important roles they play in cells, including energy storage, structural components of cell membranes, cell signaling and membrane trafficking[21].

Besides, enzymes that regulate lipids levels also play a role in modulating lipid intermediates that serve as signaling nodes to influence a wide range of physiological processes[32-34]. Particularly, the enzymes that modulate the expression of glycerolipids have been of interest as potential drug targets[33, 35].

According to a well-known chemical structure-based lipid classification[1], eight major lipid groups exist[36]: fatty acids, glycerolipids, glycerophospholipids, sphingolipids, sterols, prenols, saccharolipids and polyketides (**Table 2.3**).

Table 2.3. *Lipid categories with their respective abbreviations and major roles that each play in cell biology[36].*

Lipid class	Abbreviation	Main function
Fatty acids	FA	Building blocks for complex lipids
Glycerolipids	GL	Energy storage
Glycerophospholipids	GP	Structural and signaling lipids
Polyketides	PK	Antimicrobial. Precursors for other molecules.
Prenols	PR	Antioxidant. Precursors of vitamins. Cell trafficking
Saccharolipids	SL	Structural
Sphingolipids	SP	Signal transduction and cell recognition
Sterols	ST	Structural and signaling lipids

Fatty acids, glycerolipids, glycerophospholipids and sphingolipids are the lipid classes covered in this thesis. Consequently, a brief description will be given below.

Fatty Acids

Fatty acids are the major components of complex lipids and consequently, one of the most elemental lipid classes in biological systems. They are composed of a carboxylic acid attached to hydrocarbon chains of variable lengths and with different degree of saturation, which defines their specific function.

In mammalian cells, fatty acids naturally contains an even number of carbons (between 14 and 22) with different number of unsaturations from 0 to 6[31]. Example of some of the most relevant fatty acids are shown in **Figure 2.8.**
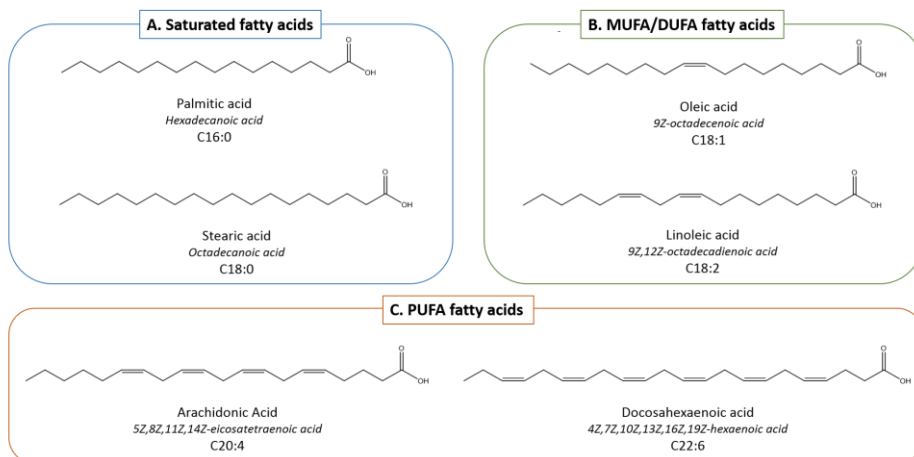
Figure 2.8. *Illustrative examples of most common fatty acids in mammalian cells. (A) Saturated FA: palmitic acid (C16:0) and stearic acid (C18:0). (B) Mono or diunsaturated FA: oleic acid (C18:1) and Linoleic acid (C18:2). (C) Polyunsaturated FA: arachidonic acid (AA-C20:4) and docosahexanoic acid (DHA-C22:6); both molecules are involved in the inflammatory response.*

Glycerolipids

Glycerolipids are a heterogeneous lipid group that play key structural and functional roles in bacterial, plant and animal cell membranes. Structurally, they all have at least one hydrophobic chain attached to a glycerol backbone by an ester or ether linkage[37]. The most abundant glycerolipid class is triglycerides, also called neutral fats, which have the three hydroxyl groups of glycerol esterified, typically by different fatty acids (**Figure 2.9**). Furthermore, monoacylglycerides (only one glycerol group esterified) or diacilglycerides (two hydrophobic chains attached to the glycerol backbone) are involved in relevant biological processes[38].
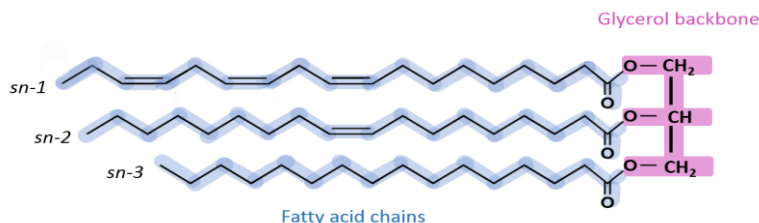
Figure 2.9. *Example of an unsaturated triglyceride (TG 52:4) with different fatty acid (blue shading) attached to the glycerol backbone (pink shading) in sn1 position (alpha linoleic acid 18:3), in sn-2 position (palmitic acid 16:0) and in sn-3 position (oleic acid 18:1).*

Regarding the glycolipids' main function, these lipids comprise the bulk of storage fat in animal tissues being the main energy store molecules. The hydrolysis of their ester bonds and the release of glycerol and fatty acids from adipose tissue are the initial steps in metabolizing fat[38].

Other subclasses of glycerolipids are described as glycosylglycerols, which are characterized by the presence of one or more monosaccharides linked to glycerol by a glyosidic linkage **(Figure 2.10).** Examples of glycosylglycerols are the digalactosyldiacylglycerols found in membranes of vegetal cells[39] and seminolipid from mammalian sperm cells[40].
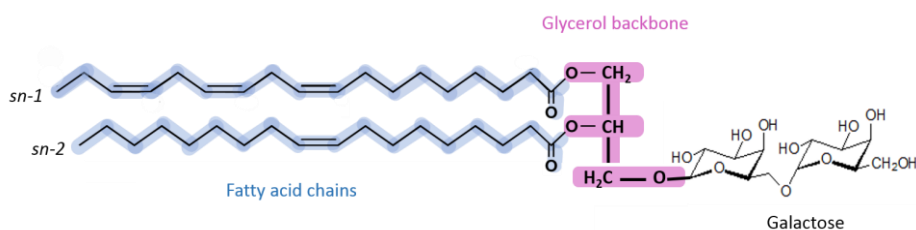
Figure 2.10. *Example of a glycosylglycerol (digalactosyldiacylglycerol) with different fatty acid (blue shading) and a disaccharide attached to the glycerol backbone (pink shading) in sn1 position (alpha linoleic acid 18:3), in sn-2 position (palmitic acid 16:0) and in sn-3 position (galactose).*

Glycerophospholipids

Glycerophospholipids (GPL), also called phospholipids or phosphoglycerides, are ubiquitous in nature and are key components of the cells lipid bilayers. Consequently, they are the lipid subclass most abundant in cells and are involved in diverse cellular metabolism pathways[41].

Their structure is similar to glycerolipids, being composed of a glycerol backbone with fatty acids linked to the sn-1 and sn-2 positions and a hydrophilic head attached to sn-3 position (**Figure 2.11**). This configuration provides the amphipathic character to these biomolecules.

Although their fatty acid length and their degree of saturation can be variable, saturated acyl chains tend to bond at the sn-1 position, while polyunsaturated and monounsaturated are more often found at the sn-2 position[42]. Moreover, the linkage group between the sn-1 position and the glycerol backbone is usually an acyl (ester) group. However, plasmanyl and plasmalogen lipid subclasses have respectively an alkyl group (ether GPL) or an alkenyl group (vinyl-ether GPL) as linkage groups. On the other

hand, the polar head group consists of a phosphate bound to a head group substituent, such as a choline, ethanolamine, glycerol, serine or inositol.
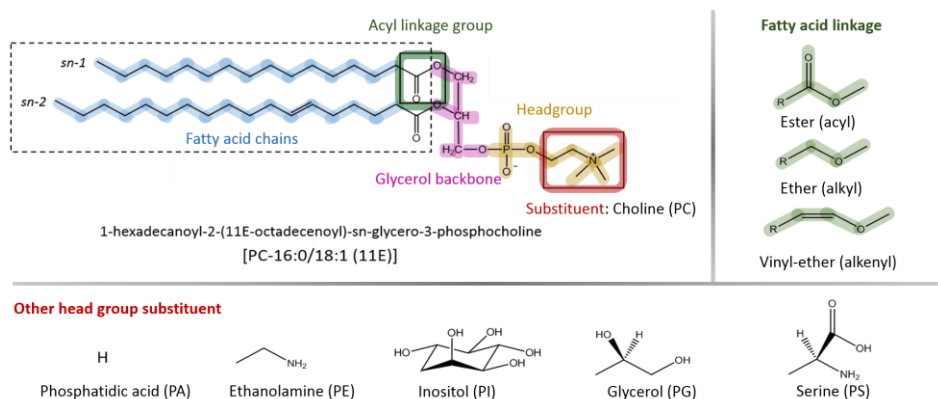
Figure 2.11. Example of a glycerophospholipid: glycerophosphocholine. Glycerol backbone is shaded in pink, the two fatty acids attached to sn-1 and sn-2 positions are in blue, the head group at sn-3 is yellow shading and the head group substituent is marked in red. Depending on the head group substituent, different classes of GP can be formed (bottom panel). Furthermore, the different fatty acid linkage groups are shown in the right panel.

Considering all the information above, the different head group subsitutents confer distinctive properties to each phosphoglyceride subclass. All head groups have a negative charge on the phosphate esterified to glycerol. However, their net charge varies depending on the substituent; neutral phosphoglycerides (glycerophosphoethanolamines (PE) and glycerophosphocholines (PC)) have a positive charge on their nitrogens, giving them a zero charge, glycerophosphoserines (PS) has extra positive and negative charges, giving it a net negative charge like the other acidic phosphoglycerides (glycerophosphophates (PA), glycerophosphoglycerols (PG), and glycerophosphoinositols (PI)) [43]. These variations on the phospholipids charge are related with the asymmetry of lipid bilayer (**Figure 2.12**). Negatively charged glycerophospholipids, especially PS, tend to be in the cytoplasmic side of the bilayer while positively charged ones (mainly PC, glycosphingolipids (GS) and sphingomyelins (SM), see following section), are predominantly found in the outer leaflet of the plasma membrane[44].
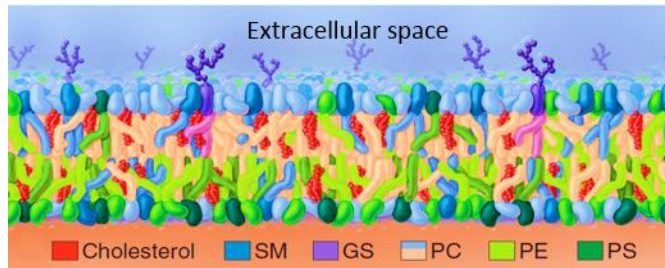
Figure 2.12. Asymmetrical distribution of lipids in the animal cellular plasma membrane. SM and cholesterol form a small cluster in the external leaflet while PS is more often found in the inner leaflet. Image adapted from ref 44.

Sphingolipids

Sphingolipids are essential components of the cell membrane which have relevant roles in signal transduction and cell recognition[45]. This lipid class gets its name from sphingosine, a nitrogen-containing base synthesized from serine and a variable fatty acid, which acts in sphingolipids as the backbone of glycerol in phosphoglycerides[44]. Moreover, variations in the sphingosine base leads to different sphingoid-base backbones that can assemble other sphingolipids.

Two more variable features can distinguish the different sphingolipids: the acyl chain (often lacking double bonds) attached by an amide bond to *sn-2* position and the nature of the polar head group esterified to the hydroxyl on *sn-1* position (**Figure 2.13**).

The vast majority of sugar-containing lipids of biological membranes are sphingolipids, which are commonly named as glycosphingolipids or cerebrosides (GS or HexCer). This lipid group includes one or more sugars in their *sn-1* position as a part of the head group. When this sugar is sulfated, the sulfatides class is formed, a lipid subclass that has relevant roles in several physiological processes including in nervous, urinary and immune systems[46].

Alternatively, a phosphate ester attached to a choline or ethanolamine molecule can also be linked to this *sn-1* position to form sphingomyelins (SM) or ceramide phosphoethanolamine (Cer-PE) respectively.
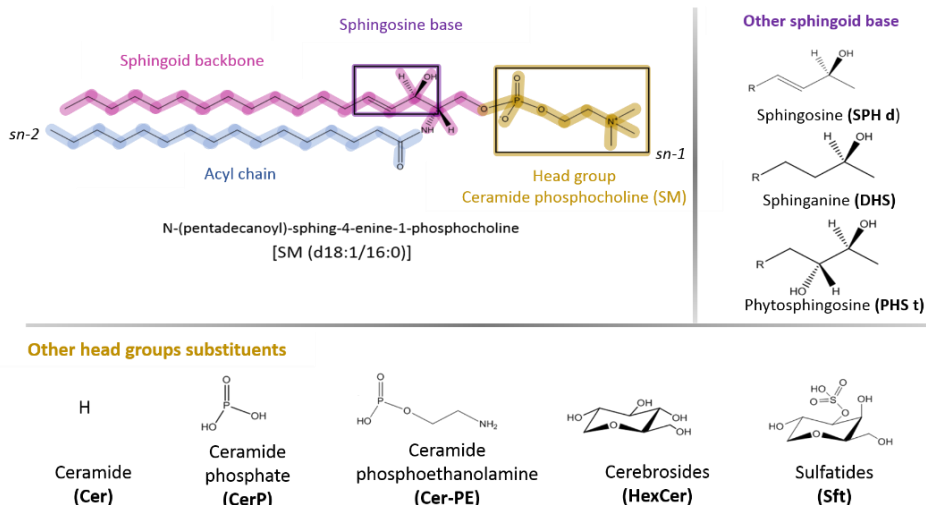
Figure 2.13. *Example of a sphingolipid; sphingomyelin is represented as an example. Sphingolipids consist of a sphingoid backbone with variable sphingoid base, an N-acyl at sn-2 position and a head group, which defines the sphingolipid type (bottom panel).*

Nomenclature

The nomenclature used in this thesis is as follows:

1. According to **Figure 2.11** and **Figure 2.13**, lipid class abbreviations (PC, PI, SM, PE…) will be used from now in figures and text.

2. Regarding the ether fatty acid linkage in glycerophospholipids, as far as we are concerned with our equipment, it is not possible to distinguish between ether (-O) or a vinyl-ether (-P) even with MS/MS. For instance, PE-vinyl-ether (PE-P), the so-called plasmalogen, and PC-ether (PC-O) are the most abundant types in mammalian cells although, once more, we cannot discard the presence of PE-O and PC-P[47, 48]. Thus, for simplicity sake, we will name them as PE-O/P and PC-O/P. Specifically, in **Chapter 9** we named all the ether bonds-contained PE as plasmalogens or PE-P, as these species are the most abundant ether linkage type in brain tissue. Nevertheless, we can not discard the presence of PE-O.

3. The number of carbons of both fatty acids and the total unsaturations will be summed and the total number will be indicated unless we have data on the precise composition of the two fatty acids.

1. Liebisch, G. *et al*. Update on LIPID MAPS classification, nomenclature, and shorthand notation for MS-derived lipid structures. *J. Lipid Res.* **61**, 1539-1555 (2020).

2. Dass, C. in *Fundamentals of contemporary mass spectrometry* (John Wiley & Sons, 2007).

3. Watson, J. T. & Sparkman, O. D. in Introduction to mass spectrometry: instrumentation, applications, and strategies for data interpretation (John Wiley & Sons, 2007).

4. Lotz, W. Electron-impact ionization cross-sections and ionization rate coefficients for atoms and ions from hydrogen to calcium. *Zeitschrift für Physik* **216**, 241-247 (1968).

5. Benninghoven, A., Nihei, Y., Shimizu, R. & Werner, H. Secondary ion mass spectrometry SIMS II. *Springer Ser.Chem.Phys* **9** (1979).

6. Smith, R. D., Loo, J. A., Edmonds, C. G., Barinaga, C. J. & Udseth, H. R. New developments in biochemical mass spectrometry: electrospray ionization. *Anal. Chem.* **62**, 882-899 (1990).

7. Hillenkamp, F., Karas, M., Ingendoh, A. & Stahl, B. Matrix assisted UV-laser desorption/ionization: A new approach to mass spectrometry of large biomolecules. *Biological Mass Spectrometry, Burlingame et al.,(eds.), Elsvier Science Pub., Amsterdam*, 49-60 (1990).

8. Nemes, P. & - Vertes, A. - Laser ablation electrospray ionization for atmospheric pressure, in vivo, and imaging mass spectrometry. - *Analytical Chemistry*, - 8098.

9. Mann, M., Meng, C. K. & Fenn, J. B. Interpreting mass spectra of multiply charged ions. *Anal. Chem.* **61**, 1702-1708 (1989).

10. Whitehouse, C. M., Dreyer, R., Yamashita, M. & Fenn, J. Electrospray ionization for mass-spectrometry of large biomolecules. *Science* **246**, 64-71 (1989).

11. Wiseman, J. M., Ifa, D. R., Song, Q. & Cooks, R. G. Tissue imaging at atmospheric pressure using desorption electrospray ionization (DESI) mass spectrometry. *Angewandte Chemie International Edition* **45**, 7188-7192 (2006).

12. Thomas, J. J., - Shen, Z. X., - Crowell, J. E., - Finn, M. G. & - Siuzdak, G. - Desorption/ionization on silicon (DIOS): A diverse mass spectrometry platform for protein characterization. - *Proceedings of the National Academy of Sciences of the United States of America*, - 4932.

13. Gandhi, K., Kumar, A., Sarkar, P., Aghav, A. & Lal, D. NALDI-TOF MS: Applications in Dairy and Related Sectors.

14. Fuchs, B., - Suss, R. & - Schiller, J. - An update of MALDI-TOF mass spectrometry in lipid research. - *Progress in lipid research*, - 450.

15. Karas, M., Bachmann, D., Bahr, U. e. & Hillenkamp, F. Matrix-assisted ultraviolet laser desorption of non-volatile compounds. *International journal of mass spectrometry and ion processes* **78**, 53-68 (1987).

16. Paul, W. & Steinwedel, H. A new mass spectrometer without a magnetic field. Zeitschrift fuer Naturforschung (West Germany) Divided into Z.Nautrforsch., A, and Z.Naturforsch., B: Anorg.Chem., Org.Chem., Biochem., Biophys., **8** (1953).

17. Stafford, G., Kelley, P., Syka, J., Reynolds, W. & Todd, J. Recent improvements in and analytical applications of advanced ion trap technology. *International Journal of Mass Spectrometry and Ion Processes* **60**, 85-98 (1984).

18. March, R. E. An introduction to quadrupole ion trap mass spectrometry. *Journal of mass spectrometry* **32**, 351-369 (1997).

19. Hu, Q. *et al*. The Orbitrap: a new mass spectrometer. *Journal of mass spectrometry* **40**, 430-443 (2005).

20. Han, X. in Lipidomics: Comprehensive mass spectrometry of lipids (John Wiley & Sons, 2016).

21. Ståhlman, M. *et al*. High-throughput shotgun lipidomics by quadrupole time-of-flight mass spectrometry. *Journal of Chromatography B* **877**, 2664-2672 (2009).

22. Chughtai, K. & - Heeren, R. M. A. - Mass Spectrometric Imaging for Biomedical Tissue Analysis. - *Chemical reviews*, - 3237.

23. McDonnell, L. A. & - Heeren, R. M. A. - Imaging mass spectrometry. - *Mass spectrometry reviews*, - 606.

24. Karas, M. & Hillenkamp, F. Laser desorption ionization of proteins with molecular masses exceeding 10,000 daltons. *Anal. Chem.* **60**, 2299-2301 (1988).

25. Spengler, B., Hubert, M. & Kaufmann, R. *MALDI ion imaging and biological ion imaging with a new scanning UV-laser microprobe* (Proceedings of the 42nd Annual Conference on Mass Spectrometry and Allied Topics Ser. 1041, Chicago, 1994).

26. Caprioli, R., Farmer, T. & Gile, J. Molecular imaging of biological samples: localization of peptides and proteins using MALDI-TOF MS. (1997).

27. Mascini, N. Mass Spectrometry Imaging for the Classification of Tumor Tissue (2016).

28. Norris, J. L. & Caprioli, R. M. Analysis of tissue specimens by matrix-assisted laser desorption/ionization imaging mass spectrometry in biological and clinical research. *Chem. Rev.* **113**, 2309-2342 (2013).

29. Snyder, L. R., Kirkland, J. J. & Dolan, J. W. in *Introduction to modern liquid chromatography* (John Wiley & Sons, 2011).

30. Griffiths, W. J. & Wang, Y. in *Lipidomics: Current and Emerging Techniques* (Royal Society of Chemistry, 2020).

31. Spener, F., Lagarde, M., Géloên, A. & Record, M. What is lipidomics? *European journal of lipid science and technology* **105**, 481-482 (2003).

32. Prentki, M. & Madiraju, S. M. Glycerolipid metabolism and signaling in health and disease. *Endocr. Rev.* **29**, 647-676 (2008).

33. Scott, S. A., Mathews, T. P., Ivanova, P. T., Lindsley, C. W. & Brown, H. A. Chemical modulation of glycerolipid signaling and metabolic pathways. *Biochimica et Biophysica Acta (BBA)-Molecular and Cell Biology of Lipids* **1841**, 1060-1084 (2014).

34. Csaki, L. S. *et al*. Lipins, lipinopathies, and the modulation of cellular lipid storage and signaling. *Prog. Lipid Res.* **52**, 305-316 (2013).

35. Zhang, P. & Reue, K. Lipin proteins and glycerolipid metabolism: Roles at the ER membrane and beyond. *Biochimica et Biophysica Acta (BBA)-Biomembranes* **1859**, 1583-1595 (2017).

36. Fahy, E. *et al*. A comprehensive classification system for lipids. *European journal of lipid science and technology* **107**, 337-364 (2005).

37. Bittman, R. Glycerolipids: chemistry. *Encyclopedia of biophysics.Springer: Heidelberg, Berlin*, 907-914 (2013).

38. Mathews, C. & HOLDE, V. KE Biochemistry. (1996).

39. Hölzl, G. & Dörmann, P. Structure and function of glycoglycerolipids in plants and bacteria. *Prog. Lipid Res.* **46**, 225-243 (2007).

40. Honke, K., Zhang, Y., Cheng, X., Kotani, N. & Taniguchi, N. Biological roles of sulfoglycolipids and pathophysiology of their deficiency. *Glycoconj. J.* **21**, 59-62 (2004).

41. Berridge, M. J. & Irvine, R. F. Inositol phosphates and cell signalling. *Nature* **341**, 197-205 (1989).

42. Yamashita, A., Sugiura, T. & Waku, K. Acyltransferases and transacylases involved in fatty acid remodeling of phospholipids and metabolism of bioactive lipids in mammalian cells. *The Journal of Biochemistry* **122**, 1-16 (1997).

43. Lodish, H. *et al*. in *Molecular cell biology* (Macmillan, 2008).

44. Pollard, T. D., Earnshaw, W. C., Lippincott-Schwartz, J. & Johnson, G. in *Cell Biology E-Book* (Elsevier Health Sciences, 2016).

45. Futerman, A. H. in Biochemistry of Lipids, Lipoproteins and Membranes 297-326 (Elsevier, 2016).

46. Xiao, S., Finkielstein, C. V. & Capelluto, D. G. in *Lipid-mediated Protein Signaling* 27-40 (Springer, 2013).

47. Braverman, N. E. & Moser, A. B. Functions of plasmalogen lipids in health and disease. *Biochimica et Biophysica Acta (BBA)-Molecular Basis of Disease* **1822**, 1442-1452 (2012).

48. Magnusson, C. D. & Haraldsson, G. G. Ether lipids. *Chem. Phys. Lipids* **164**, 315-340 (2011).

Chapter 3

Materials and Methods

This chapter includes a comprehensive description of sample preparation, experimental settings as well as data analysis. More detailed annotations or specific analysis methods will be described in following chapters.

3.1 MALDI-IMS

Sample preparation

Sample preparation is a crucial step that is directly associated with the quality of the imaging results. This includes not only the matrix application process but also tissue sampling procedures and tissue sectioning techniques. Each process can be affected by many parameters that consequently, can potentially affect the quality of the final images[1].
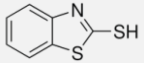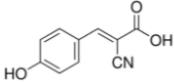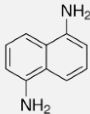
As the samples involved in this thesis are mainly from human biopsies, tissue sampling procedures and sectioning techniques were carried out by our collaborators from BioCruces (Universitary Hospital from Cruces, Bizkaia, Spain), the department of nephrology in the Fundación Jiménez Díaz universitary hospital (Madrid, Spain), from the Proteomic platform in CiC biogune (Derio, Bizkaia Spain) and from Lipids in Human Pathology group from Balearic Islands Health Research Institute (Son Espases University Hospital) complying with the current Spanish and European Union legal regulations.

Briefly, biopsies were obtained from a series of surgical interventions and subsequently sectioned on a cryostatized microtome into slices of between 10 and 20 μm. Then, they were placed on a glass sample holder which remained stored frozen (-80º) until MALDI-IMS analysis.

Regarding matrix deposition, the choice of matrices were 2-mercaptobenzothiazole (MBT, Sigma-Aldrich Chemie, Steinheim, Germany)[2] and α-cyano-4-hidroxicinamic acid (CHCA, Sigma-Aldrich Chemie, Steinheim, Germany) for positive-ion mode and 1,5-diaminonaphthalene (DAN, Sigma-Aldrich Chemie, Dteinheim, Germany)[3] for negative-ion mode. These matrices are particularly efficient for lipid analysis in an Orbitrap system, enabling the detection of a wide variety of lipid classes with outstanding signal/noise, high-resolution. They also present stability needed under vacuum conditions, enabling experiments with long acquisition times.

Another critical point is the deposition method. Most of the available methods use solutions of matrix dissolved in a water/organic solvent mixture, such as the dry droplet approach[4], electrospray deposition[5], spray coating using an airbrush[6], and inkjet printing[7]. However, there is a high risk of analyte delocalization with these methods due to the water/organic mixture. Additionally, two solvent free techniques, dry-coating[8] and sublimation[9], have been reported as a method of deposition of matrix on tissue sections for lipid analysis with, theoretically, no analyte delocalization[10]. Taking all the information above into consideration, sublimation was the main method used in this thesis in an attempt not to perturb the nature of the sample by migration of biomolecules although spraying have been also used **(Table 3.1).**

Table 3.1. Matrixes used in this work with its specifications and the deposition method applied for each one.

Matrix	Molecule	Monoisotopic mass	Ionization mode	Deposition mode
*2-mercaptobenzotiazole (**MBT**)*		166.986 Da	(+) (-)	Sublimation
*α-cyano-4-hidroxicinamic acid (**CHCA**)*		194.084 Da	(+)	Spraying AcN/H2O (4:1)
*1,5-diaminonaftalene (**DAN**)*		158.084 Da	(-)	Sublimation

A commercial glass sublimator, an in-house designed stain steel sublimator and the HTX-TM Saprayer™ were used in this thesis. Thus, a brief protocol description will be given above.

Commercial glass sublimator

As shows **Figure 3.2**, an Ace Glass 8023 standard sublimator (Vineland, NJ, USA) was filled with the appropriate matrix substance and the glass slide containing the tissue section was attached to the bottom of the cold finger. Then, the sublimator was evacuated with the aid of a mechanical pump (Pfeiffer Vacuum, model DUO 2.5, Germany) and placed on top of the hot plate that was already set at a temperature of 120°C. Therefore, the cold finger was filled with ice and water and the whole system was placed on top of a heating plate. The sublimation process was carried out with the vacuum on during 8 min for both DAN and MBT matrixes, following the protocols developed in previous optimization studies[11]. Thus, the matrix was sublimed and condensed on the surface of the cold sample generating a thin layer of ~ 0.1-0.2 mg/cm^2 of small crystals.
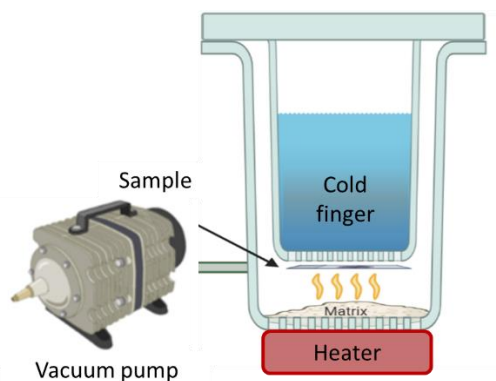
Figure 3.2. Schematic commercial glass sublimator process.

Home designed stain steel sublimator

Matrix deposition with the stainless steel sublimator followed a slightly different protocol. As figures in **Figure 3.3**, the matrix was placed inside the sublimator chamber, while the glass slide with the tissue was fixed to a Peltier cell inverted just above the matrix. The Peltier plate acts as the cooling system and enables setting the temperature at 5 ºC and controlling it during the whole process.

Vacuum was also monitored precisely, allowing us to start the sublimation when the vacuum pressure reached 0.4 mBar. Optimal deposition time was 10 min for MBT and either 8 min or 12 min for DAN, depending on the heating temperature. An extensive description of the stain steel sublimator can be found in **Chapter 4**.
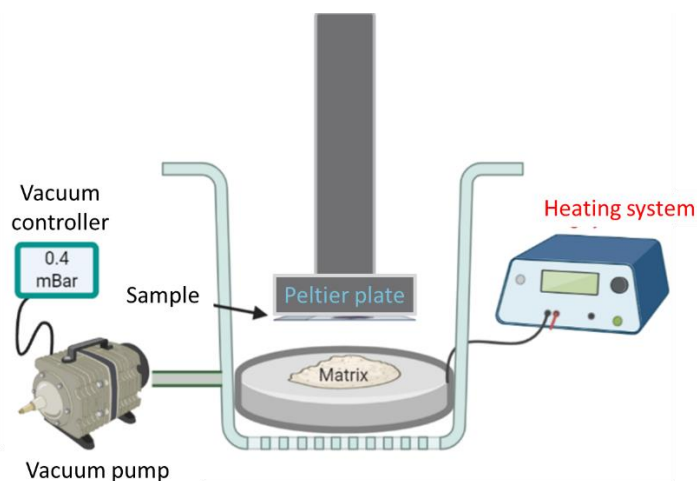
Figure 3.3. Schematic home designed stain steel sublimator process.

<u>HTX –TM Sprayer</u>

The matrix deposition of some samples included in this thesis was performed by spraying using the HTX-TM Sprayer™ (HTX technologies, Chapel Hill, NC, USA).

The HTX TM-Sprayer enables to adjust both gas flow rate and nozzle velocity to control drying time, preventing analyte delocalization and the formation of large matrix crystals. The method used was as indicated in **Table 3.2**

Table 3.2. *TM-HTX sprayer method*

Matrix	CHCA (AcN/H2O (4:1))
Number of passes	NP=8
Matrix concentration	Cm=5 mg/ml
Matrix flow rate	FRm=100 µL/min
Nozzle velocity	V=600 mm/min
Track spacing	TS= 3 min
Nitrogen pressure	10 psi
Dry gas temperature	75°C
Nozzle distance	46mm

MALDI-IMS analysis

The main MALDI-IMS experiments involved in this thesis were performed using a MALDI-LTQ-Orbitrap XL (ThermoFisher), located at SGIKER platform from UPV/EHU facilities (Leioa, Spain) The spectrometer was operated in Orbitrap mode. Data were acquired with a mass resolution of 60.000 at m/z=400 Da in the scanning range of 550-1000 for negative-ion mode and 480-1100 for positive-ion mode. Two microscans of 10 laser shots were recorded for each pixel. Instrument calibration was performed once a week using the standard calibration mixture (ProteoMass MALDI Calibration Kit for LTQ XL and LTQ Hybride, Sigma − Aldrich, MA, USA).
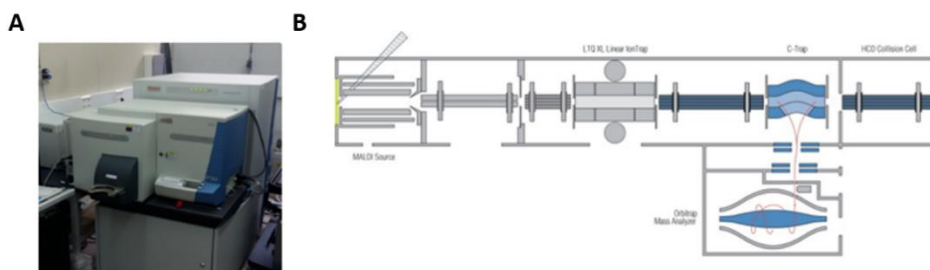
Figure 3.4. (A) *Image of MALDI-LTQ-Orbitrap XL used for the acquisition of data in this thesis.* **(B)** *Schematic diagram representing the components of the instrument.*

Additionally, an Autoflex III smartbeam MALDI TOF/TOF MS (Bruker Daltonics) located in the proteomics platform from CiC-Biogune (Derio, Spain) was involved in the second section included in **Chapter 4**.

Moreover, samples involved in **Chapter 10** were analyzed in a MALDI 8020 (Benchtop Linear MALDI-TOF Mass Spectrometer, Shimadzu) located in Kratos Analytical Ltd (Manchester, UK).

Further specific parameters for each study, such as laser energy and raster size used, will be reported in following chapters.

Hematoxylin & Eosin (H&E) staining

Once an imaging experiment was finished, the tissue section was washed off the tissue for a post hematoxylin and eosin (Sigma-Aldrich, Madrid, Spain) staining protocol.

Briefly, the matrix was removed from the surface of the sections by immersion of the glass slide in a 70% ethanol solution for approximately 1 min. After a hydration process of the sections in a graded ethanol series to water, glass slides were immersed, first in hematoxylin for 5 min and then in eosin for 2 min. This was followed by a dehydration process in graded ethanol starting with water and up to 100% ethanol before clearing it with citrosol and mounting it with DPX. Hematoxylin stains nucleic acid with a deep blue-purple color (nuclei), and eosin nonspecifically stains proteins with pink (cytoplasm and extracellular matrix). Stained tissue section were scanned in a NanoZoomer S210 Digital slide scanner (C13239-01 model) located in the PIE (Plentzia Marine Station,UPV/EHU, Pletzia, Bizkaia).

Data processing

Spectra were analyzed using in-house developed software, built in Matlab (MathWorks, Natick, USA). The spectra were subjected to peak selection using the Simple

Peak Finding (SPF) method[13]. Subsequently, spectra were aligned using the Xiong method[14] assuming a maximum misalignment of 0.02 amu. Finally, the spectra were normalized using a total ion current algorithm (TIC). During graphical representation, no interpolation or smoothing algorithm or any de-noising procedure was used, always trying to maintain the original features of the data.

Lipids assignment

Lipid assignment was based upon comparison between the experimental m/z and the species in the software's database (>33,000 lipid species and their adducts), and those in the LIPID MAPS database (www.lipidmaps.org). Mass accuracy was always better than 5 ppm and it was typically better than 3 ppm in the individual spectra. In this type of analysis, mass accuracy depends to some extent on the peaks' intensity and thus, higher intensity m/z values have a better mass accuracy.

Statistical analysis

Only reproducible lipid species were used in multiple comparative studies to minimize the inter-patient variability. For that, the 80% rule was applied, meaning that if the standard deviation of a specie was above the set threshold of 80% of its average value, it was considered not reproducible within a group and it was removed from the analysis. This was performed with the idea of obtaining the reproducible lipid profiles of the groups.

Regarding lipid abundance, MALDI-IMS is not a quantitative technique and only gives relative abundances within each lipid class. This means that signal intensity cannot be translated directly into lipid abundance, whereby one must limit the discussion in further chapters to analyze relative variations in the intensity of the species of a given family.

To group together ions with high correlation, and to represent the original IMS data in a more visual format for further analysis, the well-known *k-means*[15, 16] and an in-house programmed clustering algorithm were used. The fundamentals were already described in a previous publication[17]. The segmentation algorithm, *RankCompete*[18], is based on the properties of *Markov Chains*[19] to define *Random Walker*[20] competing to divide the imaging experiment into a number of segments with enough variability to describe independent histologic areas. The starting point for each walker was decided using a variation of the Divisive Analysis algorithm (DIANA). Thus, the final software is a segmentation algorithm based on DIANA and using RankCompete as split function. In this way, it is possible to use the correlation value between the segments to assign a color to each segment using a color scale and 1-correlation between the segments. Thus, the two segments that present the lowest correlation occupy the two extremes of the scale and those segments with more similar average spectra receive colors that are closer in the scale.

Data are presented as means ± S.E.M. Statistical analyses used in each study are described in each chapter, but results are always reported using a significance level of $p<0.05$.

The software used were SPSS Statistics 17.0 (IBM, Armonk, NY, USA)[21] for the univariate statistical analysis and Orange Biolab (Ljubljana, Slovenia)[22] for multivariate statistical analysis.

3.2   uHPLC

Reagents, equipment and software

Water, methanol, acetonitrile, 2-propanol and optima® LC / MS quality formic acid and HPLC grade chloroform were purchased from Fisher Scientific (Fair Lawn, NJ, USA). Hydrated leucine encephalin acetate (95% purity), sodium hydroxide solution (~ 0.1M, HPCE grade) and ammonium acetate (99.99% purity) were purchased from Sigma-Aldrich Chemie (Steinheim, Germany). The internal standards *Splash LipidoMix* and *Ceramide / Sphingoid Mixture I* were supplied by Avanti Polar Lipids (Alabaster, Alabama).

The internal standards Splash Lipidomix, Cer/Sph mixture I, Cardiolipin Mix I, 24:0(d4) L-carnitine, D18:1/12:0 monosulfogalactosyl (β) ceramide (NH_4 Salt) and Oleic acid (d9) were supplied by Avanti Polar Lipids (Alabaster, Alabama).

The uHPLC equipment used for this work was the model ULTIMATE 3000, (Thermoscientific), coupled with a mass-time quadrupole type detector (QqTOF QExactive HF-X, Thermoscientific).

The software used was: (I) Xcalibur 4.1 (Thermoscientific) for the acquisition and conversion of the data, respectively; (II) LipidSearch versión 4.2.2 (Thermoscientific) for the detection of peaks, alignment and structural lipid identification; (III) Excel 2016 (Microsoft Office, Redmond, WA, USA) and SPSS Statistics 17.0 (IBM, Armonk, NY, USA) for the univariate statistical analysis; and, (IV) Orange Biolab (Ljubljana, Slovenia) for multivariate statistical analysis.

Sample preparation

<u>Human sample collection</u>

The samples analyzed by uHPLC in this thesis were obtained from kidney biopsies of 20 clear cell renal cell cancer (ccRCC)-patients from the Universitary Hospital of Basurto (Bilbao, Spain). All patients were informed about the potential use for research of their surgically resected tissues, and manifested their consent by signing a specific document

approved by the Ethical and Scientific Committees of the Basque Country Public Health System (PI+CES-BIOEF 2018-04).

From each renal biopsy, adjacent normal tissue was separated from ccRCC area and they were stored frozen (-80ºC) until lipid extract preparation.

<u>Homogenate lipid extraction</u>

The homogenate lipid extraction was performed in base on the Bligh & Dyer method[23].

In a glass tube with a ground-glass mouth, the volume of homogenate corresponding to 0.5 mg of protein was added. It was completed up to 0.6 ml with PBS once 20µL of *Lipidomix* pattern and 10 µL of *Ceramide / Sphingomyelin* pattern were added. Then, 3 ml of chloroform and 6 ml of methanol were vigorously vortexed for 2 minutes. 3 more ml of chloroform were added and the mixture was vortexed for 1 minute. Finally, 4.8 ml of distilled water were added and again stirred with the vortex for 1 minute. The mixture was centrifuged at 1200 g for 15 minutes at 4 ° C. The upper phase was removed with a water tube (without rushing) and the inner phase was transferred to another glass tube with the help of a glass Pasteur pipette. The lipids of the protein interface and residual upper phase were re-extracted by adding 2.6 ml of each solvent, chloroform, methanol and distilled water to the tube. The mixture was vigorously stirred in the vortex for 2 minutes and then centrifuged at 1200g and 4° C for 10 minutes. Once centrifuged, the upper phase was removed and the chloroform lower phase was transferred and combined with the previous one. They were immediately dried in the speed-vac.

The dried extract was resuspended in 900 µL of chloroform:methanol 2:1 and transferred to a glass mini-plug with screw cap. The solvent was evaporated in the evaporator concentrator and once the final lipid extract was obtained, it was stored at -80 ° C under N_2 atmosphere.

In order to run the experiment, three types of samples were prepared:

Study samples. The lipid extracts prepared were reconstituted in 150 µL of C_7H_8: MeOH (1:9, v/v), transferred to maximum recovery chromatography vials using a micropipette and injected into the uHPLC-QqTOF.

Quality Control samples (QCsample). The QCsamples were prepared by mixing 15 µL of each study sample in a maximum recovery vial. Because QCsamples represents the whole study samples, they were used to identify the lipidoma as well as the analytical variability of the identified lipids and the stability of the sequence.

Displays Quality Control System (QCsys). The QCsys sample was prepared by reconstituting in 150 µL of C_7H_8: MeOH (1:9 v/v) two samples of lipid extracts (one of

each study group). QCsys sample was used to balance the system before the analysis of the study samples.

uHPLC-QqTOF-MS^E analysis

The study samples were analyzed randomly under the uHPLC-QqTOF analysis conditions indicated in **Table 3.3** after the injection of 2 MF (mobile phase), 3 blanks consisting of C_7H_8: MeOH (1:9, v/v), a solution of internal standards (*Splash Lipidomix* and *Ceramide / Sphingoid* IS Mixture I), 15 QCsys for system conditioning and a QC sample. The remaining QCsamples were injected periodically during the sequence and, finally, an internal standard solution in C_7H_8: MeOH (1:9, v/v), a blank and an FM solution were injected (**Figure 3.3**).

legend: ■ QC sample ■ SI ■ Blank: C_7H_8: MeOH (1:9) ■ Study sample ■ MF ■ QCys
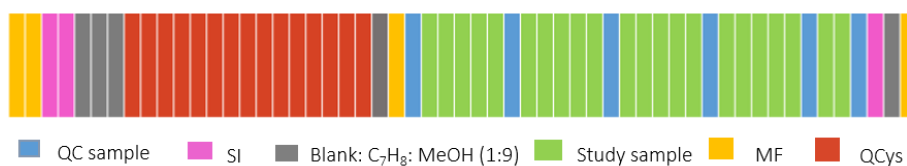
Figure 3.5. Scheme of the injection order

Table 3.3. uHPLC-Q-Exactive HF-X analysis conditions

uHPLC conditions		MS conditions			
		ESI probe		Q Exactive HF-X	
Column	ACQUITY uHPLC HSS T3 2.1x 100 Mm, 1.8 µm (Waters)	*Ionization mode*	ESI positive/ neg ative	*Pos. Ion*	(250-2000 amu)
Tª. Column:	65°C	*Sheath Gas*	35	*Neg ion*	(250-2000 amu)
Flow	500 µL/min	*Aux gas*	10	*Mass Resolution*	R= 120 K
Mobile PHASE A	Acetonitrile/H_2O (40:60) with 10 MM NH_4Ac	*Sweep gas flow rate*	0	*Top 10 dd-MS2*	R= 7.5 K
Mobile PHASE B	Acetonitrile/Isopropanol (10:90) with 10 mM NH_4Ac	*Spray voltage*	3.2kV	*FWHM*	m/z 200
Gradient	0-10 min, from 40 to 100%B; 10-11 min, 100%B; and conditioning the column	*Cap. temperatu re*	285°C	*MS2 Isolation Width*	1Da
Tª.automat ic Inyector	4 ºC	*Heater temp*	370°C	*Stepped NCE*	Pos. Ion: 25, 30 Neg. Ion: 20, 30, 40
Injection volume:	2 µL			*AGC target*	1E+6MS,240 ms max. E+5MS2, 11 ms max.

Data processing

The alignment of the chromatograms and the identification and quantification of the lipidome was carried out using the LipidSearch software version 4.2.2. First, the individual data files of the MS / MS spectra of the lipid precursor ion were searched. MS/MS fragment ions were then predicted for all precursor ions measured within a tolerance of ± 5 ppm. Product ions matching the prediction were used as fragment ions within a mass tolerance of ± 5 ppm to calculate a match score, and the candidates providing the best match quality were determined. The search results of the individual positive or negative ion files from each sample group were then aligned within a retention time window (± 0.1 min) and the data was merged for each annotated lipid.

Due to the large amount of lipids scored, the data has been filtered to reduce the number of false positives by following the following criteria (**Table 3.4**):

1. Predominant ion. As an example, for triglycerides (TG) the main adduct ion detected is [M + NH₄] +, so the TG species detected as [M + H] + and [M + Na] + are false positives; and therefore, they were eliminated from the data matrix.

2. Coefficient of variation (CV): Lipids with a CV> 30% in QCsamples, are false positives.

3. Elution order according to number of carbon atoms. Within the same lipid subclass, the same number of double bonds, the greater the number of carbon atoms, the longer elution time.

4. Elution order based on number of double bonds. Within the same lipid subclass, for the same number of carbon atoms, the greater the number of double bonds, the greater the elution time.

5. ID Quality filter.

Table 3.4 *Criterion used to filter the lipids scored.*

ESI+	Predominant ion = [M+H]+	*LPC, PC, LPE, PE, PS, LPG, PG, PI, SM, SPH, ST, CL, AcCa*
	Predominant ion = [M+H-H2O]+	*Cer, Hex1Cer, Hex2Cer*
	Predominant ion = [M+NH₄]+	*LPI, PI, PG,TG, ChE*
	Predominant ion = [M+Na]+	*DG*
ESI-	Predominant ion = [M-H]-	*LPE, PE, LPS, PS, LPG, PG, LPI, PI, FA, CL*
	Predominant ion = [M+HCOO]-	*LPC, PC, SM, Cer, Hex1Cer, Hex2Cer*
Id quality filter	Identification grade	**A**= Lipid class and FA complete identification **B**= Lipid class and some FA identification **C**= Lipid class or FA identification **D**= Lipid identification by asociated fragments

Statistical analysis

As the normality of the distribution and homoscedasticity of the data are necessary assumptions to perform parametric tests, it is recommended to check these characteristics in the data matrix to decide if the transformation of the data is necessary. In this study, the homoscedasticity of the data was examined by applying Levene-test for each characteristic (lipid) in each group using the SPSS software.

The characterization of the differences in the studied lipidome was carried out by univariate and multivariate data analysis using SPSS[12] and Orange Biolab[22] software. An unsupervised analysis of Principal Component Analysis (PCA) was performed to see if there are tendencies and grouping of the samples and identify possible outliers. Subsequently, some classification models were applied which allow classifying the samples according to the lipid composition. T-test was also applied in order to see the significantly different lipid species between the two groups.

1. Shimma, S. & Sugiura, Y. Effective sample preparations in imaging mass spectrometry. *Mass Spectrometry* **3**, S0029-S0029 (2014).

2. Astigarraga, E. *et al*. Profiling and imaging of lipids on brain and liver tissue by matrix-assisted laser desorption/ionization mass spectrometry using 2-mercaptobenzothiazole as a matrix. *Anal. Chem.* **80**, 9105-9114 (2008).

3. Thomas, A., Charbonneau, J. L., Fournaise, E. & Chaurand, P. Sublimation of new matrix candidates for high spatial resolution imaging mass spectrometry of lipids: enhanced information in both positive and negative polarities after 1, 5-diaminonapthalene deposition. *Anal. Chem.* **84**, 2048-2054 (2012).

4. Juhasz, P., Costello, C. E. & Biemann, K. Matrix-assisted laser desorption ionization mass spectrometry with 2-(4-hydroxyphenylazo) benzoic acid matrix. *J. Am. Soc. Mass Spectrom.* **4**, 399-409 (1993).

5. Axelsson, J. *et al*. Improved reproducibility and increased signal intensity in matrix-assisted laser desorption/ionization as a result of electrospray sample preparation. *Rapid communications in mass spectrometry* **11**, 209-213 (1997).

6. Wang, H. J., Post, Shelley N Jackson Jeremy & Woods, A. S. A minimalist approach to MALDI imaging of glycerophospholipids and sphingolipids in rat brain sections. *International journal of mass spectrometry* **278**, 143-149 (2008).

7. Baluya, D. L., Garrett, T. J. & Yost, R. A. Automated MALDI matrix deposition method with inkjet printing for imaging mass spectrometry. *Anal. Chem.* **79**, 6862-6867 (2007).

8. Puolitaival, S. M., Burnum, K. E., Cornett, D. S. & Caprioli, R. M. Solvent-free matrix dry-coating for MALDI imaging of phospholipids. *J. Am. Soc. Mass Spectrom.* **19**, 882-886 (2008).

9. Hankin, J. A., Barkley, R. M. & Murphy, R. C. Sublimation as a method of matrix application for mass spectrometric imaging. *J. Am. Soc. Mass Spectrom.* **18**, 1646-1652 (2007).

10. Murphy, R. C., Hankin, J. A., Barkley, R. M. & Berry, K. A. Z. MALDI imaging of lipids after matrix sublimation/deposition. *Biochimica et Biophysica Acta (BBA)-Molecular and Cell Biology of Lipids* **1811**, 970-975 (2011).

11. Garate, J. *et al*. Imaging mass spectrometry increased resolution using 2-mercaptobenzothiazole and 2, 5-diaminonaphtalene matrices: application to lipid distribution in human colon. *Analytical and bioanalytical chemistry* **407**, 4697-4708 (2015).

12. Strupat, K. *et al*. MALDI produced ions inspected with a linear ion trap-Orbitrap hybrid mass analyzer. *J. Am. Soc. Mass Spectrom.* **20**, 1451-1463 (2009).

13. Coombes, K. R. *et al*. Quality control and peak finding for proteomics data collected from nipple aspirate fluid by surface-enhanced laser desorption and ionization. *Clin. Chem.* **49**, 1615-1623 (2003).

14. Xiong, X. &De la Torre, F. *Supervised descent method and its applications to face alignment* (Proceedings of the IEEE conference on computer vision and pattern recognition, 2013).

15. McCombie, G., Staab, D., Stoeckli, M. & Knochenmuss, R. Spatial and spectral correlations in MALDI mass spectrometry images by clustering and multivariate analysis. *Anal. Chem.* **77**, 6118-6124 (2005).

16. Jones, E. A., Deininger, S., Hogendoorn, P. C., Deelder, A. M. & McDonnell, L. A. Imaging mass spectrometry statistical analysis. *Journal of proteomics* **75**, 4962-4989 (2012).

17. Fernández, R. *et al*. Microarray and Mass Spectrometry-Based Methodology for Lipid Profiling of Tissues and Cell Cultures. *Anal. Chem.* **91**, 15967-15973 (2019).

18. Cao, L. *et al*. Rankcompete: Simultaneous ranking and clustering of information networks. *Neurocomputing* **95**, 98-104 (2012).

19. Kemeny, J. G. & Snell, J. L. in *Markov chains* (Springer-Verlag, New York, 1976).

20. Spitzer, F. in *Principles of random walk* (Springer Science & Business Media, 2013).

21. Corportation, I. IBM SPSS Statistics for Windows (Version 25.0 Armonk). *NY: IBM Corp* (2017).

22. Demšar, J. *et al*. Orange: data mining toolbox in Python. *the Journal of machine Learning research* **14**, 2349-2353 (2013).

23. Bligh, E. G. & Dyer, W. J. A rapid method of total lipid extraction and purification. *Canadian journal of biochemistry and physiology* **37**, 911-917 (1959).

Chapter 4

Sample preparation and optical set up improvements in an Orbitrap MALDI-IMS system

This chapter is dedicated to describe some improvements carried out during this thesis in some critical MALDI IMS workflow steps, in attempt to increase the reproducibility and spatial resolution of MALDI IMS experiments.

The data presented here have been partialy published in:

1. Fernández, R., Garate, J., **Martín-Saiz, L**., Galetich, I., & Fernández, J. A. (2018). Matrix Sublimation Device for MALDI mass spectrometry imaging. *Analytical chemistry*, 91(1), 803-807.
2. Montero, R., Abad-García, B., Garate, J., **Martín-Saiz, L**., Barceló-Coblijn, G., & Fernández, J. A. (2020). Improving Spatial Resolution of a LTQ Orbitrap MALDI Source. *Journal of the American Society for Mass Spectrometry*, 31(8), 1755-1758

.

MALDI-IMS is a powerful technique with a wide range of applications for analyzing proteins, lipids and small molecules at both cellular and sub-cellular level. Recording free-of-artifacts signal intensity and good quality images by MALDI-IMS experiments depend on several critical parameters, such as sample handling and preparation, laser spot size and stability of the experimental and instrumental conditions. Therefore, to obtain reproducible information from MALDI-IMS experiments, comparable among different sets of tissue sections, a well optimized strategy for data analysis is necessary.

This chapter focuses on integrating some improvements involved in sample preparation and optical set up of an Orbitrap MALDI IMS system. These further enhancements, which will be extensively explained bellow, are as follows:

- Design and optimization of a new stainless steel matrix sublimation device.

- Sample preparation for Lipid and protein/peptide MALDI IMS on the same tissue.

- Spatial resolution improvement of an LTQ Orbitrap MALDI source.

4.1   Novel matrix Sublimation Device for MALDI Mass Spectrometry Imaging

Introduction

One of the essential aspects of MALDI-IMS is matrix deposition[1, 2]. Apart from using the most suitable matrix for each study, it is necessary to cover the tissue section with a uniform layer of small crystals, with the optimal amount of matrix per surface area. The two most popular methods to achieve a good matrix deposition are spraying and sublimation[3-5], although other alternatives also exist[6-8]. Matrix spraying induces a more efficient analyte extraction, increasing signal intensity at the expenses of spatial resolution. That is why this is the method of choice for proteins, where signal intensity is always an issue[9, 10]. However, in the case of lipids, whose signal intensity is usually stronger, matrix sublimation is usually the method of choice, as it avoids using solvents that could favor lipid migration.

Usually, matrix sublimation is performed using the standard glass sublimators available from different sales partners, sometimes with in-house modifications. Some of them are very sophisticated and permit obtaining images that accurately reproduce the histology of the tissue with excellent spatial resolution and signal-to-noise ratio (S/N) ratio[11-14]. However, in some occasions such devices do not enable an optimal reproducibility. For example, the surface of the cold finger is usually irregular and therefore, the temperature of the sample differs between experiments, as the contact

between the sample holder and the cold finger also varies. Matrix heating is also problematic, as the contact between the glass recipient and the heater is far from being perfect, although this may be in part solved by using sand baths[3]. Vacuum control is also a problem, due to the rudimentary rubber o-rings used to seal the sublimator and the vacuum connections, which are usually made also with rubber. Also, inserting a proper vacuum meter to monitor the pressure inside the sublimator is not simple, and it is usually positioned close to the mechanical pump, instead of directly in the sublimator container[11].

Objectives

To increase matrix deposition reproducibility, an in-house designed, fully controlled stainless steel sublimator is presented. To demonstrate the capabilities of this new device, we will present the optimization curves showing that a reproducibility better than 5% was achieved over glass slides. Furthermore, the comparison between some MALDI-IMS images of human colon sections prepared alternatively with the glass and stainless steel sublimator, demonstrates that the latter permits achieving at least similar spatial resolution, with a better reproducibility in the number of species detected.

Experimental section

Human samples collecting

Ethics Research Committee of the Balearic Islands specifically approved the sample collection for this study (#IB 2118/13 PI). Patients undergoing colonoscopy according to the clinical criteria were invited to participate in the study. Informed consent was obtained in written form from each patient before performing the colonoscopy. Endoscopic biopsies were resected using a Radial Jaw Standard Capacity Biopsy Forceps (Radial Jaw™ 4, Boston Scientific, USA) and immediately snapped frozen in liquid nitrogen and saved at −80 °C until sample preparation. Sections of ~10 μm thickness were prepared using no cryoprotective substances or embedding material in cryostat (Leica CM3050S) at −20 °C and placed on plain glass microscope slides. A consecutive section was stained with H&E (Sigma–Aldrich, Madrid, Spain) for structure identification.

Sample preparation, imaging and data analysis

Matrix deposition for MALDI-IMS was performed using the glass sublimator (G Sublimator) and the new stainless steel sublimator (SS Sublimator) with two matrices: 2-mercaptobezonthiazole (MBT)[15] for positive-ion mode and 1,5-diaminonaphtalene (DAN)[3] for negative-ion mode (both 97%, Sigma-Aldrich Chemie, Steinheim, Germany).

Detailed description of the protocol for matrix deposition using both the glass and the SS sublimator may be found in Materials and Methods (**Chapter 3**). A summary of the parameters used in **Table 4.1.**

Table 4.1 *Sublimation parameters used for this study*

Sublimator type	Matrix	Sublimation time (min)	Vacuum pressure	Heat temperature (ºC)	Cooling temperature (ºC)
Commercial glass sublimator	DAN	8	-	120	Ice
	MBT	8	-	120	Ice
Home designed stainless steel sublimator	DAN	8 or 12	Start at 0.4mBar	125 or 120	5
	MBT	10	Start at 0.4mBar	120	5

To determine the influence of all the parameters identified as important for the reproducibility of the amount of matrix deposited, ~200 sublimation experiments were carried out. Plain glass slides (75 mm × 25 mm) were used for optimization test and colon tissue samples for MALDI IMS images comparison between the two sublimators.

Optical images of the matrix layers obtained were recorded using a scanning electron microscope (JEOL JSM-6400, Japan). Instrument parameters were set as follows: U = 20 kV, I = 10^{-11} - 10^{-10} A. As the sample were non-conductive they were covered with a 20 nm Au conducting layer to remove the charge and shield the incident beam from the charge accumulated in the bulk material.

Acquisitions were made with a pixel size of 25 μm in oversampling mode. Mass resolution of 60 000 at m/z = 400 was used to record the data on a $550 - 1200$ Da mass window, in negative-ion mode. Laser energy was set in the $20 - 30$ μJ interval for the experiments to obtain an optimal S/N ratio. Data were acquired using Xcalibur software, version 2.0.7 (Thermo Fisher Scientific, Waltham, MA, USA). Image data were visualized and analyzed using an in-house designed software built in Mathlab version R2017a (MathWorks, Natick, MA, USA). Further details may be also found in **Chapter 3**.

Results and discussion

<u>Stain steel sublimation prototype</u>

Figure 4.6 shows the picture and the schematics of the new sublimation apparatus. The main advantages of this sublimator is a better control of the main variables that influence the deposition of the matrix: vacuum inside the sublimation chamber, temperature of the sample, sublimation temperature and deposition time, thanks to

several sensors incorporated in the device. It is also significantly faster than the glass sublimator we used before.
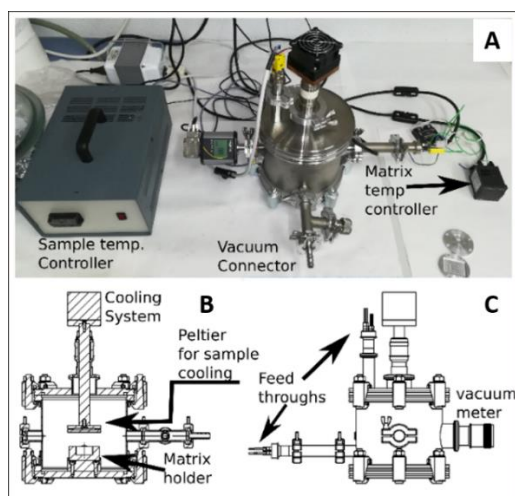
Figure 4.6. (A) Picture of the prototype. (B, C). Schematics of the chamber of the stainless steel sublimator.

To control the sample cooling, the sublimator was equipped with a Peltier cell that maintains the sample at 5 ºC during the process. In principle, it could be possible to reach lower temperatures, but then heat dissipation becomes a major issue. The Peltier cell is attached to a copper block that helps dissipating the heat produced during the cooling. This block is refrigerated with the aid of a heat dissipater cooled by a fan. The temperature of the sample is monitored in real time using a controller and a thermocouple that reeds the temperature on the copper holder.

Vacuum is also monitored in real time with the aid of a digital vacuum gauge controller. This allows one to turn the matrix heater on only once certain vacuum has been reached, reducing the variability between samples. The best results were obtained when vacuum reached 0.4 mbar, both in the case of DAN and MBT, although this optimal pressure may depend on the pump capacity and the temperature applied to the matrix holder.

Matrix warming showed to be a critical parameter. A fine control over the temperature was achieved using a digital controller and a thermocouple attached to the matrix compartment. In this way, ±1 ºC control was achieved. Another parameter whose impact in the sublimation process may not be evident is the geometry of the receptacle for the matrix (**Figure A4.2**). How the matrix is deposited in this receptacle is also important. For example, if the matrix is spread covering a large surface,

sublimation proceeds faster than if the matrix is confined to a smaller area. Also, a different contact with the metal holder has some influence on the sublimation speed. Several holder geometries were tested and the best results were achieved with a cylindrical matrix tray with a receptacle of 1 cm in the center for the matrix. The matrix substance was deposited on this receptacle as powder. Size of matrix crystals may also have some influence on the sublimation process, although that variable was not explored.

<u>Heating and deposition time optimization</u>

There is a compromise between heating temperature and deposition time to deposit an optimal amount of matrix, although not all the combinations lead to similar reproducibility. **Figure 4.7** shows the variation of the amount of matrix deposited as a function of the temperature for a deposition time of 8 minutes (MBT) and 12 minutes (DAN), which are the deposition times that resulted in better reproducibility of the amount of matrix deposited. Such reproducibility changes for MBT along the interval of temperatures explored. Apparently, there is a threshold at 120 ºC: above such temperature, sublimation proceeds faster. Conversely, DAN deposition is more reproducible and the amount of matrix is proportional to the heating temperature in the whole interval explored.

When temperature is fixed, variation on the amount of matrix deposited with time increases smoothly, for both MBT and DAN, although, once again, deposition of DAN is more reproducible, being close to 5 % for some conditions. The deposition times reported in this work were taken from the instant were the heating system was turned on, until it was turned off, and therefore it includes the warming stage, although due to the speed of the heating system, reaching the nominal temperature takes less than 1 min. In this respect, the SS sublimator is significantly faster than our old glass sublimator. The total sample preparation for deposition of DAN using a sublimation time of 12 min takes ~90 min with the glass sublimator and only ~18 min with the SS sublimator.
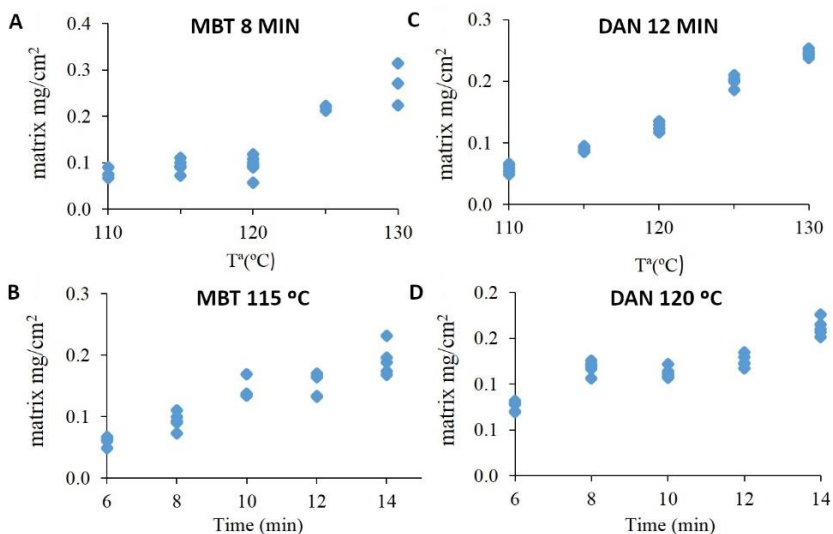
***Figure 4.7**. Influence of the temperature **(A, B)** and deposition time **(C, D)** on the amount of MBT and DAN deposited by sublimation on a glass slide. The lines are eye guides and not true fit to the data. Additional graphs in **Figure A.4.4**).*

Size of the crystals formed during deposition

While reproducibility of the amount of matrix deposited by sublimation is an important factor for multi-experiment studies, the size of the crystals formed over the tissue is a relevant parameter to achieve high spatial resolutions[16].We tested also for the new stainless steel design if a similar crystal size was achieved, using scanning electron microscopy.

Figure 4.8 shows examples of matrix deposition over plain glass slide and over a section of murine heart tissue, both for DAN and MBT. Although deposition over plain glass is substantially more homogeneous, a small crystal size was achieved with both sublimators. Apparently, differences in the experimental conditions between the two devices led to differences in the morphology of the crystals in the case of MBT: they are flat crystals in the case of the glass sublimator and elongated prismatic crystals when deposition was carried out with the new prototype. In any case, slightly smaller crystal were formed for both matrices when the new prototype was used. Inspection of the crystals in the microgarphs show an average crystal size for DAN of 1.42 ± 0.11 µm when the glass sublimator was used and of 0.76 ± 0.04 µm with the stainless steel sublimator. Comparison in the case of MBT is not easy, due to the change on crystal morphology and the larger size dispersion. Measuring the width of the biggest and

smallest crystals in the micrograph, we obtain a size interval of 0.6 – 1.3 µm for the stainless steel sublimator and of 0.7 – 1.6 µm for the glass sublimator.
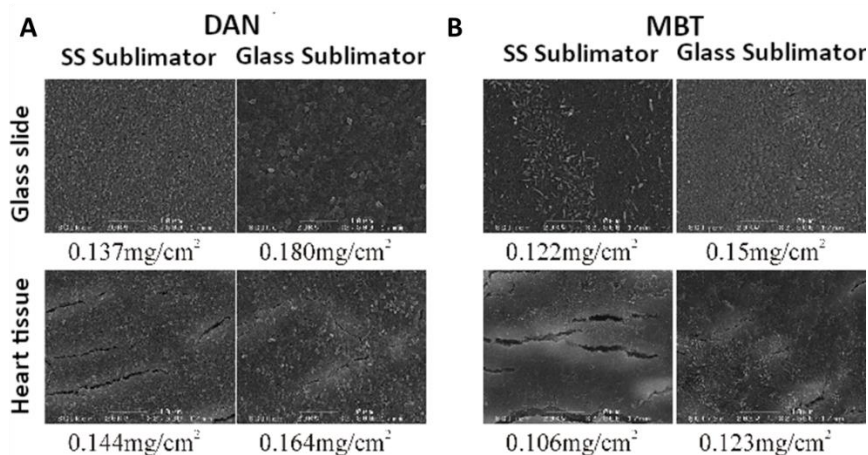
Figure 4.8. S.E.M pictures of the MBT *(A)* and DAN *(B)* matrices deposited over plain glass slides and over mouse heart tissue sections, using the stainless steel (SS) and the standard glass sublimators. See also *Figures A.4.5 and A.5.6* of the supporting information.

Comparison between MALDI-IMS images obtained with both sublimators

As a final test of the performance of the developed stainless steel sublimator, sections of biopsies of human colon were coated with DAN using both sublimators and images of lipid distribution at 25 µm/pixel were recorded, in negative-ion mode (**Figure 4.9 and Figure A.4.7**). The images of lipid distribution show similar resolution. The pixel size used allowed us to easily discriminate the colonic crypts (blue segments in **Figure 4.9**) from the lamina propria (white segments).
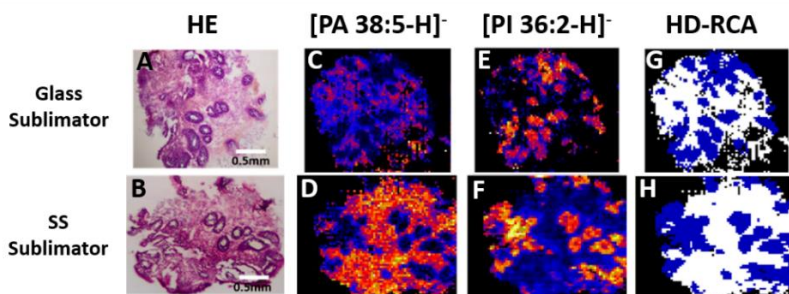
Figure 4.9. (A, B) *Optical images of two sections of biopsies of human colon, consecutive to those used to record lipid distribution using MALDI-IMS. The section in A was covered with DAN using the glass sublimator and the section in B was covered using the SS sublimator. **(C,E)** Images of the distribution of selected lipid species over section A; **(D, F)** distribution of the same species over section B; **(G, H)** segmentation images obtained setting the number of segments to 3 (the segment containing the pixels outside the tissue was omitted). The tissue architecture is easily recognize in both experiments; Images obtained in negative-ion mode using a pixel size of 25 µm. Additional experiments may be found in the supporting information **(Figure A.4.7)**. Crypt: colonic crypts.*

To estimate the relative signal intensity and reproducibility of the results with both sublimators we run several tests. **Figure 4.10A** shows the distribution of the TIC along all the spectra recorded over each section. The spectra with lower TIC correspond to those pixels outside the tissue and therefore, they only contain matrix peaks. The number of the spectra recorded outside the tissue changes between experiments and in the case of the middle panel, they account for a large number of spectra.
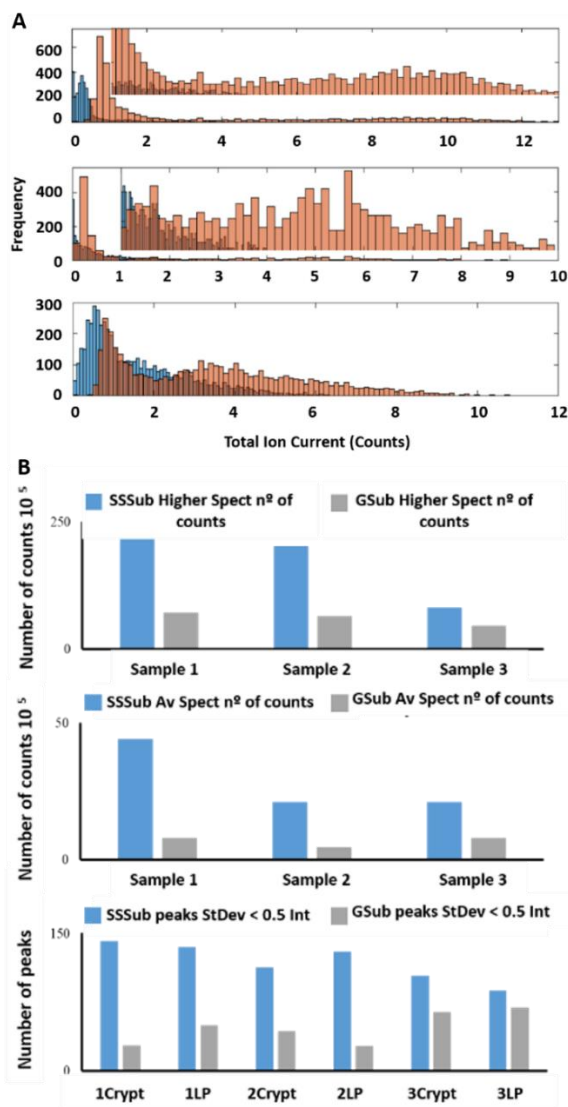
Figure 4.10. (A) *Comparison between the TIC of the spectra recorded directly from the samples covered using the Glass sublimator (GSub) (blue) and the SS sublimator (SSSub) (orange). Bimodal distributions were obtained with a maximum at lower intensities corresponding to the spectra recorded outside the tissue and that only contain matrix peaks. The insets are a zoom over the part of the graphics. In all cases, the spectra recorded over the sections covered with the SS sublimator present higher intensities.* **(B)** *Bar charts of the number of counts and the number of peaks obtained in some experiments comparing the SSSub and the GSub results. All the experiments carried out in negative-ion mode.*

Regarding the spectra recorded over tissue, in all three pairs of images, those sections covered using the SS sublimator (orange), rendered stronger signals than those covered with the glass sublimator (blue). The stronger signal resulted in a better reproducibility of the specta. **Figure 4.10B** bottom panel shows the number of species whose standard deviation < 50% of its intensity. This parameter gives an estimation of the reproducibility of the species detected, as it only takes into account those mass channels with an inter-spectrum variation below the given threshold.

Clearly, the results obtained with the SS sublimator were superior, although the reason behind such observation is not clear: in principle, the type of sublimator used should only affect to the reproducibility of the amount of matrix deposited and to the crystal size of the matrix, but one would expect to obtain similar signal intensity with both sublimators for a given amount of matrix. Perhaps the more uniform cooling of the sample during the sublimation process enabled a more uniform matrix distribution, improving the final performance of the experiment.

Conclusions

Here is presented an in-house designed stainless steel sublimator. Compared with our previous standard glass device, the new prototype enables to finely control the main parameters that influence reproducibility of matrix deposition. Thanks to the better control over sample temperature during sublimation, the vacuum inside the chamber and the sublimation temperature, more reproducible conditions for matrix deposition were achieved, also enabling a better reproducibility of the species detected in MALDI-IMS experiments over sections of human colon biopsies. The blue prints of the device are freely available under request.

4.2   MALDI-IMS profiling of Proteins and Lipids on the same tissue

Introduction

In attempt to obtain mass spectrometry images of lipids, peptides, and proteins, commonly multiple analyses on consecutive tissue sections are required using different sample preparation protocols. However, applying this approach, the correlation between molecular histopathology and IMS images is challenging, as anatomical features can vary from one tissue section to another. Consequently, the correlation of molecular information with histological features on the same tissue section is highly desired[17].

Although MALDI-IMS allows the analysis of a wide range of biomolecules, lipids and proteins are of particular interest for many researches. However, sample preparation

protocols for these two biomolecules are substantially different. In the case of lipids, sample pretreatment is not necessary, unlike for protein/peptide MALDI-IMS analysis that requires a demanding delipidation process[18, 19]. Moreover, regarding matrix deposition, spraying is the method of choice for protein/peptide analysis; at the expenses of diffusion effect caused by liquid solvent, this method guarantees best signal intensity, which for protein is always a problem[9, 10]. On the other hand, sublimation is typically used for lipids analysis, which signal intensity is stronger and it avoids liquid solvents, which cause migration effects. Consequently and due to all the protocol differences, little literature has demonstrated subsequent lipid and protein MALDI-IMS analysis on a single tissue section[17, 20].

Objectives

The goal of this chapter is to develop a detailed sample preparation protocol for both lipid and peptide/protein MALDI-IMS analysis on the same tissue. This will allow us to increase the amount of underlying molecular information obtained from the murine brain and to apply the protocol to a different types of samples.

Experimental section

Sample collection

Sample collection was approved by Spanish/European regulations on animal use under the supervision of the institutional committee at CIC bioGUNE (AAALAC-accredited facility)

Mouse brain extractions were immediately snapped frozen in liquid nitrogen and saved at -80˚C until sample preparation. 10µm thick sections were obtained using a cryotome and placed onto ITO glass slides, previously coated with polylisine to improve tissue adherence. Nevertheless, several trials were performed using non-ITO nor polylisine coated glass slides in order to optimize the protocol.

Workflow

As **Figure 4.11** shows, firstly, lipid MALDI IMS experiments were carried out followed by tissue matrix removal and subsequent protein/peptide MALDI IMS. In parallel, the traditional consecutive slices protocol (one different slide for protein/peptide MALDI IMS) was also conducted, to compare the results from both approaches.
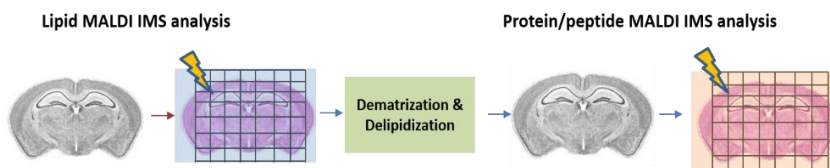
Figure 4.11. *On same tissue lipid and protein/peptide MALDI IMS workflow*

Imaging of lipids

Matrix deposition was performed by sublimation using the stainless steel sublimator with 2-mercaptobezonthiazole (MBT)[15] and CHCA (Sigma-Aldrich Chemie, Steinheim, Germany) for positive-ion mode and 1,5-diaminonaphtalene (DAN)[3] for negative-ion mode (97%, Sigma-Aldrich Chemie, Steinheim, Germany).

Brain tissue sections were recorded by a MALDI-LTQ-Orbitrap XL (ThermoFisher) with a step size of 100 µm and a mass resolution of 60.000 FWHM at m/z = 400, with a laser energy between 30-60 µJ/pulse. Image data were visualized and analyzed using an in-house software built in Mathlab version R2017a (MathWorks, Natick, MA, USA). The rest of the MALDI-IMS parameters used as the detailed information regarding data analysis, are described in Materials and Methods (**Chapter 3**).

Imaging of peptide/protein

Peptide/protein MALDI-IMS analysis was carried out by the proteome group led by Dr. Felix Elortza in CiC bioGUNE (Zamudio, Bizkaia).

In order to carry out protein/peptide MALDI-IMS, sample pretreatment is mandatory. Biological tissues contain an enormous number and variety of chemical species, whose concentration is related with their proper detection; some of the most abundant species in the tissue can hamper the detection of less-abundant species or can even cause what is known as ion supression. This is the case of salts and lipids, which can negatively affect the analysis of protein/peptides[21-23].

The main problems that the high abundance of lipids can cause are poor crystallization and ion suppression. To overcome these problems, tissue washing procedures have been developed for use prior to application of matrix in protein/peptide MALDI IMS workflows. One of the most used and validated tissue washing method is Carnoy's procedure. Consequently, this was the delipidation method of choice in this work.

Additionally, as our sample comes from lipid MALDI-IMS analysis, a dematrization process is required. Therefore, the workflow fnally used must include the steps depicted in **Figure 4.12.**
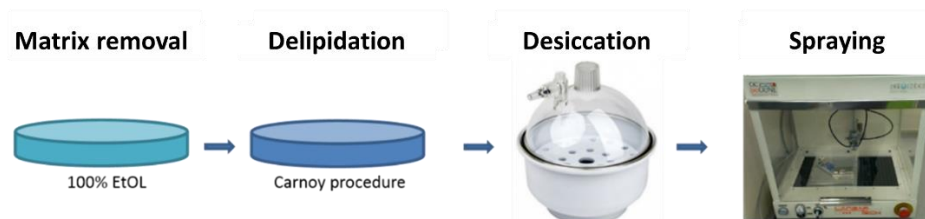
Figure 4.12 *Scheme of the protocol for protein/peptide MALDI-IMS after lipid IMS experiments.*

Matrix removal consisted of a 30 s rinse of 100% ethanol (Sigma-Aldrich Chemie, Steinheim, Germany). Carnoy's fluid was prepared from 60 mL of ethanol, 30 mL of chloroform, and 10 mL of acetic acid. Carnoy's procedure was a six-step rinse: 70% ethanol, 100% ethanol, Carnoy's fluid, 100% ethanol, H_2O and 100% ethanol. All rinse steps were carried out for 30 s except for the step with Carnoy's solution, which was for 2 min. After delipidation, the sample was stored in vacuum desiccator until matrix deposition for the subsequent protein IMS analysis.

Matrix deposition was accomplished by spraying using their custom-made automatic matrix sprayer Langartech with Sinapinic Acid (SA) (Sigma-Aldrich Chemie, Steinheim, Germany). Additionally, HTX-TM Sprayer™ located in the lipid service from SGIKER facilities (UPV/EHU, Leioa, Spain) was used to spray CHCA matrix applying the conditions displayed in **Table 3.2** (**Chapter 3**)

Brain samples were rastered with an Autoflex III smartbeam MALDI TOF/TOF MS (Bruker Daltonics) with a step size of 100 μm, 500 shots per spot (100 Hz laser) and mass range between 1000 a 30000 Da.

Results and discussion

Lipid and protein MALDI-IMS on consecutive tissue samples

Figure 4.13 shows some lipid distribution over two consecutive brain sections. As expected, spatial resolution in both negative and positive ion mode was very good, which enabled distinguishing the main brain histological structures. The lack of diffusion effect effectively made possible to achieve the required resolution.
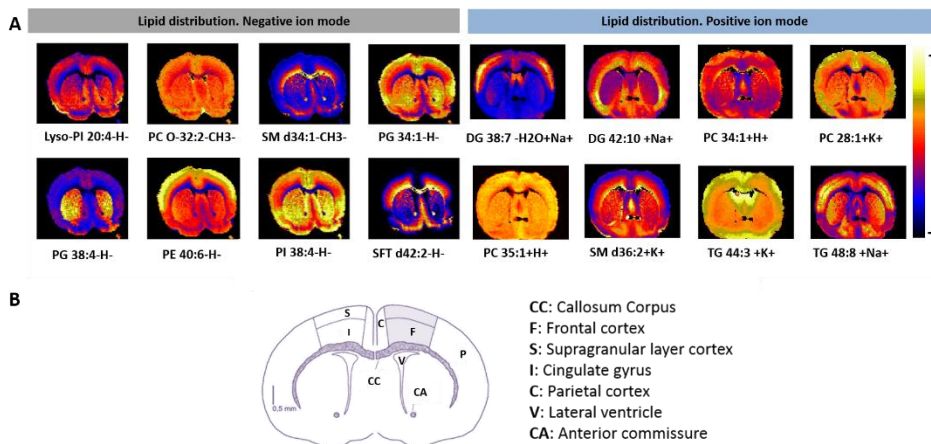
Figure 4.13. (A) *MALDI IMS lipid distributions obtained in both negative and positive ion mode.* **(B)** *Colored sketch of the main histological brain histological structures.*

121 lipid species (adducts included) were identified in negative-ion mode, while 274 in positive-ion mode. Further fragmentation experiments would be required in order to distinguish among isobaric lipid species. The percentage of the lipid species detected as well as the predominant adducts for each lipid family in both negative and positive ion mode is show in **Figure 4.14 and** Figure **4.15** respectively.

Lipid class	nº of lipids	Adducts
Hex-Cer	7	[-H]-
LPI	4	[-H]-
PC/PE	26	[-CH3]- / [-H]-
PC-OP/PE-OP	16	[-CH3]- / [-H]-
PG	4	[-H]-
PI	12	[-H]-
PS	18	[-H]-
PS-O	1	[-H]-
SM	10	[-CH3]-
SULF	23	[-H]-
total	121	
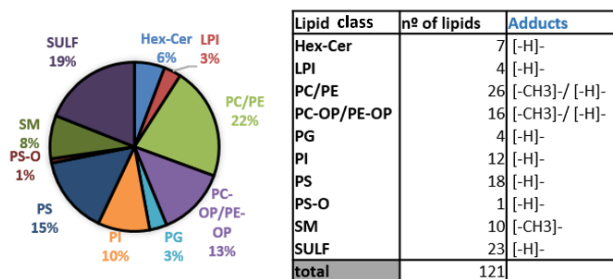
Figure 4.14. *Percentage of murine brain lipid species detected in negative-ion mode and the predominant adducts for each lipid family.*

Lipid class	nº of lipid species	Aducts					
DG	54	[Na]+	[K]+		+[H$_2$O+H]+	+[H2O+Na]+	+[H2O+K]+
DG-OP	28	[Na]+	[+K]+				
LPC	5	[+H]+					
PC	111	[+H]+	[Na]+	[+K]+			
PC-OP	14	[+H]+	[Na]+	[+K]+			
SM	34	[+H]+	[Na]+	[+K]+			
TG	28	[Na]+	[+K]+				
total	274						
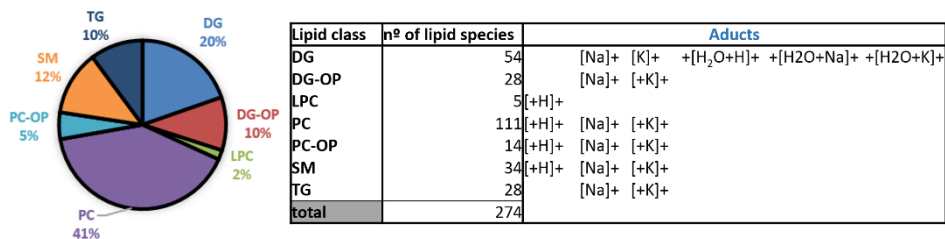
Figure 4.15 *Percentage of murine brain lipid species detected in positive ion mode and the predominant adducts for each lipid family.*

MALDI IMS of peptide/protein was performed in consecutive brain tissue slices. Although the achieved spatial resolution is not as good as MALDI-IMS of lipids, brain structures can be identified as can be seen in **Figure 4.16**.
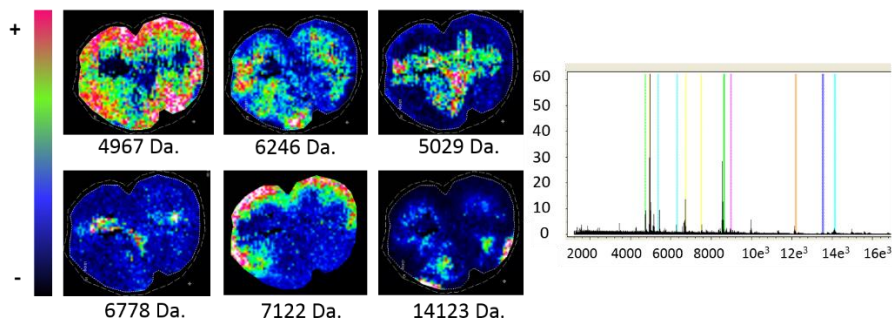
Figure 4.16. *Peptide/protein MALDI IMS distributions and mean spectrum.*

Lipid and protein MALDI IMS on same tissue sample

After several attempts, lipid and peptide/protein MALDI-IMS analysis was successfully carried out over the same tissue sample. As **Figure 4.17** shows, lipid MALDI IMS spatial resolution and ion signal intensity (e^6) was excellent. However, protein-MALDI-IMS spatial resolution is evidently affected by the treatment applied to the tissue and the previous laser shots, so the achieved resolution is slightly lower than 100 microns. Nevertheless, in both lipid and protein MALDI IMS images all major structures can be anticipated.
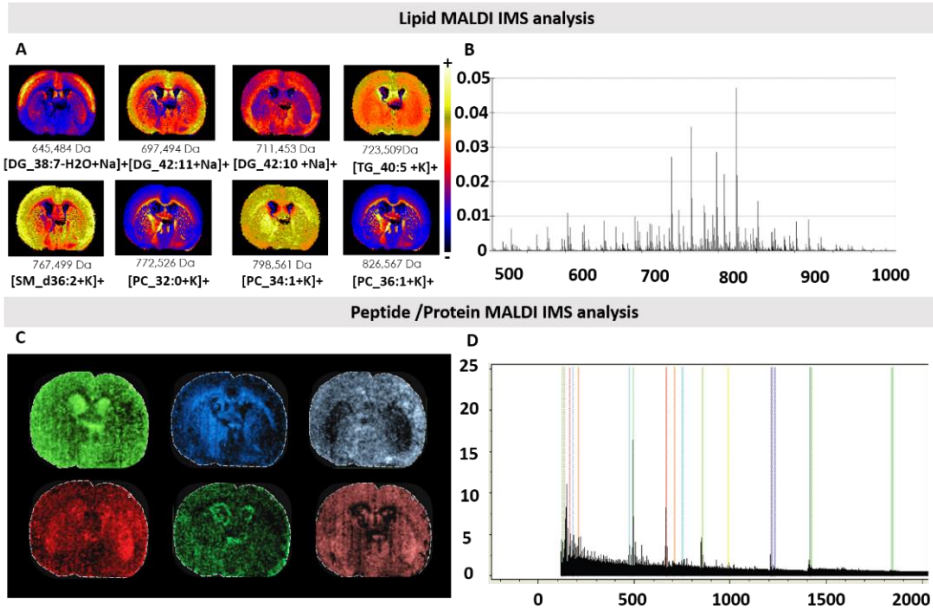
Figure 4.17. *Lipid and peptide/protein MALDI IMS analysis over the same tissue sample. (A) Lipid distribution images obtained in positive ion mode. (C) Protein/peptide distribution images. (B,D) Average spectrum of Lipid and peptide/protein MALDI IMS analysis respectively.*

Conclusions

In this section, we demonstrated that lipid and protein images can be acquired by MALDI IMS of the same tissue section. This workflow allows chemical information of two classes of molecules to be matched to histological features and enables a more complete evaluation of a single tissue section. This study introduces a new methodology with potential to be used for routine applications of IMS technology. However, there still exist several limitations, unavoidable with today's protocols which leaves room for improvement in terms of spatial resolution, especially for peptide/protein MALDI-IMS analysis. Nevertheless, this lipid and protein combined protocol can be of great assistance in diagnosis and in pathophysiology analysis.

4.3   Improving spatial resolution of a LTQ Orbitrap MALDI source

Introduction

Since its introduction in the mid 90's MALDI imaging techniques have demonstrated to be powerful tools to determine the distribution of chemical species in biological tissues with microscopic resolution[24]. During the last decade, one of the main goals for many researchers have been to push forward the resolution of commercial instruments to reach subcellular level (<10 µm)[24-28]. Although several parameters related to sample preparation can influence the final resolution achievable, another limiting factor is the laser spot size. At this point, several approaches have been developed to increase the numerical aperture and consequently reduce the spot size. As examples, Spengler et al. developed an atmospheric pressure (API) MALDI source based in a Nitrogen laser whose, beam was expanded prior to its focusing on the sample to yield an 8 µm spot[29, 30]. Lee and coworkers were also able to obtain sub 10 µm ablation spots on the matrix, by expanding the beam of a Nd:YAG laser[25, 31]. The numerical aperture can be further increased using shorter focal lengths, by means of long working distance microscope objectives, in transmission configuration. This strategy was followed by Spengler and coworkers and more recently by Caprioli and coworkers and Dreisewerd and coworkers, to reach resolutions close to 1 µm, using API and vacuum sources respectively[26, 27]. Other limiting factors for achieving sub-10 µm resolution, besides the optical parameters as numerical aperture, are the specific characteristics of the used laser beam. Some commercial systems are equipped with Nitrogen lasers due to their intrinsic robustness, simplicity and economic cost. However, the spot size of these sources largely deviates from a diffraction- limited spot, because of the low spatial coherence induced by the lack of an optical resonator. The result is a non-gaussian beam with a complex wave front. This drawback can be skipped by the substitution of the laser source by an Nd:YAG laser, or by other sources providing gaussian beams[31]. The spatial filtering techniques have also been widely used to remove non-gaussian components from laser beams in many optical applications, including MALDI-IMS with Nd:YAG, among other lasers[24].

Objectives

Here, we present an improvement in the MALDI source of an LTQ Orbitrap XL which provide an easy and cost effective procedure to upgrade this spectrometer to reach sub-10 µm spatial resolution. For this approach, spatial filtering techniques have been applied to clean the spatial mode of the original nitrogen laser without modifying the instrument enclosure nor the laser safety classification.

Experimental section

The sample collection for this study was specifically approved by the Ethics Research Committee of the Balearic Islands (IB 2118/13 PI) and they are part of a broader study on the changes in the lipidome associated to several diseases. Two human colon biopsies were used in this study. The samples were obtained in the Endoscopy Room of the Hospital Universitary Son Espases (Palma, Spain) and immediately frozen in liquid nitrogen and stored at -80 ºC. Sections of 10 µm thickness were prepared using no crioprotective substances or embedding material with the aid of a cryostat (Leica CM3050S, Wetzlar, Germany) at -20ºC and deposited over plain glass microscope slides. The samples were covered with 1,5-diaminonaphthalene (DAN)[3], using our in-house designed sublimator (detailed information in previous section). More details on sample preparation protocol can be found in Chapter 3 Materials and methods.

LTQ Orbitrap XL mass spectrometer (ThermoFisher, Ca, USA) equipped with the original MALDI source including an N_2 laser (MNL 100, LTB Laserteknik) has been used in all the experiments. Instrumental parameters for MALDI imaging experiments are provided in Chapter 3 Materials and methods.

Optical set up modification, design and installation of the optics was performed by Dr.Raul Montero Santos, service technician of the UPV/EHU Lasers facility (SGIKER). Prior to any action on the set up, the characteristics of the laser's spatial mode at the sample plane in the original experimental configuration (O), were analyzed by inspection of the ablation spots produced after 20 laser shots. The images of the ablated patterns left on bare DAN matrix, taken by optical microscopy, are presented in **Figure 4.18** as a function of the pulse energy. At this initial stage, the ablation threshold was located at some point in the 5-15 µJ range. Increasing the pulse energy produced a rapid increase in the spot size, reaching ~200 µm length and ~100 µm width at high intensities.
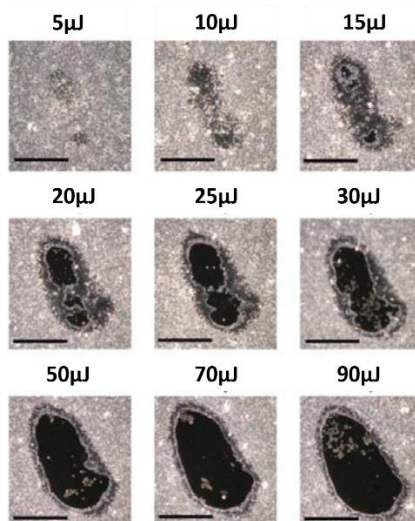
Figure 4.18. Optical microscope images of the laser ablation spots left on bare DAN matrix after 20 laser shots for O configuration. Scale bar = 100 μm.

The first step in the upgrade system consisted in a new beam routing and in introducing new focusing optics (*L* configuration). The new set up (**Figure 4.19**) includes four mirrors to provide more flexibility during alignment, and two f = 100 mm spherical lenses, mounted on precision translation stages, so they produce an intermediate focus. This enables translating the final focal plane to the sample's surface. The pulse energies indicated below, make reference to the energy at the laser output as provided by the spectrometer's software. It is worth to mention that the required opto-mechanics used to extend the cage system was installed without modifying the original cage. **Table A.4.1** includes the part list with all optics and opto-mechanics used.

Once the new set up was properly aligned and characterized, a 20 μm ceramic pinhole was mounted in a quick-release XY precision translation stage, installed at the intermediate focal plane, to remove non-gaussian components of the laser beam (*P* configuration). As illustrated in Fig. S1, the whole system fits into the original enclosure of the spectrometer, so that the covers can be installed and therefore, the safety classification of the instrument remains intact.
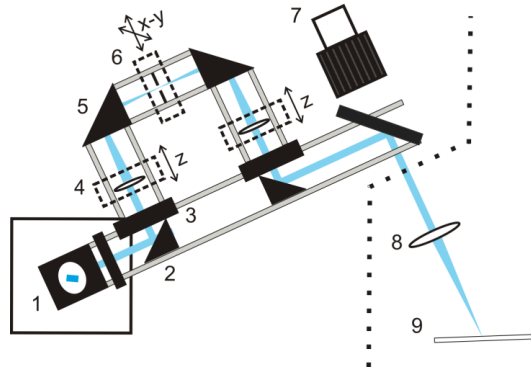
Figure 4.19. *Schematic top view of the upgraded optical set up. Nitrogen Laser (1). (Original) 45º mirror and mount (2). Rail coupling assembly (3). F=100 mm lens and precision translation stage (4). 45º mirror and mount (5). 20 μm ceramic pinhole mounted in a XY precision stage (6). (Original) CCD camera (7). (Original) focusing lens (8). Sample (9).*

Results and discussion

After the upgrade process, the system performance was examined by optical inspection of the laser spot size left in the matrix after 20 shots at different pulse energies (**Figure 4.20**). In *L* configuration, the ablation threshold was found at lower energy with respect to the original set up (< 2 μJ), meaning that the radiation is now more tightly focused. This fact was also confirmed by the notable reduction of the spot sizes at higher pulse energies respect to the original performance (**Figure 4.19**). As illustrated, further improvement of the spatial resolution was achieved with *P* configuration. After pinhole insertion, the evaporation threshold appeared at the same energy than in the former case (< 2 μJ), which means that the spatial filtering of the non- gaussian components of the transverse mode, did not affect the intensity, which remained constant. Therefore, the reduction in signal intensity observed upon pinhole insertion, was exclusively due to a reduction in the sample volume probed at the laser focus.
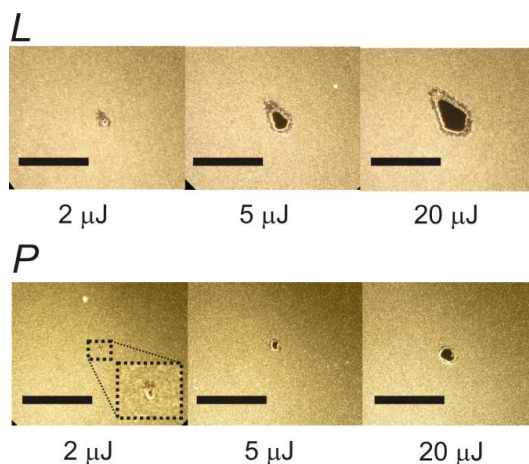
Figure 4.20. Optical microscope images of the laser ablation spots left on bare DAN matrix after 20 laser shots for L and P configurations. The size of the scale bar is 100 μm.

To compare the performance of the different configurations, **Figure 4.21A** shows the spot sizes as a function of the pulse energy. As illustrated, resolution (spot size) is intensity dependent. Therefore, characterization of the beam profile at the sample plane is mandatory. In this sense, the profile reconstruction from the observed spot sizes presented in **Figure 4.21B** (see **Figure A.4.8** for details on this procedure), shows that the beam diameter (FWHM) at sample plane is ~50 μm, ~15 μm and ~8 μm (close to diffraction limit) for the *O*, *L* and *P* configurations respectively. According to this plot, the potential resolution, defined as the spot size corresponding to the evaporation threshold, was reduced from ~35 μm to ~12 μm and ~3 μm with *L* and *P* configurations respectively. However, due to sensitivity issues, typically, energies in the order of 15 μJ for the original set up and around 5 μJ for the upgraded system were employed for MALDI imaging experiments.
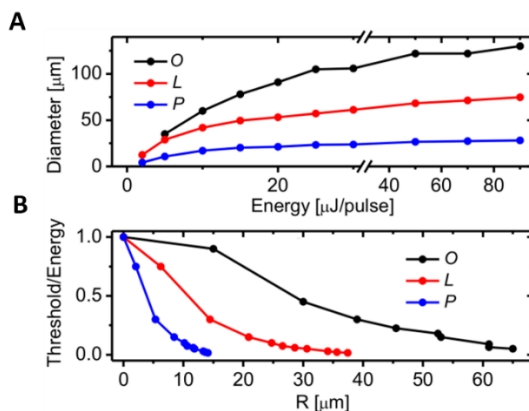
Figure 4.21. *(A). Diameter (x direction) of the ablation spots in DAN matrix after 20 laser shots as a function of the pulse energy for O, L and P configurations. (B) Intensity profile reconstruction (see* **Figure A.4.8***)*

As a final test of the performance of the new set up, **Figure 4.22** shows a comparison between the optical image of an H&E stained section and the images (0.6 mm x 1.2 mm; $\Delta x = \Delta y = 10$ μm) of distribution of three representative lipids over the same section. Colonic crypts are structures composed of a single layer of cells. Such structures are well resolved in the images and the wall of the crypt is composed of several pixels, highlighting once more that sub 10 μm resolution was achieved with the modified MALDI source. Despite the dramatic reduction in the laser spot size, the signal intensity at each pixel was $\sim 10^6$ ion counts, resulting in spectra with excellent S/N ratio. Finally, the segmentation analysis using our HD-CRA algorithm[32] shows that the histology of the section was perfectly captured in the IMS experiment.
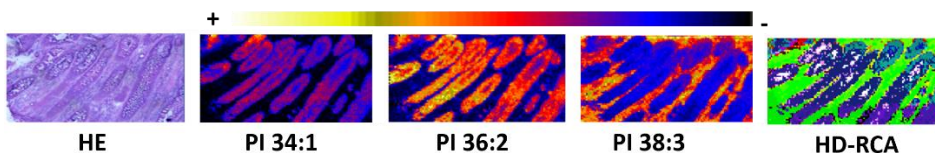
Figure 4.22. Comparison between the H&E stained optical image of a colon section and the images of the distribution of three representative lipids. The HD-CRA clustering analysis highlight that the histology of the tissue is faithfully captured in the IMS experiment.

Conclusions

In this section, we present a simple and cost effective procedure to improve the spatial resolution of the commercial MALDI source of a LQT Orbitrap. Based on spatial

filtering techniques, we demonstrate that, with minimal modifications of the original set up, the system resolution can be pushed forward to <10 μm.

The incorporation of the focusing optics enables a fine adjustment of the focal plane on the sample, producing a better lateral resolution. Insertion of the pinhole produced a spot ~8 μm (close to the diffraction limit) with the subsequent increase in resolution. The performance of the improved setup has been tested in real MALDI imaging experiments

It has been also observed that the resolution is intensity dependent, which points towards the possibility of achieving even better results at very low fluences. We note however, that reduction of the pulse energy below 2 μJ gives rise to sensitivity issues.

The new optical arrangement enables quickly switching between high (< 10 μm) and low resolution configuration (>50 μm) for better sampling in low resolution experiments.

1. Stoeckli, M. & Staab, D. Reproducible matrix deposition for MALDI MSI based on open-source software and hardware. *J. Am. Soc. Mass Spectrom.* **26**, 911-914 (2015).

2. Swales, J. G., Hamm, G., Clench, M. R. & Goodwin, R. J. Mass spectrometry imaging and its application in pharmaceutical research and development: A concise review. *International Journal of Mass Spectrometry* **437**, 99-112 (2019).

3. Thomas, A., Charbonneau, J. L., Fournaise, E. & Chaurand, P. Sublimation of new matrix candidates for high spatial resolution imaging mass spectrometry of lipids: enhanced information in both positive and negative polarities after 1, 5-diaminonapthalene deposition. *Anal. Chem.* **84**, 2048-2054 (2012).

4. Hankin, J. A., Barkley, R. M. & Murphy, R. C. Sublimation as a method of matrix application for mass spectrometric imaging. *J. Am. Soc. Mass Spectrom.* **18**, 1646-1652 (2007).

5. Goodwin, R. J. Sample preparation for mass spectrometry imaging: small mistakes can lead to big consequences. *Journal of proteomics* **75**, 4893-4911 (2012).

6. Baker, T. C., Han, J. & Borchers, C. H. Recent advancements in matrix-assisted laser desorption/ionization mass spectrometry imaging. *Curr. Opin. Biotechnol.* **43**, 62-69 (2017).

7. Muller, L. *et al*. Lipid imaging within the normal rat kidney using silver nanoparticles by matrix-assisted laser desorption/ionization mass spectrometry. *Kidney Int.* **88**, 186-192 (2015).

8. Wu, Q., Comi, T. J., Li, B., Rubakhin, S. S. & Sweedler, J. V. On-tissue derivatization via electrospray deposition for matrix-assisted laser desorption/ionization mass spectrometry imaging of endogenous fatty acids in rat brain tissues. *Anal. Chem.* **88**, 5988-5995 (2016).

9. Angel, P. M. *et al*. Advances in MALDI imaging mass spectrometry of proteins in cardiac tissue, including the heart valve. *Biochimica et Biophysica Acta (BBA)-Proteins and Proteomics* **1865**, 927-935 (2017).

10. Schwamborn, K., Kriegsmann, M. & Weichert, W. MALDI imaging mass spectrometry—from bench to bedside. *Biochimica et Biophysica Acta (BBA)-Proteins and Proteomics* **1865**, 776-783 (2017).

11. Chaurand, P., Cornett, D. S., Angel, P. M. & Caprioli, R. M. From whole-body sections down to cellular level, multiscale imaging of phospholipids by MALDI mass spectrometry. *Mol. Cell. Proteomics* **10**, O110.004259 (2011).

12. Kompauer, M., Heiles, S. & Spengler, B. Atmospheric pressure MALDI mass spectrometry imaging of tissues and cells at 1.4-μm lateral resolution. *Nature methods* **14**, 90-96 (2017).

13. Soltwisch, J. *et al*. Mass spectrometry imaging with laser-induced postionization. *Science* **348**, 211-215 (2015).

14. Yang, J. & Caprioli, R. M. Matrix sublimation/recrystallization for imaging proteins by mass spectrometry at high spatial resolution. *Anal. Chem.* **83**, 5728-5734 (2011).

15. Astigarraga, E. *et al*. Profiling and imaging of lipids on brain and liver tissue by matrix-assisted laser desorption/ionization mass spectrometry using 2-mercaptobenzothiazole as a matrix. *Anal. Chem.* **80**, 9105-9114 (2008).

16. Jurchen, J. C., Rubakhin, S. S. & Sweedler, J. V. MALDI-MS imaging of features smaller than the size of the laser beam. *J. Am. Soc. Mass Spectrom.* **16**, 1654-1659 (2005).

17. Kaya, I. *et al*. Novel trimodal MALDI imaging mass spectrometry (IMS3) at 10 μm reveals spatial lipid and peptide correlates implicated in Aβ plaque pathology in Alzheimer's disease. *ACS chemical neuroscience* **8**, 2778-2790 (2017).

18. Anderson, D. M., Spraggins, J. M., Rose, K. L. & Schey, K. L. High spatial resolution imaging mass spectrometry of human optic nerve lipids and proteins. *J. Am. Soc. Mass Spectrom.* **26**, 940-947 (2015).

19. Angel, P. M. *et al*. Advances in MALDI imaging mass spectrometry of proteins in cardiac tissue, including the heart valve. *Biochimica et Biophysica Acta (BBA)-Proteins and Proteomics* **1865**, 927-935 (2017).

20. Eberlin, L. S. *et al*. Desorption electrospray ionization then MALDI mass spectrometry imaging of lipid and protein distributions in single tissue sections. *Anal. Chem.* **83**, 8366-8371 (2011).

21. Castaing, R. & Slodzian, G. MICROANALYSIS BY SECONDARY ION EMISSION. *Advance.Mass Spectrometry* **3** (1966).

22. Börnsen, K. O. in *Mass Spectrometry of Proteins and Peptides* 387-404 (Springer, 2000).

23. Goodwin, R. J., Pennington, S. R. & Pitt, A. R. Protein and peptides in pictures: imaging with MALDI mass spectrometry. *Proteomics* **8**, 3785-3800 (2008).

24. Buchberger, A. R., DeLaney, K., Johnson, J. & Li, L. Mass spectrometry imaging: a review of emerging advancements and future insights. *Anal. Chem.* **90**, 240-265 (2018).

25. Feenstra, A. D., Dueñas, M. E. & Lee, Y. J. Five micron high resolution MALDI mass spectrometry imaging with simple, interchangeable, multi-resolution optical system. *J. Am. Soc. Mass Spectrom.* **28**, 434-442 (2017).

26. Kompauer, M., Heiles, S. & Spengler, B. Atmospheric pressure MALDI mass spectrometry imaging of tissues and cells at 1.4-μm lateral resolution. *Nature methods* **14**, 90-96 (2017).

27. Niehaus, M., Soltwisch, J., Belov, M. & Dreisewerd, K. Transmission-mode MALDI-2 mass spectrometry imaging of cells and tissues at subcellular resolution. *Nature methods* **16**, 925-931 (2019).

28. Spivey, E. C., McMillen, J. C., Ryan, D. J., Spraggins, J. M. & Caprioli, R. M. Combining MALDI-2 and transmission geometry laser optics to achieve high sensitivity for ultra-high spatial resolution surface analysis. *Journal of Mass Spectrometry* **54**, 366-370 (2019).

29. Guenther, S., Koestler, M., Schulz, O. & Spengler, B. Laser spot size and laser power dependence of ion formation in high resolution MALDI imaging. *International Journal of Mass Spectrometry* **294**, 7-15 (2010).

30. Li, B., Bhandari, D. R., Römpp, A. & Spengler, B. High-resolution MALDI mass spectrometry imaging of gallotannins and monoterpene glucosides in the root of Paeonia lactiflora. *Scientific reports* **6**, 36074 (2016).

31. Korte, A. R., Yandeau-Nelson, M. D., Nikolau, B. J. & Lee, Y. J. Subcellular-level resolution MALDI-MS imaging of maize leaf metabolites by MALDI-linear ion trap-Orbitrap mass spectrometer. *Analytical and Bioanalytical Chemistry* **407**, 2301-2309 (2015).

32. Garate, J. *et al*. Influence of Lipid Fragmentation in the Data Analysis of Imaging Mass Spectrometry Experiments. *J. Am. Soc. Mass Spectrom.* **31**, 517-526 (2020).

Chapter 5

Modification of Lipid Expression in Acute kidney injury and possible reversion with Ferrostatin treatment characterized by MALDI-IMS

Current advances in mass spectrometry have further increased the focus on complete lipid description in diverse pathological contexts. Moreover, the combination of biochemical techniques with mass spectrometry, such as transcriptome approaches, can provide a deep insight into specific metabolic states of a disease.

In this chapter, we present a thorough characterization of the kidney lipidome in a rat model of acute kidney injury (AKI), combining MALDI-IMS and transcriptome techniques. We also evaluate the impact of the ferroptosis inhibitor Ferrostatin-1, in order to identify potential biomarkers of ferroptosis and therapeutic targets.

The data presented here have been partially published in:

1. **Lucia Martin-Saiz**, Juan Guerrero-Mauvecin, Diego Martin-Sánchez, Olatz Fresnedo, Susana Carrasco, Pablo Cannata-Ortiz, Alberto Ortiz, Jose A. Fernández, Ana B Sanz. Ferrostatin-1 modulated dysregulated kidney lipids in acute kidney injury. *Submitted to The Journal of Pathology.*

5.1   Introduction

Acute kidney injury (AKI) is a renal syndrome characterized by an abrupt decline in kidney function typically diagnosed by the accumulation of end products of nitrogen metabolism (urea and creatinine) or decreased urine output, or both. It is a serious complication associated with increased morbidity and mortality (up to 50%), hospital stay and cost. Moreover, it is associated with a higher rate risk of chronic kidney disease (CKD) progressing to end-stage renal disease (ESRD)[1, 2].

AKI is not a single disease but rather a loose collection of syndromes as diverse as sepsis, cardiorenal syndrome and urinary tract obstruction. Thereby, the events that cause AKI are still controversial. However, extensive renal tubular cell death is the main shared pathological episode among AKI patients[1]. Tubular cell death is followed by tubular dedifferentiation, proliferation and regeneration all associated with inflammation processes[3]. Recently, it has been reported that different pathways of regulated necrosis (e.g. necroptosis, ferroptosis) contribute to tubular cell loss in different models of AKI[4-7]. In fact, ferroptosis participates in a first wave of cell death in nephrotoxic AKI, promoting an inflammatory response that leads to a second wave of cell death mediated by necroptosis that amplifies injury and leads to persistence of AKI over several days[5] (**Figure 5.1**).

Ferroptosis is morphologically and biochemically different from other type of cell death. It is characterized by the massive lipid peroxidation, which leads to plasma membrane rupture. The sensitivity to ferroptosis depends on numerous biological and metabolic processes, including amino acid, iron and polyunsaturated fatty acid (PUFA) metabolism, and the biosynthesis of phospholipids and glutathione[8]. In fact, arachidonic acid (AA)-containing phosphatidylethanolamine (AA-PE) species are specifically oxidized during ferroptosis and incubation with AA promotes ferroptosis in cultured fibroblasts[9]. These hallmarks of ferroptosis could be potential biomarkers in the clinic. Ferroptosis can be prevented with different molecules belonging to the ferrostatin family such as ferrostatin-1 (Fer-1) that acts as a lipid peroxidation scavenger[10]. Indeed, a protective effect of ferrostatin has been observed in different models of AKI[5, 6, 11].
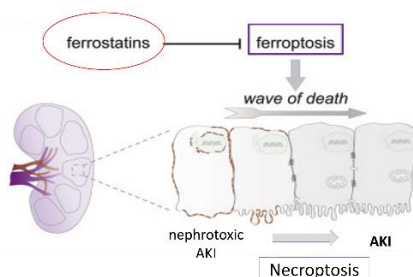
Figure 5.1. *Scheme of Acute kidney injury pathogenesis.*

5.2   Objectives

In this chapter we will explore the kidney lipidome from control, AKI and AKI+Fer-treated mice by MALDI-IMS. We will determine lipid features that distinguish cortical, glomerular and medullary structures to build a classification model for the three study groups.

Moreover, we will study the lipid differences among the three kidney models, trying to find AKI biomarkers as well as some lipids which can explain the effect of Fer-1 in the AKI kidney metabolism.

5.3   Experimental section

Sample collection

Sample collection was carried out by the nephrology department from the Fundación Jiménez-Diaz universitary hospital (Madrid, Spain). All procedures were conducted in accordance with the NIH Guide for the Care and Use of Laboratory and were approved by the animal ethics committee of IIS-FJD. Folic acid nephropathy is a classical model of AKI characterized by tubular cell death, interstitial leukocyte infiltration and subsequent tubular regeneration that has been reported in humans[16, 17]. Female C57BL/6 mice (12 to 14-week-old) received a single intraperitoneal (i.p.) injection of folic acid (Sigma, St. Louis, MO) 250 mg/kg in 0.3 mol/l sodium bicarbonate or vehicle. A third group of mice received an i.p. dose of 5 mg/kg Fer-1 (Santa Cruz Biotechnology, Santa Cruz, CA), 30 minutes before folic acid injection. Doses were based on previous report[5]. Mice were sacrificed 48 hours later (n=5 per experimental group). Plasma samples were collected at the time of sacrifice. Kidneys were perfused in situ with cold saline before removal, and snap-frozen in liquid nitrogen until sample preparation. Sections of 15 μM were performed for MALDI-IMS and histological analyses. Another set of folic acid model was used to validate enzyme gene expression among control and AKI group (n=4-6 per experimental group).

Imaging and data analysis

Detailed explanation of the experimental protocol may be found in **Chapter 3**. Histological sections of 15 murine kidneys (n=5 for control, AKI and AKI+Fer-1respectively) were prepared in a cryostat and placed on glass slides. Sample preparation was carried out in our in-house designed sublimator device[18] and approximately 0.2 mg/cm^2 of DAN were deposited on each sample. MALDI-IMS analyses were performed using a MALDI-LTQ-Orbitrap XL (Thermofisher). Data were acquired with mass resolution of 60000 at m/z = 400 in a scanning range of 550-1000 in negative-ion mode. Laser energy was set to 20-25 μJ/pulse. Two raster size were used: 10 and 25 microns. The rest of MALDI IMS parameters used are described on Chapter 3. H&E staining (Sigma Aldrich

Quimica, Madrid, Spain) was carried out for all the samples after MALDI IMS experiment were completed.

Data analysis was performed with our in-house made software built in Matlab (MathWorks, Natick, USA) using specific parameters described in **Chapter 3**. For clustering, data from each section were analyzed using a segmentation algorithm (HD-RCA) to isolate and identify lipid signatures of each histological area in the section. Three number of segments were tested: 3, 4 and 5 in to find the optimal number of segments to best visualize the different histological areas. We expected to find two different tubules and a glomeruli segments in cortical samples while in sections which include cortex and medulla, three cortical and one or two medullary segments were expected. The signatures from the final histological areas (cortical tubules, glomeruli and medullary tubules) were later used in subsequent multi-experiments analysis.

To statistically evaluate the differences in the lipid fingerprints among healthy, AKI and AKI+Fer-1 murine kidney and among cortex, glomeruli and medulla of each model, Levene-test, analysis of variance (ANOVA) univariate statistical analysis and Tukey /Games Howell post-hoc were computed using SPSS Statistics 17.0 (IBM, Armonk, NY, USA)[19]. Levene-test determines the homocedasticity (H_0 = groups have equivalent variance) to choose the post-hoc method: Tukey if Levene $p \geq 0.05$ and Games-Howell if Levene $p \leq 0.05$. PCA analysis and separation models were carried out using Orange Biolab 2.7.8 (Ljubljana, Slovenia)[20].

RNA-seq

Total RNA of control and AKI kidneys (3 animals per group) obtained 48h post induction of AKI was extracted with PureLink® RNA Mini Kit (Invitrogen, Thermo Fisher, Waltham, MA). From 1 μg total kidney RNA, the PolyA+ fraction was purified and randomly fragmented, converted to double stranded cDNA and processed through subsequent enzymatic treatments of end-repair, dA-tailing, and ligation to adapters with NEBNext® Ultra™ II DNA Library Prep Kit (New England Biolabs, Ipswich, MA) following the manufacturer's recommendations. The adapter-ligated library was completed by PCR with Illumina PE primers (10 cycles). The resulting purified cDNA library was applied to an Illumina flow cell for cluster generation and sequenced for 50 bases in a single-read format (Illumina HiSeq 2000).

Sequencing quality was first checked with FastQC. The FASTQ files were pre-processed to filter by size quality and content in Ns using the Prinseq tool. Reads were then aligned to the mouse genome (GRCm38.p5. genome) with TopHat-2.0.1050. Transcripts assembly, estimation of their abundance and differential expression were calculated with Cufflinks-Cuffdiff tool in combination with CummeRbund. R package Transcripts with FPKM (Fragments per kilo base per million mapped reads) expression

values lower than 0.05 in both conditions were considered not expressed and were excluded from further analysis

Real-time polymerase chain reaction (rt-PCR)

Total RNA was extracted by the TRI Reagent method (Invitrogen, Carlsbad, CA) and 1 µg RNA was reverse transcribed with High-Capacity cDNA Archive Kit (Applied Biosystems, Foster City, CA). Quantitative PCR was performed in a 7500 Real Time PCR System with the Prism 7000 System SDS Software using pre-developed primers (Applied Biosystems) and RNA expression of different genes was corrected for GAPDH expression.

Western blot

Tissue samples were homogenized in lysis buffer (50 mM TrisHCl, 150 mM NaCl, 2 mM EDTA, 2 mM EGTA, 0.2% Triton X-100, 0.3% NP-40, 0.1 mM PMSF and 1 µg/ml pepstatin A) and separated by 10% SDS-PAGE under reducing conditions. After electrophoresis, samples were transferred to nitrocellulose membranes (Bio-Rad, Hercules, CA), blocked with 5% BSA in TBS/0.5% v/v Tween 20 for 90 min, washed with TBS/Tween, and incubated with primary antibody anti-phosphatidylethanolamine N-methyltransferase (*PEMT*, 1:200, Merck Millipore, Burlington, MA). Blots were washed with TBS/Tween and incubated with appropriate anti-rabbit peroxidase-conjugated secondary antibody (1:2000, Amersham, Aylesbury, UK). After washing with PBS/Tween, blots were developed with the chemiluminescence method (ECL) (Amersham) and probed with mouse monoclonal anti-α-GAPDH antibody (1:2000, Merck Millipore). Levels of expression were corrected for minor differences in loading.

RNA-seq, rt-PCR and western blot experiments were performed by the nephrology department from the Fundación Jiménez-Diaz universitary hospital (Madrid, Spain).

5.4   Results and discussion

Nephrotoxic AKI

Nephrotoxic AKI was induced in mice by a folic acid overdose after pretreatment with vehicle or Fer-1. Fer-1 prevented the increase in plasma creatinine and urea levels (**Figure 5.23**)[5].
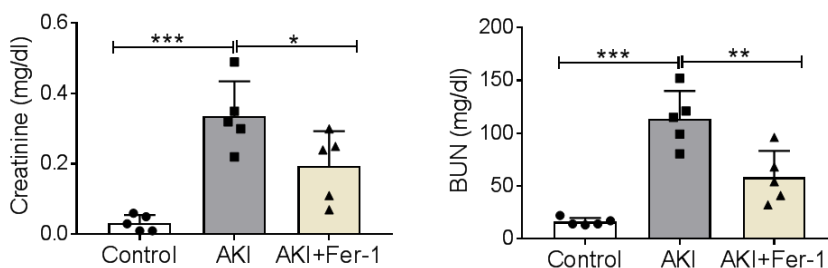
Figure 5.23. Characterization of experimental nephrotoxic AKI in mice. Nephrotoxic AKI was induced by a folic acid overdose with or without pretreatment with the ferroptosis inhibitor Fer-1. Kidney function was assessed by plasma creatinine and blood urea nitrogen (BUN) levels. Fer-1 preserved renal function. Mean ± SD of 5 mice per group. **p<0.005; **p<0.01; *p<0.05 in ANOVA and Tukey's post-hoc test.

Characterization of kidney regions by IMS in control, AKI and AKI+Fer-1 samples

Figure 5.3 shows the optical image of three H&E stained sections of control, AKI and AKI+Fer-1murine kidney. The same sections were scanned in IMS experiments using a pixel size of 25 μm in negative-ion mode. The intensities of 140 lipid species belonging to 16 lipid families (**Figure 5.4**) were directly captured from the fresh tissue sections, obtaining a distribution map for each of the species. Example images for the distribution of the SM d34:1, PE 38:4, PI 38:4 and SFT t42:1 are also shown in **Figure 5.3**. Distribution of these lipids is not uniform in any of the tree study groups: control, AKI and AKI +Fer-1. Conversely, SM 34:1 is preferentially found in glomeruli, PE 38:4 shows a higher abundance in cortical tubules while PI 40:6 and SFT t42:1 relative concentration is higher in medullary structures.

The differential lipid fingerprint at each pixel was further analyzed to define areas with similar lipid profiles. For this purpose, a segmentation algorithm was applied to group the pixels according to the similarity of their lipid fingerprints. An example of the result from this analysis is found in the right column of **Figure 5.3,** where five different clusters were found: two cortical tubules (white and blue), glomeruli (green) and two medullary tubules (red and brown). Additional images for all the kidney samples analyzed at 10 μm of spatial resolution are collected in the **Figures A.5.1, A.5.2 and A.5.3**.
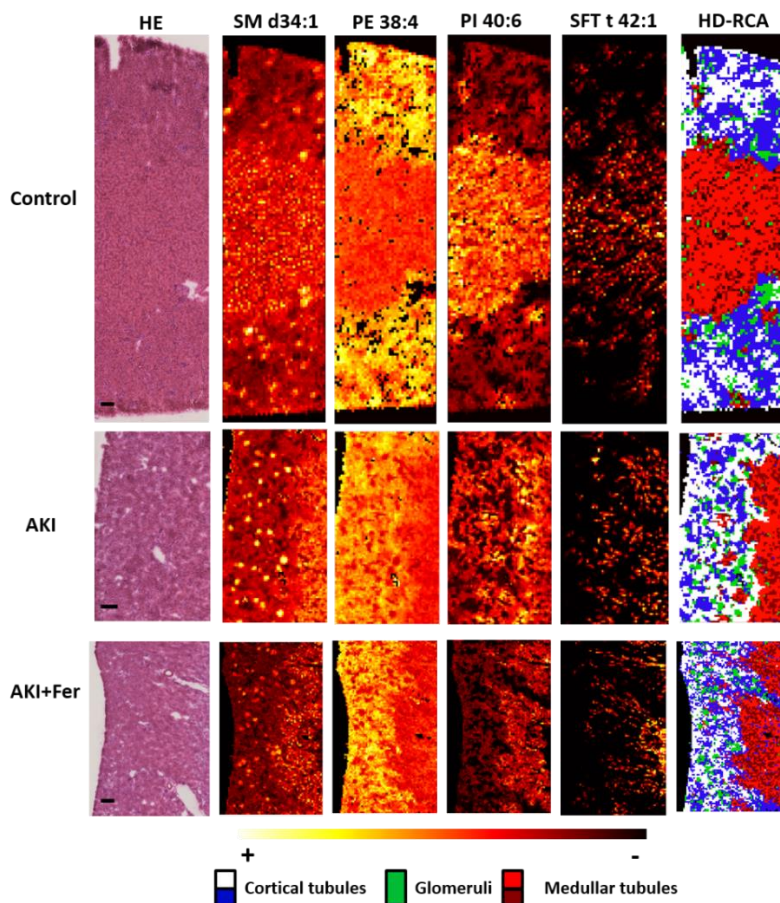
Figure 5.3. *MALDI IMS images of control, AKI and AKI+Fer-1 kidney. From left to right, H&E of three example kidney sections, distribution of four representative lipids over the three example sections and segmentation analysis of the lipid fingerprint at each pixel (HD-RCA) for each renal sample. The algorithm automatically detected five histologic areas labelled as cortical tubules (white and blue), glomeruli (green) and medullary tubules (red and dark red).*
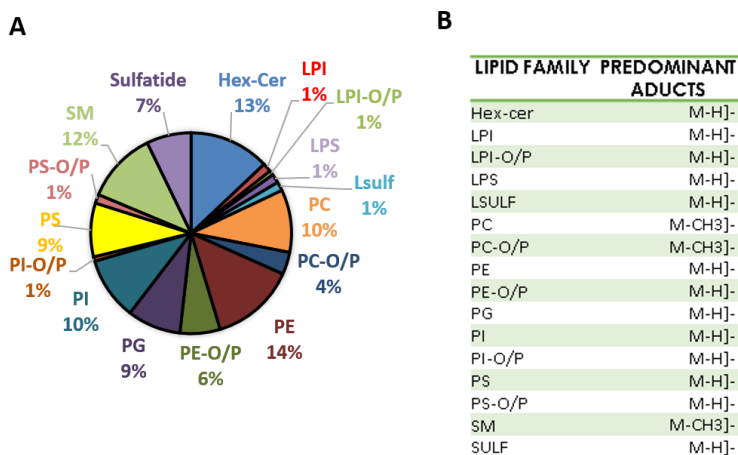
Figure 5.4. *Kidney lipids detected by MALDI IMS in negative-ion mode. (A) Percentage of lipid species detected from each family. (B) Predominant adducts from each lipid family. The lipids included in this analysis have been detected in control, AKI and AKI+Fer-1 kidney (n=5 for each group) in at least 80% of the samples of each group.*
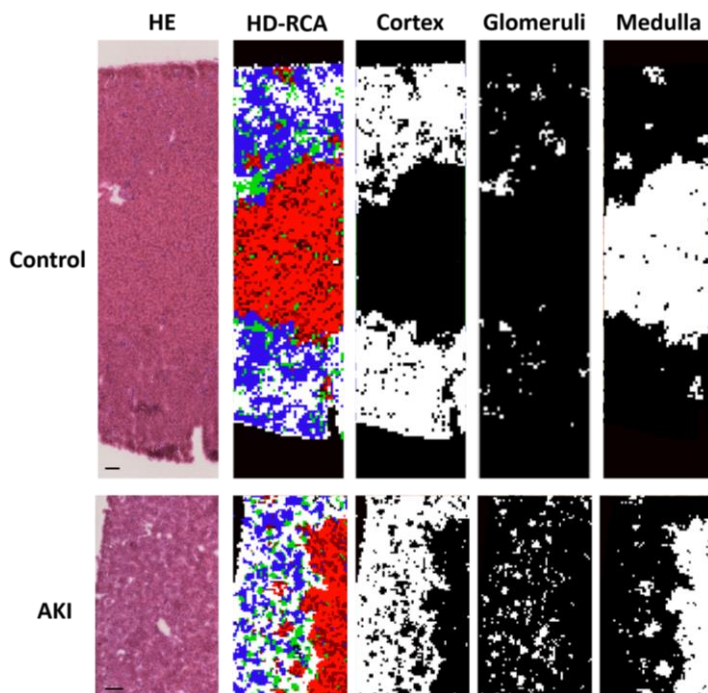
Figure 5.5. *Comparison between the optical image of H&E staining, the HD-RCA clustering images and an example of the corresponding clusters named as cortex, glomeruli and medulla in control and AKI kidney which will be used in following analysis.*

To test the differences in lipid fingerprints between histological areas obtained by IMS, a multi-class analysis was carried out in Control, AKI and AKI+Fer-1 kidney data sets. An example of the clusters selected as cortex, glomeruli and medulla can be found in **Figure 5.5**.

A neat separation was obtained among cortex, glomeruli and medulla for all the models as shown in **Figure 5.6B, E and H**. The confusion matrices may also be found in **Figure 5.6C, F and I.** The method that achieved the best results was random forest, with a ROC of 1, a precision of 1 and a recall of 1. All these values indicate that the lipid fingerprint of the histological areas found is representative of each area and invariant among individuals.

Figure 5.6A, D and G show the summation of intensities of the lipid species corresponding to the major subclasses of glycerophospholipids and sphingolipids detected in cortex, glomeruli and medulla for the three study models. Statistically significant differences for lipid subclasses among the histological areas are reported in **Tables A.5.1, A.5.2 and A.5.3,** where 36, 33 and 32 lipids show significant differences among cortex, glomeruli and medulla in Control, AKI and AKI+Fer-1 kidney respectively.
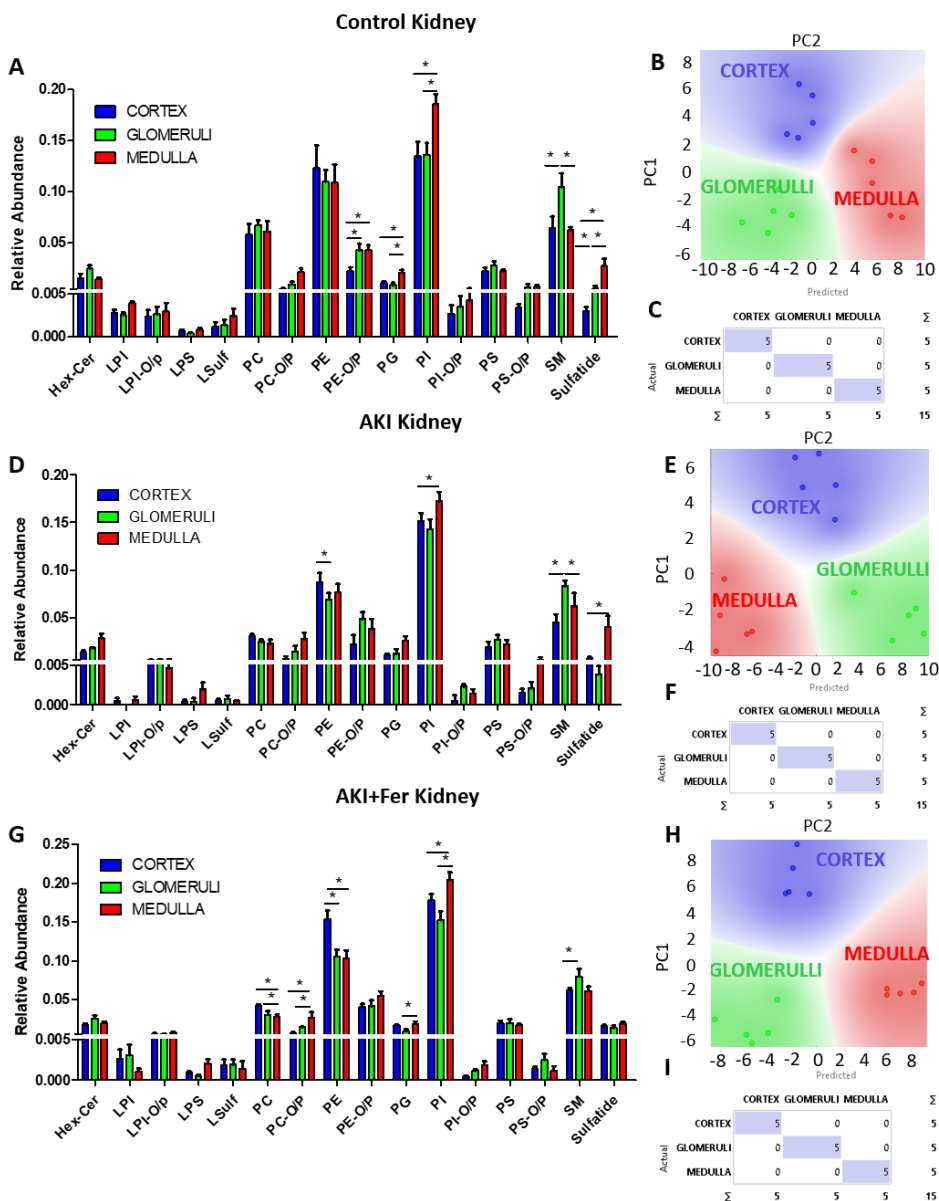
Figure 5.6. *Lipid characterization of control, AKI and AKI+Fer-1 samples.* **(A, D, G)** *Summation of intensities of the lipid species corresponding to major glycerophospholipid and sphingolipid families detected in the cortex, glomeruli and medulla area for the three study models: control, AKI and AKI+Fer-1 respectively.* **(B, C, H)** *PCA analysis of the lipid fingerprint in the different kidney regions.* **(C, F, I)** *Confusion matrix for random forest model in control, AKI and AKI+Fer-1 kidney.* * = p-value < 0.05 in t-studenT-test between the two indicated groups*

Notably, for all the study models, a significative higher expression of SM exists in glomeruli structures and more abundant expression of PI is found in medulla clusters. In control and AKI kidney, sulfatides relative abundance is higher in medullary structures, while in AKI and in AKI+Fer-1 models, PE levels are predominant in renal cortex. These findings indicate that each renal area has a characteristic lipid fingerprint which could be modified after injury and therapeutically.

Changes in renal lipid profile occasioned by AKI

After characterizing the lipid profile of each renal region, we focused on finding the lipid differences between healthy and AKI samples. IMS data sets from the whole kidney section of the two groups were compared resulting in 35 species (20.5%) with significant differences (**Table 5.1Table 5.1.** Significantly different lipid species between control and AKI kidney. The table shows the mean intensity AKI/control ratio, p-values for Levene-test to determine the homogeneity (H0 = groups have equivalent variance) to choose the T-test method (for equivalent variance or not) and T-test p-value.)**.** While 23 lipid species suffered from a marked upregulation, 12 were highlighted decreased in AKI model.

Specifically, PG's (6/18, 26.7% of upregulated species), PC's (3/18, 16%) and HexCer's (4/18, 22%) accounted for two thirds of upregulated species, while PE's (5/12, 42% of downregulated species) and HexCer's (3/12, 25%) accounted for two thirds of downregulated species (**Table 5.1**). The most upregulated lipid species were PG 38:6 (10.7-fold), HexCer d28:1 (5.2-fold), PC 34:0 (4.4-fold) and PG 40:8 (4.1-fold). The most downregulated lipid species in AKI were HexCer t44:4 (decreased 35.5-fold) and HexCer t40:2 (decreased 16.2-fold), being the latter the most abundant specie of this family. This suggests that lipid metabolism is clearly modified by FA-AKI pathology.

Further demonstration of the AKI influence in the renal lipidome may be found in **Figure 5.7** in which the volcano plot shows the existence of different lipid fingerprints in the two groups and PCA analysis correctly group control and AKI samples independently. Therefore, four different classification models (Logistic Regression, Naïve Bayes, Random Forest and Support Vector Machine (SVM) verify the lipid fingerprint differences between control and AKI kidney with an agreement up to 90%. The data was trained to build a two-class classification model using 5-fold internal cross-validation. The confusion matrix for Naïve Bayes, whose classification results were the best, demonstrates that it was able to classify almost all tissues from control and AKI sections. Only 6% of the data were misclassified (**Figure 5.7D**), which may be due to the similarity among each kidney region lipid fingerprint (cortex, glomeruli and medulla) independently from the pathological state.

Table 5.1. Significantly different lipid species between control and AKI kidney. The table shows the mean intensity AKI/control ratio, p-values for Levene-test to determine the homogeneity (H0 = groups have equivalent variance) to choose the T-test method (for equivalent variance or not) and T-test p-value.

UPREGULATED SPECIES

Lipid specie	AKI/Control ratio	Levene p-value	t-Test p-value
HexCer d28:1	5.202	0.004	0.001
HexCer d34:0	1.746	0.697	0.049
HexCer d36:2	3.311	0.000	0.034
HexCer t35:1	2.772	0.218	0.007
Lyso-PI 20:4	2.032	0.138	0.035
Lyso-PI O-18:2/P-18:1	2.127	0.518	0.000
PC 23:5	2.482	0.339	0.000
PC 34:0	4.396	0.036	0.007
PC 40:7	2.260	0.968	0.001
PC O-34:2 /P-34:1	3.392	0.099	0.001
PC O-36:6 /P-36:5	2.395	0.157	0.006
PE 25:5	2.506	0.416	0.000
PE O-36:2 /P-36:1	2.772	0.218	0.007
PG 23:1	3.317	0.010	0.022
PG 36:1	1.871	0.723	0.007
PG 36:4	3.496	0.035	0.001
PG 38:6	10.707	0.000	0.003
PG 40:7	2.817	0.032	0.005
PG 40:8	4.144	0.001	0.003
PI 38:4	1.747	0.515	0.016
PI 38:5	1.863	0.225	0.009
PS 38:5	2.115	0.218	0.008
SM d34:2	2.539	0.038	0.004

DOWNREGULATED SPECIES

Lipid specie	AKI/Control ratio	Levene p-value	t-Test p-value
HexCer d36:4	0.345	0.035	0.002
HexCer t40:2	0.062	0.000	0.009
HexCer t44:4	0.028	0.000	0.005
Lyso-SFT d19:2	0.311	0.003	0.034
PC 38:6	0.614	0.273	0.019
PE 34:0	0.304	0.050	0.001
PE 38:3	0.721	0.519	0.047
PE 38:5	0.519	0.116	0.015
PE 39:4	0.362	0.016	0.027
PE 40:6	0.605	0.325	0.017
PI 34:1	0.662	0.157	0.031
SM d41:4	0.110	0.000	0.001

Moreover, in order to easily visualize the changes in the lipid metabolism due to AKI, we grouped the lipids by families and statistical analysis was performed to compare the lipidome of the two groups. Although some minority lipid families such as LPI, LPI-O/P and LSFT were significantly modified, the most relevant differences were the significant decrease in PE species and the highlighted increase in PI lipid family (**Figure 5.7D**).This confirms the high influence that AKI pathology has in the lipid metabolism.
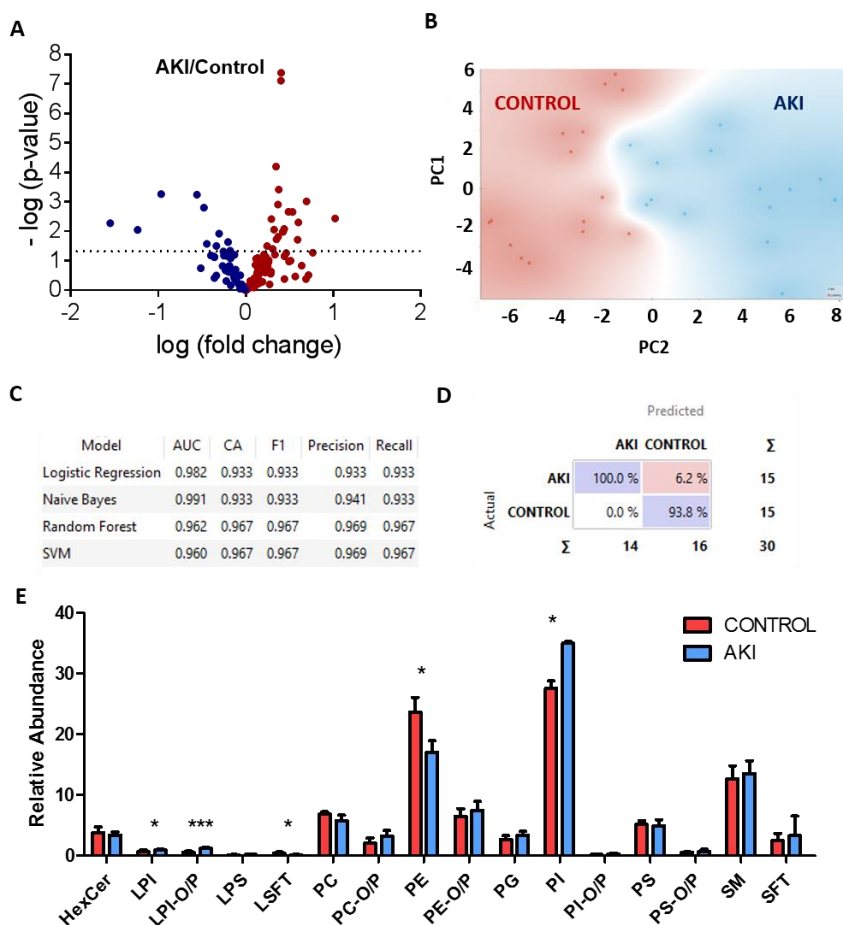
Figure 5.7. *Comparison of lipid profile between AKI and control kidneys. **(A)** Volcano plot comparing control and AKI lipid data set. **(B)** PCA analysis of the lipid fingerprint of the two groups. **(C)** Performance of the classifier models built. **(D)** Confusion matrix of the Naïve Bayes model. **(E)** Summation of intensities of the lipid species corresponding to major glycerophospholipid and sphingolipid families detected in the whole kidney for control and AKI samples. * = p < 0.05, ** = p-value < 0.01, *** = p-value< 0.001 in T-test.*

Unraveling AKI modifications in the different kidney regions

In the previous section, the whole AKI kidney IMS data sets were studied. However, it was also interesting to independently analyze the different kidney regions to discover the specific region-dependent lipid changes caused by AKI.

For this purpose, IMS clusters from cortex, glomeruli and medulla from control and AKI samples were separated and analyzed. An example of the selected clusters as cortex, glomeruli and medulla can be found in **Figure 5.5** in the previous section.

As regards cortical IMS clusters, 30 lipid species (21,42 % of the total species detected) belonging to ten lipid families show significant differences between control and AKI sections. It is worth stressing that most of these lipid species are in higher concetration in AKI cortex (**Table 5.2**). PG 38:6, HexCer d28:1 and HexCer t35:1 were the lipid species whose abundance experienced the biggest increase in AKI, while HexCer d40:2 and HexCer t40:2 experienced a reduction in its abundance.

Moreover, a PCA analysis was performed with the lipid species that passed the T-test (p-value < 0.05) and the result confirmed the clear distinction between control and AKI renal cortex (**Figure 5.8A**) Also, molecular classification and confusion matrix was generated using four different models resulting in an overall agreement of 100% (**Figure 5.8B and C**). As a final analysis, lipid species from control and AKI cortex were grouped by families and statistical comparison was performed (**Figure 5.8D**). Three lipid families showed significant differences: LPI-O/P's and SFT's were both upregulated while PE's decreased in AKI cortex.

Table 5.2. *AKI/CONTROL ratio of the significant upregulated and downregulated lipid species between control and AKI cortex. p-value of Levene-test. p-value < 0.05 = non-equivalent variance (red shadowed) and T-test are also shown.*

CORTICAL UPREGULATED SPECIES   CORTICAL DOWNREGULATED SPECIES

Lipid specie	AKI/CONTROL RATIO	Levene test p-value	t-Test p-value	Lipid specie	AKI/CONTROL RATIO	Levene test p-value	t-Test p-value
HexCer d28:1	6.22110	0.21903	0.00658	HexCer d40:2	0.08835	0.03847	0.03384
HexCer d36:2	1.96761	0.65731	0.02583	HexCer t40:2	0.09349	0.04292	0.03741
HexCer t33:1	2.65935	0.37446	0.02923	Lyso-PI 18:0	0.92512	0.06367	0.04209
HexCer t35:1	15.63276	0.00885	0.01415	PC O-38:7	0.47095	0.31952	0.04848
HexCer t39:4	3.54742	0.87002	0.02608	SM d41:4	0.23023	0.23284	0.03300
Lyso-PI 20:4	1.74344	0.06367	0.04209	SFT t40:0	0.34649	0.00645	0.02433
PC 23:5	2.01348	0.56454	0.01389	SFT t40:1	0.76226	0.63997	0.00384
PC 40:7	3.48408	0.87083	0.00229	SFT t40:2	0.44961	0.35371	0.00929
PC O-40:7	4.67364	0.91637	0.00554	SFT t41:1	0.78429	0.12436	0.04005
PE 25:5	2.80823	0.57518	0.00062	SFT t42:0	0.32482	0.00331	0.02096
PE 34:2	2.04579	0.38068	0.01285	SFT t42:1	0.41086	0.58310	0.00003
PE 40:3	1.94665	0.97087	0.03123				
PE 40:8	1.37022	0.41346	0.01836				
PE O-34:2	2.16995	0.71715	0.01260				
PE O-40:8	2.70635	0.22355	0.00069				
PG 36:3	3.79619	0.63905	0.00382				
PG 36:4	8.29664	0.88555	0.00111				
PG 38:6	12.66964	0.02050	0.04038				
PG 40:7	2.72936	0.95910	0.02271				
PG 40:8	4.45278	0.30984	0.00350				
PI 36:2	2.46591	0.10856	0.00147				
PI 36:3	1.75768	0.83145	0.02736				
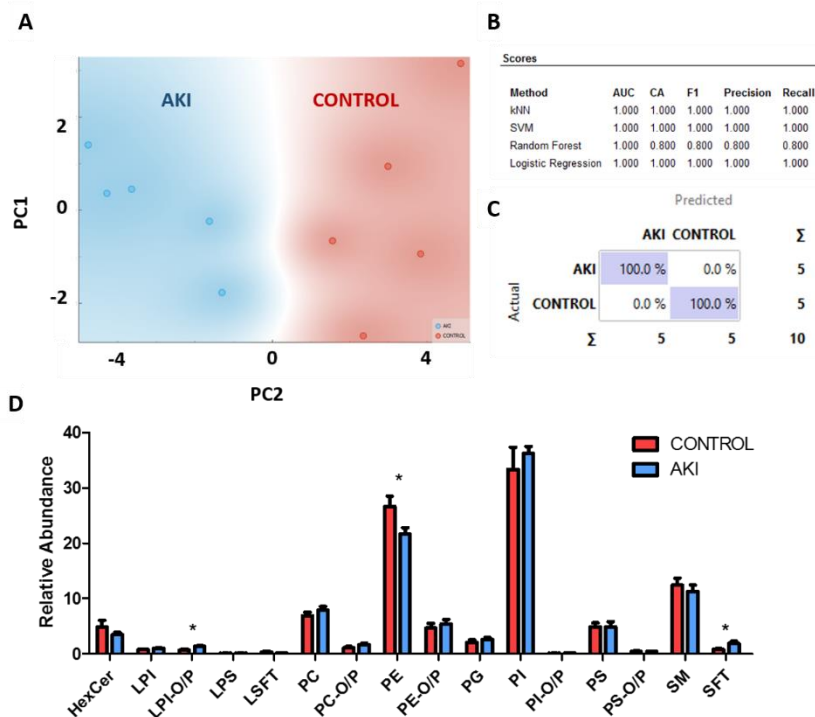
Figure 5.8. (A) *PCA separating control and AKI cortex lipid fingerprint (n=5 for both groups).* **(B)** *Summary of the models' performance for the two-class classification.* **(C)** *Confusion matrix showing classification results by Logistic Regression.* **(D)** *Summation of intensities of the lipid species corresponding to the main lipid families detected in the renal cortex for control and AKI samples. * = p < 0.05, in T-test.*

The same analysis was performed with glomeruli and medulla IMS data sets. With regard to glomeruli areas, 21 lipid species (belonging to seven lipid families) were positive in a T-test analysis (p-value < 0.05) comparing control and AKI samples (**Table 5.3**). Although the number of significant lipid species in cortex was higher and the lipid species intensity ratio AKI/control was larger in cortical structures, glomeruli lipid biomarkers were also able to perfectly separate the IMS data sets of the two study groups in a PCA scatter plot (**Figure 5. 9A**). Therefore, the perfect results of the four classification models and the confusion matrix showed in **Figure 5.9B and C** respectively, verifies the change in the lipid metabolism of the glomeruli due to AKI. Therefore, by analyzing the changes in the lipid families, it is possible to clearly see the significant upregulation of LPI-O/P's, PC-O/P and PI-O/P's and the downregulation of LPI's, PC's and PE's in AKI glomeruli structures (**Figure 5.9 D**).

.

Table 5.3. *AKI/CONTROL ratio of the significant upregulated and downregulated lipid species between control and AKI glomeruli. p-value of Levene-test (p-value < 0.05 = non-equivalent variance (red shadowed)) and T-test are also shown.*

GOMERULAR UPREGULATED SPECIES

Lipid specie	AKI/CONTROL RATIO	p-value Levene test	p-value t-Test
HexCer_d28:1 -H-	4.76418	0.18601	0.00821
HexCer_d30:1 -H-	1.77675	0.87996	0.02668
HexCer_d36:2 -H-	2.18423	0.07377	0.01925
HexCer_t35:1 -H-	4.58195	0.83003	0.00652
Lyso-PC_23:5-CH3-	3.22590	0.04179	0.03420
PC_38:3-CH3-	1.92784	0.32147	0.02975
PC_38:5-CH3-	2.07762	0.87751	0.01737
PC_40:7-CH3-	3.73584	0.56176	0.00914
PE_25:5-H-	3.15672	0.18585	0.01493
PE_36:3-H-	2.50659	0.68198	0.04121
PE_40:3-H-	2.19885	0.09827	0.00689
PG_36:4-H-	4.19723	0.37567	0.03613
PG_38:6-H-	1.34706	0.05628	0.00849
PG_40:8-H-	4.92224	0.08613	0.02087
SM_d34:1-CH3-	1.27311	0.32427	0.02169
SM_d34:2-CH3-	2.18925	0.00347	0.04946
SFT_d34:1 -H-	4.99318	0.21318	0.02207

GLOMERULAR DOWNREGULATED SPECIES

Lipid specie	AKI/CONTROL RATIO	p-value Levene test	p-value t-Test
PE_38:6-H-	0.34016	0.57408	0.03443
PE_40:7-H-	0.33798	0.73541	0.03967
SM_d41:4-CH3-	0.04449	0.00254	0.00679
SFT_d40:1 -H-	0.45657	0.56894	0.01913
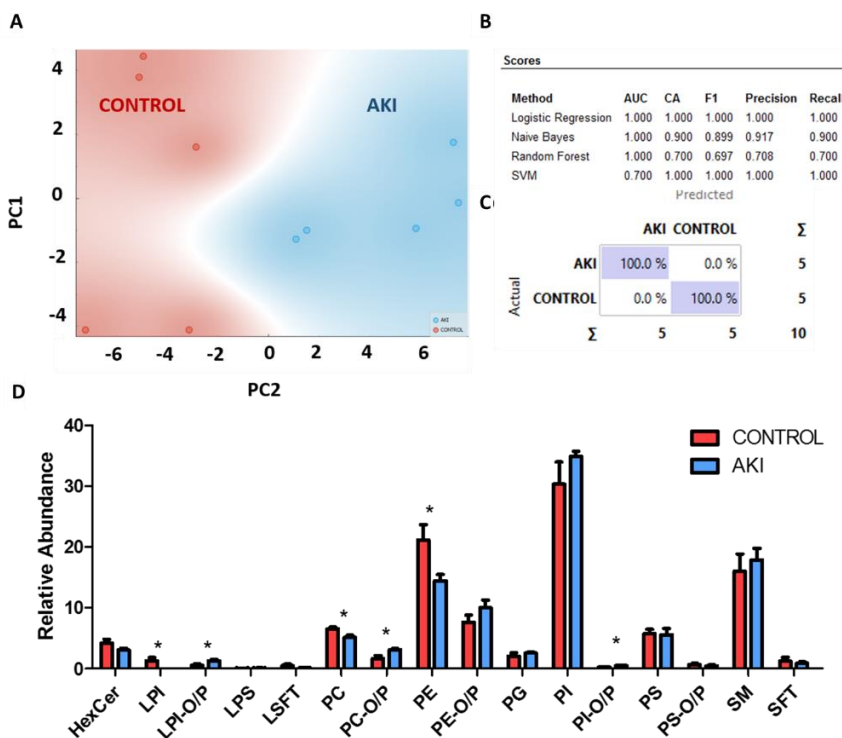
Figure 5.9. (A) *PCA separating control and AKI glomeruli lipid fingerprint (n=5 for both control and AKI).* **(B)** *Summary of the models' performance for the two-class classification.* **(C)** *Confusion matrix showing classification results by Logistic Regression.* **(D)** *Summation of intensities of the lipid species corresponding to major glycerophospholipid and sphingolipid families detected in the renal glomeruli for control and AKI samples. * = p < 0.05, in T-test.*

Regarding medulla analysis, as it is shown in **Table 5.4**, only 11 lipid species included in six lipid families differed significantly in the comparison of control vs AKI. This suggest that medullar metabolism remains more stable than in the other kidney regions during AKI pathology. Nevertheless, these lipid differences allows the PCA analysis to correctly separate control and AKI medulla data sets, as supported in **Figure 5.10A**. The results of the classification models, all of them with an overall agreement above 70%, also demonstrate that an alteration of the metabolism in the medulla of AKI model clearly occurs (**Figure 5.10C and D**). Finally, the results of the lipid families' analysis, which can be found in **Figure 5.10E**, demonstrate that the total relative intensities of PC's and PE's is decreased in AKI medulla. Thus, this pathology modifies the PC- and PE-related medullar metabolic pathways.

Table 5.4. *AKI/CONTROL ratio of the significant upregulated and downregulated lipid species between control and AKI medulla. p-value of Levene-test (p-value < 0.05 = non-equivalent variance (red shadowed)) and T-test are also shown.*

MEDULLARY UPREGULATED SPECIES

Lipid specie	AKI/CONTROL RATIO	Levene test p-value	t-Test p-value
HexCer d28:1	4.969	0.332	0.011
PC 34:0	8.322	0.072	0.038
PE 25:5	4.506	0.022	0.025
PI 37:6	1.520	0.141	0.003
PI 38:5	1.989	0.272	0.021
SFT t42:1	5.796	0.851	0.000

MEDULLARY DOWNREGULATED SPECIES

Lipid specie	AKI/CONTROL RATIO	Levene test p-value	t-Test p-value
HexCer d36:4	0.278	0.165	0.044
HexCer t40:2	0.189	0.830	0.002
PI 34:1	0.464	0.866	0.012
PI 36:4	0.778	0.494	0.013
SM d41:4	0.076	0.003	0.027
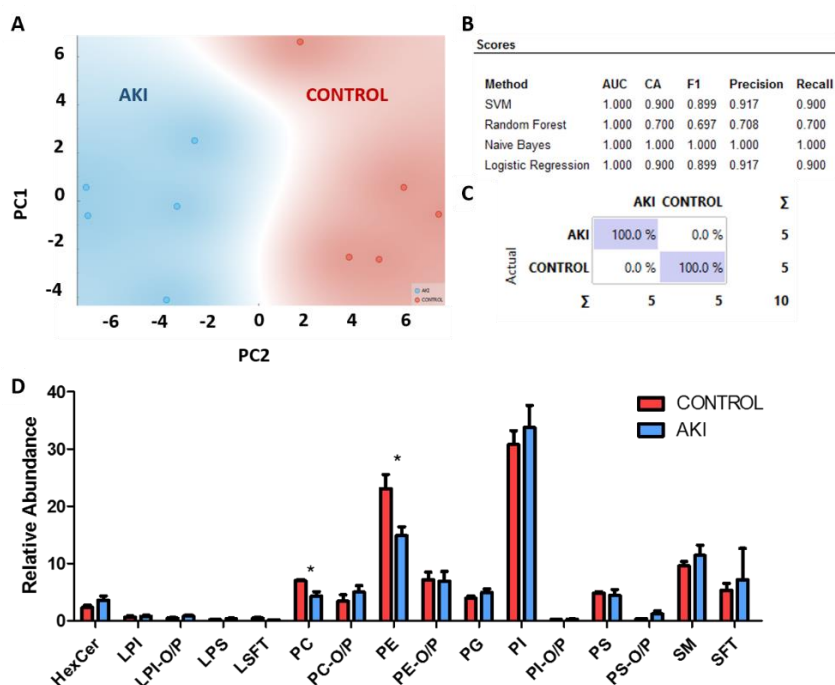
Figure 5.10. (A) *AKI/CONTROL ratio of the significant upregulated and downregulated lipid species between control and AKI medulla. p-value of Levene-test (p-value < 0.05 = non-equivalent variance (red shadowed)) and T-test are also shown.* **(B)** *PCA separating control and AKI medulla lipid fingerprint (n=5 for both control and AKI).* **(C)** *Summary of the models' performance for the two-class classification.* **(D)** *Confusion matrix showing classification results by SVM.* **(E)** *Summation of intensities of the lipid species corresponding to major glycerophospholipid and sphingolipid families detected in the renal medulla for control and AKI samples. * = p < 0.05 in T-test.*

Taking into account all these results, a last analysis was performed in order to summarize all the information in a single graph. The ratio AKI/control of the lipid families was calculated for the whole kidney section, the cortex, glomeruli and medullary areas.

It is surprising that the most variable lipid subclass was LPI-O/P whose significant upregulation (x2) in AKI samples can be seen in almost all the structures analyzed with the exception of the medulla. Similarly, the downregulation of PE's is not only significative in the entire kidney but also in cortex and glomeruli, as **Figure 5.11** shows. This finding leads us to think that the most modified histological regions by FA administration are cortical tubules and glomeruli, remaining almost invariable the medullary structures. In good agreement, according to the literature, AKI mostly affects cortical structures[5].

Another interesting observation is the reproducibility of the variations in the relative abundance of the lipid families detected, over the distinctive renal structures. Although it is true that none of the lipid subgroups shows significant differences in the isolated histological structures analyzed, it is remarkable that the same tendency can be appreciated for all the data subsets. LPI's, LPI-O/P's and PI's have a clear AKI upregulation in the whole AKI kidney and the same pattern was observed in cortex, glomeruli and medulla. Likewise, LSFT´s and PE´s shows a negative AKI/control ratio for the whole kidney section and the same trend was found in the structures analyzed independently (**Figure 5.11**).

In this regard, these results were compared with the kidney function determined by plasma creatinine levels in control and AKI renal samples (**Table 5.5**). Interestingly, medullary PE species inversely correlated with kidney function assessed as plasma creatinine while PI species positively correlated with kidney function in all regions. This result suggests that changes in lipid metabolism occurs during AKI, and that they are compartmentalized and associated with the severity of AKI.

Table 5.5. *Spearman correlation of kidney PE and PI species with plasma creatinine in control and AKI mice.*

	PE vs plasma creatinine		PI vs plasma creatinine	
	R	p-value	R	p-value
Whole kidney	-0.535	n.s	0.474	n.s
Cortex	-0.207	n.s	0.717*	0.02
Glomeruli	-0.267	n.s	0.772**	0.009
Medulla	-0.717*	0.02	0.14	n.s
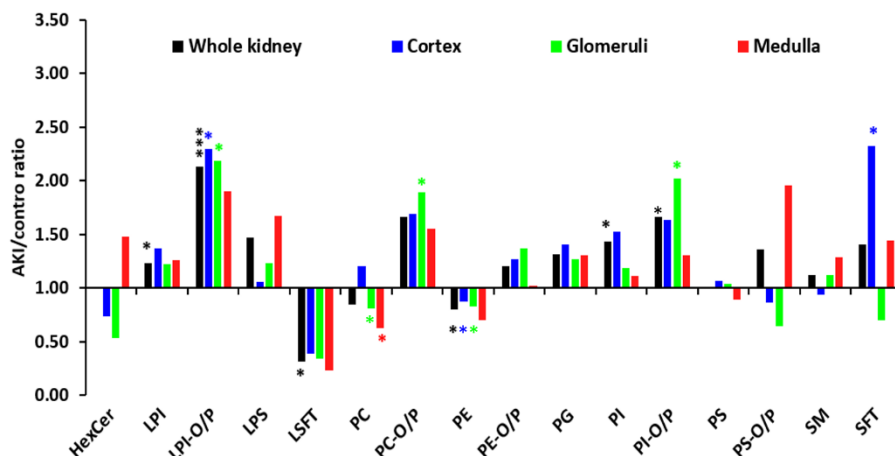
Figure 5.11. *AKI/Control ratio of the lipid subclasses corresponding to major glycerophospholipid and sphingolipid families detected in the whole kidney, cortex, glomeruli and medulla for control and AKI kidney. * = p < 0.05, **= p-value < 0.01, *** = p-value< 0.001 in T-test.*

AKI lipid metabolism reversion by Ferrostatin treatment

Fer-1 is a strong inhibitor of necroptosis, producing a notable improving of the renal function and reduces renal injury in AKI[10] (**Figure 5.2).** Thus, to study the influence of this inhibitor in AKI lipid metabolism, we analyzed MALDI IMS data from AKI and Fer-1 treated AKI sections.

Firstly, the whole kidney IMS data sets of the two groups were compared resulting in 26 (18,57%) lipid species with significant differences (**Table 5.6).**

When Control vs AKI samples were compared, 65,7% of the lipids were found to present significant increase in relative concentration in AKI model (**Table 5.1**). However, it is worth of mention that in AKI+Fer-1 vs AKI comparison, 73% of the lipid species experienced a decrease in their concentration after Fer-1 administration. This means Fer-1 has a recovery effect in the renal lipidome.

Consistently, the volcano plot, PCA analysis and classification models displayed in **Figure 5.12** show that Fer-1 undoubtedly modified AKI lipid levels. The overall agreement of the four classification methods used is up to 93%, which means a clear distinction can be observed between AKI and AKI+Fer-1 lipid fingerprints. Thus, Logistic Regression, Naïve Bayes and SVM models achieve a perfect lipid-based classification (**Figure 5.12C and D**).

Table 5.6. Significantly different lipid species between AKI and AKI+Fer-1 samples. The table shows the mean intensity AKI/control ratio (n=5 for both groups), p-values for Levene-test to determine the homogeneity (H_0 = groups have equivalent variance) to choose the T-test method (for equivalent variance or not) and T-test p-value.

UPREGULATED SPECIES				DOWNREGULATED SPECIES			
Lipid specie	AKI+Fer-1/AKI ratio	Levene Test p-value	T-test p-value	Lipid specie	AKI+Fer-1/AKI ratio	Levene Test p-value	T-test p-value
PE 36:2	2.781	0.007	0.000	HexCer d36:0	0.622	0.114	0.035
PE O-38:7/P-38:6	3.297	0.948	0.000	PC 38:8	0.123	0.003	0.001
PG 34:1	2.406	0.296	0.015	PC 40:7	0.429	0.002	0.017
PG 38:1	1.607	0.058	0.042	PC 40:8	0.087	0.000	0.001
PI 38:4	1.206	0.000	0.043	PE 25:5	0.652	0.795	0.039
PS 38:4	1.211	0.651	0.016	PE 36:3	0.400	0.079	0.002
SM t32:2	1.998	0.728	0.001	PE 40:3	0.426	0.000	0.033
				PE 40:8	0.091	0.000	0.000
				PE O-36:2/P-36:1	0.644	0.269	0.049
				PG 23:1	0.075	0.000	0.002
				PG 36:0	0.471	0.895	0.008
				PG 36:1	0.551	0.953	0.013
				PI 32:0	0.300	0.000	0.033
				PI 36:1	0.278	0.037	0.044
				PS 40:6	0.362	0.005	0.034
				SFT t38:1	0.740	0.027	0.010
				SM d36:1	0.779	0.644	0.018
				SM d42:0	0.035	0.000	0.019

Furthermore, **Figure 5.12E** shows the comparison of the main lipid families between AKI and AKI+Fer-1.The results of the T-test analysis demonstrate that renal LSFT and PE levels significantly increase when Fer-1 is administered, while the relative abundance of PI-O/P and PS lipid families experience a statistically significant reduction.

Additionally, samples from AKI and AKI+Fer-1 were also compared to control samples not only to confirm the high impact of Fer-1 in lipid metabolism but also the reversion of the impact in lipid metabolism caused by AKI, as displayed in **Figure 5.13**. As expected, PCA analysis enables the neat separation among the three groups (**Figure 5.13A**), based on their lipid profile. Regarding the most dysregulated species in AKI, Fer-1 prevented the increase in PG 38:6 as well as the decrease in HexCer t40:2, while having only a marginal impact on the other top dysregulated species (HexCer d28:1, PG40:8, PC 34:0 and HexCer t44:4, **Figure 5.13B).** These variations in the lipid levels enable the classifier methods and the confusion matrix to yield excellent results in the segregation of the three groups **(Figure 5.13C,D).**

As regards minority lipid families, a remarkable increase in relative intensity of LPI-O/P's species was observed in AKI model. Such increase was not prevented with administration of Fer-1. However, LSFT's and PI-O/P relative levels recovered their control values in AKI+Fer-1 samples (**Figure 5.13E**).

Likewise, in the context of more abundant lipid families (**Figure 5.13F**), it should be noted the recovery effect that AKI+Fer-1 has in PE species, which is not only appreciated

in the whole kidney but also in cortex, glomeruli and medulla when independently analyzed (**Figure 5.13G**). Specifically, AKI-Fer-1 prevented the decrease in the levels of PE species that were among the most downregulated in AKI (**Figure 5.13H**).

On the other hand, it has also to be mentioned the case of the PI lipid family, whose levels are upregulated when AKI occurs but Fer-1 does not have a clear recovery effect. As an additional point, although PS's family remains constant in AKI kidney, the treatment has a marked downregulation effect (**Figure 5.13F**).

In the following section, a closer look at the effect of Fer-1 treatment on the different histologic areas will be provide.
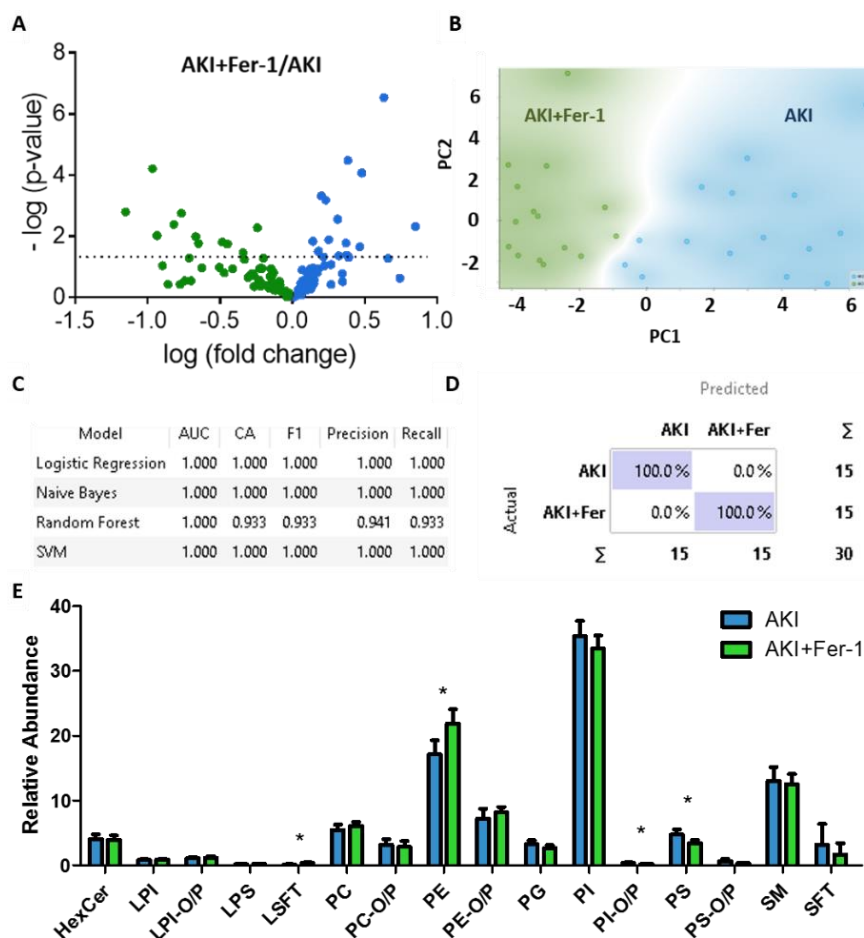
Figure 5.12. Comparison between the lipid profile of AKI and AKI+Fer-1. *(A)* Volcano plot comparing AKI and AKI+Fer-1 lipid data set*. (B)* PCA analysis of the lipid fingerprint of the two groups*. (C)* Classifiers summary*. (D)* Confusion matrix of the Naïve Bayes model. *(E)* Summation of intensities of the lipid species corresponding to major glycerophospholipid and sphingolipid families detected in sections of AKI and AKI+Fer-1. * = p < 0.05 in T-test.
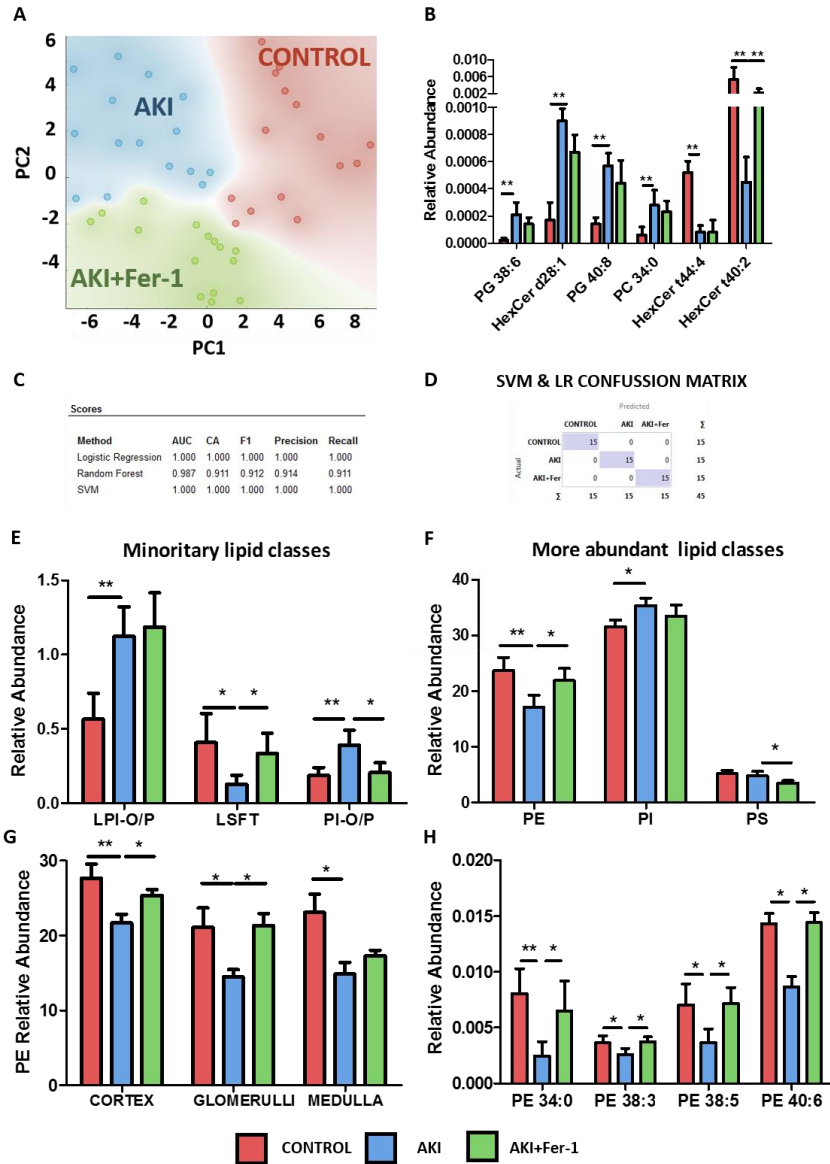
Figure 5.13. **(A)** PCA analysis of the lipid fingerprint of the Three study groups. **(B)** Fer-1 reversion of some lipids modified by AKI. **(C)** Classifiers models summary. **(D)** Confusion matrix of the SVM and Logistic Regression (LR) model. Summatory of the intensity of all the lipid species belonging to minoritary lipid family **(E)** and more abundant lipid subgroups **(F)** in Control, AKI and AKI+Fer-1 samples. Only lipid families whose difference was significative at least in one of the two-class comparison (control vs AKI and AKI vs AKI+Fer-1) are displayed. **(G)** Summation of intensity of PE lipid species detected in cortex, glomeruli and medulla from control, AKI and AKI+Fer-1 samples **(H)** Fer-1 reversion of relative intensity of PE species downregulated in AKI samples * = p < 0.05, **= p-value < 0.01 in T-test.

Effect of Fer-1 administration on the lipidome of different kidney regions

The impact of Fer-1 inhibitor over the whole AKI kidney samples was previously studied in the previous section. Now, we focus the analysis on the different histological areas. IMS clusters from cortex, glomeruli and medulla were extracted and their lipid fingerprint compared between AKI and AKI+Fer-1 kidney samples (see **Figure 5.5** for further information regarding on the clusters selected as cortex, glomeruli and medulla)

Table 5.7 shows the AKI+Fer-1/AKI ratio of the 24 lipid species significantly different in the cortical area of AKI+Fer-1 when compared to AKI samples. It is surprising that only six lipid species show a level increase due to Fer-1 treatment. The vast majority are downregulated in AKI Fer-1 model.

Furthermore, **Figure 5.14A** also displays a PCA analysis separating the cortical region of AKI and AKI+Fer-1 samples. It can be appreciated the perfect separation between the groups and an outstanding classification supported by the results from the four classifier models used (**Figure 5.14B**). In addition, the confusion matrix obtained by the Logistic Regression model verifies the noticeable differences comparing the two study groups (**Figure 5.14C**). Finally, the summatory of the intensity of all the lipid species by lipid families, suggests that PE's relative abundance is significantly increased in AKI+Fer-1 samples, while the SFT class is downregulated (**Figure 5.14D**).

Table 5.7. AKI+Fer-1/AKI ratio of the significantly different lipid species between control and AKI cortex. p-value of Levene-test (p-value < 0.05 = non-equivalent variance (red shadowed)) and T-test are also shown.

CORTICAL UPREGULATED SPECIES

Lipid specie	AKI+Fer1/AKI ratio	Levene testp-value	t-Test p-value
Lyso-PI 18:0	1.060	0.963	0.004
PE 34:0	3.057	0.043	0.014
PE 36:2	5.747	0.013	0.002
PE O-38:7/P-38:6	5.398	0.730	0.023
PG 34:1	5.876	0.287	0.003

CORTICAL DOWNREGULATED SPECIES

Lipid specie	AKI+Fer1/AKI ratio	Levene testp-value	t-Test p-value
HexCer d34:0	0.515	0.704	0.032
Lyso-PI 20:4	0.682	0.963	0.004
PC 38:8	0.076	0.054	0.001
PC 40:8	0.055	0.001	0.011
PE 25:5	0.644	0.670	0.014
PE 40:8	0.076	0.028	0.004
PE O-34:2/P-34:1	0.440	0.808	0.009
PE O-36:2/P-36:1	0.381	0.775	0.032
PE O-40:8/P-40:7	0.439	0.210	0.001
PG 36:2	0.447	0.415	0.029
PG 36:3	0.322	0.818	0.002
PG 36:4	0.424	0.450	0.040
PG 40:7	0.294	0.477	0.007
PG 40:8	0.453	0.595	0.029
SFT t41:1	0.797	0.060	0.035
SM d35:1	0.106	0.074	0.020
SM d42:0	0.043	0.001	0.006
SFT t38:1	0.741	0.019	0.003
SFT t40:0	0.712	0.064	0.014
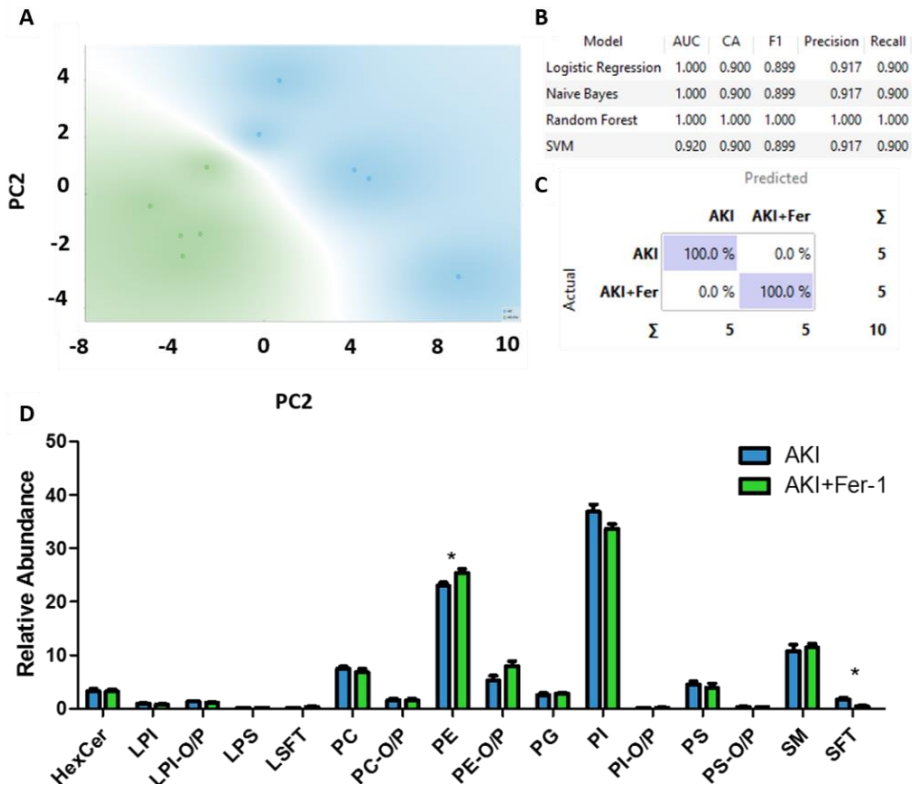
Figure 5.14. (A) *PCA separating AKI and AKI+Fer-1 cortex lipid fingerprint (n=5 for both groups).* **(B)** *Summary of the models' performance for the two-class classification.* **(C)** *Confusion matrix showing classification results by Logistic Regression.* **(D)** *Summation of intensities of the lipid species corresponding to major glycerophospholipid and sphingolipid families detected in the renal cortex for AKI and AKI+Fer-1 samples. * = p < 0.05.*

In the context of glomeruli, also clear differences characterize AKI and AKI+Fer-1 samples. 24 lipid species belonging to 7 lipid families showed significant modification due to Fer-1 treatment and, as in cortical area, a higher percentage of the significant modified lipids present a loss of intensity in AKI+Fer-1 renal glomeruli (**Table 5.8**). Moreover, the PCA scatter plot allow us to perfectly discriminate between the lipid fingerprint of the glomeruli of AKI or AKI+Fer-1 sections, as **Figure 5.15A** shows. This is supported by the results of the classifier models performed, with an overall agreement up to 86%, and the confusion matrix obtained from Logistic Regression model (**Figure 5.15B and C**)

Table 5.8. *AKI+Fer-1/AKI ratio of the significantly different lipid species between control and AKI glomeruli. p-value of Levene-test (p-value < 0.05 = non-equivalent variance (red shadowed)) and T-test are also shown.*

GLOMERULAR UPREGULATED SPECIES

Lipid specie	AKI+Fer1/AKI ratio	Levene test p-value	t-Test p-value
HexCer d28:0	2.554	0.043	0.042
PE 36:2	2.978	0.048	0.015
PE O-38:7/P-38:6	3.759	0.166	0.004
PS 33:0	5.887	0.789	0.001
PS 33:1	12.769	0.021	0.039
SM d40:1	0.178	0.101	0.007
SM t30:1	3.111	0.737	0.007
SM t32:2	2.059	0.918	0.031

GLOMERULAR DOWNREGULATED SPECIES

Lipid specie	AKI+Fer1/AKI ratio	Levene test p-value	t-Test p-value
HexCer d28:1	0.29	0.02	0.03
HexCer d30:1	0.52	0.01	0.03
HexCer d36:2	0.39	0.00	0.04
HexCer t35:1	0.39	0.08	0.04
PC 38:8	0.06	0.01	0.02
PC 40:7	0.25	0.07	0.00
PC 40:8	0.05	0.00	0.05
PE 36:3	0.24	0.94	0.01
PE 40:3	0.54	0.05	0.02
PE 40:8	0.06	0.01	0.02
PG 36:0	0.35	0.21	0.04
PG 40:7	0.12	0.06	0.01
PI 36:1	0.15	0.28	0.03
PI 37:6	0.04	0.00	0.01
SM d34:1	0.87	0.53	0.03
SM d42:0	0.05	0.00	0.04
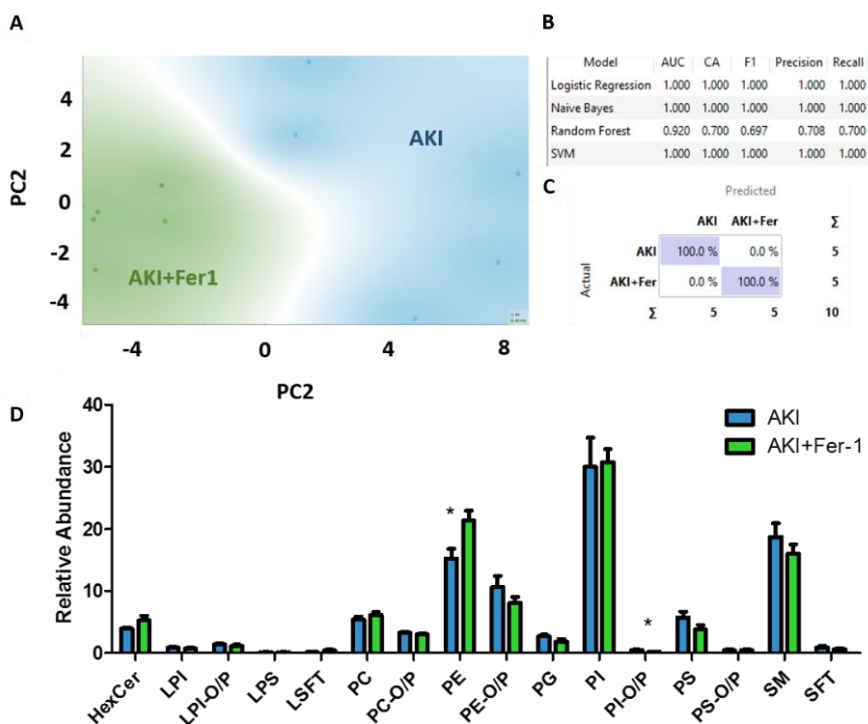
Figure 5.15. (A) *PCA separating AKI and AKI+Fer1 glomeruli lipid fingerprint (n=5 for both control and AKI).* ***(B)*** *Summary of the models' performance for the two-class classification.* ***(C)*** *Confusion matrix showing classification results by Logistic Regression.* ***(D)*** *Summation of intensities of the lipid species corresponding to major glycerophospholipid and sphingolipid families detected in the renal glomeruli for control and AKI samples. * = p < 0.05, in T-test.*

In the same vein, medullary areas from AKI and AKI+Fer-1samples were compared. The 7 significant lipid species between the two groups displayed in **Table 5.8,** enables a good separation in the PCA scatter plot in Figure 5.16A and an overall excellent agreement of the classifier models (Figure 5.16B,C). However, the low number of modified lipid species suggest that Fer-1 treatment does not drastically modified medullary lipid metabolism in AKI. This finding is confirmed by the comparison of the intensity of lipid families, which highlights the absence of significant modifications in their relative abundance (**Figure 5.16D**).

Table 5.8. *AKI+Fer-1/AKI ratio of the significantly diverse lipid species between control and AKI medulla. p-value of Levene-test (p-value < 0.05 = non-equivalent variance (red shadowed)) and T-test are also shown.*

MEDULLARY UPREGULATED SPECIES

Lipid specie	AKI+Fer1/AKI ratio	Levene test p-value	t-Test p-value
PI 38:4	1.115	0.738	0.032
PI 34:0	5.643	0.649	0.000

MEDULLARY DOWNREGULATED SPECIES

Lipid specie	AKI+Fer1/AKI ratio	Levene test p-value	t-Test p-value
HexCer d38:1	0.356	0.128	0.044
PC 40:8	0.055	0.001	0.024
PE 40:8	0.025	0.000	0.016
PI 37:6	0.307	0.008	0.000
PI 38:5	0.505	0.259	0.023
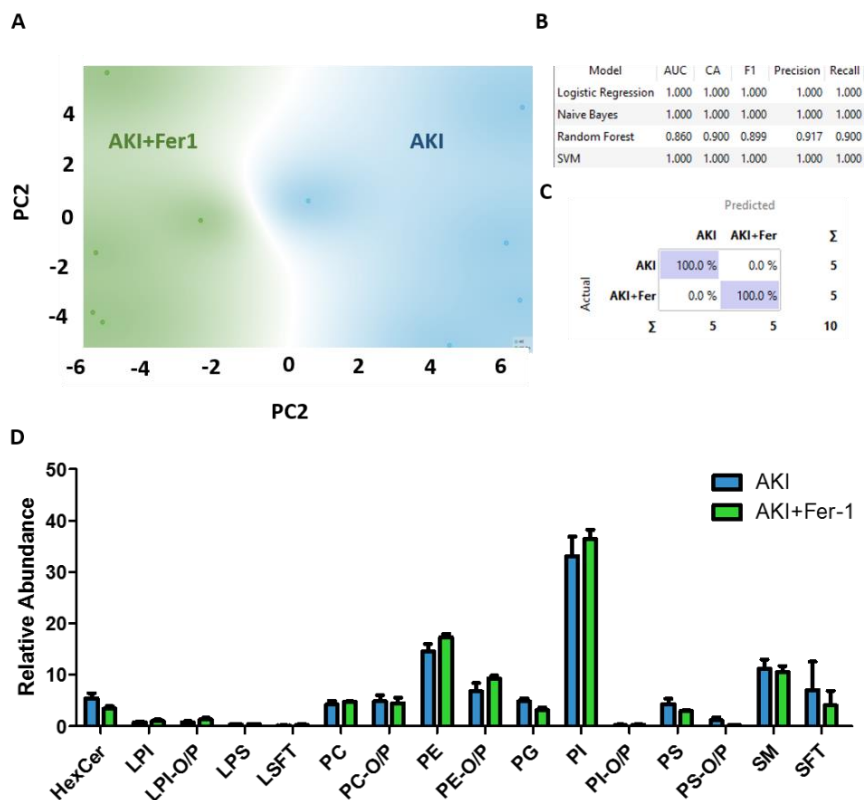
Figure 5.16. *(A)* *PCA separating AKI and AKI+Fer-1 medulla lipid fingerprint (n=5 for both groups).* *(B)* *Summary of the models' performance for the two-class classification.* *(C)* *Confusion matrix showing classification results by Logistic Regression.* *(D)* *Summation of intensities of the lipid species corresponding to major glycerophospholipid and sphingolipid families detected in the renal medulla for AKI and AKI+Fer-1 samples. * = p < 0.05, **= p-value < 0.01, *** = p-value< 0.001 in T-test.*

Differentially expressed lipid metabolism enzymes in AKI

Subsequently, we assessed the potential drivers of lipid dysregulation in AKI. A renal RNA-seq analysis disclosed altered expression of various enzymes implicated in PE and PI metabolism. The cytidine diphosphate diacylglycerol (CDP-DAG) pathway connects PE and PI synthesis, driving DAG away from PE synthesis and towards PI synthesis (**Figure 5.17A**).

The expression of several genes encoding enzymes in the CDP-DAG pathway was upregulated in AKI at 48 hours, as determined by RNA-seq transcriptomics (**Figure 5.17B**). Moreover, the increase of *Cdipt* (CDP-diacylglycerol-inositol 3-phosphatidyltransferase),

Pgs1 (phosphatidylglycerophosphate synthase 1) and *Tamm41* (TAM41 mitochondrial translocator assembly and maintenance homolog) were confirmed by rt-PCR **(Figure 5.17C).** The upregulation of this pathway may drive the increase in kidney PI levels observed in AKI. However, consistent with the absence of impact on renal PI levels, Fer-1 did not prevent the upregulation of *Cdipt* (**Figure 5.17D**).

Additionally, the CDP-ethanolamine pathway (Kennedy pathway) is key for PE biosynthesis while PE N-methyl transferase (*Pemt*) catalyzes PE methylation to PC[21] (**Figure 5.18A**). RNA-seq also showed reduced expression of genes encoding enzymes of Kennedy pathway in AKI at 48 hours, while the expression of *Pemt* was increased **(Figure 5.18B**). The expected global impact of these changes is a decrease in PE levels. The decreased expression of *Etnk1* (Ethanolamine kinase 1) and *Pcyt2* (phosphate cytidylyltransferase 2, ethanolamine) was validated by rt-PCR **(Figure 5.18C)..** Moreover, the overexpression of *PEMT* was validated at the mRNA level by rt-PCR and at the protein level by Western blot (**Figure 5.18D, E**). These results suggest that the decrease of PE species in AKI may be due to dysregulation of enzymes involved in PE synthesis by the Kennedy pathway and in PE methylation to PC.
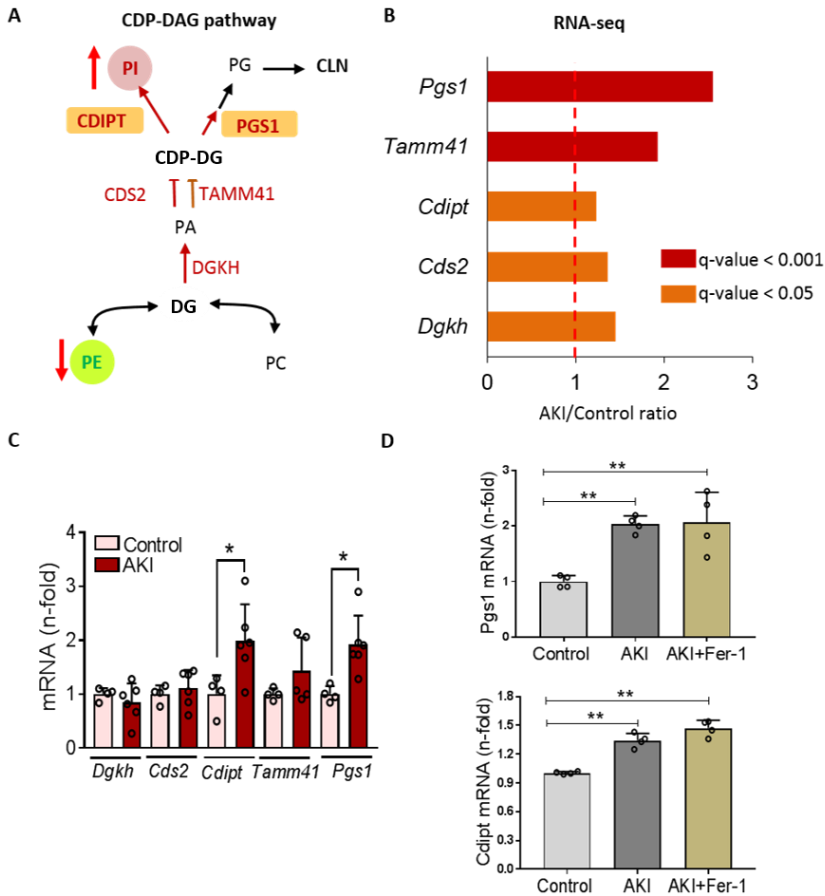
Figure 5.17. *Expression of genes encoding enzymes of the cytidine diphosphate diacylglycerol (CDP-DG) pathway during AKI. **(A)** CDP-DG pathway. PE and PI as well as the direction of observed changes in MALDI-IMS during AKI are shown. **(B)** RNA-seq analysis of genes encoding CDP-DG pathway enzymes in samples from experimental AKI or control kidneys at 48 hours. AKI/Control ratio (FPKMs). **(C)** Kidney mRNA expression of genes encoding CDP-DG pathway enzymes assessed by rt-PCR at 48 hours after AKI induction. **(D)** Fer-1 treatment did not prevent Pgs1 and Cdipt overexpression after AKI induction, as assessed by rt-PCR. **(C, D)** Mean ± S.E.M of 4-7 animals per group. *p<0.05, **p<0.01 in T-test between the two indicated groups.*
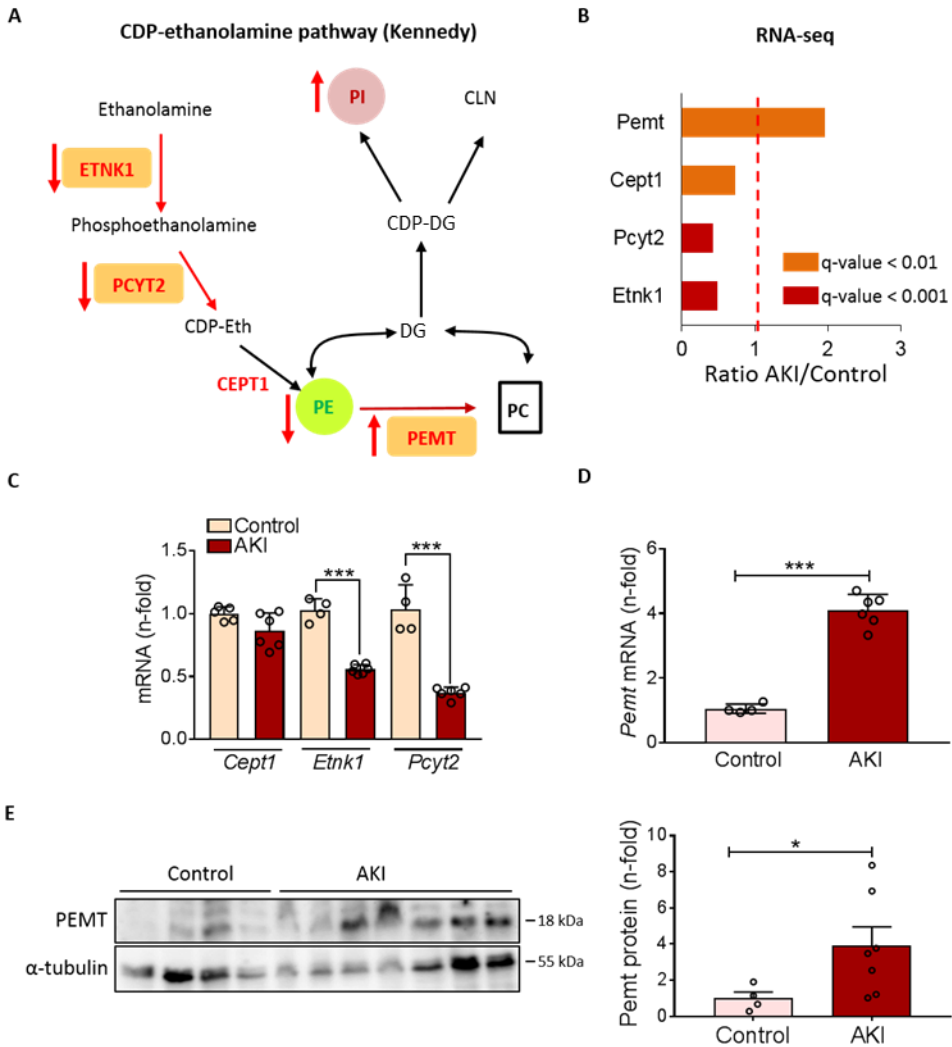
Figure 5.18. Expression of genes encoding PE metabolism enzymes is dysregulated during AKI. (A) Pathways of PE metabolism. PE and PI as well as the direction of observed changes in MALDI-IMS during AKI are shown. (B) RNA-seq analysis of genes encoding PE metabolism enzymes in samples from experimental AKI or control kidneys at 48 hours. AKI/Control ratio (FPKMs). (C) Kidney mRNA expression of Cept1, Etnk1 and Pcyt2 assessed by rt-PCR at 48 hours after AKI induction. (D, E) Kidney PEMT mRNA (D) and protein levels (E) assessed by rt-PCR and Western blot respectively at 48 hours after AKI induction. (C, D, E) Mean ± S.E.M of 4-7 animals per group. *p<0.05, ***p<0.001 in T-test between the two indicated groups

5.5   Discussion

The main finding of this study is the definition of a specific lipid fingerprint for the different kidney regions, cortex, glomeruli and medulla, by MALDI-IMS analysis. A total of 140 lipid belonging to 16 lipid subclasses were detected. In addition, we observed that the changes in the lipid pattern in PE and PI species during experimental AKI is associated with changes in the expression of genes encoding enzyme that may explain the observed related changes. Finally, Fer-1 reverts some changes observed in untreated AKI kidneys.

MALDI-IMS is a novel technique that enables mapping individual molecules in tissue sections with high resolution that has been applied in different tissues and mostly in brain[22]. Various studies have used this technique to describe lipid and protein profiles in healthy kidney tissue,[23-27] but in lesser detail than in the present study. It has been demonstrated that experimental kidney ischemia/reperfusion injury, IgA nephropathy, PKD and diabetic nephropathy all introduce specific changes in lipid profiles[28-31]. However, these were exclusive descriptive studies and potential metabolic pathway changes and response to therapy were not explored. Here we report that MALDI-IMS provides specific lipid pattern for each renal region in both, healthy and injured kidneys by a folic acid overdose, and identify AKI-associated changes in specific regions as well as its relationship to the severity of AKI and to dysregulation of lipid metabolism enzymes. Specifically, we observed that the amount of PE is decreased in AKI compared with control kidneys, and in medullary PE was significantly and negatively correlated with the severity of kidney dysfunction. Additionally, we also observed an increase of total PI and cortex and glomerular PI showed a significant positive correlation with the severity of kidney dysfunction. Therefore, our results suggest that the different kidney regions could contribute in different grade to the overall modifications of the kidney lipidome observed during AKI, however we cannot confirm if these changes are a cause or a consequence of kidney injury.

Lipids compose about 3% of kidney weight, and more of 50% are phospholipids, the main constituent of plasma membranes[32]. Lipids also have key signaling roles and lipid β-oxidation is the major source of energy in tubular cells. Therefore, changes in lipid homeostasis could disturb both membrane stability and metabolism in renal cells. Our results show a change in 140 lipid species. Among the most significantly upregulated lipids in AKI, we found two glycerophosphoglycerol species PG 38:6 and PG 40:8, which are listed by the human metabolome database[33] as having a role in cardiolipin biosynthesis and lipid peroxidation.

Lipid peroxidation is a key event in ferroptosis and AKI[34] and these lipids may be a fuel for this process. The weak reduction of these species by Fer-1, maybe related to the fact that Fer-1 only scavenges oxidized lipids[35]. Among the most significantly downregulated species, 25 % (3/12) were HexCer compounds and 41.6 % (5/12) were PE.

Fer-1 increased the levels of one HexCer and of over 4 PE species, suggesting that changes in these species could be a consequence of ferroptosis. However, Fer-1 did not normalize the full pattern of lipid composition changes observed in AKI, pointing out specific lipids that may be key to its protective role.

To understand the metabolic pathways underlying the changes in lipid composition, we focused on the most upregulated and downregulated families during AKI, i.e., PI and PE, respectively. Gene expression changes potentially underlying the upregulation of PI levels were observed, including changes in the expression of gene encoding CDIPT. Moreover, kidney protection by Fer-1 was not associated to prevention of PI changes or of the expression of genes in the PI biosynthesis pathway. Regarding PE levels, the mRNA expression of genes encoding enzymes of the CDP-ethanolamine pathway, a predominant pathway for PE biosynthesis[21], were reduced in AKI. This pathway is localized in the endoplasmic reticulum (ER). Thus, downregulation of the pathway might reflect ER stress, Indeed, ER stress plays a role in tubular cell death induced by various toxins, although most studies predate the current concept of ferroptosis [36-38]. By contrast, the expression of PEMT that catalyzes the methylation of PE to PC was increased in experimental AKI. PEMT contributed to kidney injury in diabetic nephropathy where PEMT was associated with ER stress, apoptosis and inflammation and PEMT deficiency was protective, although the impact on lipid composition was not explored[39]. In this regard, PEMT deficiency may result in higher PE levels. However, how the decrease in PE may contribute to the pathogenesis of kidney disease is yet unclear.

5.6   Conclusions

To summarize, we have characterized the lipid composition of different regions of the healthy and AKI kidney using MALDI-IMS and identified AKI-associated changes in lipid composition in the different kidney regions. Some of these changes may be related to alteration in the gene expression of enzymes of the lipid metabolic pathways. As an example, changes in PEMT expression are consistent with some of the changes in lipid composition observed in AKI samples. However, nephroprotection by ferroptosis inhibition did not reverse the observed changes in gene expression and did not normalize the full lipid composition changes observed in AKI, but prevented certain decrease in PE species, thus identifying specific lipids with a potential pathogenic role in AKI.

1. Bellomo, R., Kellum, J. A. & Ronco, C. Acute kidney injury. *The Lancet* **380**, 756-766 (2012).

2. Rodriguez, E. *et al*. Impact of Recurrent Acute Kidney Injury on Patient Outcomes. *Kidney Blood Press. Res.* **43**, 34-44 (2018).

3. Linkermann, A., Stockwell, B. R., Krautwald, S. & Anders, H. Regulated cell death and inflammation: an auto-amplification loop causes organ failure. *Nature Reviews Immunology* **14**, 759-767 (2014).

4. Linkermann, A. *et al*. Two independent pathways of regulated necrosis mediate ischemia-reperfusion injury. *Proc. Natl. Acad. Sci. U. S. A.* **110**, 12024-12029 (2013).

5. Martin-Sanchez, D. *et al*. Ferroptosis, but Not Necroptosis, Is Important in Nephrotoxic Folic Acid-Induced AKI. *J. Am. Soc. Nephrol.* **28**, 218-229 (2017).

6. Guerrero-Hue, M. *et al*. Curcumin reduces renal damage associated with rhabdomyolysis by decreasing ferroptosis-mediated cell death. *The FASEB Journal* **33**, 8961-8975 (2019).

7. Martin-Sanchez, D. *et al*. TWEAK and RIPK1 mediate a second wave of cell death during AKI. *Proc. Natl. Acad. Sci. U. S. A.* **115**, 4182-4187 (2018).

8. Stockwell, B. R. *et al*. Ferroptosis: a regulated cell death nexus linking metabolism, redox biology, and disease. *Cell* **171**, 273-285 (2017).

9. Wenzel, S. E. *et al*. PEBP1 wardens ferroptosis by enabling lipoxygenase generation of lipid death signals. *Cell* **171**, 628-641. e26 (2017).

10. Zilka, O. *et al*. On the mechanism of cytoprotection by ferrostatin-1 and liproxstatin-1 and the role of lipid peroxidation in ferroptotic cell death. *ACS central science* **3**, 232-243 (2017).

11. Linkermann, A. *et al*. Synchronized renal tubular cell death involves ferroptosis. *Proc. Natl. Acad. Sci. U. S. A.* **111**, 16836-16841 (2014).

12. Aichler, M. & Walch, A. MALDI Imaging mass spectrometry: current frontiers and perspectives in pathology research and practice. *Laboratory investigation* **95**, 422-431 (2015).

13. Rao, S. *et al*. Early lipid changes in acute kidney injury using SWATH lipidomics coupled with MALDI tissue imaging. *American Journal of Physiology-Renal Physiology* **310**, F1136-F1147 (2016).

14. Van Smaalen, T. *et al*. Rapid identification of ischemic injury in renal tissue by mass-spectrometry imaging. *Anal. Chem.* **91**, 3575-3581 (2019).

15. Bestard-Escalas, J. *et al*. Lipid fingerprint image accurately conveys human colon cell pathophysiologic state: A solid candidate as biomarker. *Biochimica et Biophysica Acta (BBA)-Molecular and Cell Biology of Lipids* **1861**, 1942-1950 (2016).

16. Sanz, A. B., Sanchez-Niño, M. D., Martin-Cleary, C., Ortiz, A. & Ramos, A. M. Progress in the development of animal models of acute kidney injury and its impact on drug discovery. *Expert opinion on drug discovery* **8**, 879-895 (2013).

17. Metz-Kurschel, U. *et al*. Folate nephropathy occurring during cytotoxic chemotherapy with high-dose folinic acid and 5-fluorouracil. *Ren. Fail.* **12**, 93-97 (1990).

18. Fernández, R., Garate, J., Martín-Saiz, L., Galetich, I. & Fernández, J. A. Matrix Sublimation Device for MALDI mass spectrometry imaging. *Anal. Chem.* **91**, 803-807 (2018).

19. Fernández, R., Garate, J., Martín-Saiz, L., Galetich, I. & Fernández, J. A. Matrix Sublimation Device for MALDI mass spectrometry imaging. *Anal. Chem.* **91**, 803-807 (2018).

20. Demšar, J. *et al*. Orange: data mining toolbox in Python. *the Journal of machine Learning research* **14**, 2349-2353 (2013).

21. Calzada, E., Onguka, O. & Claypool, S. M. Phosphatidylethanolamine metabolism in health and disease. *International review of cell and molecular biology* **321**, 29-88 (2016).

22. Dai, Z., Sun, Y., Zhao, X. & Pu, X. Novel imaging and related techniques for studies of diseases of the central nervous system: a review. *Cell Tissue Res.* **380**, 415-424 (2020).

23. Fujino, Y. *et al*. Comparative proteome analysis of wild-type and klotho-knockout mouse kidneys using a combination of MALDI-IMS and LC-MS/MS. *PROTEOMICS–Clinical Applications* **11**, 1600095 (2017).

24. Angel, P. M. & Caprioli, R. M. Matrix-assisted laser desorption ionization imaging mass spectrometry: in situ molecular mapping. *Biochemistry* **52**, 3818-3828 (2013).

25. Marsching, C., Eckhardt, M., Gröne, H., Sandhoff, R. & Hopf, C. Imaging of complex sulfatides SM3 and SB1a in mouse kidney using MALDI-TOF/TOF mass spectrometry. *Analytical and bioanalytical chemistry* **401**, 53-64 (2011).

26. Prejbisz, A. *et al*. Smaller caliber renal arteries are a novel feature of uromodulin-associated kidney disease. *Kidney Int.* **88**, 160-166 (2015).

27. Lalowski, M. *et al*. Imaging mass spectrometry: a new tool for kidney disease investigations. *Nephrology Dialysis Transplantation* **28**, 1648-1656 (2013).

28. Rao, S. *et al*. Early lipid changes in acute kidney injury using SWATH lipidomics coupled with MALDI tissue imaging. *American Journal of Physiology-Renal Physiology* **310**, F1136-F1147 (2016).

29. Kaneko, Y. *et al*. Imaging mass spectrometry analysis reveals an altered lipid distribution pattern in the tubular areas of hyper-IgA murine kidneys. *Exp. Mol. Pathol.* **91**, 614-621 (2011).

30. Grove, K. J. *et al*. Diabetic nephropathy induces alterations in the glomerular and tubule lipid profiles. *J. Lipid Res.* **55**, 1375-1385 (2014).

31. Moreno-Gordaliza, E. *et al*. Lipid imaging for visualizing cilastatin amelioration of cisplatin-induced nephrotoxicity. *J. Lipid Res.* **59**, 1561-1574 (2018).

32. Druilhet, R., Overturf, M. & Kirkendall, W. Cortical and medullary lipids of normal and nephrosclerotic human kidney. . **Int J Biochem 9(10)**, 729 (1978).

33. Wishart, D. S. *et al*. HMDB 4.0: the human metabolome database for 2018. *Nucleic Acids Res.* **46**, D608-D617 (2018).

34. Yang, W. S. & Stockwell, B. R. Ferroptosis: death by lipid peroxidation. *Trends Cell Biol.* **26**, 165-176 (2016).

35. Zilka, O. *et al*. On the mechanism of cytoprotection by ferrostatin-1 and liproxstatin-1 and the role of lipid peroxidation in ferroptotic cell death. *ACS central science* **3**, 232-243 (2017).

36. Lorz, C. *et al*. Paracetamol-induced renal tubular injury: a role for ER stress. *J. Am. Soc. Nephrol.* **15**, 380-389 (2004).

37. Justo, P. *et al*. Cytokine cooperation in renal tubular cell injury: the role of TWEAK. *Kidney Int.* **70**, 1750-1758 (2006).

38. Justo, P., Lorz, C., Sanz, A., Egido, J. & Ortiz, A. Intracellular mechanisms of cyclosporin A-induced tubular cell apoptosis. *J. Am. Soc. Nephrol.* **14**, 3072-3080 (2003).

39. Watanabe, M. *et al*. Pemt deficiency ameliorates endoplasmic reticulum stress in diabetic nephropathy. *PloS one* **9**, e92647 (2014).

Chapter 6

High resolution human kidney molecular histology by IMS of lipids

For many years, traditional histology has been the gold standard for diagnoses of many diseases. However, alternative and powerful techniques have appeared in recent years that complement the information extracted from a tissue section. One of the most promising ones is imaging mass spectrometry applied to lipidomics. Here we demonstrate the capabilities of this technique to highlight the architectural features of human kidney. These results set the foundation for further studies on the metabolic bases of the diseases affecting the human kidney.

The data presented here have been partially published in:

1. **Martín-Saiz, Lucía**, Lorena Mosteiro, Jon D. Solano-Iturri, Yuri Rueda, Javier Martín-Allende, Igone Imaz, Iván Olano, Begoña Ochoa, Olatz Fresnedo,José A. Fernández & Gorka Larrinaga High-Resolution Human Kidney Molecular Histology by Imaging Mass Spectrometry of Lipids. *Analytical Chemistry*, 2021.
2. **Martín-Saiz, Lucía**, José A. Fernández, Gorka Larrinaga & Olatz Fresnedo High resolution imaging mass spectrometry unveils differences into tubules from the kidney medulla. *Manuscript for publication in preparation.*

6.1 Introduction

Traditional histology has been over the years the gold standard for diagnoses of many diseases. The importance of this technique is reflected in the large number of chemical and immunohistochemical (IHC) procedures developed, which enable highlighting multiple aspects of the architecture of a tissue[1, 2]. However, in the last years, new image techniques have appeared that add a different point of view and try to avoid the use of labels for visualization of the tissues, precluding tissue alteration. Perhaps, the most impressive advances in histological images have come from MALDI-IMS[3].

Probably, the main complication of the technique lies in hardware development and data interpretation. To fully develop the IMS it has been necessary an important effort to design new mass spectrometers, able to record up to 50 pixels/s, yielding enough information to achieve a precise identification of multiple species extracted directly from the tissue[4, 5]. Development of new and imaginative protocols for sample preparation has also been necessary[6, 7].

Regarding data interpretation, there are still open questions: normalization, segmentation of the images and identification of the species are still not fully resolved questions[8, 9]. Even with this pending tasks, IMS is showing a tremendous potential to characterize the proteomics and lipidomics of tissue sections. An increasing number of studies show for the first time the tissue architecture through the eyes of (mainly) lipids and proteins, unraveling features not previously described. For example, the exquisite regulation of lipids during colonocytes maturation[10] or the differential lipid expression of epidermis, dermis and melanocytes in nevi[11]. All these studies are the foundation and the next step in the understanding of the metabolic basis of the diseases.

The pathological diagnosis of kidney function and disease is currently based on the examination of tissue biopsies by optic and electron microscopy, and immunofluorescence (IF)[2]. However, the incorporation of innovative techniques based on transcriptomic characterization of isolated cells or microdisected tubule segments has given rise to new approaches to classify renal structures and their specific diseases[1, 12]. In this context, MALDI-IMS emerges as a technique that enables the exploration of kidney molecular features and that has a great potential as a complement for imaging techniques in clinical routine[13].

Several studies have already appeared in which IMS has been used to either describe the lipidome of healthy rat [14, 15] and mouse[13, 16-18] kidney, or in the context of a disease[19]. However, none of them was carried out with enough spatial resolution as to establish how large the differences in lipid expression are between the different sections of a human nephron. This is an important issue, as each specific segment of

the nephron is susceptible to different mechanisms of damage that lead to both non-neoplastic[20] and neoplastic diseases[21, 22]. Thus, mapping the lipidome of those cells and understanding their differences is an important step forward towards shedding light on the metabolic origins of the diseases affecting the kidney.

6.2   Objectives

The major purpose of this chapter is to demonstrate that a large number of regions of the nephron may be identified using their IMS lipid signature. We will also show that the lipid profile is reliable enough to enable tissue classification using standard statistical models. This also implies that the lipid signature of each section of the nephron is preserved among individuals.

6.3   Experimental section

Sample collection

All the experiments carried out in this study comply with the current Spanish and European Union legal regulations. Samples and data from patients included in this study were provided by the Basque Biobank for Research-OEHUN (www.biobancovasco.org).

Kidney samples were obtained prospectively from a series of nephrectomies from 32 renal cancer patients (18 males and 14 females, age: 65 ± 8 years) in the University Hospitals of Cruces (Barakaldo, Spain) and Basurto (Bilbao, Spain). All patients were informed about the potential use for research of their surgically resected tissues, and manifested their consent by signing a specific document approved by the Ethical and Scientific Committees of the Basque Country Public Health System (PI+CES-BIOEF 2018-04).

Uninvolved part of the kidney was stored fresh frozen (-80ºC) and contiguous sections of 16 µm and 3 µm were performed for MALDI-IMS and preliminary histological analyses, respectively. This preliminary histological analysis was required to select the most interesting areas of the samples for the subsequent MALDI-IMS exploration, as the whole area of the sections could not be scanned due the speed of the mass spectrometer.

Once the 16 µm sections were explored by MALDI-IMS, they were stained with H&E, so the pathologists could assigned the histological areas and structures in order to compare them with the clusters obtained by MALDI-IMS. It is important to highlight that H&E was performed in the same sections used for MALDI-IMS, and not in paraffin sections, because the complexity of the tissue makes not possible to correlate the structures in two sequential sections and MALDI-IMS has to be carried out in fresh

tissue. This procedure limited the degree of the detail the pathologists could extract from the histological analysis of kidney structures. Therefore, it was not possible to establish a univocal correspondence with the IMS images for all the structures. An improved identification of the histologic areas could be accomplished by comparison with IHC images. However, this also involves several methodologic problems: the samples for MALDI-IMS are not fixed because the use of fixing chemicals perturbs the original distribution of lipids. Also, to achieve a perfect match between IMS and immunocytochemistry images, both experiments should be carried out in the same section, multiplying by more than one order of magnitude the number of experiments.

Imaging and data recording

Histological sections from 32 different patients were prepared and analyzed by MALDI-IMS as described in **Chapter 3**. Briefly, DAN was used as matrix for negative-ion detection and deposited with the aid of our in-house designed sublimator, which enables perfect control over all the parameters involved in the sublimation process[23]. Sections of kidney biopsies were scanned in negative-ion mode, using the orbitrap analyzer of a MALDI-LTQ-Orbitrap XL (Thermo Fisher, San Jose, CA, USA). The MALDI source used in this study was an in-house modified version of the original one provided by the manufacturer (see last section of **Chapter 4**). After the modification, the laser spot size at the sample was < 10 μm. Laser pulse energy was kept below 10 μJ, as higher fluences did not result in a substantial increase in signal intensity and may even produce tissue damage, avoiding the use of the sections for optical microscopy after MALDI-IMS recording.

Data were acquired with a mass resolution of 60000 at m/z = 400. Two microscans of 10 laser shots were recorded for each pixel and the raster size used was 10 μm. Scan region was chosen as a compromise between covering a representative portion of lipid classes while maintaining high enough sensitivity as to detect low-abundance species. Therefore, it was set to m/z = 550-1000. Spectra were aligned and analyzed using in-house developed software, built in Matlab (MathWorks, Natick, USA). Lipid assignment was based on the comparison between the experimental m/z and the species in the software's database (< 33,000 lipid species plus adducts) and in the lipid maps database (www.lipidmaps.org). Mass accuracy was 5 ppm For m/z channels with several candidates for the assignment, "on-tissue" MS/MS and MS[3] was carried out to reach a univocal assignment. Moreover, fatty acid chains were obtained from an uHPLC/ESI-study of lipid homogenates from human renal samples (see **Chapter 8**).

Detailed description of data processing may also be found in **Chapter 3**, but briefly, the spectra were normalized using a TIC algorithm, and aligned using the Xiong method during the parsing stage[24]. All peaks with intensity values lower than 0.5% of the intensity of the strongest peak were filtered to reduce the number of _m/z_ values and

speed up the analysis. Unwanted peaks due to fragmentation, matrix and other species that only introduce noise in the analysis were removed following the basis of our previous work[25]. Only reproducible lipid species were used in multiple comparative studies to minimize the inter-patient variability. For that, the species whose standard deviation was larger than 80% of the peak intensity and the ones that were detected in less than 80% of a sample group were also filtered.

Data analysis

Data from each section were analyzed using the HD-RCA segmentation to isolate and identify the lipid signatures of each histological area in the section. A comparison between the performance of HD-RCA and k-means may be found in **Figure 6.1**. As more defined clusters were obtained from HD-RCA rather than from k-means, HD-RCA was the segmentation algorithm employed in further analysis.
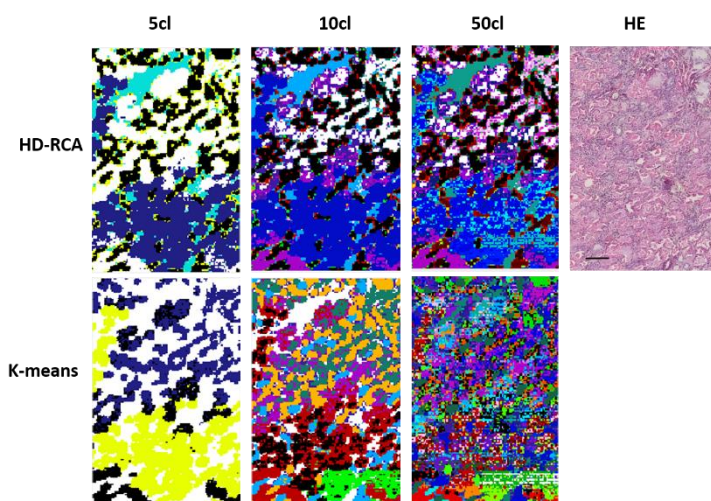
Figure 6.1. Comparison between HD-RCA and k-means analysis in a corticomedullary transition sample. Scale bar=150μm.

To establish the number of segments, an additional heuristic approach was used; the initial number of clusters was set in 5 for cortical and medullary samples and 8 for cortical-medullary transition sections. Then, the segments suggested by the algorithm were verified by examining the correlation between them. The clusters whose correlation was higher than 95% were grouped together. In the end, the total number of clusters found in all the samples was 131, divided in eight histologic areas. The signatures from the final histological areas were later used in subsequent multi-experiments analysis.

To estimate the covered area by each IMS histological structure, the percentage of pixels per structure in base of the total number of pixels of the sample was calculated.

To statistically evaluate the differences in the lipid fingerprints among the eight identified histological areas, Levene-test, ANOVA univariate statistical analysis and Tukey /Games Howell post hoc were computed using SPSS Statistics 17.0 (IBM, Armonk, NY, USA)[30]. Levene-test determines the homogeneity (H$_0$ = groups have equivalent variance) to choose the post hoc method: Tukey if Levene p ≥ 0.05 and Games-Howell if Levene p ≤ 0.05. PCA analysis and separation models were carried out by Orange Biolab 2.7.8 (Ljubljana, Slovenia)[31] .

Immunofluorescence (IF) microscopy

Sections analyzed by MALDI-IMS were fixed with 4 % paraformaldehyde in PBS (Sigma Aldrich, MO,USA) for 10 min at room temperature and washed in cold methanol/acetone (1:1) (minimum purity 99.5%, Scharlab, BA, Spain) for 5 min in order to remove the MALDI matrix. Corticomedullary sections were stained with Lotus tretragonolobus lectin (LTL)-fluorescein and dolichos biflorus agglutinin (DBA)-rhodamine (both at 1:33 dilution) (Vector Laboratories,CA,USA) essentially as described[14]. In addition to DBA, medullary tissue sections were immunostained to detect tamm horsfall glycoprotein (THP). Samples were incubated at room temperature for 2 h with mouse anti-human THP (B-2) primary antibody (1:200) (Santa Cruz Biotechnology,TX,USA) and, afterward, with Alexa Fluor 488-labeled goat anti-mouse IgG secondary antibody (1/200) (Invitrogen) for 1 h. All the sections were counterstained with 10 µg/ml Hoechst-33342 (Invitrogen,CA,USA). After mounting (ProLong Gold, Life Technologies,CA,USA), stained sections were analyzed with a Nikon-Ti-U fluorescence microscope (Nikon instruments,NY,USA) and processed with Nikon Ds-Qi2 and Nikon DS-Fi1 softwares.

6.4   Results

Identification of kidney histological structures by IMS of lipids.

Figure 6.2 shows the optical image of six H&E stained sections of cortex, corticomedullary transition and medulla of human kidney. Glomeruli, proximal and distal tubules, collecting ducts and interstitial vessels were identified by optical microscopy. The same sections were scanned in IMS experiments using a pixel size of 10 µm in negative-ion mode. The intensities of 130 lipid species were directly captured from the fresh tissue sections, obtaining a distribution map for each of the species. Example images for the distribution of the sphingomyelin (SM) d34:1, phosphatidyletanolamine (PE) 38:4 and sulfatide (SFT) d42:1 are also shown in **Figure**

6.2. These lipids are not uniformly distributed. Conversely, SM 34:1 is preferentially found in glomeruli but also in the interstitial vascular structures surrounding glomeruli and tubules from both cortex and medulla of the kidney. On the other hand, PE 38:4 shows a higher abundance in proximal tubules while SFT t42:1 relative concentration is higher in medullary tubules.
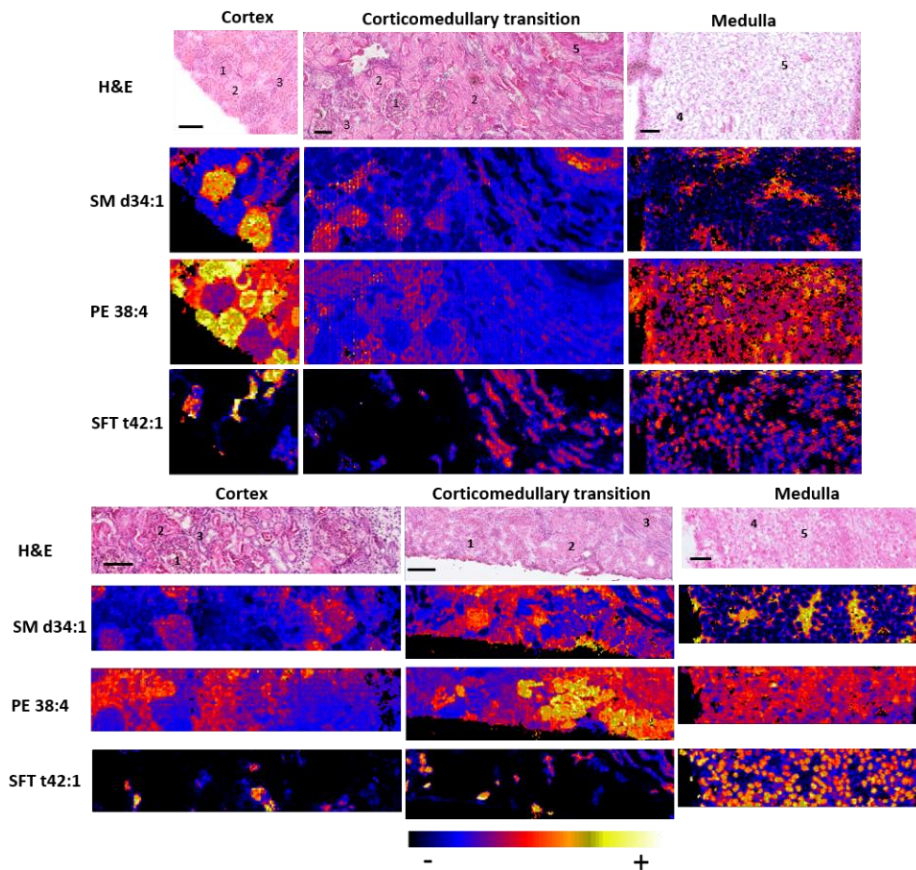
Figure 6.2. *Distribution of three representative lipids over six examples of sections of human kidney cortex, corticomedullary transition and medulla. The numbers on the H&E stained optical images represent the five different histological structures found in fresh frozen samples: 1, Glomerulli; 2, Proximal tubules; 3, Distal tubule; 4, Medullary tubules and 5, Interstitial vascular structures. Scale bar 150 µm.*

The differential lipid fingerprint at each pixel was further analyzed to define areas with similar lipid profiles. For this purpose, a segmentation algorithm was applied to group the pixels according to the similarity of their lipid fingerprints. An example of the result from this analysis may be found in **Figure 6.3A**, while the images for all the samples analyzed in this work are collected in the **Appendix Chapter 6** (**Figures A.6.1-A.6.3**).
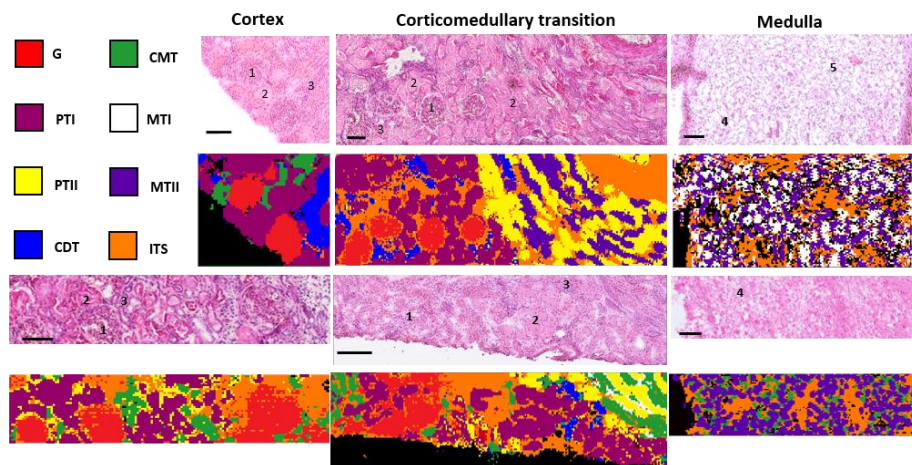
Figure 6.3. Renal tissue characterization by MALDI-IMS of lipids. Segmentation analysis of the lipid fingerprint at each pixel (HD-RCA) in each renal sample. The algorithm automatically detected eight histologic areas labelled as Glomeruli (G, red), Proximal tubules I (PT I, garnet), Proximal tubules II (PT II, yellow), Cortical distal tubules (CDT, blue), Corticomedullary tubules (CMT, green), Medullary tubules I (MT I, white), Medullary tubules II (MT II, purple) and interstitial vascular structures (ITS, orange. Images were recorded in negative-ion mode at a pixel size of 10 µm. 1, Glomeruli; 2, Proximal tubules; 3, Cortical distal tubule; 4, Medullary tubules and 5, Interstitial vascular structures. .Scale bar = 150 µm.

Up to eight different fingerprints were found in the sections measured, using the segmentation algorithm. Analysis of their localization in the sample and comparison with the observations from the pathologists enabled their assignment to glomeruli (G), proximal tubules (PTI and II), cortical distal tubules (CDT), corticomedullary tubules (CMT), medullary tubules (MTI and II) and interstitial structures (ITS). All these structures are distributed among cortical, corticomedullary transition and medullary samples. A summary of all the information from the IMS images may be found in **Figure 6.4A** in the form of a colored nephron.

We also calculated the percentage that each structure with a specific lipid fingerprint represents in the total structures detected by IMS in all the samples (**Figures 6.4B,C,D and Figure A.6.4**). Thus, lipid fingerprints corresponding to proximal tubules (PTI and PTII) represent the 56 % of total epithelial structures detected. CMTs represent 14 %, CDTs 13 %, MT IIs 13 % and MT Is 4 %. If we take into account epithelial and vascular structures, these ratios vary slightly and both G and ITS account for a similar percentage, 9 % of the total structures detected with IMS (**Figure 6.4C,D**).
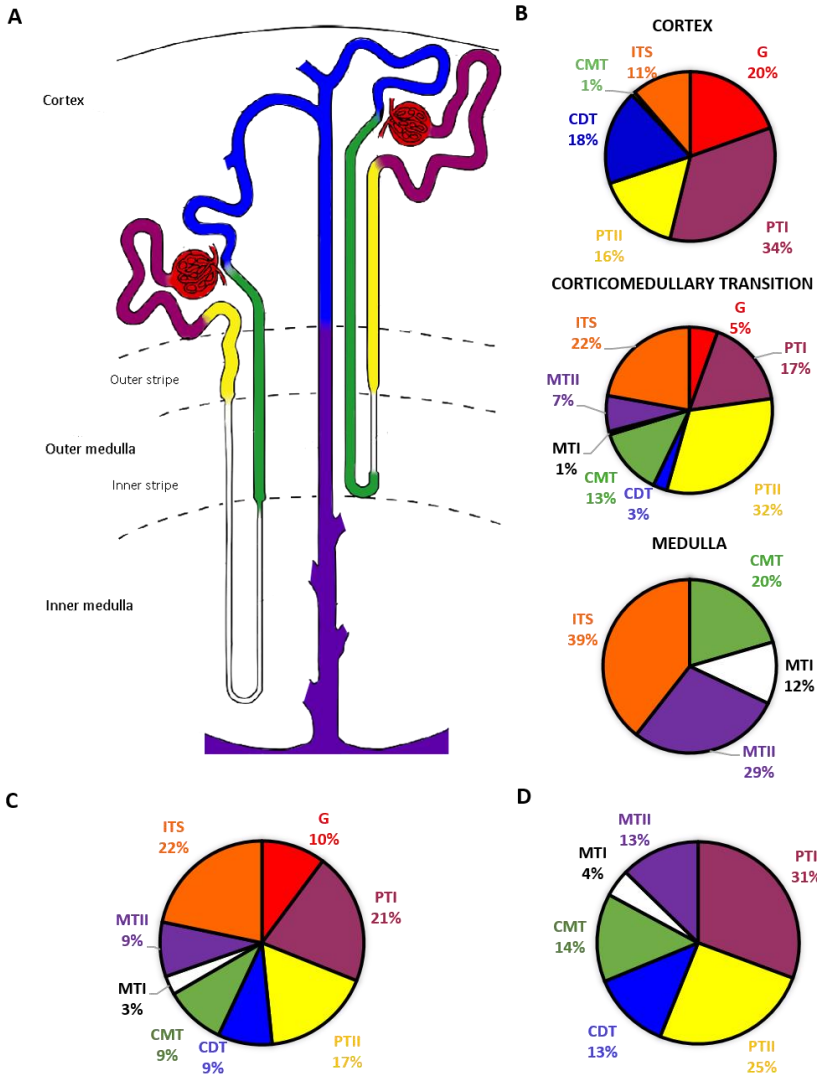
Figure 6.4. (A) *Sketch of a nephron, with the different segments colored following the code in* ***Figure 6.3****. The scheme shows a hypothetical distribution of seven renal areas with characteristic lipid profile detected by IMS. The ITS correspond with the eighth structure and therefore, it is not shown in this diagram;* ***(B)*** *Percentage of the total area covered by each histologic structure in cortex, corticomedullary and medullary samples, including the vascular structures (G and ITS).* ***(C)*** *A similar analysis, but performed over all the samples, including vascular structures* ***(D)*** *Same analysis as in* ***(D),*** *but excluding vascular structures. The analysis in* ***(B,D)*** *was performed with the final number of clusters (131) obtained from IMS images. Drawing follows the original Renal Commission of the International Union of Physiologic Sciences publication[32]. Adapted from ref 32 with permission from John Wiley and Sons.*

A closer look at the IMS results highlight the existence of additional information in the images. Certainly, the large differences between glomeruli and tubules hide other subtler differences. When each of the segments found were isolated and re-analyzed, the results shown in **Figure 6.5 and 6.6** were obtained. The images show the existence of further differences in the lipid profile inside each histologic area that may correspond to different cell subpopulations and cross-sectional heterogeneity. Such diversity is already observed in the distribution of the example lipids shown in **Figure 6.7** for one cortex and one corticomedullary transition section. A thorough analysis of the renal corpuscles shows a new structure surrounding the glomeruli which may correspond to the Bowman's capsule (**Figure 6.8**). Although this structure has similar lipid profile to glomeruli, IMS experiments are able to distinguish between both structures in several samples.
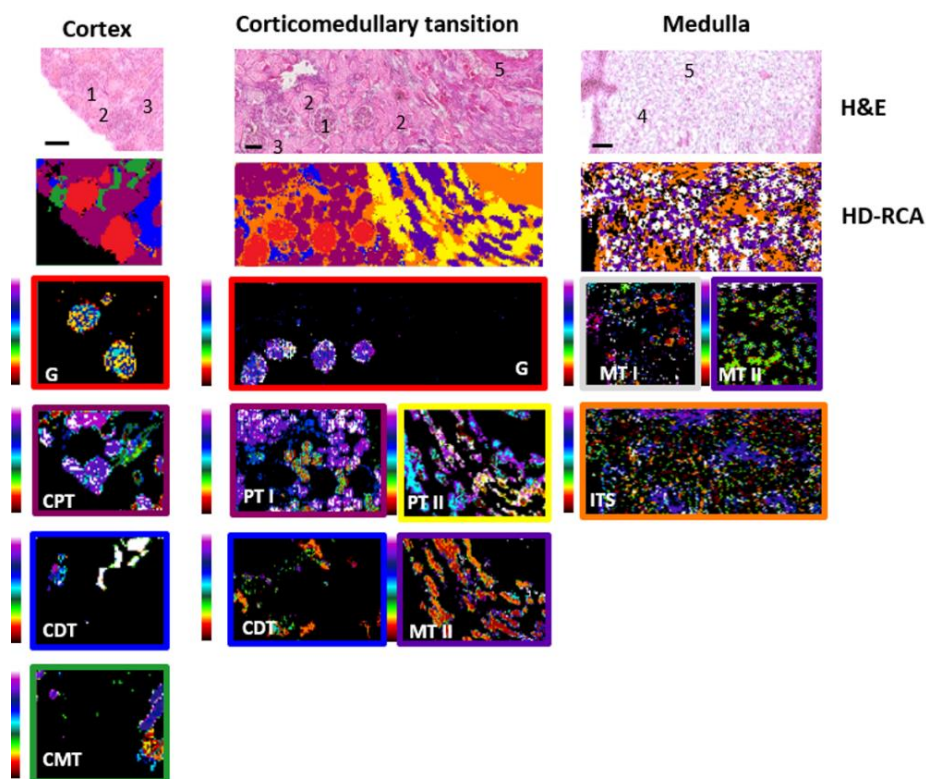
Figure 6.5. Separate renal segmentation of each IMS histological area of one cortical, corticomedullary transition and medullary sample. Number of segments was set in 10. Clustering results are represented with a cluster separation of 1-correlation between groups, meaning that the clusters with more similar lipid fingerprint receiving colors that are closer in the color bar. Each image has its own scale bar. Images were recorded in negative-ion mode at a pixel size of 10 µm. 1, Glomeruli; 2, Proximal tubules; 3,

Cortical distal tubule; 4, Medullary tubules and 5, Interstitial vascular structures Scale bar = 150 µm.
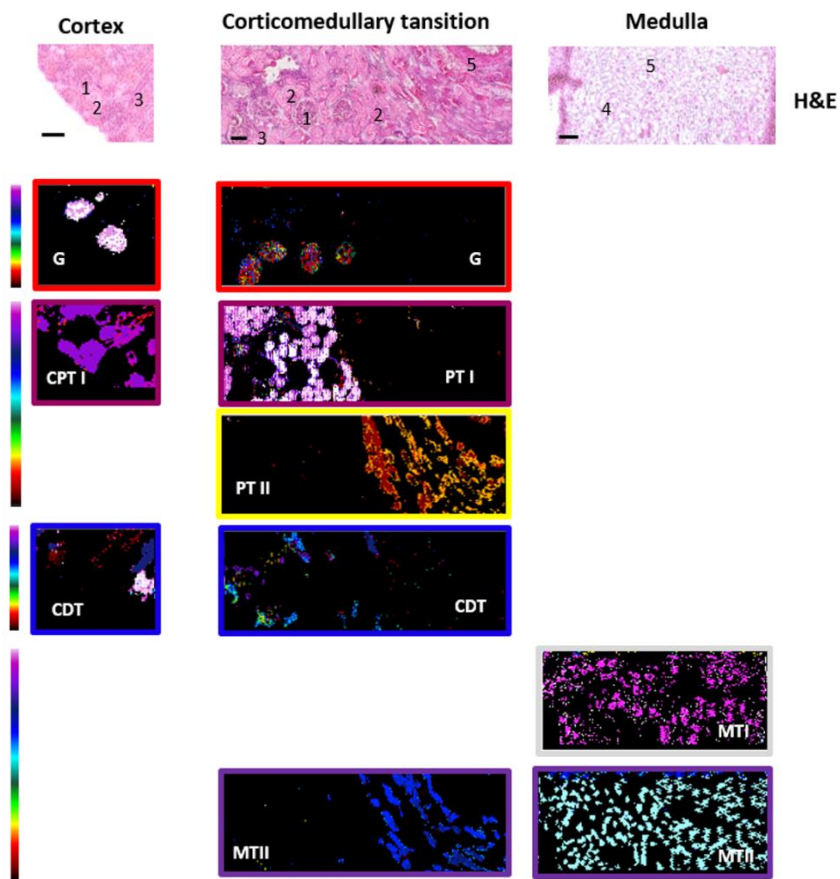
Figure 6.6. *Separate renal segmentation of each IMS histological area of one cortical, corticomedullary transition and medullary sample. Number of segments was set in 10. Clustering results are represented with a cluster separation of 1-correlation between groups, meaning that the clusters with more similar lipid fingerprint receiving colors that are closer in the color bar. Each structure has its own bar scale which makes easy to see the differences among the same structure in different samples. Images were recorded in negative-ion mode at a pixel size of 10 µm. 1, Glomeruli; 2, Proximal tubules; 3, Cortical distal tubule; 4, Medullary tubules and 5, Interstitial vascular structures Scale bar = 150 µm.*
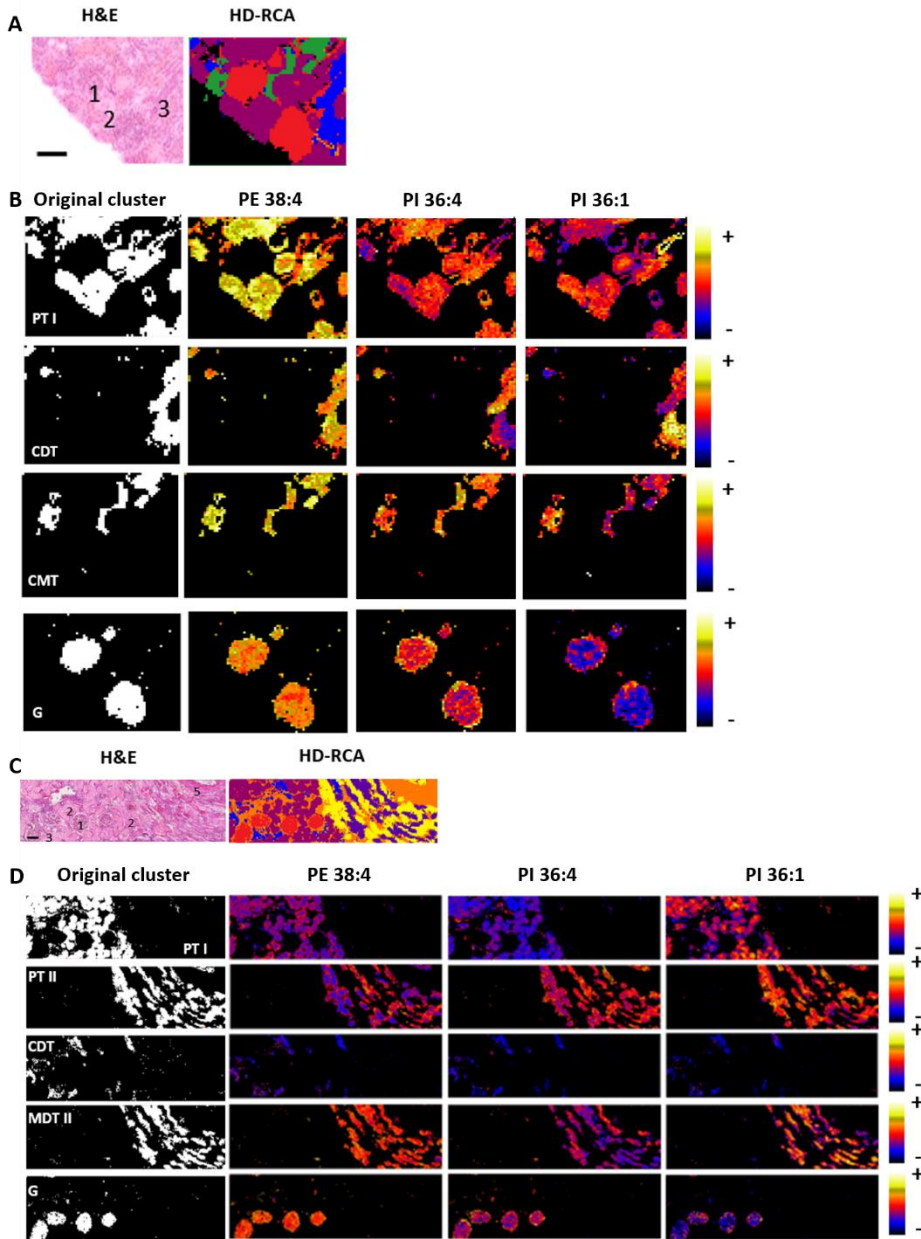
Figure 6.7. *Histological segmentation of human renal sample.* **(A,C)** *Comparison between H&E optical image of cortical and corticomedullary renal sample and segmentation analysis of the lipid fingerprint at each pixel (HD-RCA).* **(B,C)** *Separate renal segments and distribution of PE 38:4, PI 36:4 and PI 36:1 lipids over each renal cluster. Images were recorded in negative-ion mode at a pixel size of 10 μm. Scale bar = 150 μm.*
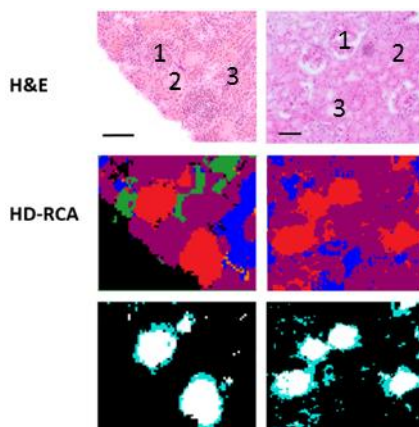
Figure 6.8. *Separate renal segmentation of renal corpuscle IMS histological area in two cortical samples. Clustering results setting the number of segments in two represent the possible separation between glomeruli (white) and Bowman's capsule (blue). Images were recorded in negative-ion mode at a pixel size of 10 μm. Scale bar = 150 μm.*

Statistical analysis of the differences observed between histological areas

To test if the differences in lipid fingerprints between the histological areas defined by IMS are statistically significant, the clusters obtained from the renal samples were randomly divided into a discovery group and a validation group. Then, a PCA was carried out on the first group, obtaining the neat separation shown in the **Figure 6.9A**. The lipid species that experienced a significant variation between tissue areas **(Table A.6.1** and **Figures A.6.5-A.6.15**) were then used to analyze the validation group, resulting in a neat separation between areas (**Figure 6.9B**). The confusion matrix and the performance of each statistical model tested may be found in **Figure 6.C, D, E, F**. The method that achieved the best results was random forest, with an AUC of 0.987, a precision of 0.885 and a recall of 0.844. All these values indicate that the lipid fingerprint of the histological areas found are representative of each area and invariant among individuals. Furthermore, additional information can be extracted from **Figure 6.9A**; the proximity among the colored areas in the PCA means a higher lipid correlation among the histological structures found in the IMS segmentation images. Consequently, the lipid expression of the cortical predominant tubules PTI, PTII and CDT is more similar and differs from that of prevalent medullarytubules (CMT, MTI and MTII). Vascular structures, including G and ITS, present closer profiles of lipid expression with this analytical platform.
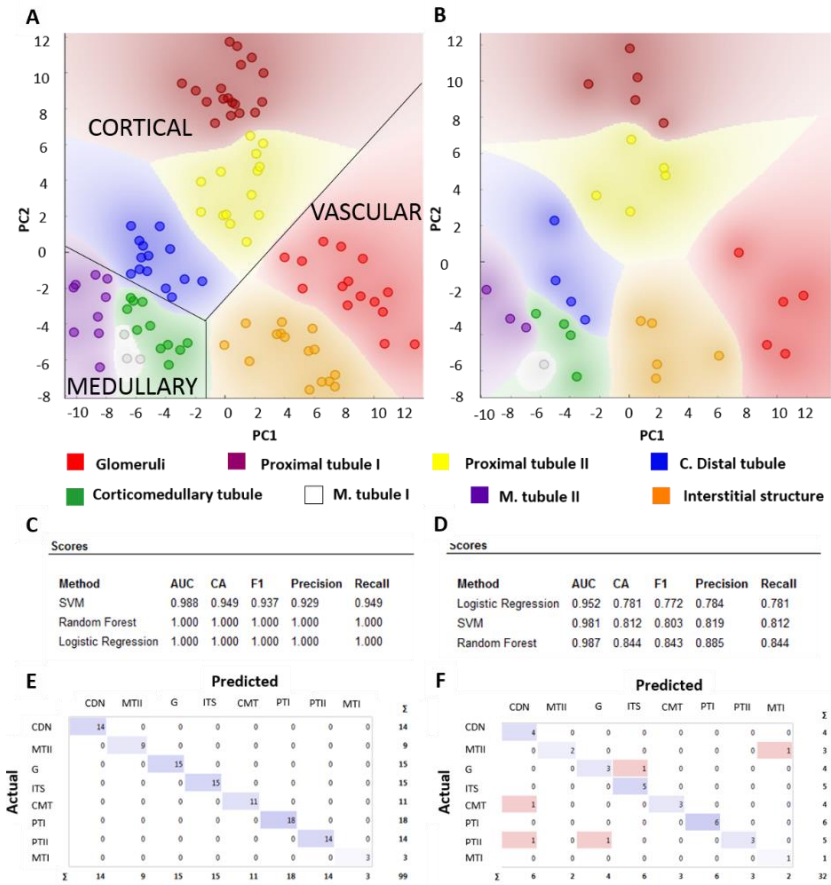
Figure 6.9. PCA analysis of the clusters obtained from the IMS images. The clusters were randomly divided into discovery (n = 99) and validation (n = 32) groups. (A) Using all the species identified in the 32 tissue sections, a perfect separation among the eight IMS histological structures was achieved in the discovery group. An additional division can be established between cortical, medullary and vascular clusters; (B) PCA analysis of the clusters in the validation group using the significant lipids deduced from the discovery group. The full list of lipid species may be found in Table A.6.1.

Analysis of the differences of lipid composition between the histological areas

If the histology of the kidney is readily identified in the IMS images then, it is due to a differential lipid expression at cellular level. **Figure 6.10** shows the summation of intensities of the lipid species corresponding to major subclasses of glycerophospholipids and sphingolipids detected in each of the histological areas (relative abundance of all the species identified may be found in **Figures A.6.5-A.6.15**. Statistically significant differences have been observed among the kidney structures for most of the lipid subclasses analyzed (**Table A.6.2**). Notably, a gradient in the expression of sphingomyelins (SM), sulfatides (SFT) and hexosylceramides (HexCer) exists along the epithelial structures of the nephron, following the path from the cortex to the medulla. While SM and HexCer relative abundances are higher in cortical structures, SFT are mainly found in medullarytubules (MTI and MTII). As a particular case, vascular structures are characterized by a higher abundance of SM, which would explain the similarity between the G and ITS lipid profile, as depicted in the proximity of the G (red) and ITS (orange) colored areas in the PCA of **Figure 6.9**.
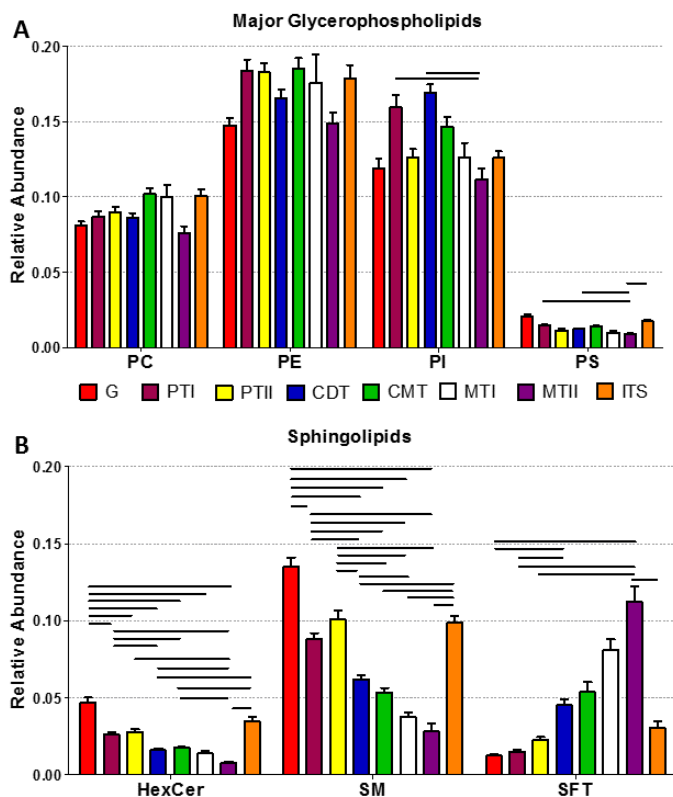
Figure 6.10 *Relative abundance of main glycerophospholipids **(A)** and sphingolipid **(B)** families in the eight histological structures identified in the IMS images. Abbreviations: PC, phosphatidylcholine; PE, phosphatidylethanolamine; PI, phosphatidylinositol; PS, phosphatidylserine; HexCer, Hexosylceramides; SM, Sphingomyelin; SFT, Sulfatide; G, Glomeruli; PT I, Proximal tubule I; PT II, Proximal tubule II; CDT, Cortical distal tubule; CMT, Corticomedullary tubule; MT I, Medullary distal tubule I; MT II, Medullary distal tubule II; ITS, Interstitial structures. Values are expressed as mean ± SEM. The statistical significance bars were assessed using Post-Hoc analysis with p-value ≤ 0.0005. Complete Statistical analysis is reported in Supplementary **Table A.6.1 and A.6.2**.*

Distribution patterns of selected lipids in renal structures

A closer look at the IMS images shows that lipid gradients are also observed at cellular level. Analysis of cross sections of specific areas in **Figure 6.11** allows for differentiating a significant gradient in the distribution of SMs in proximal tubules. For example, in PT II (cortical yellow areas) SM d34:1 levels are higher in the luminal/apical side, where proximal tubules display a highly developed plasma membrane system[33], than in basolateral membranes. Deeper analysis of other segments also point to the

existence of subtle differences within the structures reported in this work (**Figure 6.5, 6.6 and 6.7**), but their analysis is complex and requires of additional experiments to confirm their nature. Identification of those structures will be the subject of future works.
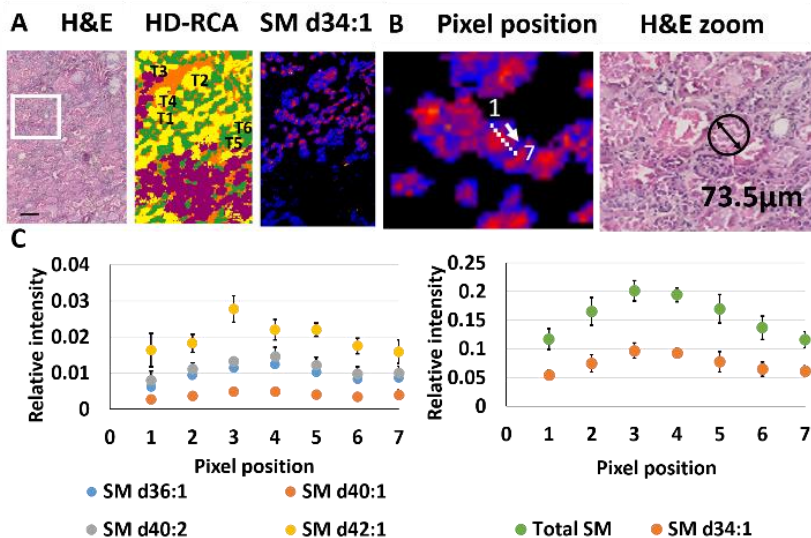
Figure 6.11. Distribution of sphingomyelins in renal sections. (A) Comparison between a cortical-medullary transition renal sample, its segmentation analysis (HD-RCA) and the distribution of SM d34:1 and d34:2 in proximal tubules II (PT II). (B) Representative spectra associated to different pixels, which show the path drawn to make the analysis. (C) Changes in SM distribution along the pixels conforming the diameter of one proximal tubule. The analysis was performed over six proximal tubules (T1-T6 in HD-RCA image). The right panel shows the variation of SM d34:1 and of the total SM, while the left panel shows the changes in four SM species. There is clearly a higher abundance of SM in the apical membrane. Images were recorded in negative-ion mode at a pixel size of 10 µm. Scale bar = 150 µm.

Similar in-depth analysis was performed over MTII clusters which can include collecting ducts (CD's). These clusters (purple colored in **Figure 6.10B**) had high levels of sulfatides, which are known to be necessary for the ammonium handling in kidney's medulla and acid-base homeostasis[34]. CDs are epithelial structures with high cell plasticity and it is well known that the distribution of epithelial cell types and subtypes in CDs is not homogeneous along the outer medulla[35]. In fact, at least two cell types can be found (**Figure 6.12A**): principal (PCs) and intercalated cells (ICs). Type A ICs are more predominant than type B, and non-A non-B ICs have been also described[35] .

With the aim to detect this heterogeneity, this sulfatide-enriched independent cluster (purple colored in **Figure 6.12B** bottom) was further subsegmented. The result of the subsegmentation in two clusters (x2) showed a single pixel line surrounding the tubules **Figure 6.12C**. The lipid profile of these delimiting pixels seemed to contain contribution of basal membrane of CDs and stroma. Consequently, it was removed, naming cCD to the remaining cluster (right side of **Figure 6.12C**).

Sub-segmentation of the cleared CD (cCD) cluster (**Figure 6.D**) into two (x2) and six (x6) clusters showed further heterogeneity in lipid profiles. Blue cluster in x2 was characterized by higher content in SFT and lower in glycerolipids (PC-O/P, PE-O/P, PI, PS). Moreover, the blue cluster was more heterogeneous than the yellow one, as four of the clusters obtained in the x6 cCD subsegmentation were grouped in this cluster (graph in **Figure 6.12D**).

Taking all the information above into account, we hypothesize that two or more types of epithelial cells with distinctive lipid fingerprints could constitute the blue cluster. That may be related with heterogeneous medullary CDs consisting of PC's and IC's. Likewise, the yellow cluster is more homogeneous and occupied the larger area (62%) of the image analyzed, suggesting that it could correspond to medullary CDs with a unique cell type, likely PCs. These are the most abundant CD cells and the predominant or unique cells in CDs a one approaches to the inner medulla[35]. Nevertheless, additional IMS and IHC/IF experiments need to be performed in order to confirm this hypothesis.
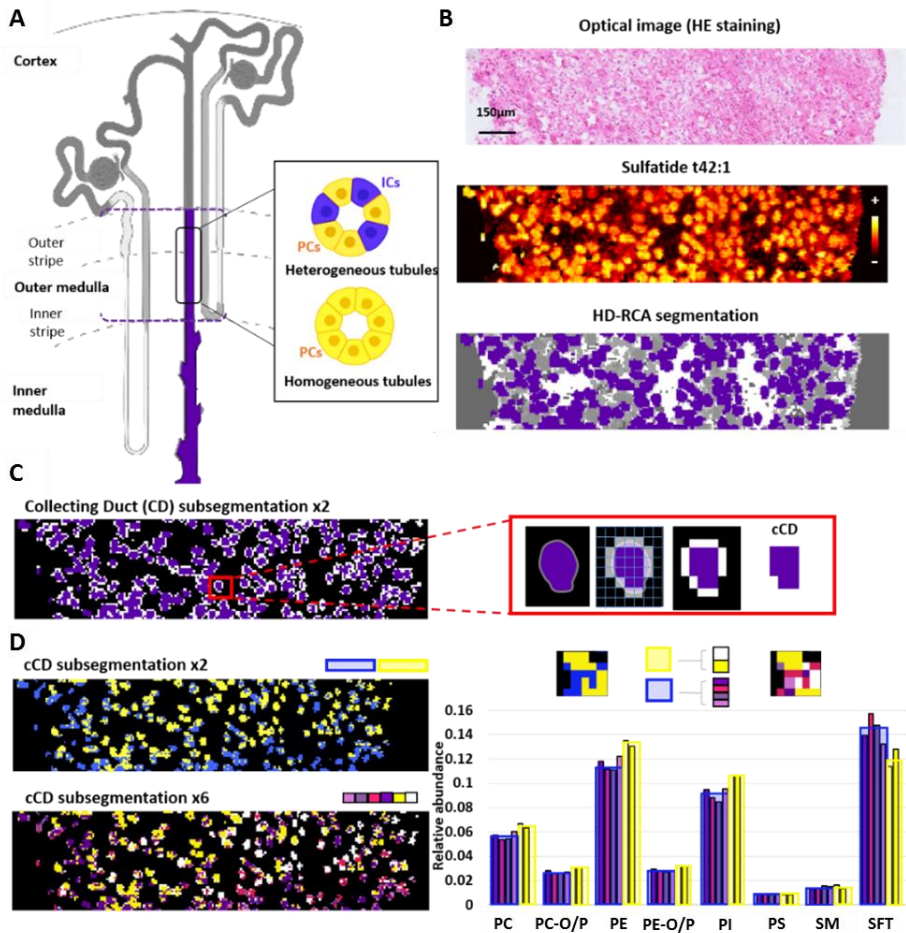
Figure 6.12. Subsegmentation analysis of MTII by MALDI IMS of lipids. *(A)* Nephron scheme focused the collecting ducts of the outer medulla. Principal (PC`s) and intercalated (IC's) cells formed the collecting ducts. *(B)* Comparison between a medullary renal sample, the distribution of SFT t42:1 and the segmentation analysis (HD-RCA) highlighting MTII cluster. *(C)* Subsegmentation analysis of MTII cluster in two (x2) and a zoom of a medullary tubule indicating the procedure to select the clear collecting duct cluster (c CD). *(D)* Subsegmentation analysis of c CD in two (x2) and in 6 segments (x6) and the summation of the intensities of the lipid species detected in each cluster grouped by lipid families.

6.5   Discussion

The kidney is an organ with a high metabolic activity[36]. Although there is evidence that different metabolic pathways predominate in each segment of the nephron, there are few studies that have investigated it using imaging techniques in human biopsies[13]. Regarding lipid metabolism, studies in animal models have described significant differences between the renal cortex and medulla in the levels of some lipid species[15, 37]. However, the level of resolution achieved in such studies did not allow the authors to deepen into the different structures of the nephron. This is the first MALDI-IMS systematic study at high enough spatial resolution to clearly identify up to eight histologic areas, based on their *in situ* lipid signature. Besides, the significant number of samples included in the study, sections from 32 patients, allowed us to demonstrate that the lipid fingerprint of each of the histologic areas is maintained among different individuals. A clear correlation between the areas identified based on the lipid profiles and the canonical histologic areas of the nephron can be readily established, as it will be shown below.

The renal corpuscle is the blood-filtering component of the nephron and is composed of two structures, the glomerulus and the Bowman's capsule[33]. The MALDI-IMS shows a characteristic lipid fingerprint for the glomerulus and even enables to differentiate the Bowman's capsule in some samples. Interestingly, interstitial vascular structures surrounding the glomerulus (afferent and efferent arterioles) and from the medullary interstitium (peritubular capillaries and vasa recta), also have a specific lipid profile, which is similar to that of the glomerular capillary tufts. These structures present higher levels of SMs. Additional experiments are needed to establish the functional significance of this lipid family in the vascular structures of the kidney, but it is known that its imbalance could be a biomarker of kidney damage. With this regard, Miyamoto et al[38] described using MALDI-IMS at 25 µm of spatial resolution, high levels of SMs in the glomeruli. Furthermore, they demonstrated in mice and in cell cultures that the accumulation of SM d18:1/16:0 in the glomerulus is involved in the physiopathology of the diabetic nephropathy.

The data presented here also demonstrate the existence of proximal tubules with two different lipid fingerprints, which we designed as PT I and PT II. The formers are located in the renal cortex, near the glomeruli, while PT IIs are found in the transition zones on both sides of the cortex and medulla. These tubular structures fit well with the classical histology[32], which describes two clearly differentiated parts: the convoluted part of the tubule, more external in the cortex, and the straight part, which reaches the outer medulla (**Figure 6.3 and Figure 6.4**). The characterization of the lipidome of proximal tubules is important to better understand the neoplastic processes that originate in this part of the nephron, such as clear cell (ccRCC) and

papillary (pRCC) renal cell carcinomas[21]. A recent study using single-cell RNA-sequencing demonstrated that the cells of the first segment of the convoluted part have common transcriptional characteristics with ccRCC and pRCC cells[39]. Studies specifically designed to this purpose will allow us to demonstrate if these common genomic roots also have a reflection in the lipid signature of both PT I cells and tumor cells. The association between the lipidomic profile of ccRCC and Bowman's capsule should not been discarded either, since this nephron structure has been recently proposed as another possible origin of the most common subtype of renal cell carcinoma[18, 22].

Limited to the cortex, we detected another tubular structure with a specific lipid profile, labelled as CDT. In the inner part of the cortex and in the outer medulla, there was another class of tubule with specific lipid fingerprint (CMT). Finally, limited to the medulla, especially in the inner areas, we detected two other tubule types, MT I and MT II. These four tubular structures have similarities in their lipid fingerprint. However, there is an important characteristic that distinguishes them: as the tubules progress into the medulla, the levels of sulfatides increase. This gradient between cortex and medulla was previously described in rodent kidney[15, 37]. The presence of this family of lipids is known to be necessary to maintain a high concentration of ammonium in the medullary interstitium, and for a correct function of medullary collecting ducts in the secretion of ammonium to the urine either in basal conditions or in metabolic acidosis[34].

One of the problems faced during this work to correlate the collection of lipid fingerprints detected by IMS with well-known histologic areas, was the difficulty of identifying the architecture of the tissue with a level of detail similar to that offered by IMS. One must keep in mind that the application of this technique is limited to fresh tissue and therefore, it was not possible to use fixed tissue sections or sections embedded in paraffin, which allow the pathologist to discern the histologic structures with higher precision but precludes its molecular definition.

Therefore, additional IF experiments were carried out to further test the identity of the sections of the nephron located using lipid signatures. **Figure 6.13** shows the comparison between the IF staining of various segment-specific tubular markers and the segmentation of the IMS experiment recorded over the same tissue. In the corticomedullary transition sample (**Figure 6.13A**), proximal tubules are LTL-positive and they correlate with the dark red and yellow MSI segments named as PTI and PTII (numbered as 2 and 3 in the figures), confirming the assignment based on the lipid signature. Additionally, distal convoluted tubules and collecting ducts are DBA positively stained and show a clear correlation with the blue and purple segments named as CDT (number 4) and MTII (number 5). Furthermore, the same correlation

between MTII and the DBA positively stained tubules is shown in the medullary section, allowing us to confirm the assignment of these tubules as collecting ducts.

Figure 6.13C also shows the THP (Horse Tamm Horsfall Protein)/Hoesch IF experiment over a section of kidney medulla. The THP-positive tubules (in green) correspond to thick ascending Henle limbs. These structures perfectly match the location of the green segments in the corresponding segmentation image, which were attributed to CMT (see **Figure 6.3**). As it can be seen, descendent thin libs are not stained in any of the images and they very well match the attribution of the white segment in the IMS experiments to this section of the nephron.
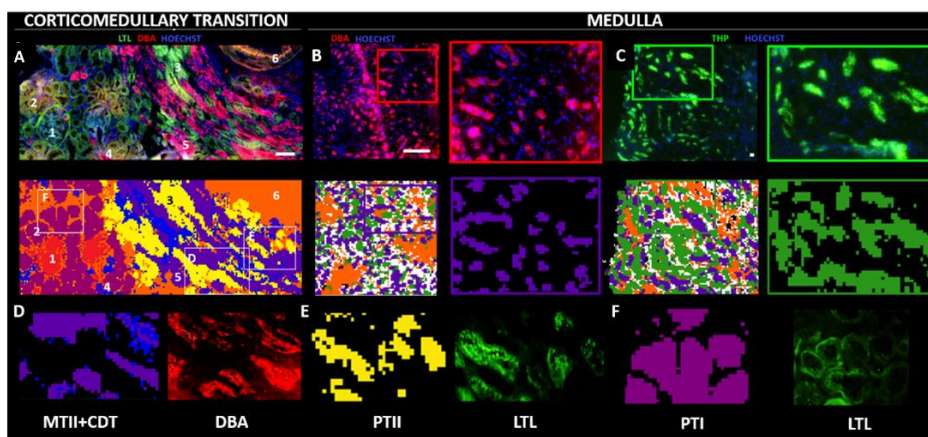
Figure 6.13. Comparison between the IF staining and the segmentation analysis of the IMS experiment carried out over the same section. *(A)* Section of a cortical-medullary transition. Segment-specific tubular markers used are as follows: proximal tubule, Lotus tetragonolobus lectin (LTL); distal convoluted tubules and collecting ducts, Dolichos biflorus agglutinin (DBA). The correspondence of the numbers are 1: G; 2: PTI; 3: PTII; 4: CDT; 5: MTII and 6: ITS; *(B)* Comparison between the IF of a section of a medullary biopsy and the corresponding MS image. DBA positive collecting ducts tubules correlate with the purple segment, attributed to MT II based on its lipid signature. *(C)* Comparison between the segmentation analysis of an IMS experiment over a section of medulla and the THP/Hoesch IF image. The THP-positive tubules correspond to thick ascending Henle limbs and correlate with the cluster correctly attributed to CMT (green segment) in the IMS experiment; *(D-F)* Zoomed areas of the figures in panel A showing the good correlation between the areas highlighted in the IF experiment and the segments found by IMS. Scale bar = 150 μm. An enlarged version of this figure may be found in supplemental material (Figure A.6.15)

The location of the segments identified in renal tissue and the differences in sulfatide expression levels allow us to hypothesize about these four tubular structures detected by MALDI-IMS (see **Figure 6.4**): MT II are present in higher proportion in the inner medulla and have the highest level of sulfatides, suggesting that they correspond

to the medullary portion of the collecting ducts, the most abundant structures in this area of the kidney[32, 40]. MT I are also found in the inner medulla, but in lesser proportion, and have high levels of sulfatides, indicating that they could correspond to the thin descending limbs of Henle's loops of the yuxtamedullary nephrons. Due to its high presence at the corticomedullary level and their content in sulfatides, which is intermediate between those of the exclusively cortical and medullary tubules, CMT could correspond to the thick ascending limb. Finally, CDTs are only found in renal cortex and have lower sulfatide levels, which suggests that they correspond to the cortical portion of the distal nephron, which comprises distal convoluted tubules (DCT), connecting tubules (CNT) and cortical collecting ducts (CCT)[40].

Comparison between the relative abundance of these structures in the sections analyzed in the present work and those cell type distribution percentages reported in mouse kidney[40, 41] shows similar proportions. For example, proximal tubules are the most abundant epithelial cell type in the mouse kidney, amounting to 44%, whereas the lipid fingerprints of PT Is and IIs reach 56% of the total detected epithelial structures in the human kidney. Cortical and medullary thick ascending limb cells (CTAL and MTAL) represent 21% in mouse kidney, while according to this work, CMTs represent 14% in human kidney. Moreover, the lipid fingerprint of CDTs represent 13% of the area of our analyzed sections while the cortical portion of distal nephron in mouse kidney constitute around 22% of total epithelial cells. Furthermore, cells from thin limbs and medullary collecting ducts of mouse kidney amount to 6% and 7% of the total cellularity respectively, whereas lipid fingerprints of MT I and II represent 4% and 13% of the total area in the sections, respectively. These similarities between our data and previously reported cell type distributions[40] in mice support the assignment proposed in our study.

The high spatial resolution achieved in our MALDI-IMS experiments allowed us to take a step forward and to analyze the variation of lipid relative abundance within very small (from the point of view of IMS) histologic structures. For example, there is a clear gradient in the relative abundance of sphingomyelins from the apical membrane to the basal side of the proximal tubule cells (**Figure 6.11**). These lipids may play an important role in sodium-coupled reabsorption mechanisms[42]. Likewise, although confirmation with orthogonal techniques is required, sulfatide levels could help to identify the cellular subpopulations in medullary collecting ducts, as shown in **Figure 6.12**.

Furthermore, it is tempting to speculate that the defined eight structures with a characteristic lipid fingerprint could correspond to previously described cell subpopulations from each part of nephron[40], or to cells from the same subpopulation in different metabolic state (**Figure 6.5, 6.6 and 6.7**). Future studies isolating kidney cells, analyzing their lipidome by MALDI-IMS and associating these results with the transcriptome of these subpopulations will throw light to these questions.

6.6   Conclusions

In this chapter, we present a detailed study on the architecture of human kidney using MALDI-IMS, which can be taken as a form of molecular histology. Using this technology, it is possible to create lipid distribution maps that describe the histology of the tissue from a metabolic point of view without the drawbacks associated to cell isolation procedures and culture. Comparison with the optical images and with the description in the literature of the structure of the nephron allowed us to demonstrate that at least eight different parts of the nephron present characteristic and unique lipid fingerprints, which are maintained among different individuals. The differences in lipid profiles are related to differences in cell composition between the histologic areas. Further exploiting the high spatial resolution achieved in the experiment, we can demonstrate the existence of gradients in lipid expression along the cells of the different segments of the nephron. This study is a starting point for further studies in which precise identification of even more histologic areas of the nephron by comparison with IF images will be tackled. It also sets the foundations for further studies on the metabolic basis of the diseases affecting to human kidney.

1. Eddy, S., Mariani, L. H. & Kretzler, M. Integrated multi-omics approaches to improve classification of chronic kidney disease. *Nature Reviews Nephrology*, 1-12 (2020).

2. Stewart, B. J. & Clatworthy, M. R. Applying single-cell technologies to clinical pathology: progress in nephropathology. *J. Pathol.* **250**, 693-704 (2020).

3. Buchberger, A. R., DeLaney, K., Johnson, J. & Li, L. Mass spectrometry imaging: a review of emerging advancements and future insights. *Anal. Chem.* **90**, 240-265 (2018).

4. Djambazova, K. *et al*. Resolving the Complexity of Spatial Lipidomics Using MALDI TIMS Imaging Mass Spectrometry. *Anal. Chem.* (2020).

5. Neumann, E. K. *et al*. Spatial Metabolomics of the Human Kidney using MALDI Trapped Ion Mobility Imaging Mass Spectrometry. *Anal. Chem.* (2020).

6. Fernández, R., Garate, J., Martín-Saiz, L., Galetich, I. & Fernández, J. A. Matrix Sublimation Device for MALDI mass spectrometry imaging. *Anal. Chem.* **91**, 803-807 (2018).

7. Zink, K. E., Tarnowski, D. A., Mandel, M. J. & Sanchez, L. M. Optimization of a minimal sample preparation protocol for imaging mass spectrometry of unsectioned juvenile invertebrates. *Journal of Mass Spectrometry* **55**, e4458 (2020).

8. Verbeeck, N., Caprioli, R. M. & Van de Plas, R. Unsupervised machine learning for exploratory data analysis in imaging mass spectrometry. *Mass Spectrom. Rev.* **39**, 245-291 (2020).

9. Jones, E. A., Deininger, S., Hogendoorn, P. C., Deelder, A. M. & McDonnell, L. A. Imaging mass spectrometry statistical analysis. *Journal of proteomics* **75**, 4962-4989 (2012).

10. Maimó-Barceló, A. *et al*. Confirmation of sub-cellular resolution using oversampling imaging mass spectrometry. *Analytical and Bioanalytical Chemistry* **411**, 7935-7941 (2019).

11. Garate, J. *et al*. Imaging Mass Spectrometry-Based Lipidomic Approach to Classification of Architectural Features in Nevi. *J. Invest. Dermatol.* **139**, 2055-2058.e7 (2019).

12. Lee, J. W., Chou, C. L. & Knepper, M. A. Deep Sequencing in Microdissected Renal Tubules Identifies Nephron Segment-Specific Transcriptomes. *J. Am. Soc. Nephrol.* **26**, 2669-2677 (2015).

13. Prentice, B. M., Caprioli, R. M. & Vuiblet, V. Label-free molecular imaging of the kidney. *Kidney Int.* **92**, 580-598 (2017).

14. Aboulmagd, S. *et al*. Dual internal standards with metals and molecules for MALDI imaging of kidney lipids. *Anal. Chem.* **89**, 12727-12734 (2017).

15. Muller, L. *et al*. Lipid imaging within the normal rat kidney using silver nanoparticles by matrix-assisted laser desorption/ionization mass spectrometry. *Kidney Int.* **88**, 186-192 (2015).

16. Spraggins, J. M. *et al*. High-performance molecular imaging with MALDI trapped ion-mobility time-of-flight (timsTOF) mass spectrometry. *Anal. Chem.* **91**, 14552-14560 (2019).

17. Marsching, C., Eckhardt, M., Gröne, H., Sandhoff, R. & Hopf, C. Imaging of complex sulfatides SM3 and SB1a in mouse kidney using MALDI-TOF/TOF mass spectrometry. *Analytical and bioanalytical chemistry* **401**, 53-64 (2011).

18. Bowman, A. P. *et al*. Evaluation of lipid coverage and high spatial resolution MALDI-imaging capabilities of oversampling combined with laser post-ionisation. *Analytical and bioanalytical chemistry* **412**, 2277-2289 (2020).

19. Grove, K. J. *et al*. Diabetic nephropathy induces alterations in the glomerular and tubule lipid profiles. *J. Lipid Res.* **55**, 1375-1385 (2014).

20. Ammirati, A. L. Chronic Kidney Disease. *Revista da Associação Médica Brasileira* **66**, s03-s09 (2020).

21. Eble, J. Neoplasms of the kidney. *Urologic surgical pathology* (1997).

22. Manini, C. & Lope. The Labyrinth of Renal Cell Carcinoma. *Cancers (Basel)* **12**, 10.3390/cancers12020521 (2020).

23. Fernández, R., Garate, J., Martín-Saiz, L., Galetich, I. & Fernández, J. A. Matrix Sublimation Device for MALDI mass spectrometry imaging. *Anal. Chem.* **91**, 803-807 (2018).

24. Xiong, X. &De la Torre, F. *Supervised descent method and its applications to face alignment* (Proceedings of the IEEE conference on computer vision and pattern recognition, 2013).

25. Garate, J. *et al*. Influence of Lipid Fragmentation in the Data Analysis of Imaging Mass Spectrometry Experiments. *J. Am. Soc. Mass Spectrom.* **31**, 517-526 (2020).

26. Fernández, R. *et al*. Microarray and Mass Spectrometry-Based Methodology for Lipid Profiling of Tissues and Cell Cultures. *Anal. Chem.* **91**, 15967-15973 (2019).

27. Cao, L. *et al*. Rankcompete: Simultaneous ranking and clustering of information networks. *Neurocomputing* **95**, 98-104 (2012).

28. Kemeny, J. G. & Snell, J. L. in *Markov chains* (Springer-Verlag, New York, 1976).

29. Spitzer, F. in *Principles of random walk* (Springer Science & Business Media, 2013).

30. Corportation, I. IBM SPSS Statistics for Windows (Version 25.0 Armonk). *NY: IBM Corp* (2017).

31. Demšar, J. *et al*. Orange: data mining toolbox in Python. *the Journal of machine Learning research* **14**, 2349-2353 (2013).

32. Kriz, W. & Bankir, L. The Renal Commission of the International Union of Physiological Sciences (IUPS): A standard nomenclature for structures of the kidney. *Kidney Int.* **33** (1988).

33. Madrazo-Ibarra, A. & Vaitla, P. in *StatPearls* (StatPearls Publishing LLC, Treasure Island (FL), 2020).

34. Stettner, P. *et al*. Sulfatides are required for renal adaptation to chronic metabolic acidosis. *Proc. Natl. Acad. Sci. U. S. A.* **110**, 9998-10003 (2013).

35. Rao, R., Bhalla, V. & Pastor-Soler, N. M. *Intercalated Cells of the Kidney Collecting Duct in Kidney Physiology* (Seminars in Nephrology Ser. 39, Elsevier, 2019).

36. Cargill, K. & Sims-Lucas, S. Metabolic requirements of the nephron. *Pediatric Nephrology* **35**, 1-8 (2020).

37. Marsching, C. *et al*. Quantitative imaging mass spectrometry of renal sulfatides: validation by classical mass spectrometric methods. *J. Lipid Res.* **55**, 2343-2353 (2014).

38. Miyamoto, S. *et al*. Mass spectrometry imaging reveals elevated glomerular ATP/AMP in diabetes/obesity and identifies sphingomyelin as a possible mediator. *EBioMedicine* **7**, 121-134 (2016).

39. Young, M. D. *et al*. Single-cell transcriptomes from human kidneys reveal the cellular identity of renal tumors. *Science* **361**, 594-599 (2018).

40. Chen, L. *et al*. Renal-Tubule Epithelial Cell Nomenclature for Single-Cell RNA-Sequencing Studies. *J. Am. Soc. Nephrol.* **30**, 1358-1364 (2019).

41. Clark, J. Z. *et al*. Representation and relative abundance of cell-type selective markers in whole-kidney RNA-Seq data. *Kidney Int.* **95**, 787-796 (2019).

42. Vrtovsnik, F., Le Grimellec, C. & Friedlander, G. Sphingomyelin and cholesterol modulate sodium coupled uptakes in proximal tubular cells. *Kidney Int.* **41**, 983-991 (1992).

Chapter 7

Divergence of lipid profile between murine and human kidney studied by MALDI-IMS.

Animal models are useful for deciphering the physiological mechanisms underlying pathological processes. Mice is one of the most widely used animal model but physiopathological differences between species, specifically in lipid biology, are not properly taking into account during the interpretation of the results. Thus, trying to compare the lipidome of human and mice kidney, here we present a complete analysis with the aim of bringing new insights in the similarity or differences between these two species. Data sets were selected from cortex, glomeruli and medulla clusters extracted from mass spectrometry images acquired at 10 and 25 μm. This allows for the identification of the specific changes associated to the different histological areas of the kidney.

7.1   Introduction

Research in several biological fields broadly relies on the availability of efficient model organisms. The preservation of physiological mechanisms between species and general traits that include their amenability to growing/breeding and to genetic manipulation are key aspects during model organism election. Besides these general properties, some models are chosen due to specific characteristics: the genome compactness of *Saccharomyces cerevisiae* and *Arabidopsis thaliana* makes their genetic study easier; the simplicity of generating mutations and identifying their phenotypical consequences are the two main properties that made the common fruit fly (*Drosophila melanogaster*) the most studied organism; the small and fixed number of constituting cells and the large fraction of those undergoing apoptosis during the life cycle has made the *Caenorhabditis elegansa* nematode a widely used model for studying development and apoptosis and the transparency of the zebrafish (*Danio rerio)* body during early development enables analysis of its internal anatomy[1].

In addition, anthropomorphic considerations are taken into account if the model of choice is a mammalian, such as the resemblance to Homo sapiens in order to better understand the development, physiology and physiopathology of our species. Consequently, primates like the Rhesus macaque (*Macaca mulatta*) are frequently selected for cognition studies. In other fields of physiology, the rat (*Rattus norvegicus*) has long been a universal model because of the larger size of its organs compared with those of the mouse.

However, in the last years, the development of efficient methods for homologous gene recombination in mice (*Mus musculus*)[2] and lower breeding costs have boosted the use of mice, which have supplanted rats in most fields of physiology and physiopathology. Nevertheless, although these strong scientific and economic considerations are significantly valuable, it should not been forgotten the first requirement of a good model: the similarity of its physiological properties to those of humans[1].

Nevertheless, there are many examples where knock-out mice for a gene, whose loss-of-function mutations are responsible for a disease in humans, do not correlate with the expected phenotype[3-5]. In fact, not only the genetic information, but also several intermediate steps are involved in the translation of this information to the phenotype level. These steps include changes in epigenetic modification levels of DNA and histone proteins, RNA and protein expression levels, as well as changes in the concentration of small molecules, metabolites and lipids, that participate in all biological processes[1, 6].

Lipidomics is of increasing interest in studies of biological systems. However, differences in lipid biology between animal species and humans are not adequately considered in experimental designs.

In the renal context, considerable differences can be appreciated in kidney function and pathology between men and mice. For example, the level of basal proteinuria observed in mice is viewed as pathological in humans and mice are resistant to many drugs that induce glomerulopathies in humans[7].

In order to determine whether divergence in lipidomics along the different sections of the nephron might underlie physiological differences between humans and mice, we performed a well-defined comparison of lipid profiles across the main functional structures constituting the nephron in these two species.

7.2   Objectives

The goal of this chapter is to perform a comparison between the lipid fingerprint of murine and human renal samples across the main histological structures: Cortex, glomeruli and medulla studied by MALDI-IMS. To the best of our knowledge, this is the first detailed analysis of differences in lipid expression between these two species, and it will contribute to evaluate the suitability of mice as a good animal model, specifically focus on renal studies.

7.3   Experimental section

This chapter contains a comparative analysis of the lipidome from human and murine renal samples included in **Chapter 5 and 6**. Thus, the complete sample collection section can be found in those chapters.

Briefly, C57BL/6 mice used in this study (n=5) were between 12 and 14 weeks of age at the time of kidney removing. Kidneys were perfused in situ with cold saline before removal, and snap-frozen in liquid nitrogen until sample preparation. Sections of 15 µM were performed for MALDI-IMS and histological analyses. H&E stain was performed after MALDI-IMS exploration as indicated in **Chapter 3**.

Additionally, the 26 human renal biopsies involved in this study belonged to cortex or medullar renal regions and they were obtained from a series of nephrectomies in the Universitary Hospital of Basurto (Bilbao, Spain) and Univesitary Hospital of Galdácano (Galdácano, Spain). Kidneys were stored fresh frozen (-80ºC) immediately after extraction and sections of 16 µm were performed for MALDI-IMS analysis. Once

the 16 μm sections were explored by &MALDI-IMS, they were stained with H&E following the protocol described in **Chapter 3**.

MALDI-IMS analysis

A total of 39 histological sections obtained from 26 different human patients and 5 mice were prepared and analyzed by MALDI-IMS as described Chapter 3. To equilibrate the number of data sets from human and mouse kidney, some replicates of the five mice were included.

Briefly, DAN were used as matrix for negative-ion detection and was deposited with the aid of our in-house designed sublimator device[8] (see Chapter 4). Sections were scanned using a MALDI-LTQ-Orbitrap XL (Thermo Fisher, San Jose, CA, USA). Data were acquired with a mass resolution of 60000 at m/z = 400 in the scanning range of 550-1000 in negative-ion mode. Human samples were acquired at 10 μm of spatial resolution while 10 μm and 25 μm were used in murine samples. Spectra alignment and lipid assignment was performed as described in Chapter 3. For m/z channels with several lipid assignment, "on-tissue" MS/MS and MS[3] was carried out in order to propose an univocal assignment. With this procedure, it is not possible to distinguish between alkyl-ether and vinyl-ether lipids.

Data analysis:

Data from each section were analyzed using segmentation algorithm (HD-RCA) which group the pixels in base of lipid spectra similarity. The fundamentals were already described in a previous publication[9] and in **Chapter 3**. The three groups of study were cortex, glomeruli and medulla. To properly select the clusters which correlate with these histological structures, the number of clusters was set from 4 to 6. In some human samples, the whole section belonged to a single renal area, thus, the average spectrum from the whole section was selected.

As in previous chapters, to statistically evaluate the differences in the lipid fingerprints among the study groups, *Levene*-test, and *T-test* were computed using SPSS Statistics 17.0 (IBM, Armonk, NY, USA)[10]. *Levene*-test determines the homogeneity (H_0 = groups have equivalent variance) to choose the T-test method. PCA analysis and separation models were carried out by Orange Biolab 2.7.8 (Ljubljana, Slovenia)[11].

7.4   Results

In a first attempt to compare the lipidome of human and murine kidney, IMS clusters data sets of glomeruli, cortex and medulla from human and murine samples were selected. The distribution of the clusters selected from human and murine

samples appears in **Figure 7.1**. Besides, an example of the IMS clusters picked is shown in **Figure 7.2.**
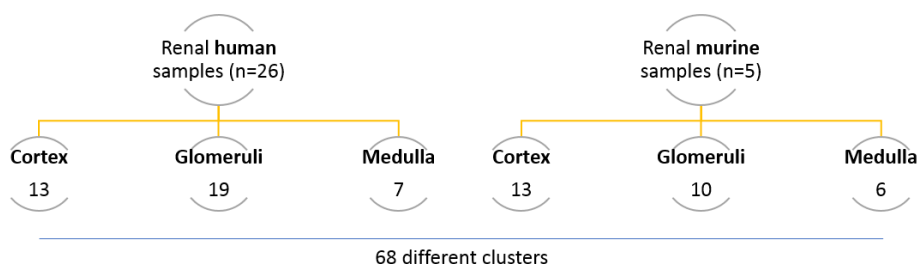
Figure 7.1. Diagram depicting the sample distribution into human and murine sets.
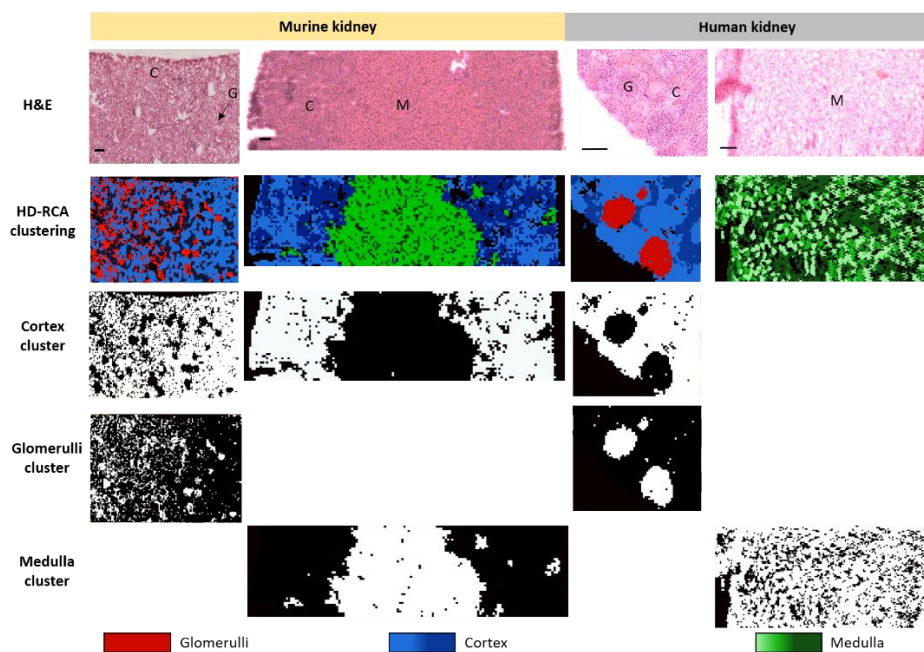
Figure 7.2. Example of the clusters selected as glomeruli, cortex and medulla in two human and two murine renal samples. Histological area corresponds to glomeruli, cortex and medulla are labelled with G, C and M respectively. Scale bar chart=150 μm, H&E= hematoxylin eosin staining.

The assignment of the spectra from all the selected IMS clusters allowed us to identify 128 ad 112 lipid species in human and mice kidney respectively. From the total of the detected species, 50 were exclusively detected in human kidney while 34 were

only found in mice. Thus, 78 lipids were identified in both species (**Figure 7.3** right panel).
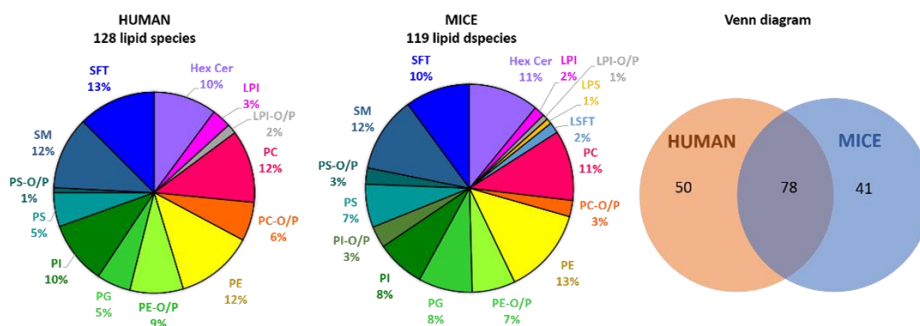
Figure 7.3. *Identified lipids in human and mouse kidney. From left to right, percentage of each lipid class in human and murine kidney and Venn diagram of the total of lipid species detected.*

The lipid species identified in human and in murine kidney belong to 12 and 17 lipid families respectively, being minority lipid subclasses such as LPS's, LSFT's, and PI-O/P's exclusively found in mouse kidney. Moreover, as appears in

Figure 7.3, the percentage of the main glycerophospholipid subclasses based on the total number of lipids detected remains almost constant for both models. Nevertheless, a comparison between the individual lipids detected in human and in mouse was carried out (**Figure 7.4**).

Most lysophospholipids (**Figure 7.4A**) were detected in both tissues at expenses of Lyso PS, which were only found in murine kidney. In addition, a thorough analysis of the main phospholipid families (**Figure 7.4B-F**) shows that the 60% of the total PG, PC, PE, PI and PS species have been found in both models. In the case of PG's, only three PUFA-containing PG were not found in human kidney while the seven PG's detected in human were also visible in mice (**Figure 7.4B**). Additionally, in the context of PE subclass, only 26 % of the molecular species were not found in both tissues. It is remarkable that the species undetected in human kidney contained an even number of double bonds (PE 34:0 and PE 36:2), while in murine renal samples the species that were not detected were those containing an odd number of unsaturations (PE 36:1, PE 38:5 and PE 40:7, **Figure 7.4C**). Finally, for PC, PI and PS no patterns were observed for the species that did not appear in both tissues (**Figure 7.4D-F**)**.**

The analysis of ether/vinyl-ether phospholipids (**Figure 7.4G-J**)**,** shows important differences in lipid expression. In the case of PE-O/P and PC-O/P, human kidney shows a substantial abundance of species compared to mouse kidney (**Figure 7.4G**)**.** As an

exceptional case, PC-O 38:6/ PC-P 38:5 was uniquely found in mice. Moreover, it is worth of mention that no PI-O/P's or PS-O/P were found in human kidney with the exception of PS-O 38:2/PS-P 38:1, which was detectable in both species. (**Figure 7.4I,J**).

Finally, clear differences were found in the sphingolipids between human and mouse (**Figure 7.4K-N**), with the exception of HexCer: 90% of the HexCer identified were found in both tissues and only two t-HexCer were not found in human samples. (**Figure 7.4K**). Regarding SM's, only 50% of the species were found in both models. For example, SM d41:1 and SM d41:4 were only visible in mouse while six MUFA and PUFA-containing SM were exclusive for human (**Figure 7.4L**). As a last note, no LSFT were detected in human renal samples (**Figure 7.4M**). Moreover, a remarkably higher percentage of dSFT was detected in human compared to murine kidney (75% and 33% respectively). However, the 66% of the detected SFT's in mice belonged to the t-SFT subtype in contrast with the 25% found in human kidney (**Figure 7.4N**).
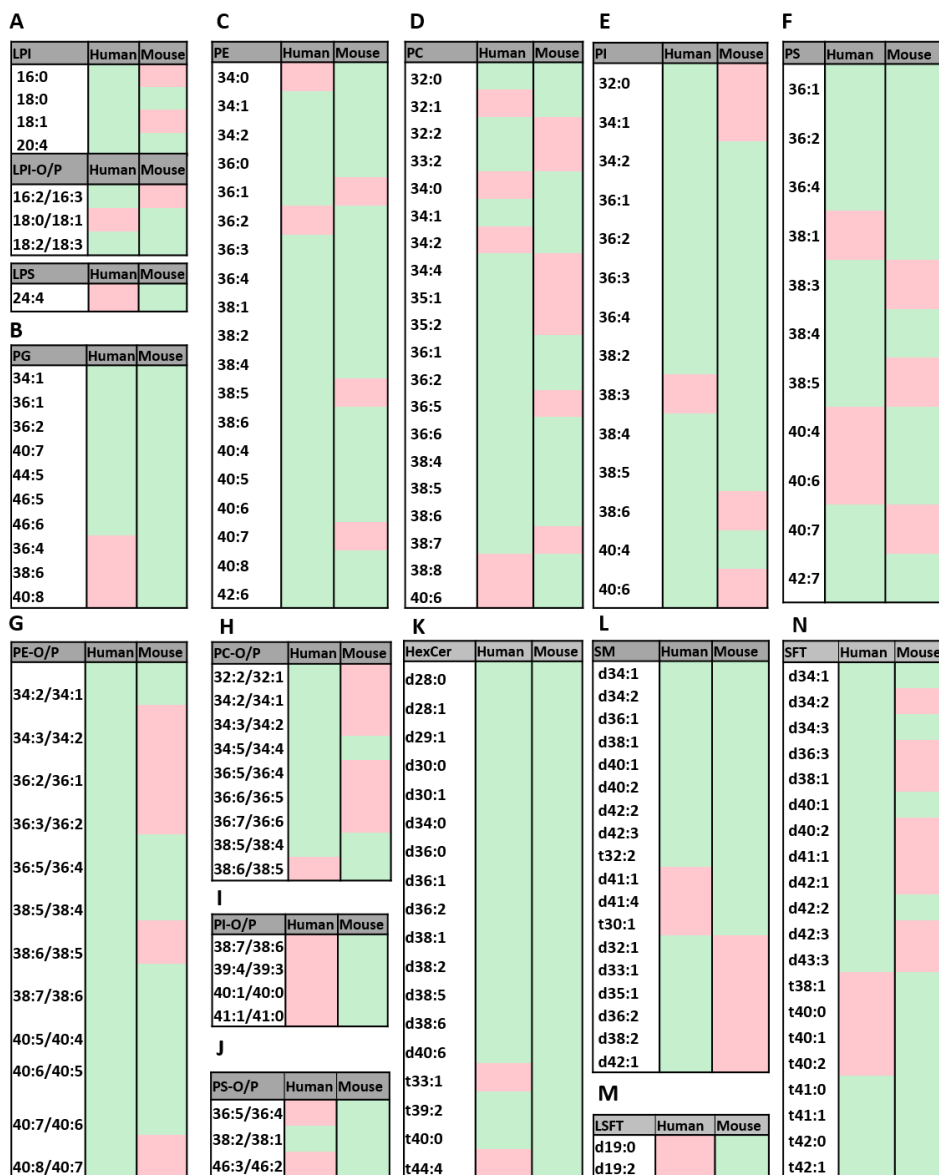
Figure 7.4. *Individual lipid species detected (green shadowed) and non detected (red shadowed) in human and murine kidney. The lipid subclasses studied were **(A)** Lysophospholipids (Lyso PI, Lyso PI-O/P and Lyso PS), **(B)** PG, **(C)** PE, **(D)** PC, **(E)** PI, **(F)** PS, **(G)** PE-O/P, **(H)** PC-O/P, **(I)** PI-O/P, **(J)** PS-O/P, **(K)** HexCer, **(L)** SM, **(M)** LSFT and **(N)** SFT.*

After analyzing the detection differences of individual lipid species in human and murine kidney, lipid data sets from glomeruli, cortex and medulla from both models were included in an unsupervised PCA analysis in order to see the separation

tendencies. Only those lipids with an ANOVA p-value lower than 0.05 for at least one of the multi-comparison analysis (the six features selected as target were the following ones: Human cortex, Human glomeruli, Human medulla, Murine cortex, Murine glomeruli and Murine medulla) were included in the analysis

As can be appreciated in **Figure 7.5A**, the lipidome of human and murine renal samples present such differences to be perfectly separated by PC1. All the classification models applied reveal a perfect separation between the two groups with a precision and a recall of 100%. In addition, the same analysis also reveals clear differences among the three main histological areas (**Figure 7.5B);** PC2 is able to differentiate glomeruli (red in the top) from cortex and medulla (blue and green in the bottom). Although the classifier models resulted in an excellent overall agreement (up to 82.4%), two medulla samples were misclassified as can be seen in the confusion matrix of kNN model (**Figure 7.5B bottom**). This result suggest that the lipid differences between glomeruli and the remaining histological structures are more evident than the divergence between cortex and medulla lipidome of each kidney model. Similar results can be appreciated in the PCA analysis of **Figure 7.5C** where the lipidome of the six target groups were consistently different in base on the classification models results (overall agreement up to 89.7%). As PC1 segregate samples according to the animal species and PC2 according to the histological structure, four marked groups were obtained in the PCA scatter plot, using the two first principal components. Human and murine glomeruli can be perfectly divided by PC1 (green and orange colored samples) and human cortex+medulla and murine cortex+medulla are separated by PC2 (blue and yellow from human structures and red and pink for murine ones). Again, this finding confirms that the differences between human and mice lipidome and the specific lipid fingerprint of the glomeruli could hide other dissimilarities expected from each renal region from the two animal models. Indeed, evident differences not only between glomeruli and the others histological regions but also between cortex and medulla were reported in **Chapters 5 and 6** in both human and murine kidney, respectively. Nevertheless, only 8% of the samples were misclassified (6 /68) in this multiclass comparison (**Figure 7.5C**).

Comparison of the relative abundance of the lipid families detected in kidney (**Figure 7.5D**) shows substantial differences, although both species present a similar intensity profile. For example, PE and PI are the most abundant classes, followed by PC and SM. Also, there is a negative gradient in HexCer and SM from glomeruli to medulla in both human and murine kidney while an increasing gradient was observed in PG and SFT. These findings denote that human and mice lipid metabolism have share some features. However, the relative abundance of some families in the glomeruli-cortex-medulla progression. For example, PI seems to be downregulated in murine's medulla compared to cortex. To analyze these differences, it is necessary to focus the analysis in each type of tissue separately.

Panel A Scores

Method	AUC	CA	F1	Precision	Recall
Logistic Regression	1.000	1.000	1.000	1.000	1.000
Naive Bayes	1.000	1.000	1.000	1.000	1.000
Random Forest	1.000	1.000	1.000	1.000	1.000
SVM	1.000	1.000	1.000	1.000	1.000
kNN	1.000	1.000	1.000	1.000	1.000

Panel B Scores

Method	AUC	CA	F1	Precision	Recall
Logistic Regression	0.979	0.941	0.942	0.944	0.941
Naive Bayes	0.982	0.824	0.833	0.868	0.824
Random Forest	0.975	0.882	0.882	0.882	0.882
SVM	0.993	0.956	0.956	0.960	0.956
kNN	0.985	0.971	0.970	0.973	0.971

Panel C Scores

Method	AUC	CA	F1	Precision	Recall
Logistic Regression	0.986	0.971	0.970	0.973	0.971
Naive Bayes	0.993	0.897	0.901	0.921	0.897
Random Forest	0.994	0.926	0.925	0.929	0.926
SVM	0.993	0.941	0.937	0.955	0.941
kNN	0.989	0.971	0.969	0.975	0.971

Panel A confusion matrix

Actual \ Predicted	Human	Mice	Σ
Human	39	0	39
Mice	0	29	29
Σ	39	29	68

Panel B confusion matrix

Actual \ Predicted	Cortex	Glomeruli	Medulla	Σ
Cortex	26	0	0	26
Glomeruli	0	29	0	29
Medulla	2	0	11	13
Σ	28	29	11	68

Panel C confusion matrix

Actual \ Predicted	HC	MC	HG	MG	HMe	MMe	Σ
HC	12	0	0	0	0	1	13
MC	0	12	0	0	0	1	13
HG	1	0	18	0	0	0	19
MG	0	0	0	10	0	0	10
HMe	0	0	0	0	7	0	7
MMe	0	2	0	1	0	3	6
Σ	13	14	18	11	7	5	68

Figure 7.5. Statistical analysis of the differences in lipid expression between human and mouse kidney. PCA analysis of renal samples, according to the species (A), the histological area (B) and a combination of model and histological region (C). (D) Relative abundance of the lipid families in cortex, glomeruli and medulla from human and murine kidney. Values are expressed as mean ± SEM (n= 29 for mice group -13 for cortex, 10 for glomeruli and 6 for medulla- and n=39 for human group -13 for cortex, 19 for glomeruli and 7 for medulla). Statistical analysis was assessed using T-test analysis. * = p-value<0.05. Complete statistical results are compiled in Table A.7.1.

Lipid differences between human and murine renal cortex

IMS data from human and murine cortical clusters were included in a PCA analysis and in several classification models. As expected from previous section, murine and human renal cortex present distinctive lipid fingerprints, which are the reason for their perfect separation by the PC1 in the PCA analysis (**Figure 7.6A**) and of the outstanding performance of the classification models, which achieve the 100% in accuracy, precision and recall (**Figure 7.6B**). As a consequence, all the samples were perfectly classified, as can be appreciate in the Random Forest's confusion matrix (**Figure 7.6C**).
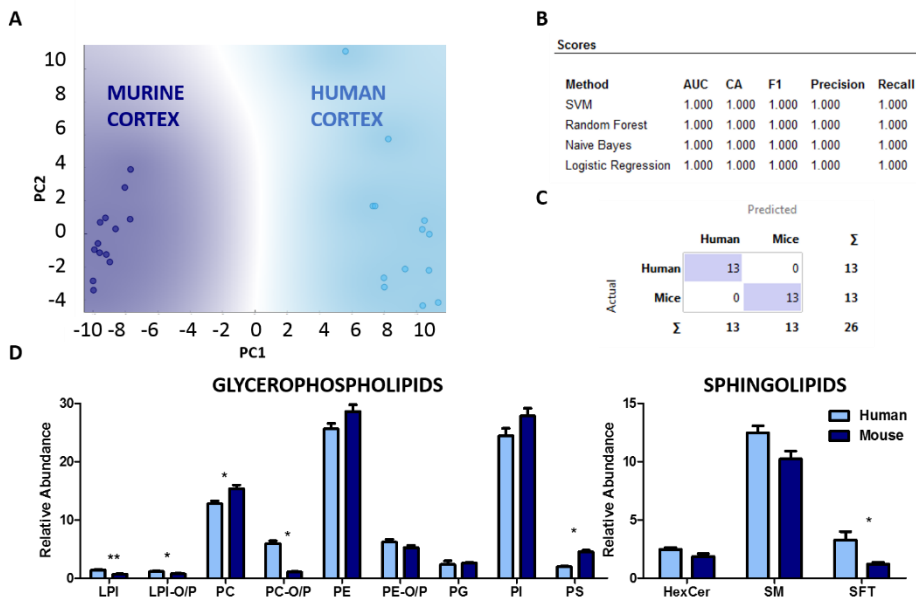
Figure 7.6. Analysis of the similarity of the lipidome of murine and human renal cortex. **(A)** PCA analysis separates murine and human cortex; **(B)** summary of the performance of the classification; **(C)** Confusion matrix for the Random Forest classifier; **(D)** relative abundance of the lipid families in murine and human renal cortex. Values are expressed as mean ± SEM (n=13 for both groups). Statistical analysis was assessed using T-test analysis. * = p-value<0.05; **= p-value<0.01;.Complete statistical results are compiled in **Table A.7.1**.

Figure 7.6D additionally shows the comparison between the relative intensity of the summation of the intensities of the main glycerophospholipids and sphingolipids classes of murine and human renal cortex. The two most intense glycerophospholipid classes are PE and PI in both murine and human cortex. Moreover, PC's and PS's are significantly upregulated in mice while LPI, LPI-O/P and PC-O/P are less expressed in human cortex. On the other hand, sphingolipid levels are considerably similar in both species. Conversely, SFT contribution seems to be higher in human than in murine cortex.

A closer look at the relative abundance of the individual molecular species shows that PC and PE contain longer fatty acids in mouse (nº of carbons >36) while species carrying short fatty acids are more abundant in human cortex. Also, as long as fatty acid chains tend to be polyunsaturated, a clearly higher abundance of PUFA-containing PC and PE is observed in mouse in comparison with human cortex, where MUFA/DUFA-containing species are predominant (Figure 7.**7A,B**).

Likewise, analysis of ether/vinyl ether lipid species, show similar results. PE-O/P's and PC-O/P containing long fatty acids (nº of carbons >36) seem to be more relevant in mice, while species containing shorter fatty acids (nº of carbons < 36) are more important in PC-O/P and PE-O/P in human renal cortex **(Figure 7.7C,D).**
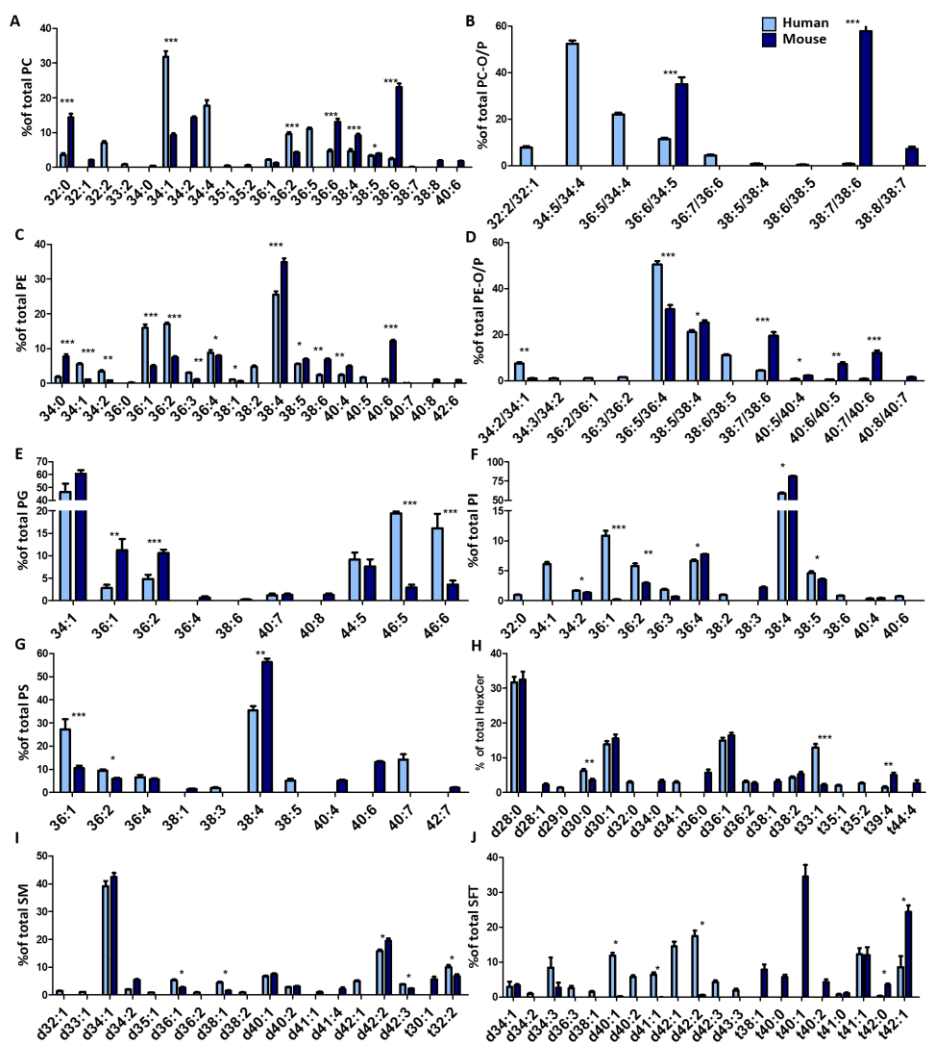
Figure 7.7. *Relative abundance in human vs murine cortex of individual molecular species belonging to **(A)** PC's, **(B)** PE's, **(C)** PC-O/P's **(D)** PE-O/P's, **(E)** PG's, **(F)** PI's, **(G)** PS's, **(H)** HexCer's, **(I)** SM's, **(J)** SFT's lipid families. Values are expressed as mean ± S.E.M (n=13 for both groups). Statistical analysis was assessed using T-test analysis. * = p-value<0.05; **= p-value<0.01; *** =p-value<0.001.*

PG family show the opposite trend: while the relative abundance of short chain- and MUFA/DUFA-containing species is higher in mice, PUFA-containing PG's are significantly upregulated in human cortex (**Figure 7.7E**).

In the case of PI's, the most stricking observation is the lower abundance detected of PI 36:1 in mice, while it is the second most abundant species in human renal cortex. For both models PI 38:4 is the main lipid specie although it is upregulated in mice in contrast with human samples **(Figure 7.7F)**. Moreover, as in the case of PC, PE, PC-O/P and PE-O/P lipid subclasses, the PI species containing short fatty acids seem to be more abundant in human than in mouse.

Finally, focusing on PS's, we can see again a clear difference between mouse and human: the species with longer fatty acids (total number of carbons > 36) are more abundant in the former, while those with shorter fatty acids are more prevalent in the latter in the length of the fatty acids of more abundant species, with the exception of 38:5 and 40:7 which were exclusively detected in human renal cortex (**Figure 7.7G**).

Following the same trend, sphingolipids also reveal noticeable differences concerning human and mice cortex*.* Although HexCer's, d28:0 is the most abundant species in both human and mouse, d30:0 and t33:1 are upregulated in human while d36:1 and t39:4 are more expressed in mouse (**Figure 7.7H**). Furthermore, in the case of SM's, d34:1, d42:2 and t33:1 are the predominant species not only in human but also in murine cortex. Additionally, the relative intensity of the species containing fatty acids with an even number of carbons is higher in mouse, whereas SM with odd number of unsaturations seem to be prevalent in human (**Figure 7.7I**). Finally, only six sulfatides were detected in both renal models and, as can be seen in **Figure 7.7J**, their distribution is considerably dissimilar in human and mouse: while SFT d43:3 and SFT t41:1 are more intense in human, SFT t42:0 and t42:1 predominant in mouse. It is also interesting the higher importance that d-type SFT have on human lipidome, while those species are replaced by SFT t species.

In summary, substantial differences were found between the lipidome of human and mouse renal cortex.

Lipid differences between human and murine renal glomeruli.
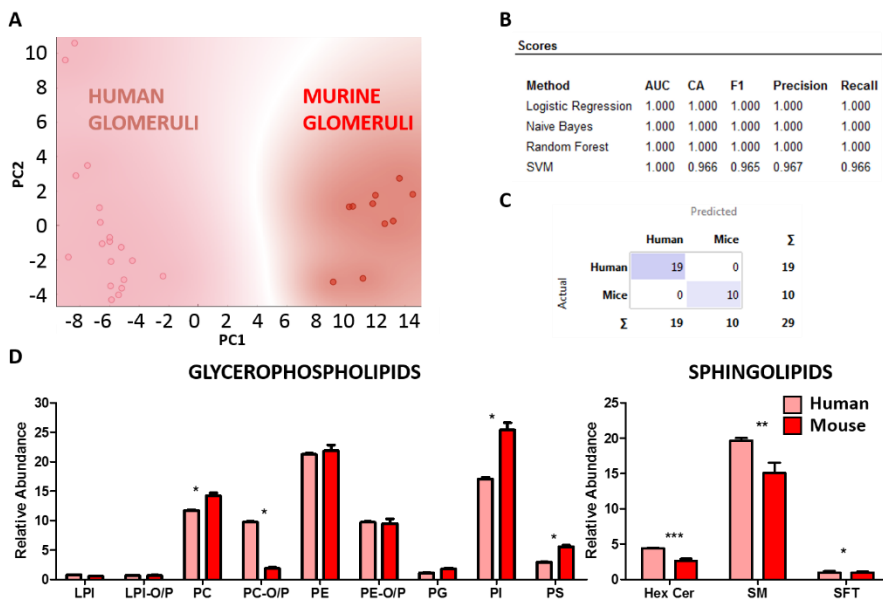
Figure 7.8. Comparison between the lipid profile of murine and human glomerulus *(A)* PCA analysis separates murine and human glomerulus samples, *(B)* summary of the classifier models results, *(C)* Random Forest's matrix of confusion, *(D)* relative abundance of the lipid families in murine and human renal glomeruli. Values are expressed as mean ± S.E.M (n=19 for human and n=10 for mice). Statistical analysis was assessed using T-test analysis. * = p-value<0.05; **= p-value<0.01; *** =p-value<0.001.Complete statistical results are compiled in **Table A.7.1.**

The same analysis was carried out for the IMS clusters corresponding to glomeruli. The perfect separation achieved by PC1 in the PCA analysis (**Figure 7.8A**) points to substantial differences in the lipid signature of both species. Further evidence comes from the excellent performance of the classification models teste, which achieve perfect classification almost in all cases (**Figure 7.8B**). To reinforce these results, the confusion matrix of the Random Forest classifier showed that all the samples were perfectly classified (**Figure 7.8C**).

As in the last section, the relative abundance of the different glycerophospholipids and sphingolipids subclasses were compared (**Figure 7.8D**). As can be observed, PC's, PI's and PS's relative intensity is bigger in glomeruli mice, while PC/O-P and HexCer lipid families are more abundant in human glomeruli lipid metabolism.

Detailed analysis of the individual lipid species shows also remarkable differences between mice and human glomeruli. In the context of PC and PE, short length fatty acid containing species are upregulated in human while there exist an increase in the relative intensity of the long-chain PC and PE species in mouse (**Figure 7.9A,B**).
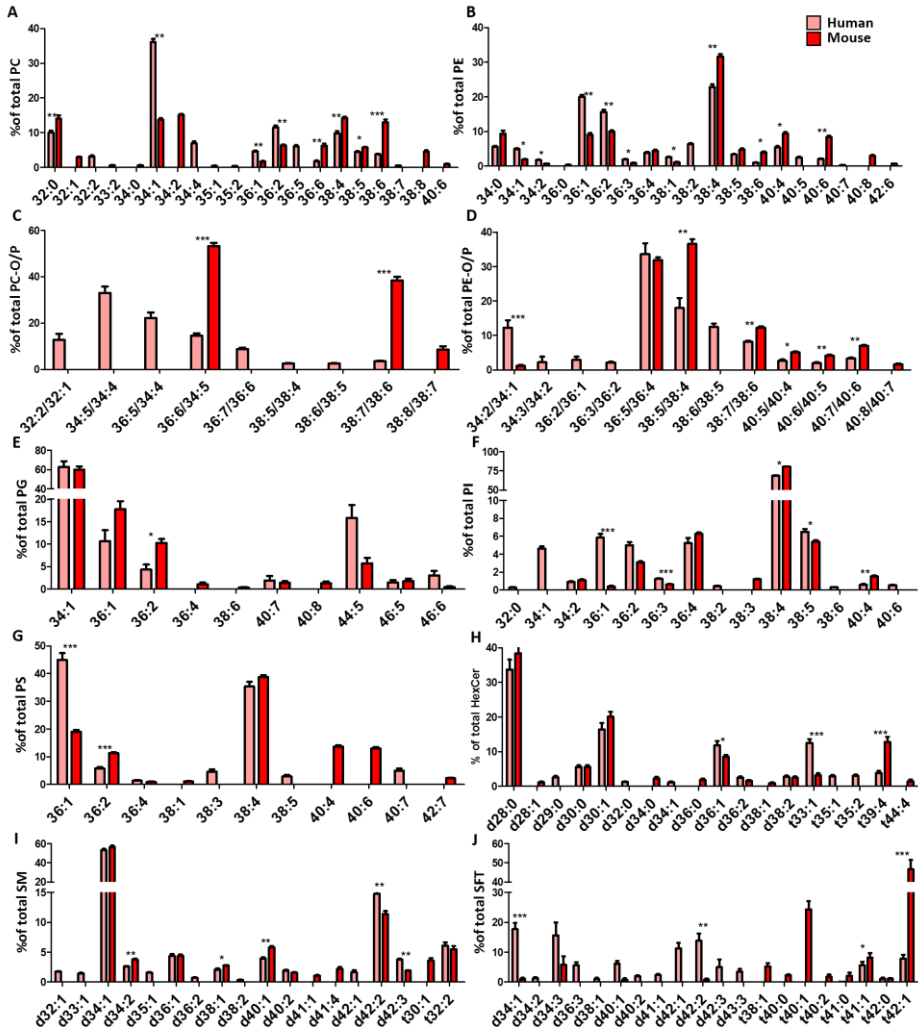
Figure 7.9. *Relative abundance of individual molecular species in glomerulus belonging to **(A)** PC's, **(B)** PE's, **(C)** PC-O/P's **(D)** PE-O/P's, **(E)** PG's, **(F)** PI's, **(G)** PS's, **(H)** HexCer's, **(I)** SM's, **(J)** SFT's. Values are expressed as mean ± S.E.M (n = 19 for human and n = 10 for mouse). Statistical analysis was assessed using T-test analysis. * = p-value<0.05; **= p-value<0.01; *** =p-value<0.001.*

Focusing on PC-O/P and PE-O/P species (**Figure 7.9C,D**), similar conclusions were achieved: there is clear upregulation of PUFA–containing species in mouse, whilst MUFA- and DUFA-containing PE-O/'s and PC-O/P's are predominant in human glomerulus.

On the other hand, PG's comparison shows no remarkable differences between mice and human at expenses of PG 36:2 which is overexpressed in mice (**Figure 7.9E**).

As for PI lipid family (**Figure 7.9F**), the significant differences are a substantial upregulation of the species containing short-length fatty acids in human, at expenses of a decrease in AA containing species (PI 38:4 and PI 40:4).

Additionally, in the case of PS, the most stricking observation is the noticeable upregulation of the species containing an odd number of insaturations in human while in mice, species with an even number of insaturations seem to have more importance, specially PS 40:4 and PS 40:6, which were undetectable in human (**Figure 7.9G**).

In the context of glomeruli sphingolipids, some differences were also found. Although the vast majority of the HexCer detected show similar levels in both species, HexCer d36:1 and HexCer t33:1 shows a significant upregulation in human glomerulus, while HexCer t39:4 seem to be more abundant in mouse (**Figure 7.9H**).

Besides, in terms of SM's, SM d34:1 is the main SM molecular specie in human as well as in mouse, accounting in both species for almost the 60% of the SMs detected. However, there are still some significant differences. SMs containing short length MUFAS (SM d32:1 d33:1 and d35:1) were exclusively found in human and a downregulation of SM d42:2 and SM d42:3 was observed in mouse at expenses of an increase in SM d34:2, d38:1 and d40:1 relative abundance (**Figure 7.9I**).

Finally, there is a clear increase of SFT t in mouse, while SFT-d are more relevant in human, following the trend observed in human (**Figure 7.9J**).

Lipid differences between human and murine renal medulla

We will end the comparative analysis of the lipid expression between human and mouse kidney with the examination of the medullary lipidome (**Figure 7.10**). Following the trend observed in previous sections, there are clear differences between the lipidome of human and mouse medulla. This leads to a perfect separation of the samples in a PCA analysis, using the first PC. In good agreement, all the classification methods tested offer outstanding performance, with Random Forest being the only one below 100% of classification power.

A close look at the relative abundance of the lipid families shows that the main differences were found between PC-O/P, PI and SFT.
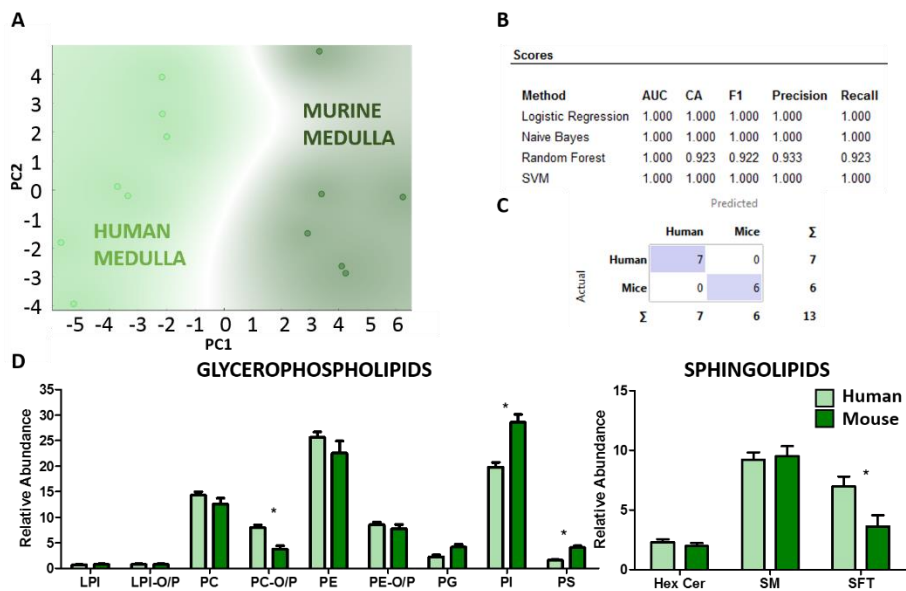
Figure 7.10. *Lipidome comparison between murine and human renal medulla **(A)** PCA analysis distinguishing murine and human medulla, **(B)** summary of the classifier models results, **(C)** Logistic Regression's matrix of confusion, **(D)** Bar charts of the relative abundance variation of the lipid families in murine and human renal medulla. Values are expressed as mean ± S.E.M (n=7 for human and n=6 for mice). Statistical analysis was assessed using T-test analysis. * = p-value<0.05; **= p-value<0.01; *** =p-value<0.001.Cmoplete statistical results are compiled in **Table A.7.1.***

Strikingly, the analysis of the expression of individual species among each family, shows the existence of only subtle differences (**Figure 7.11**), and they were mainly found in PC and PE. These results point to a separation based on multiple variables and to a more conserved lipidome between the two species.
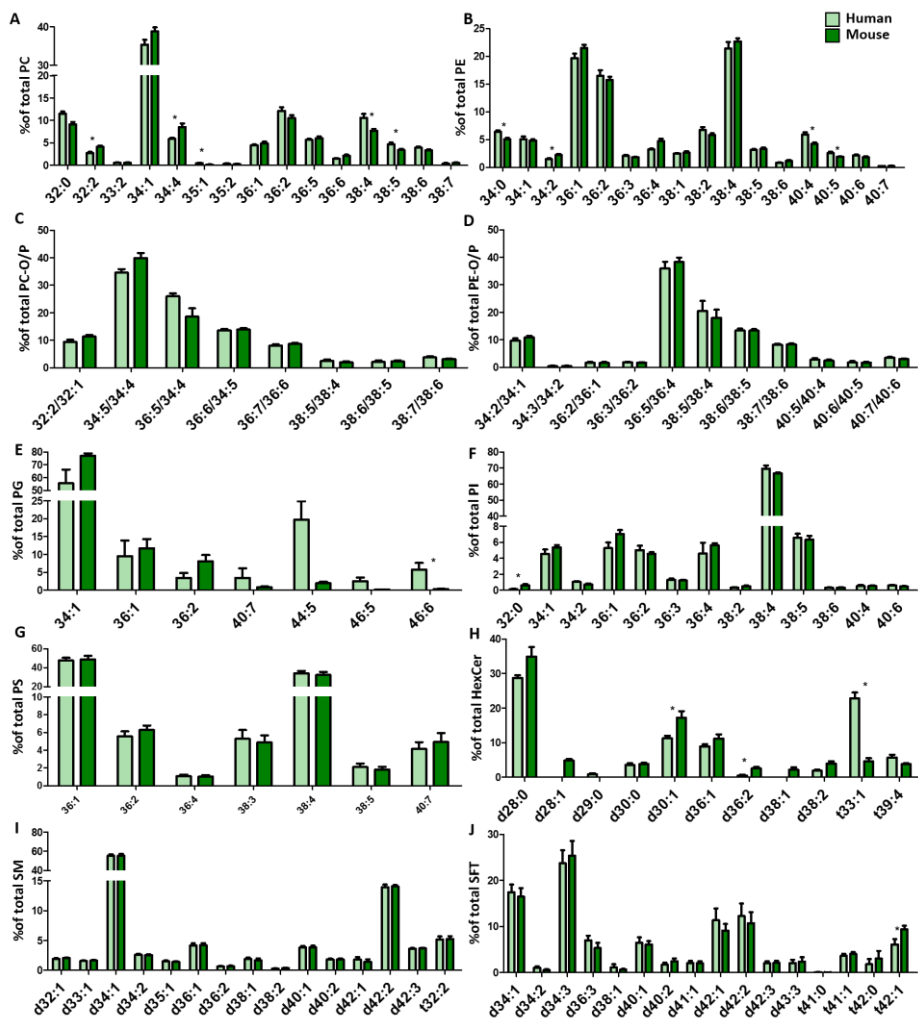
Figure 7.11. *Human vs murine medulla relative abundance of individual molecular species belonging **(A)** PC's, **(B)** PE's, **(C)** PC-O/P's **(D)** PE-O/P's, **(E)** PG's, **(F)** PI's, **(G)** PS's, **(H)** HexCer's, **(I)** SM's, **(J)** SFT's lipid family. Values are expressed as mean ± S.E.M (n=7 for human and n=6 for mice). Statistical analysis was assessed using T-test analysis. * = p-value<0.05; **= p-value<0.01; *** =p-value<0.001.*

7.5   Discussion

Animal models are widely used to investigate and understand the physiopathology of diseases and to facilitate the development of treatments. Lipidomics helps to select relevant lipid biomarkers to target lipid disturbances and also to better understand the related metabolism. In the present study, we showed that mouse and human kidney,

present important differences in their lipidome. This finding should alert researchers about the divergence in the metabolism of both species. Several renal pathologies are region-specific, such as glomerulonephritis, acute kidney injury or medullary cystic kidney disease, which originate in glomeruli, cortex and medulla respectively[12-14]. Each histologic section presents its own differences between both species, from a lipidomic point of view. These differences were highlighted by the outstanding performance of the classification models, which did not encounter any problem to distinguish between human and mouse samples.

The most evident difference found is the number of lipids detected: 128 and 112 in human and murine kidney respectively, 50 of which were only detected in human and 34 were exclusively found in mice. The remaining 78 species were detected in both tissues (

Figure 7.3. Identified lipids in human and mouse kidney. From left to right, percentage of each lipid class in human and murine kidney and Venn diagram of the total of lipid species detected.*)*. Additionally, some low-abundant lipid subclasses were only identified in mice, such as LPS's, LSFT's and PI-O/P's. This is probably related to the physiological dissimilarities between renal tissues of both species. For example, compared to a mouse, a human has nearly 100 times more nephrons due to a gene called SIX1, which is expressed only in humans[15].

Despite the existence of clear differences between the two species, still the classification models show that the lipidome of each histologic area is more similar to their counterpart in the other species than to other histologic areas of the kidney of the same species. This is clearly shown in **Figure 7.B,C**. Human and murine glomerulus lipid profile showed a well-defined cluster which enables to perfectly discriminate it from cortex and medulla. Several significant lipid differences allow for clearly discerning the three histological regions, such as the increasing HexCer's and SM's gradient and the decreasing gradient of SFT's observed from cortex to medulla. Moreover, higher levels of SM's, specifically SM d34:1, is a noticeable glomeruli biomarker for both animal models[16].

To the best of our knowledge, only two studies have investigated the differences between the lipidome of healthy human and animal species (rat, mouse and rabbit) kidney including data from glycerophospholipids (LPC, LPE, PC, PE, PI), sphingolipids (SM, Cer, SFT), glycerolipids (DG) and sterol lipids (CE)[17, 18]. These two studies showed lower sphingolipid abundances as well as higher unsaturated PC levels in rodents plasma in comparison to humans. In line with these results, our data showed that PC levels were not only overall higher in mice structures but also species carrying longer and PUFA (>C36, >3 double bonds) tended to be more abundant in mice than in

humans. Similar observations were made in this work in the three histological regions: cortex, glomeruli and medulla (**Figure 7.12**).

Similar results were obtain for the main glycerophospholipid subclasses, whose long fatty acid-containing species have a higher intensity in mouse. However, for PE, PE-O/P, PC-O/P, PI and PS species, this variation is not visible in medullary areas (**Figure 7.12**). This confirms kidney cortex and glomerulus present the bigger differences in lipid expression between both species. Interestingly, the PG lipid family seems to exhibit an opposite trend, compared to the rest of the glycerophospholipids: while the observed tendency is the upregulation of the long fatty acid-containing species in mice, shorter PG's were overexpressed in rodent kidney, specifically in cortex and medulla (**Figure 7.12**).
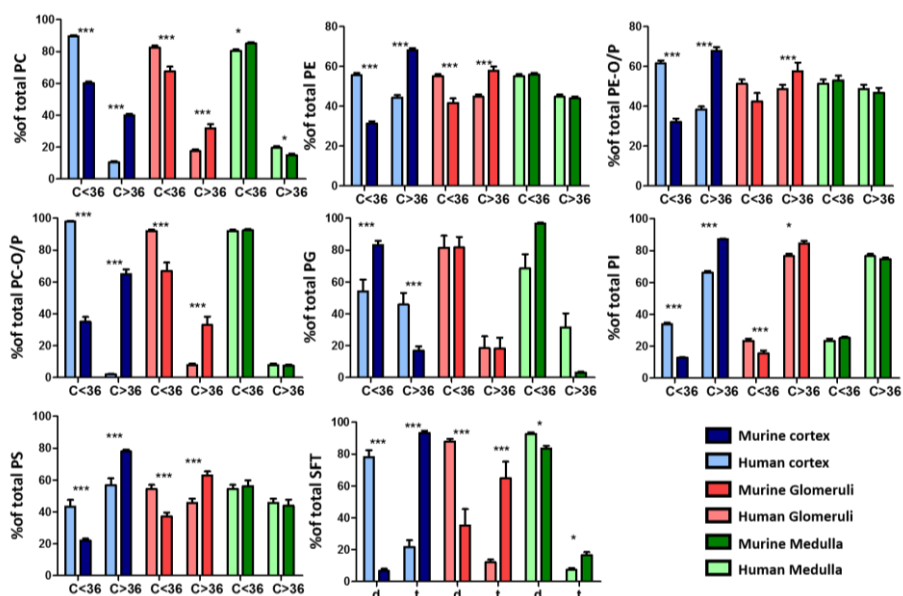
Figure 7.12. Lipidome comparison between cortical, glomerular and medullary lipid subgroups from human and murine samples. The bar charts are showing the summation of the intensities of the molecular lipid species containing short fatty acids(C<36) or long ones(C>36) Exceptionally, the last graph shows the differential distribution of d-SFT (d) and t-SFT(t) in the three histological renal regions from human and mice.

It is worthy of mention that overall levels of PC-O/P's are significantly downregulated in the three murine historical regions. Such reduction is accompanied by a global increase in PS levels. Additionally, PC relative abundance is higher in rodent

cortex and glomeruli while PI levels were higher in glomeruli and medulla of mouse (**Figure 7.5D**).

Likewise, sphingolipid levels were significantly lower in rodent than in humans[17, 18]. Specifically, our results showed a significant decrease in the overall glomerular HexCer level as well as a marked downregulation for SFT levels in cortex and medulla. Besides, beyond punctual differences, individual HexCer and SM species are very similar in renal structures of both species. Among them, the relative concentration of SM d34:1, which is a relevant glomeruli biomarker[16] and SM d38:2, which was proposed as a precursor marker for cardiovascular diseease[19], remain invariable between species.

Finally, interesting differences were found in SFT lipid class: t-type SFT species are predominant in murine renal samples while d-type SFT's are more abundant in human structures. This trend was observed for the three histological region (**Figure 7.12**).

7.6   Conclusions

To the best of our knowledge, this is the first study that makes a detailed comparison between lipid expression of three histologic areas of mouse and human kidney, using MALDI-IMS. The results demonstrate that all three regions present characteristic lipid profiles, which maintain some similarities between both species. The most relevant differences in lipid profiles observed between the two species are related to number of insaturations and length of the fatty acids. The present study sets the foundations for future studies on the metabolic differences between both species.

1. Cheval, L., Pierrat, F., Rajerison, R., Piquemal, D. & Doucet, A. Of mice and men: divergence of gene expression patterns in kidney. *PloS one* **7**, e46876 (2012).

2. Bronson, S. K. & Smithies, O. Altering mice by homologous recombination using embryonic stem cells. *J. Biol. Chem.* **269**, 27155-27158 (1994).

3. Lorenz, J. N. *et al*. Impaired renal NaCl absorption in mice lacking the ROMK potassium channel, a model for type II Bartter's syndrome. *J. Biol. Chem.* **277**, 37871-37880 (2002).

4. Nomura, N. *et al*. Generation and analyses of R8L bartttin knockin mouse. *American Journal of Physiology-Renal Physiology* **301**, F297-F307 (2011).

5. Schultheis, P. J. *et al*. Phenotype resembling Gitelman's syndrome in mice lacking the apical Na -Cl– cotransporter of the distal convoluted tubule. *J. Biol. Chem.* **273**, 29150-29155 (1998).

6. Khrameeva, E., Kurochkin, I., Bozek, K., Giavalisco, P. & Khaitovich, P. Lipidome evolution in mammalian tissues. *Mol. Biol. Evol.* **35**, 1947-1957 (2018).

7. Yang, H., Zuo, Y. & Fogo, A. B. Models of chronic kidney disease. *Drug Discovery Today: Disease Models* **7**, 13-19 (2010).

8. Fernández, R., Garate, J., Martín-Saiz, L., Galetich, I. & Fernández, J. A. Matrix Sublimation Device for MALDI mass spectrometry imaging. *Anal. Chem.* **91**, 803-807 (2018).

9. Fernández, R. *et al*. Microarray and Mass Spectrometry-Based Methodology for Lipid Profiling of Tissues and Cell Cultures. *Anal. Chem.* **91**, 15967-15973 (2019).

10. Corportation, I. IBM SPSS Statistics for Windows (Version 25.0 Armonk). *NY: IBM Corp* (2017).

11. Demšar, J. *et al*. Orange: data mining toolbox in Python. *the Journal of machine Learning research* **14**, 2349-2353 (2013).

12. Bellomo, R., Kellum, J. A. & Ronco, C. Acute kidney injury. *The Lancet* **380**, 756-766 (2012).

13. Chadban, S. J. & Atkins, R. C. Glomerulonephritis. *The Lancet* **365**, 1797-1806 (2005).

14. Kirby, A. *et al*. Mutations causing medullary cystic kidney disease type 1 lie in a large VNTR in MUC1 missed by massively parallel sequencing. *Nat. Genet.* **45**, 299-303 (2013).

15. O'Brien, L. L. *et al*. Differential regulation of mouse and human nephron progenitors by the Six family of transcriptional regulators. *Development* **143**, 595-608 (2016).

16. Abbas, I. *et al*. Kidney lipidomics by mass spectrometry imaging: A focus on the glomerulus. *International journal of molecular sciences* **20**, 1623 (2019).

17. Ishikawa, M. *et al*. Comparison of circulating lipid profiles between fasting humans and three animal species used in preclinical studies: mice, rats and rabbits. *Lipids in health and disease* **14**, 1-6 (2015).

18. Kaabia, Z. *et al*. Plasma lipidomic analysis reveals strong similarities between lipid fingerprints in human, hamster and mouse compared to other animal species. *Scientific reports* **8**, 1-9 (2018).

19. Fernandez, C. *et al*. Plasma lipid composition and risk of developing cardiovascular disease. *PloS one* **8**, e71846 (2013).

Chapter 8

Lipidomic study in Clear Cell Renal Cell Carcinoma by mass spectrometry analysis.

Renal cell carcinoma (rCC) is the most common histological type of adult kidney cancer. In this study, we obtained lipidomic profiles of clear cell RCC (ccRCC), a major RCC subtype, by performing a lipidomic analysis of samples of cancerous tissue and the surrounding normal tissue analyzed by two complementary techniques uHPLC-ESI and MALDI-IMS.

Additionally, the results obtained from these two techniques were compared in order to evaluate whether the same conclusions were reached and to test the reliability of the non-quantitative values provided by MALDI-IMS.

8.1 Introduction

Renal cell carcinoma (RCC) accounts for about 2–3% of all malignant diseases in adults. GLOBOCAN 2020 estimates of worldwide cancer incidence and mortality were 431.288 new cases and 179.368 deaths for kidney cancer[1, 2]. Recent estimates have calculated that, in 2040, 666.000 new cases will be diagnosed and 301.000 patients will die of this tumor[2]. Specifically, clear cell renal cell carcinoma (ccRCC) represents the most common subtype of RCC (65%–70%) and is highly variable in prognosis, biological behavior, and response to therapies[3-6]. Genome-wide studies have confirmed significant genetic diversity among ccRCC and found several important driver mutations and multiple passenger changes in RCCs, which partially explain the heterogeneous clinical outcomes of patients with similar histopathological type[7-10]. In addition to inter-tumor heterogeneity, intra-tumor heterogeneity with diverse genetic subclones within a single tumor has been gradually recognized in ccRCC[11]. Sporadic ccRCC frequently carries an inactivating mutation of the von Hippel-Lindau (VHL) tumor suppressor gene on chromosome 3p, with subsequent upregulation of the HIF/VEGF pathway, leading to intense tumor angiogenesis[12-14]. The Tumor Cancer Genome Atlas (TCGA) analysis of gene and protein expression has confirmed major alterations in glucose, amino acid, and lipid metabolism in ccRCC, characterized histologically by prominent storage of glycogen and lipids[15, 16].

Altogether, these observations strongly suggest that reprogrammed lipid metabolism in ccRCC may provide not only biomarkers of oncological aggression, but perhaps therapeutic targets and insights in tumor heterogeneity as well. Thus, one of the most used technique to study the lipidomics is mass spectrometry. Several studies have reported lipid characterization of ccRCC samples by using uHPLC[17, 18] and imaging techniques[19-21] couple with mass spectrometry analysis. Here we present an in depth lipid description combining uHPLC-ESI and MALDI-IMS, trying to integrate the spatial information provided by MALDI-IMS with the precise lipid concentration obtained from the quantitative analysis by uHPLC. This approach could validate the non-quantitative MALDI-IMS approach reinforcing this and further studies.

8.2 Objectives

This chapter is divided in three parts:

1. ccRCC lipid characterization by uHPLC-ESI. In this first section, we try to explore the lipid alteration occasioned by ccRCC as well as the lipid interpatient heterogeinity.

2. ccRCC lipid characterization by MALDI-IMS. As ccRCC is one of the most aggressive, complex and heterogeneous cancers, the second objective of this chapter is to elucidate some common patterns of lipid distribution over ccRCC samples.

3. Comparison of uHPLC and MALDI-IMS lipid results in adjacent normal renal tissue and in ccRCC sections.

8.3 Experimental section

Human sample collection

Kidney samples were obtained from 40 renal cancer patients from the University Hospital of Basurto (Bilbao, Spain) and 9 from University Hospital of Galdakao (Galdakao, Spain). All patients were informed about the potential use for research of their surgically resected tissues, and manifested their consent by signing a specific document approved by the Ethical and Scientific Committees of the Basque Country Public Health System (PI+CES-BIOEF 2018-04).

From each removed kidney, adjacent normal tissue was separated from the ccRCC portion. A certain part of each normal and ccRCC biopsy was stored fresh frozen (-80ºC) until lipid extract preparation. The remaining part was used to obtain contiguous sections of 15 µm to be analyzed by MALDI-IMS. In this way, sections and tissue from normal and ccRCC biopsies belonging to the same patients were analyzed by MALDI-IMS and uHPLC respectively.

uHPLC

Lipid extracts preparation and uHPLC experimental section are extensively described in Chapter 3. Briefly, 80 lipid extracts from human renal tissue were reconstituted in 150 µL of C_7H_8: MeOH (1: 9, v / v) and transferred to maximum recovery chromatography vials These extracts were injected into the uHPLC column coupled to the QExactive HF-X mass spectrometer. First, the individual data files of the MS/MS spectra of the lipid precursor ion were searched and MS/MS fragment ions were then predicted within a tolerance of ± 5 ppm.

The data obtained were analyzed using the LipidSearch software version 4.2.2 and compared with the standards Splash Lipidomix, Cer/Sph mixture I, Cardiolipin Mix I, 24:0(d4) L-carnitine, D18:1/12:0 monosulfogalactosyl (β) ceramide (NH_4 Salt) and Oleic acid (d9) (Avanti Polar Lipids, Inc.), which were analyzed in the same way than the lipid extracts.

For the statistical analysis, SPSS Statistics 17.0 (IBM, Armonk, NY, USA) and Orange Biolab (Ljubljana, Slovenia) software were used.

Imaging and data analysis

A detailed description of MALDI-IMS sample preparation and equipment employed can be found in Chapter 3. Data were acquired in negative-ion mode with 25 μm spatial resolution and mass resolution of 60.000 FWHM at m/z = 400, and a laser energy of 20-30 μJ/pulse. Staining with H&E (Sigma Aldrich Química, Madrid, Spain) was carried out for all biopsies once MALDI-IMS experiments were completed and matrix removed.

Data analysis was carried out with in-house made software built in MatLab (MathWorks, Natick, USA) using the import parameters described in Chapter 3. For clustering, an in-house algorithm was used. IBM SPSS Statistics for Windows (Version 23.0; IBM, Chicago, IL, USA) was used for Levene-test, one-way ANOVA and Tukey/Games-Howell post multiple comparison. Levene-test determines the homogeneity of the variables (H_0 = groups have equivalent variances) in order to choose the correct post hoc method: Bonferroni if Levene $p \geq 0.05$ and Games-Howell if Levene $p \leq 0.05$. Orange (Bioingormatics Lab, University of Ljubljana, Slovenia)[1] was used for PCA and for the development of classification model with different algorithms.

8.4   Results

uHPLC

<u>Lipid assignment and stability of the system</u>

301 molecular lipid species were detected and identified by uHPLC-Q-TOF from normal adjacent and ccRCC samples; 344 were detected in negative ion mode, 547 in positive and 155 were detected in both ionization modes. Consequently, 736 different lipid species were found in renal tissue (**Figure 8.1**).
The stability of the system was checked during the whole acquisition sequence to correct from possible variations and experimental fluctuations. For that, the total area of the detected peaks in the QC samples and the m/z and retention time (Rt) of one lipid from each polarity mode (PI 38:4 and PC 34:2 respectively) extracted from the QC samples were monitored. As can be appreciated in **Figure 8.2**, the values of m/z and Rt for the selected lipids as well as the total area remained almost unchanged throughout the sequence, confirming the appropriate stability of the system.
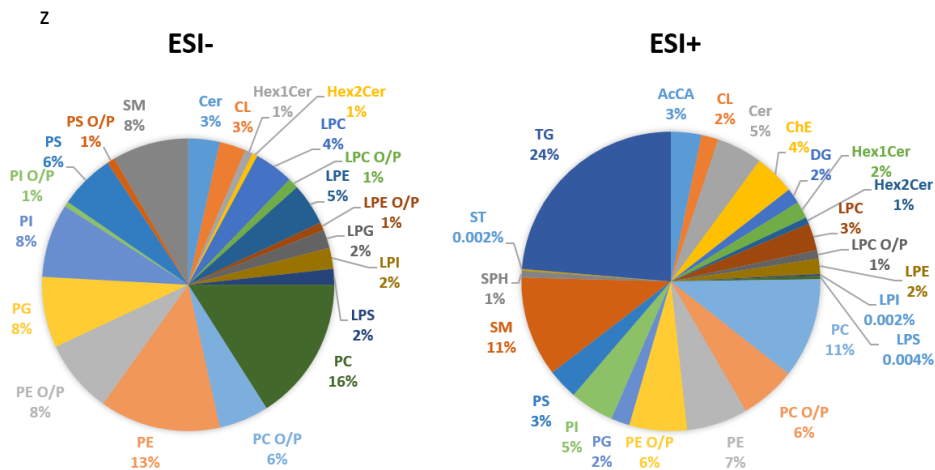
Figure 8.1. *Lipid families identified in negative- and positive-ion mode in renal tissue and their corresponding percentage to the total lipids found. All the lipid families were quantified.*
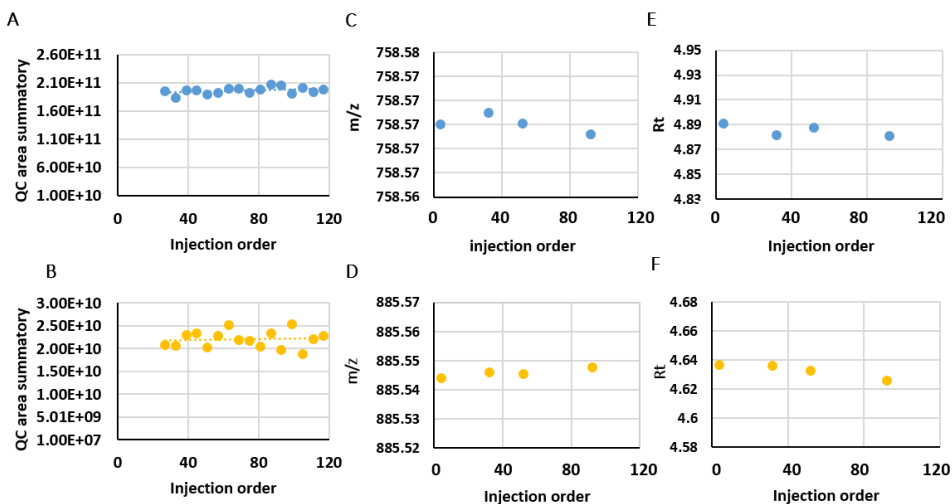
Figure 8.2. *System stability. (**A**) QCsample area summation monitoring in positive-ion mode. (**B**) QCsample area summation monitoring in negative-ion mode. (**C**) Monitoring of the PC (16:0/18:2)-H$^+$ m/z (758.5715). (**D**) Monitoring of the PI (18:0/20:4)-H$^-$ m/z (885.5499). (**E**) PC (16:0/18:2)-H]$^+$ Rt monitoring. (**F**) PI (18:0/20:4)-H]$^-$ Rt monitoring.*

Unraveling lipid interpatient heterogeneity

ccRCC has proved to be one of the most heterogeneous cancer. A landmark paper by Gerlinger et al. demonstrated clear cell renal cell carcinoma as a tumor with marked genetic intratumor and intermetastasis heterogeneity[22]. In this section, we will explore the interpatient heterogeneity in terms of lipids comparing the dispersion of the lipid detected in the adjacent normal and ccRCC renal tissue.

With this purpose, the coefficient of variation (CV) and the Fisher-test was calculated for each individual lipid specie detected in ESI+ and ESI- from normal adjacent and ccRCC samples. The CV, also known as relative standard deviation (RSD), is a standardized measure of dispersion of a probability distribution and it is widely used to express the precision and repeatability of an assay. It is often expressed as a percentage, and is defined as the ratio of the standard deviation (σ) to the mean (μ) (**Equation 8.1**).

$$CV = \frac{\sigma}{\mu}$$

Equation 8.1. Coefficient of variation.

In the case of Fisher-test, it is used to test whether two populations have the same variance. The null hypothesis (H_0) requires that the variance within each population is equal. Therefore, by calculating these parameters, interesting insight about the samples heterogeneity will be provide[23].

As can be seen in Figure 8.**3A,B,** the dispersion of the PI 40:5 and TG 52:2 detected in negative- and positive-ion mode respectively seems to be higher in ccRCC samples (dark blue) than in healthy samples (light blue). This fact is supported by the results of the variance and CV analysis (Figure 8.**3C**), which in both cases confirmed a higher interpatient heterogeneity for these two molecular species in ccRCC samples.

The CV and the variance were obtained for all the individual lipid species and, in agreement with PI 40:6 and TG 52:2, the results suggested that tumoral samples are more dispersed than healthy ones. For example, average CV for healthy samples was 75.85% and 98.88% in positive- and negative-ion mode respectively, while for ccRCC samples, the average CV was 104.58% and 139.57% respectively confirming that for both ionization modes, the whole lipid heterogeneity along the samples is significantly higher in tumoral biopsies (Figure 8.**3D**).

Furthermore, as displayed in Figure 8.**3E,** Fisher-test showed that the 58% and the 62% lipid species detected in ESI- and ESI+ respectively were heteroscedastic variables comparing healthy and ccRCC lipid species' variance. This means that variances from lipid species belonging to healthy samples are significantly different from ccRCC lipid

variances. Additionally, the 90% and 92% of these heteroscedastic variables show a higher variance in ccRCC samples. Consequently, taking all the above information into account, it is clear that tumoral samples present a higher interpatient heterogeneity.
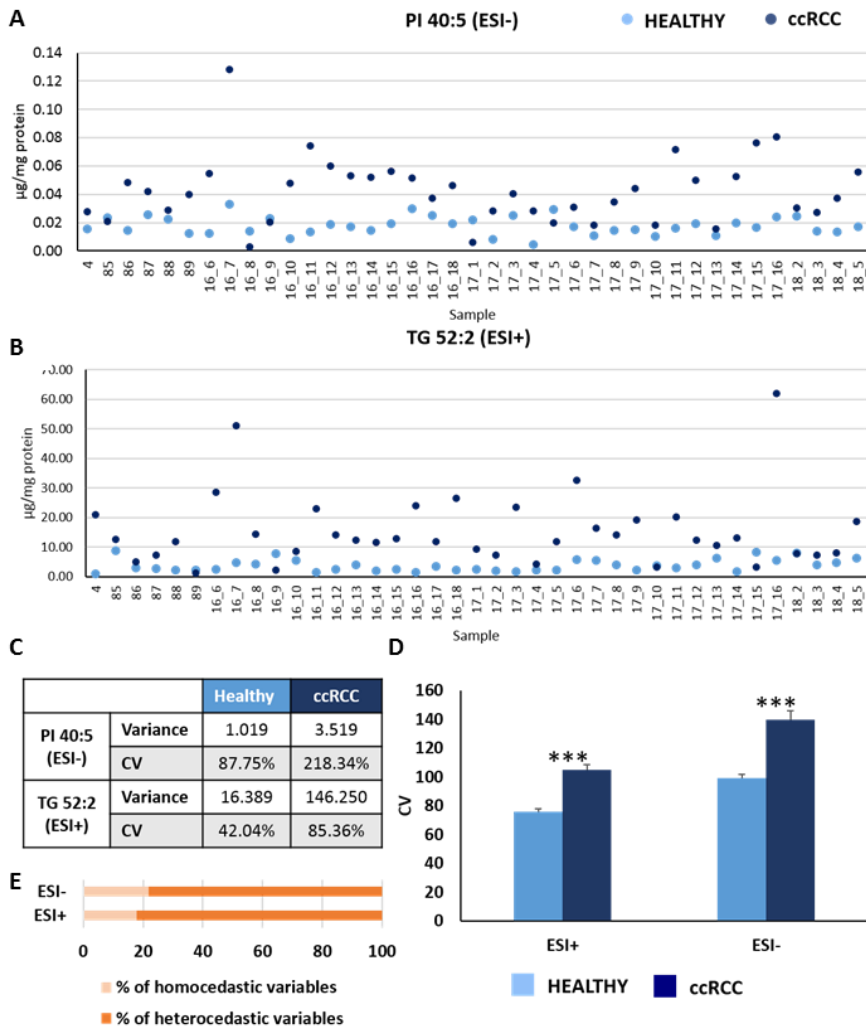
Figure 8.3. *Lipid interpatient heterogeneity analysis in healthy and ccRCC samples.* **(A)** *PI 40:5 µg /mg protein detected in the different healthy (light blue) and ccRCC (dark blue) samples.* **(B)** *TG 52:2 µg /mg protein detected in the different healthy (light blue) and ccRCC (dark blue) samples.* **(C)** *Variance and CV of PI 40:5 ad TG 52:2 in healthy and ccRCC samples.* **(D)** *Average CV in healthy and ccRCC samples for both ionization modes.* **(E)** *% of homoscedastic and heteroscedastic variables for ESI- and ESI+ lipid profile detected in healthy and ccRCC samples. Heteroscedasticity of each variable was determined by the Fisher-test, which compares the variance of each lipid specie in healthy and ccRCC samples.*

Comparison between Healthy and ccRCC lipididome

To visualize trends and clusters of data, a non-supervised PCA was carried out. For both ESI- and ESI+ a neat separation between healthy and ccRCC samples was observed (**Figure 8.4A, Figure 8.5A**).
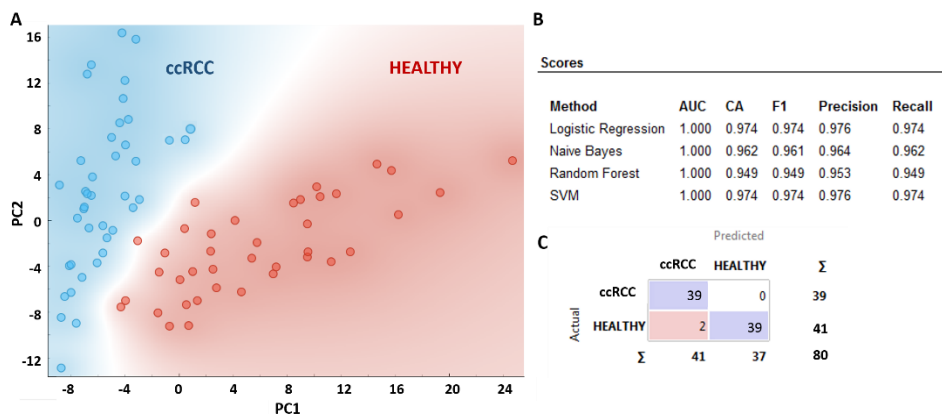
Figure 8.4. *Non-supervised multivariate analysis comparing healthy and ccRCC lipidome obtained from ESI-.* **(A)** *Scores plot of the first two main components of the PCA model,* **(B)** *Classification model's scores,* **(C)** *Matrix of confusion of the Logistic Regression model.*
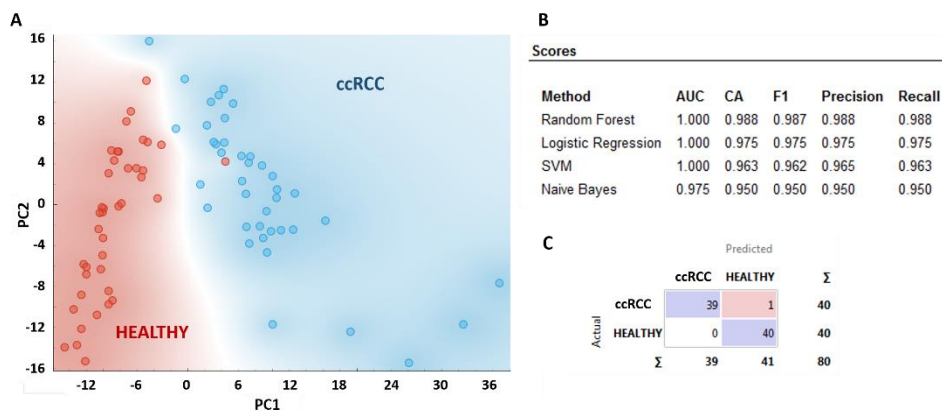
Figure 8.5. *Non-supervised multivariate analysis comparing healthy and ccRCC lipidome obtained from ESI+.* **(A)** *Score plot of the first two main components of the PCA model,* **(B)** *Classification model's scores,* **(C)** *Matrix of confusion of Random Forest.*

Four classification models were tested in the data sets, giving all of them excellent results. For ESI-, the model that performed the best was Logistic Regression with an AUC of 1.00, a classification accuracy of 0.974, a precision of 0.976 and a recall of 0.974 (**Figure 8.4B**). On the other hand, for ESI+, Random forest model yielded the best results with an AUC of 1.00 and a classification accuracy, a precision and a recall of 0.988 (**Figure 8.5B**). Finally, as can be appreciated in the confusion matrixes, only two samples and one sample were not correctly classified for the model in ESI- and ESI+ respectively (**Figure 8.4C**, **Figure 8.5C),** demonstrating that the differences between healthy and ccRCC renal lipid profiles are statistically significant. Only one sample was considered as an outlier, so this sample was removed from further analysis.

In order to visualize the changes in the different lipid classes occasioned in the context of ccRCC, the summation of the intensities of the lipid species from each class was calculated. Then, a T-test was performed to identify significant variations in the lipid classes. A different t-Test analysis was used, depending on the homoscedasticity of each variable. Homoscedasticity was verified using the *Levene*-test, considering that the characteristics with p values <0.05 reject the null hypothesis - H_0 = both groups have equivalent variances - and therefore do not have equivalent variances.
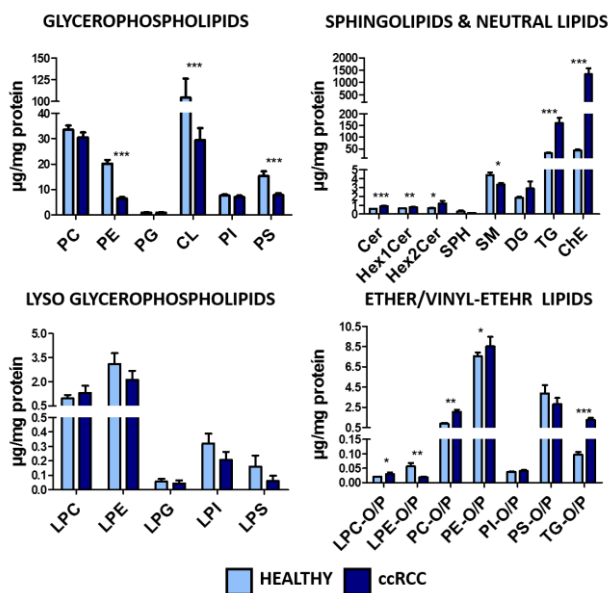
Figure 8.6. *Comparison of the abundance of the main lipid classes between healthy and ccRCC renal samples. Values are expressed as mean ± SEM (n=40 for both groups). Statistical analysis was assessed using T-test analysis. * = p-value<0.05; **= p-value<0.01; *** =p-value<0.001*

In the case of glycerophospholipids classes, PE, CL and PS showed a significant downregulation in ccRCC samples. However, the differences in sphingolipids and neutral lipids; Cer, Hex1Cer and Hex2Cer, TG and ChE were larger, being these lipid classes significantly upregulated while SM was reduced in ccRCC. No significant differences were observed in lyso-glycerophospholipids classes but regarding ether/vinyl ether lipid classes, LPC-O/P, PC-O/P, PE-O/P and TG-O/P are more abundant in cancerous tissue while LPE e concentration is higher in healthy kidney (**Figure 8.6**).

Detailed analysis of lipid signature in healthy vs ccRCC shows that 168 and 387 individual lipid species in ESI- and ESI+ respectively, exhibited statistically significant differences (T-test p-value<0.05).

As regards PE's, the abundance of 80% of the molecular species was significantly modified in ccRCC. All of them are clearly downregulated in tumoral tissue with the exception of PE 16:0/22:4, which is overexpressed in ccRCC sections. It is worth stressing that the most abundant PE species in both healthy and ccRCC tissue was PE 18:0 /20:4, whose concentration in healthy samples was multiplied by 2.6 in ccRCC samples (**Figure 8.7**).
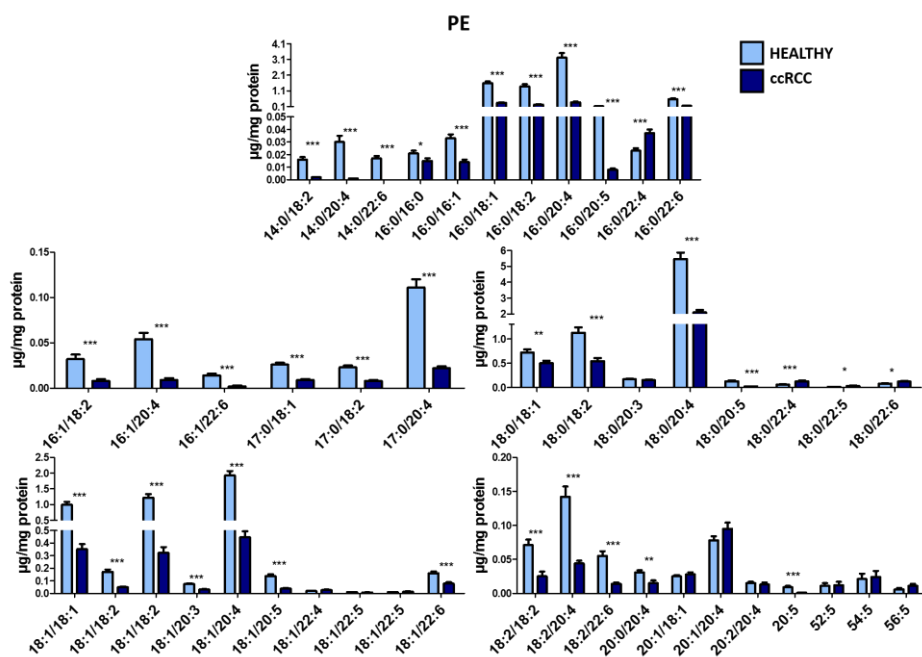
Figure 8.7. *Comparison between the concentration of the individual PE species between healthy and ccRCC renal samples. Values are expressed as mean ± SEM (n=40 for both groups). Statistical analysis was assessed using T-test analysis. * = p-value<0.05; **= p-value<0.01; *** =p-value<0.001.*

Conversely, Cardiolipins (CL) and PS´s showed a significant decrease in tumoral samples. The 80% of the detected CL's experiences substantial changes in renal cancer, and all of them were downregulated in comparison with healthy sections. Interestingly, CL 18:2/18:2/18:2 was the most abundant CL and its concentration in ccRCC was 6.74 times lower than in healthy kidney. Additionally, in the case of PS's, all the significantly modified species (51%) showed a notable decrease in ccRCC with the exception of PS (18:0/18:2) and PS (18:0/22:5), which are less abundant in healthy tissue (**Figure 8.8**). However, no remarkable differences were observed in neither PC, PG nor in PI lipid classes with the exception of punctual changes.
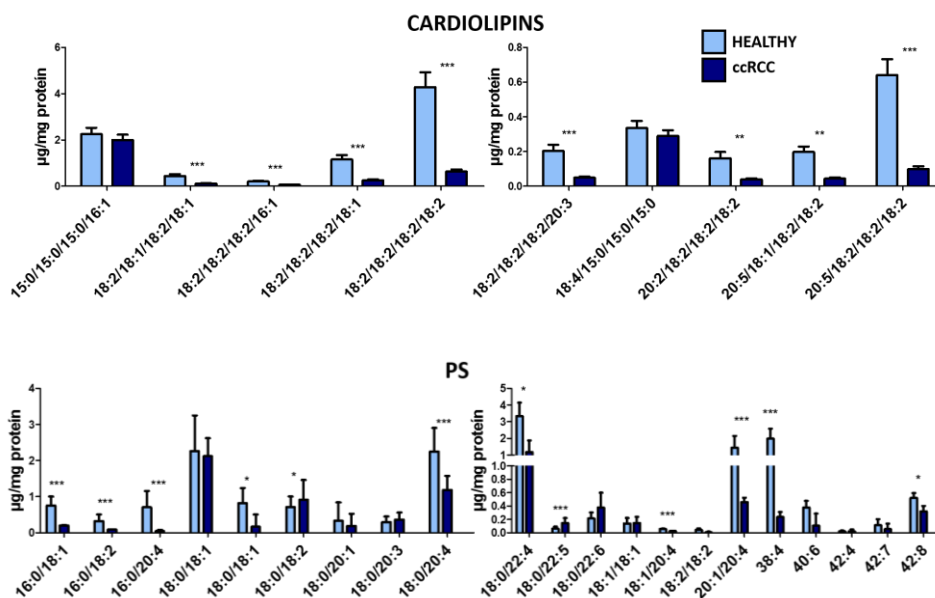
Figure 8.8. *Comparison between the concentration of the individual Cardiolipins (CL) and phosphatidylserines (PS) species between healthy and ccRCC renal samples. Values are expressed as mean ± SEM (n=40 for both groups). Statistical analysis was assessed using T-test analysis. * = p-value<0.05; **= p-value<0.01; *** =p-value<0.001.*

Moreover, focusing on sphingolipids, some interesting differences in Ceramides, Hexocyl ceramides and Sphingomyelins were observed (**Figure 8.9**). As regards individual molecular species, the abundance of 73.2% of the detected ceramide species was significantly modified, being all of them upregulated in ccRCC samples. Exceptionally, Cer m18:0/24:0 and Cer t18:0/24:1 were more expressed in healthy renal tissue. Furthermore, the Hexocyl ceramides followed similar tendency; HexCer d18:1/16:0 and HexCer d18:1/18:1, which were the most abundant HexCer's, were significantly upregulated (x2.5 and x3.2 respectively).
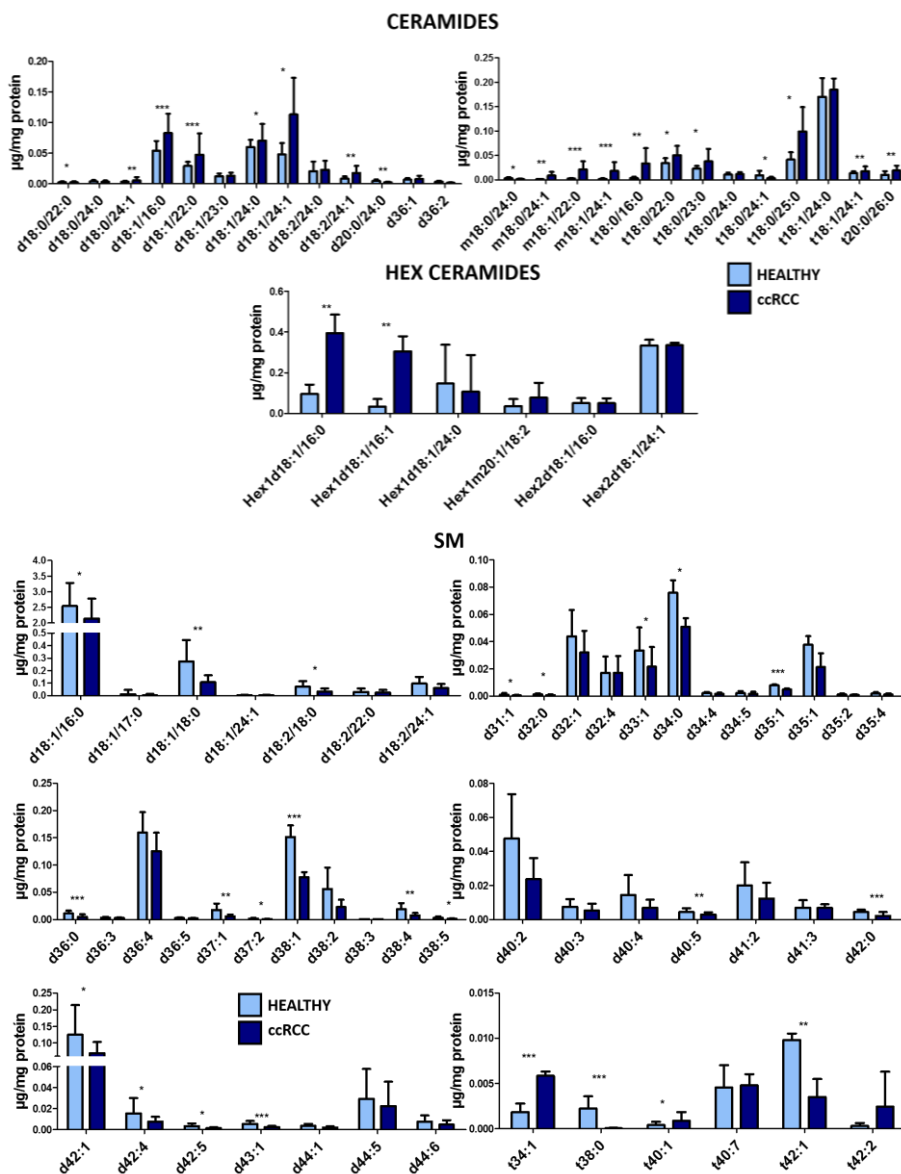
Figure 8.9. *Comparison between the concentration of individual Cer, HexCer and SM species between healthy and ccRCC renal samples. Values are expressed as mean ± SEM (n=40 for both groups). Statistical analysis was assessed using T-test analysis. * = p-value<0.05; **= p-value<0.01; *** =p-value<0.001.*

However, SM's showed an opposite trend to that of Cer and HexCer; the vast majority of the SM species were more abundant in healthy tissue although some

exceptions were also noticeable, such as SM t34:1, which was the most abundant specie in ccRCC samples (**Figure 8.9**).

Another striking observation was the impressive modification occasioned by ccRCC in neutral lipids. As can be seen in **Figure 8.10**, Cholesteryl ester's (ChE) individual species were extensively upregulated in tumoral renal tissue. The abundance of all the species increased at least 5 times in ccRCC samples. Furthermore, as a remarkable point, the most upregulated ChE specie was ChE (20:1) whose concentration was multiplied by 264 in renal tumoral tissue (**Figure 8.10**).

Similar results were observed for triglycerides (TG), which is the second most upregulated neutral lipid class. Thus, the 86% of the 122 different TG's detected showed a significant increase in ccRCC samples. In order to visualize this trend, comparison between healthy and ccRCC of the 16 most abundant TG's is displayed in **Figure 8.10**, where the upregulation in cancer samples is evident. As a last note, this concentration increase can be extrapolated to the triglyceride-ether/vinyl-ether class (TG-O/P's), where all the identified species significantly increased, as can be seen also in **Figure 8.10**.
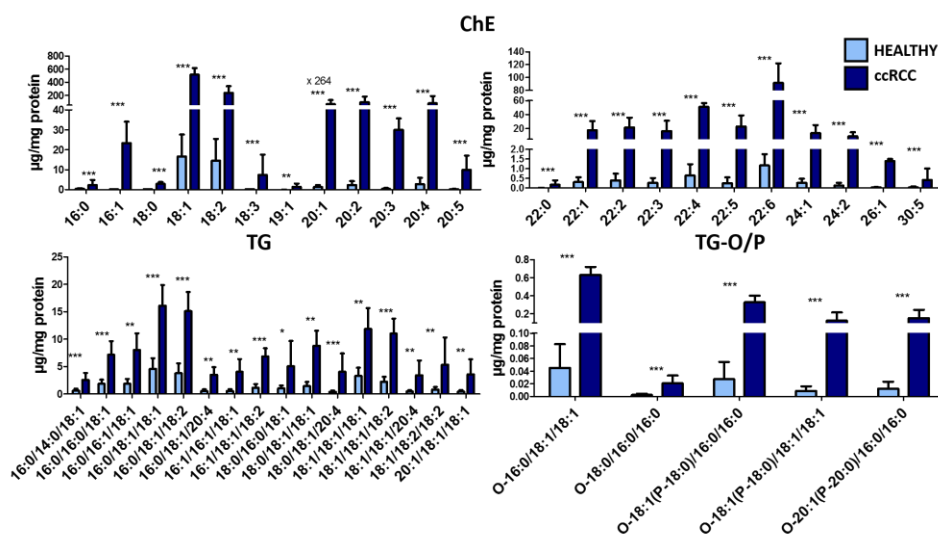
Figure 8.10. *Comparison between the concentration of the individual ChE, TG and TG-O/P species between healthy and ccRCC renal samples. Values are expressed as mean ± SEM (n=40 for both groups). Statistical analysis was assessed using T-test analysis. * = p-value<0.05; **= p-value<0.01; *** =p-value<0.001.*

With reference to ether/vinyl-ether lipid classes, some clear trends were observed. LPC-O/P and PC-O/P, **Figure 8.11**, are more abundant in renal cancer samples, while a decrease in LPE-O/P was observed. For example, substantial reduction in the concentration of the most abundant specie, LPE O-16:1/P-16:0 , was clearly observed. Conversely, PE-O/P's did not show uniform changes; some species were more abundant in ccRCC, such as PE O-16:0/20:4 and PE O-16:0/22:6, while others were downregulated (**Figure 8.11**). Additionally, no relevant changes were observed in the remaining ether lipid classes (PI-O/P and PS-O/P).

Figure 8.11. *Comparison between the concentration of the individual LPC-O/P, PC-O/P, LPE-O/P and PE-O/P species between healthy and ccRCC renal samples. Values are expressed as mean ± SEM (n=40 for both groups). Statistical analysis was assessed using T-test analysis. * = p-value<0.05; ** = p-value<0.01; *** =p-value<0.001.*

Correlation between the lipid profile and Fuhrman grade of the ccRCC samples
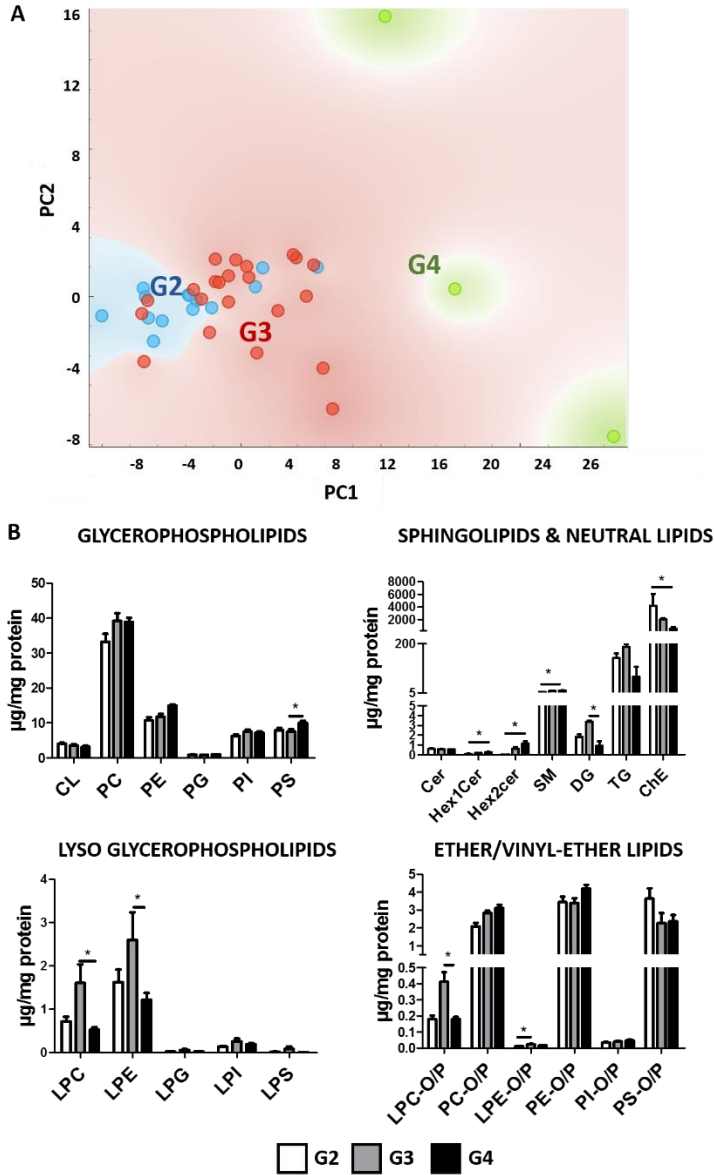
Figure 8.12. *Analysis of ccRCC samples labelled according to their Fuhrman grade (G2, G3 and G4). **(A)** Scores plot of the first two main components of the PCA model separating G4 from G2 and G3 samples. **(B)** Comparison between the summation of the concentration of the main lipid classes among G2,G3 and G4. Values are expressed as mean ± SEM (n=16 for G2, n=21 for G3 and n=3 for G4). Statistical analysis was assessed using T-test analysis. * = p-value<0.05; **= p-value<0.01; *** =p-value<0.001.*

As an additional analysis, the Fuhrman grade classification was considered as a new variable to find specific lipid fingerprints. As it can be seen in **Figure 8.12A**, G4 samples are notably different from samples belonging to G2 and G3 groups, although only three samples of G4 tumor were obtained. This suggest G4 biopsies have a specific lipid fingerprint while samples from G2 and G3 have a similar lipid profile. Thus, the total concentration variation of the main lipid classes indicates that some changes may correlate with the Furhman grade of the samples.

Concerning the main glycerophospholipid classes, only total concentration of PS are significantly upregulated in G4 compared with G3. In the case of sphingolipids and neutral lipids, Hexocyl ceramides and SM are more abundant in G4 than in G2 while ChE are downregulated in G4 in comparison with G3 (**Figure 8.12B**).

Lastly, as regards of lysophospholipids, LPC's and LPE's total concentration is significantly higher in G3 than in G4. Moreover, similar results can be observed in ether lipid classes, where LPC e and LPE e are significantly more abundant in G3 (**Figure 8.12B**).

Detailed analysis of the changes in the individual lipid species may be found in **Figure 8.13**. Specifically, PC, PE, PG and PI lipid classes contained molecular lipid species whose variation between at least two grades resulted significant. In fact, the trend for these species is an increasing gradient from G2 to G4 (**Figure 8.13**).
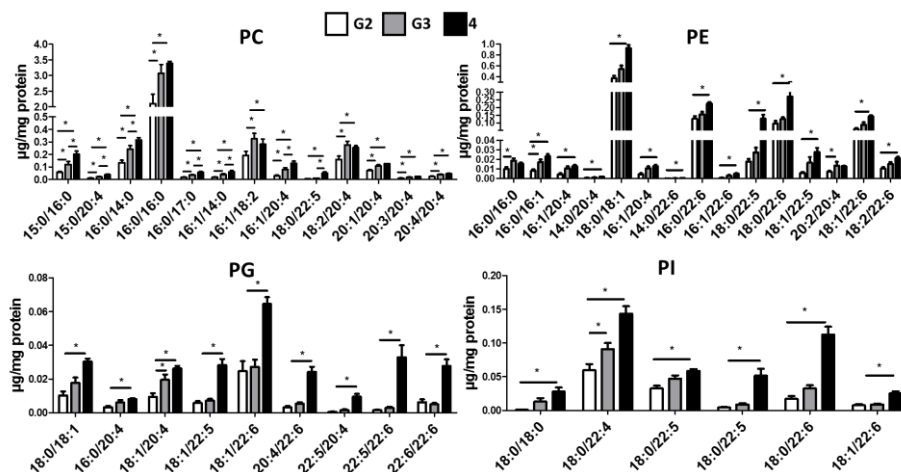
Figure 8.13. *Concentration comparison of the individual PC's, PE's, PG's and PI's species among G2, G3 and G4 Fuhrman grade samples. Values are expressed as mean ± SEM (n=16 for G2, n=21 for G3 and n=3 for G4). Statistical analysis was assessed using T-test analysis. * = p-value<0.05; **= p-value<0.01; *** =p-value<0.001.*

Similar results were obtained for the individual lipid species from ether/vinyl-ether lipid classes, whose concentration is significant higher in G4 samples. However, individual species from LPC-O/P class showed a significant increase in G3 and a reversion in G4 samples (**Figure 8.14**).
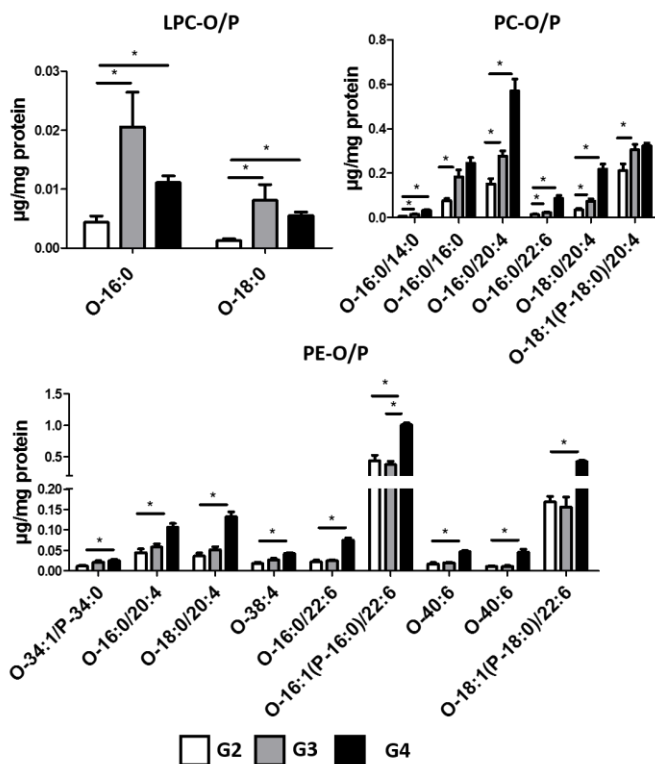
Figure 8.14*. Concentration of the individual LPC e , PC e and PE e species among G2, G3 and G4 Fuhrman grade samples. Values are expressed as mean ± SEM (n=16 for G2, n=21 for G3 and n=3 for G4). Statistical analysis was assessed using T-test analysis. * = p-value<0.05; **= p-value<0.01; *** =p-value<0.001.*

Finally, focusing on individual lipid species belonged to sphingolipids and neutral lipids, several Fuhrman grade-related differences have been found (**Figure 8.15**). With reference to HexCer lipids, two Hex1Cer were significantly more abundant in G3 in comparison with G2 while the concentration of two Hex2Cer was notably lower in G2 compared to G3 and G4. In addition, in the case of SM's, eight individual species showed a higher concentration in G4 compared with G2.

The opposite trend was observed for ChE, there was a clear decreasing gradient from G2 to G4 in eleven species. This trend was also noticeable in two DG species and

42 TG species, being generally significant the variation between G3 and G4 grade samples. **Figure 8.15** only collects some examples of the TG species more substantially modified, but the same tendency was observed in all the 42 species.

Taking all the information above into consideration, it is clear that there are marked changes in the lipid signature of tumoral samples and some of those changes can be associated to their Fuhrman. Specifically, the vast majority of the significant changes observed involved G4 group, which suggest G4 samples have a characteristic lipid fingerprint. More G4 samples analysis would be needed in order to confirm this hypothesis.
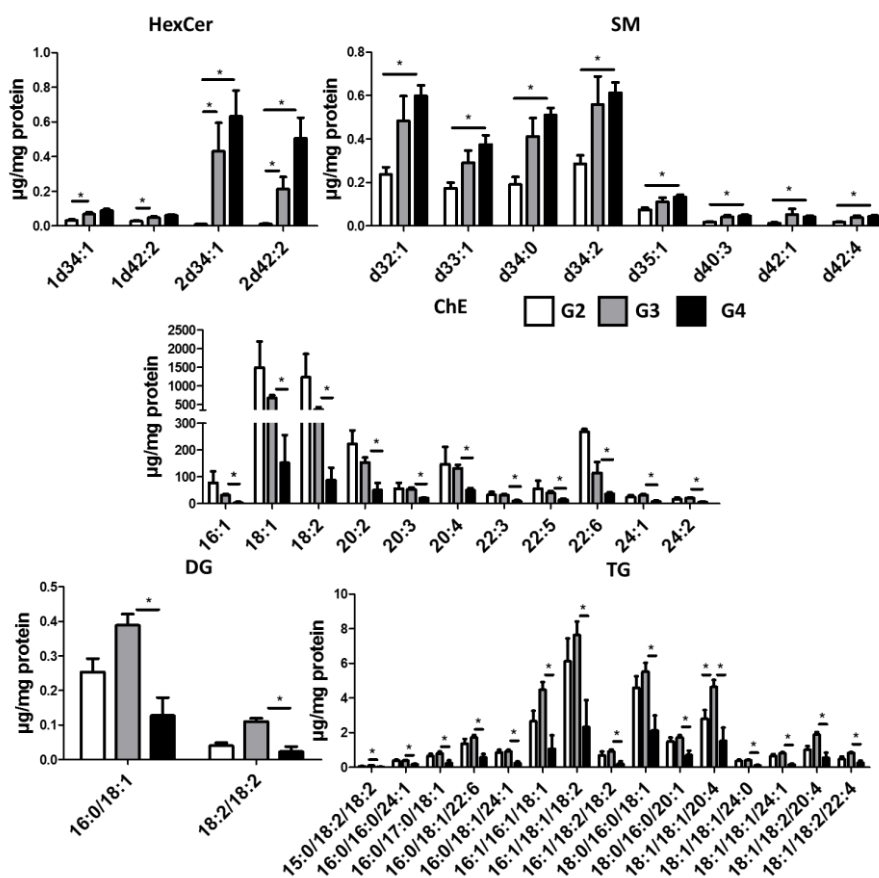
Figure 8.15. Concentration comparison of the individual HexCer, SM, ChE, DG and TG species among G2, G3 and G4 Fuhrman grade samples. Values are expressed as mean ± SEM (n=16 for G2, n=21 for G3 and n=3 for G4). Statistical analysis was assessed using T-test analysis. * = p-value<0.05; **= p-value<0.01; *** =p-value<0.001

MALDI-IMS of sections of ccRCC
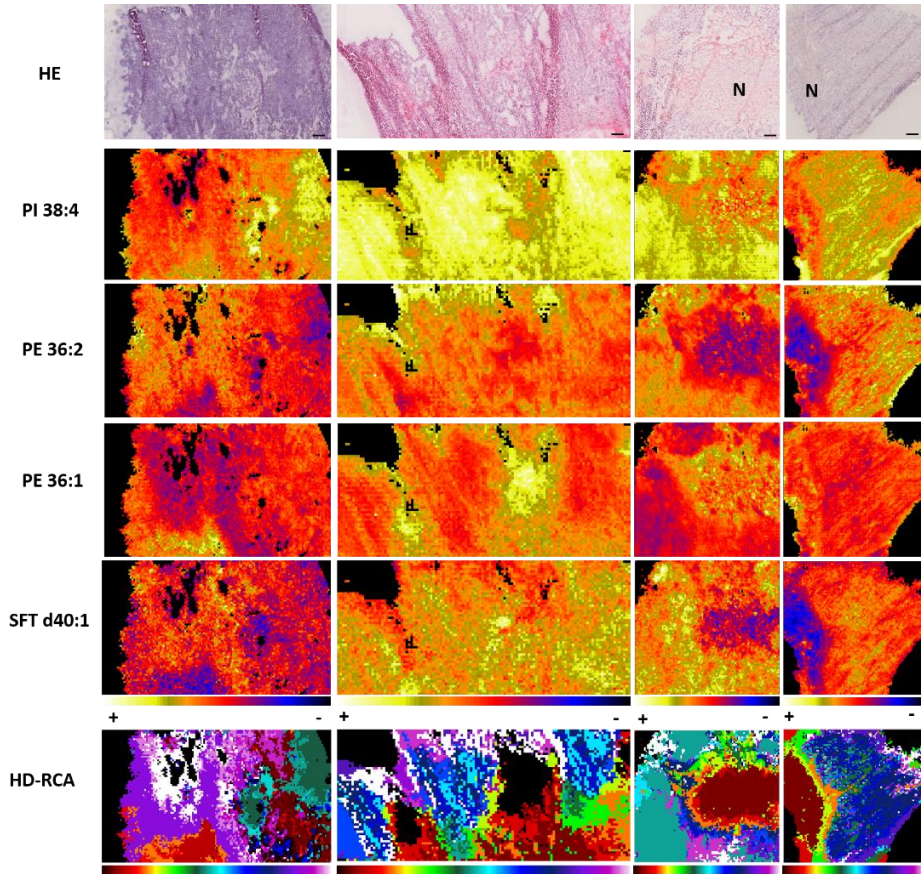
Figure 8.16. *Comparison between the histologic and molecular images of ccRCC. From up to down, HE optical image of three ccRCC samples; expression of four representative lipids over the same section using the color scale below and segmentation analysis of the lipid fingerprint at each pixel (HD-RCA). Images were recorded in negative-ion mode at a pixel size of 25 µm.HE=Hematoxilin eosin staining, N=necrotic area.*

MALDI-IMS experiments allowed us to identify 148 individual lipid species in negative-ion mode in the 49 samples measured. **Figure 8.16** shows a comparison between the distributions of four representative lipids along four sections of ccRCC biopsies. Clearly, each lipid species presented a characteristic distribution. However, these maps do not apparently correlate with any histological structure observed in the HE images, except from necrotic areas (marked as N in HE images) which seem to have a lower relative intensity of PI 38:4, PE36:2 and SFT d40:1 and a higher relative abundance of PE 36:2. In fact, when a supervised *HD-RCA* segmentation algorithm was

applied independently over different ccRCC experiments, no correlation was found between any of the different segments proposed by the algorithm and the histological features. This suggest ccRCC tissue is extremely heterogeneous and different among patients, at least, regarding lipid expression.

As necrotic areas seem to have a characteristic and common lipid fingerprint among patients, non-necrotic tumoral tissue and necrotic areas were compared. As displayed in **Figure 8.17A**, a clear separation was obtained in the PCA scores plot. This separation was further confirmed by the results obtained from the four classification models applied (**Figure 8.17B).** The best model was Random Forest with an AUC of 0.989, an accuracy of 0.979, a precision of 0.980 and a recall of 0.917 and, as shown in **Figure 8.17C,** only one sample was misclassified.

Regarding the intensities of the lipid classes, several differences were observed in the comparison between non-necrotic and necrotic areas. Specifically, HexCer and SM classes were upregulated in necrotic areas, while LPI-O/P, PI and SFT were downregulated. These variations suggest that necrosis can be readily identified in tissue sections based on its lipid fingerprint.
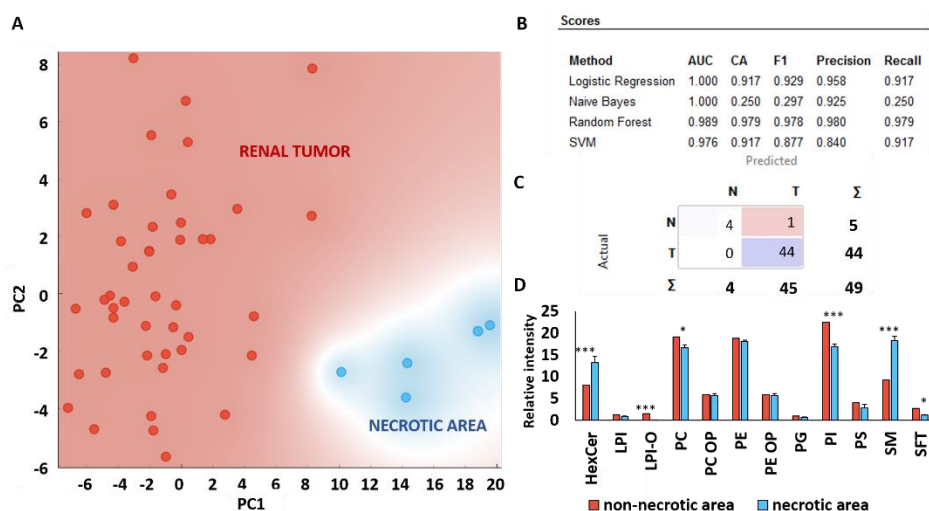
Figure 8.17. Lipid classification of necrotic areas from ccRCC samples and non-necrotic ccRCCC tissue (A) Score plot of the first two main components of the PCA model separating necrotic and non-necrotic regions. Score plot of the first two main components of the PCA model, (B) Classification model's scores, (C) Matrix of confusion of Random Forest.

Next, a comparison between healthy and ccRCC lipid fingerprint was performed. For this purpose, data from renal healthy tissue belonging to cortical and medullar

areas was selected and compared with the main spectrum from each ccRCC samples excluding necrotic segments.
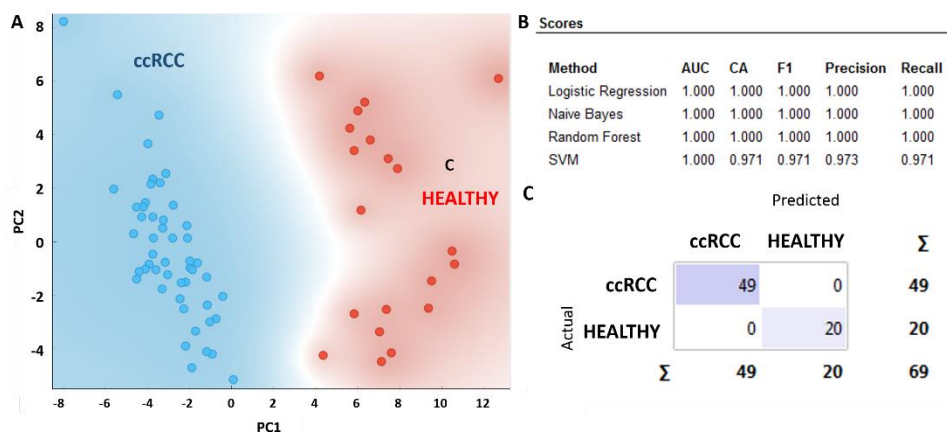
Figure 8.18. *Non-supervised multivariate analysis comparing healthy and ccRCC lipidome obtained from MALDI-IMS. (A) Score plot of the first two main components of the PCA model, (B) Classification model's scores, (C) Matrix of confusion of Random Forest.*

As it can be appreciated in **Figure 8.18A**, a perfect separation was obtained in the score plot between healthy and ccRCC samples. The classification methods were able to perfectly segregate the samples as can be seen in **Figure 8.18B and C,** indicating that the lipid profile of each group is singular and reproducible among patients.

A comparison of the relative abundance of the main lipid classes between healthy and ccRCC sections was performed showed that LPI-O/P and PC-O/P, PE-O/P classes were upregulated, whereas PE's, PG's and PS's seemed to be less abundant in ccRCC samples. Regarding sphingolipids classes, HexCer's shows a significant higher relative abundance while a decrease in SM when ccRCC occurs (**Figure 8.19**).

Analysis of the changes in individual species unveiled 122 lipid species with significant variations between groups. These individual lipid species belonged to several lipid families but the most remarkable changes were found in PC-O/P, PE and HexCer classes, as displayed in **Figure 8.20**. Focusing on PC-O/P individual lipid species, they were overall upregulated with the exception of PC-O 32:2/PC-P 32:1 and PC-O 34:5/PC-P 34:4 whose relative abundance remained constant. In the case of PE's, the 60% of the molecular species identified were downregulated, whereas the 40% were upregulated in tumoral samples. Strikingly, PE 38:4, which is the most abundant in both groups, is 1.48 times more abundant in healthy tissue than in ccRCC samples. In the

same line, PE 36:4 relative abundance is 6.02 higher in healthy group. However, PE 38:2 and those PE's containig 40 carbons are significantly more abundant in the ccRCC group. Lastly, concerning HexCer individual lipid species, the 78% of the species detected showed a significant increase in tumoral samples (**Figure 8.20).**
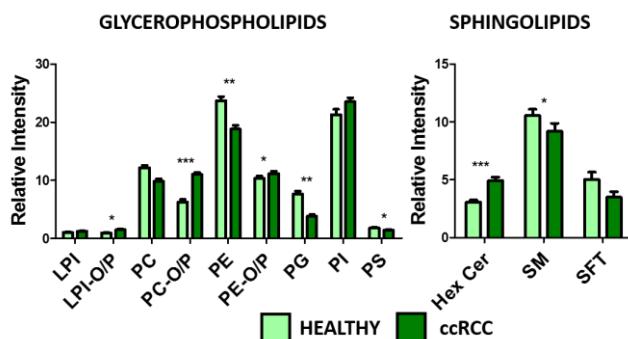
Figure 8.19. *Comparison between the summation of the concentration of the main lipid classes between healthy and ccRCC renal samples. Values are expressed as mean ± SEM (n=20 for healthy and n=49 for ccRCC samples). Statistical analysis was assessed using T-test analysis. * = p-value<0.05; ** = p-value<0.01; *** =p-value<0.001*
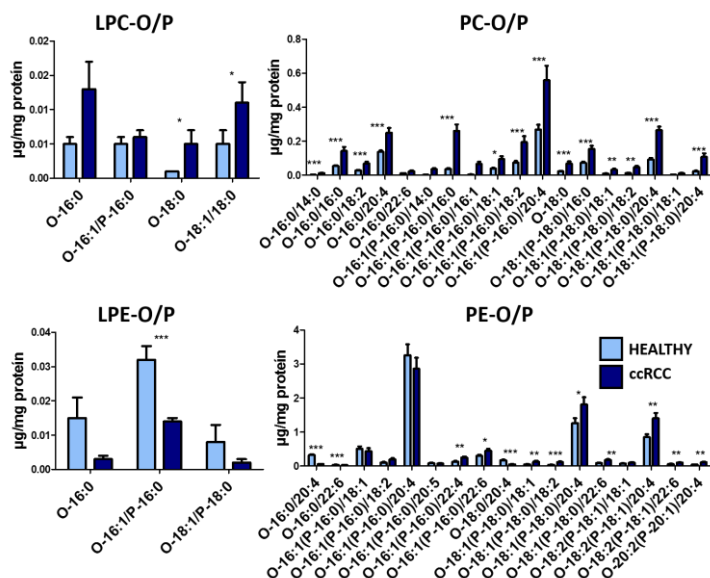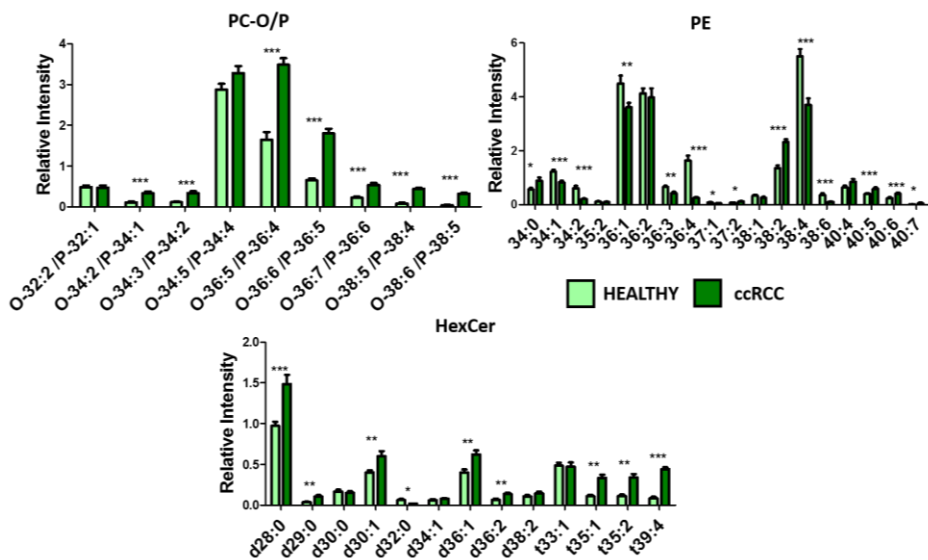

Figure 8.20. *Comparison between the concentration of the individual PC-O/P, PE, and HexCer species between healthy and ccRCC renal samples. Values are expressed as mean ± SEM (n=40 for both groups). Statistical analysis was assessed using T-test analysis. * = p-value<0.05; ** = p-value<0.01; *** =p-value<0.001.*

<u>Correlation between the lipid profile and Fuhrman grade of ccRCC samples</u>

The Fuhrman grade of the ccRCC samples was also taken into account in an attempt to find specific lipid fingerprints in the MALDI IMS data.

Figure 8.21A shows a PCA scores of the ccRCC samples labelled as G2, G3 and G4, attending to their Fuhrman grade. It seems, as in uHPLC results, that G4 lipid fingerprint is notably different from that of G2 and G3 samples, which have more similar lipid profiles.

Comparison of the relative abundance of each lipid class showed an increasing gradient from G2 to G4 in HexCer, PS and SM classes, being significant the comparison between G2 and G4 **(Figure 8.21B)**.
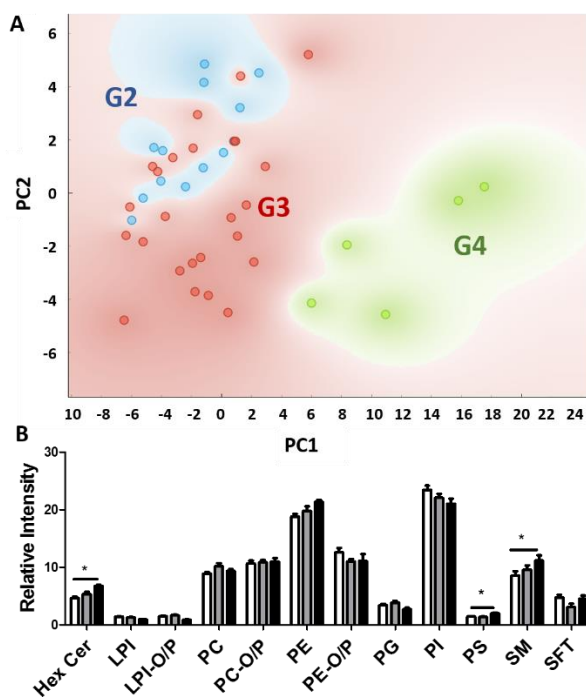
Figure 8.21. Lipid classification of ccRCC samples analyzed by MALDI-IMS in based on the Fuhrman grade (G2,G3 and G4). **(A)** Score plot of the first two main components of the PCA model separating G2, G3 and G4 samples**. (B)** Comparison between the summation of the concentration of the main lipid classes among G2,G3 and G4. Values are expressed as mean ± SEM (n=19 for G2, n=24 for G3 and n=5 for G4). Statistical analysis was assessed using T-test analysis. * = p-value<0.05; **= p-value<0.01; *** =p-value<0.001.

Additionally, 60 individual lipid species showed a significant variation between at least two groups. As can be appreciated in **Figure 8.22** and **Figure 8.23**, they belonged to five glycerohospholipid and two sphingolipid classes (PE, PE-O/P, PG, PI, PS and HexCer and SM respectively).

Concerning PE's, seven molecular species resulted more abundant in G4 compared to G2 or G3. As an exception, PE 36:4 relative abundance showed a decrease in G4 in comparison with G2 and G3. In the case of PE-O/P's, the PE-O 38:5/PE-P 38:4 showed a clear decreasing gradient from G2 to G4 while the rest of the PE's with notable variations were upregulated in G4. Finally, variations in some individual PG, PI and PS follow the Fuhrman grade of the samples. Overall, they are significantly more abundant in G4 with the exception of PI 36:4 and PS 40:5 whose relative abundance is lower in G4 samples (**Figure 8.22**).
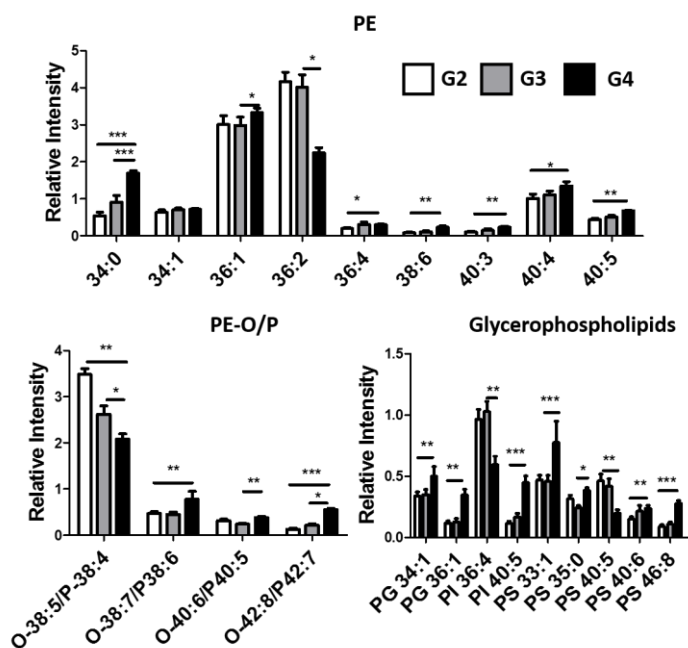
Figure 8.22. *Concentration comparison of the individual PE, PE-O/P, PG, PI and PS species among G2, G3 and G4 Fuhrman grade samples with some significant change among groups. Values are expressed as mean ± SEM (n=19 for G2, n=21 for G3 and n=5 for G4). Statistical analysis was assessed using T-test analysis. * = p-value<0.05; **= p-value<0.01; *** =p-value<0.001.*

Finally, the analysis of the changes in individual species of sphingolipids showed that seven HexCer's and eight SM's resulted significantly modified among groups.

Briefly, an increasing trend from G2 to G4 was observed in all these individual sphingolipids, suggesting that tumor aggressiveness modifies sphingolipids metabolism pathways (**Figure 8.23**).
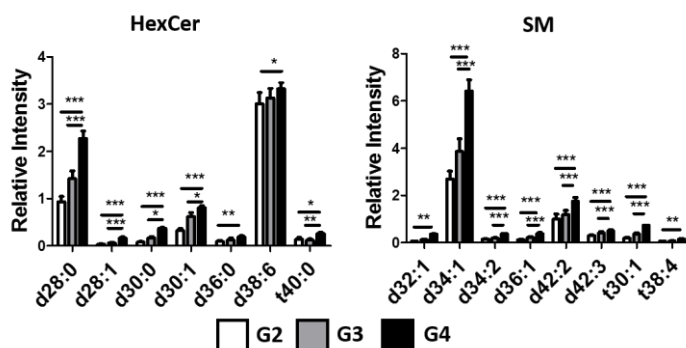
Figure 8.23. *Concentration comparison of the individual HexCer and SM species among G2, G3 and G4 Fuhrman grade samples with some significant change among groups. Values are expressed as mean ± SEM (n=19 for G2, n=21 for G3 and n=5 for G4). Statistical analysis was assessed using T-test analysis. * = p-value<0.05; **= p-value<0.01; *** =p-value<0.001.*

Comparison between uHPLC and MALDI-IMS lipid data

As mention above, healthy and ccRCC renal samples were analyzed by two orthogonal techniques: uHPLC-ESI and MALDI-IMS. uHPLC is a quantitative method while MALDI–IMS only reports relative intensities. Thus, comparing the results obtained from these two different techniques could be very interesting, especially to validate the non-quantitative MALDI –IMS results. For this purpose, the data from the same patients obtained from both uHPLC-ESI and MALDI-IMS techniques were compared. Thus, only lipids detected by both techniques were included in the analysis.

Comparison between uHPLC and MALDI-IMS data for healthy renal samples

Firstly, uHPLC-ESI and MALDI-IMS results from healthy renal samples were compared. In **Chapter 6**, the lipidome of seven specific regions of the human nephron was characterized by MALDI-IMS. As the exact renal region where each biopsy originated was not provide in the clinical data, this previous MALDI-IMS characterization allowed us to determine for which area of the kidney belonged each sample: cortex, medulla o corticomedullary transition. Thus, only spectra from samples whose localization was confirmed by MALDI-IMS were selected for the MALDI/uHPLC comparison.

As shown in **Figure 8.24**, cortical and medullary samples analyzed by MALDI-IMS were perfectly classified in the PCA score plot based on its own lipid fingerprint (**Figure 8.24A**). The performance of all classification models tested was excellent, being Logistic regression the most accurate, with only two cortical samples misclassified (**Figure 8.24C,E**).

The same samples analyzed by MALDI-IMS were also studied by uHPLC and assigned as cortex or medulla in based on the corresponding MALDI-IMS image. When analyzing the uHPLC data, a clear separation was also obtained in the PCA score plot between samples assigned as cortex or medulla, confirming that each renal region has a specific lipid profile define (**Figure 8.24B**). The classification models also confirmed the lipid differences between the two groups and demonstrated excellent classification power (**Figure 8.24D**). The logistic regression model proved to be the best one, with only one misclassified sample (**Figure 8.24F**).
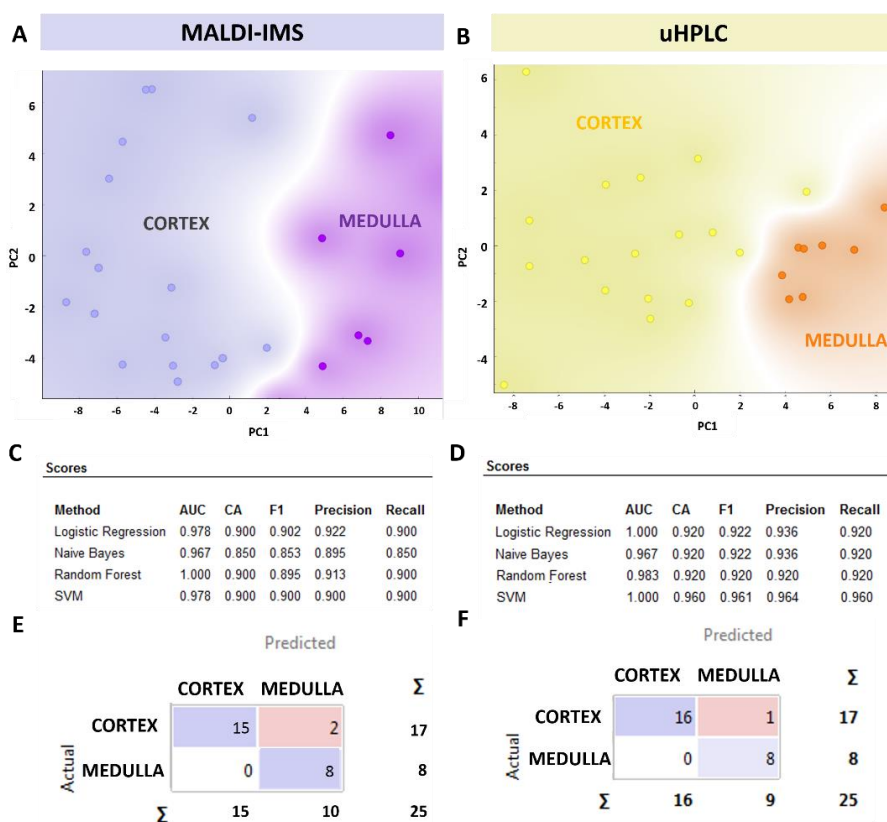
Figure 8.24*. Lipid classification of healthy samples analyzed by MALDI-IMS and uHPLC (**A,B**) Score plot of the first two main components of the PCA model separating cortical and medullary samples analyzed by MALDI-IMS and uHPLC respectively. (**C,D**) Classification model's scores, (**E, F**) Matrix of confusion of Logistic Regression model.*
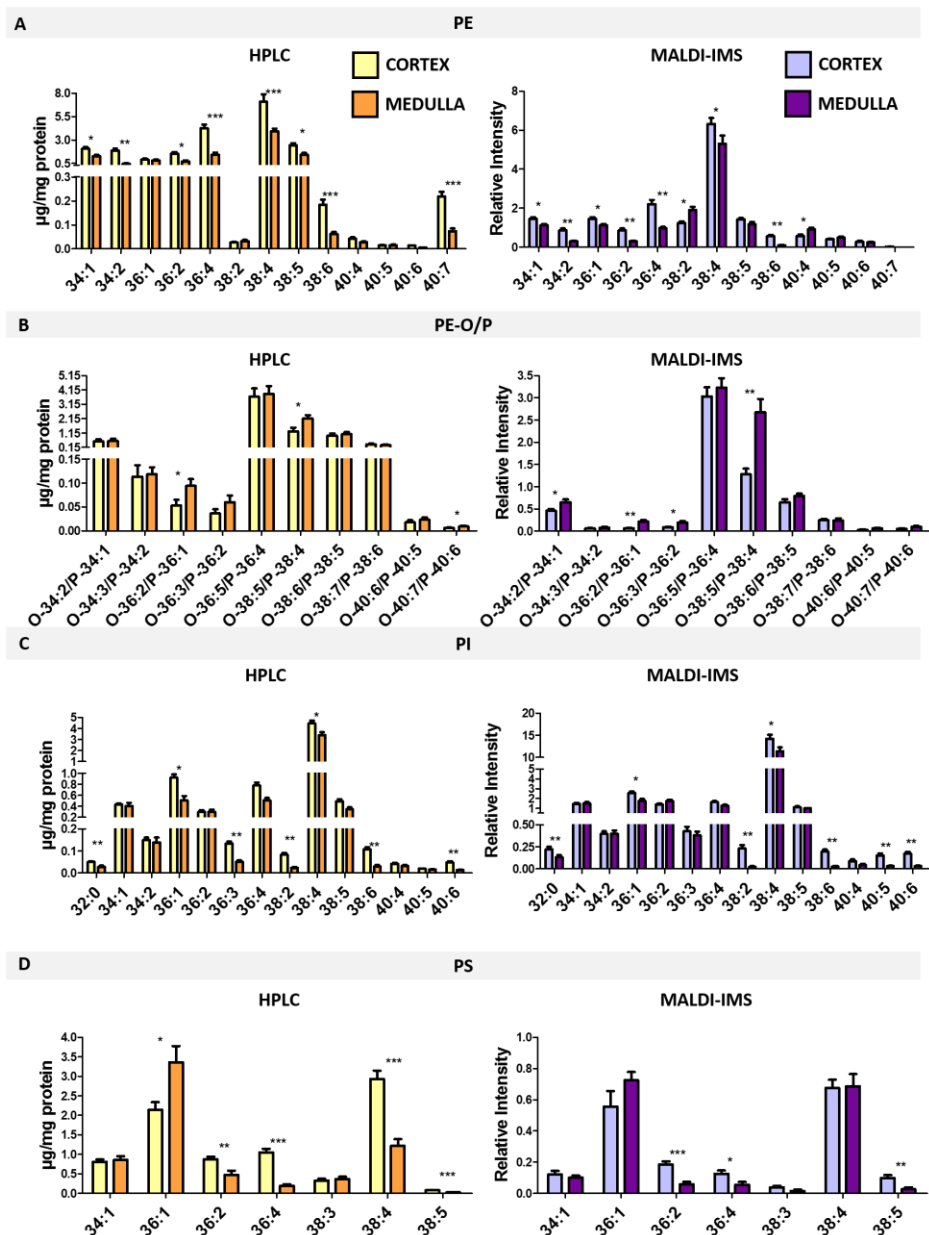
Figure 8.25. *Comparison of individual glycerophospholipids concentration and relative intensity between cortex and medulla samples studied by uHPLC and MALDI-IMS respectively. uHPLC values are expressed in µg/mg protein while MALDI-IMS data, they are expressed by relative intensity. Values are expressed as mean ± SEM (n=17 for cortical samples and n=8 for medulla samples). Statistical analysis was assessed using T-test analysis. * = p-value<0.05; **= p-value<0.01; *** =p-value<0.001*

Next, cortex-medulla comparison was performed using the individual species detected by both techniques, to test if they report similar patterns. As displayed in **Figure 8.25**, comparable results were obtained from both techniques in most cases.

Detailed analysis of PEs shows marked differences in the relative abundance of individual species, but the changes reported by both techniques follow the same trend: the abundance of the vast majority of the species is reduced in medulla. Some exceptions are also observed, such as PE 38:2 and PE 40:4 for which uHPLC did not find significant regions between kidney regions, while MALDI-IMS reported an increase in medulla (**Figure 8.25A**).

In the same line, the results obtained for PE-O/P show similar trends, although the relative abundance of the species is sometimes very different. For example, uHPLC reported higher abundance of PE-O 36:2/-P 36:1, PE-O 38:5/P 38:4 and PE-O 40:7/-P 40:6 in medulla and, in good agreement, MALDI-IMS reported higher abundance of PE-O 36:2/-P 36:1 and PE-O 38:5/P 38:4 in medullar (**Figure 8.25B**).

The best agreement between both techniques was probably obtained for PI and PS (**Figure 8.25C,D**). For example, both IMS and uHPLC reported upregulation of PI species in cortex, but also both techniques reported PI 38:4, PI 36:1, and PI 36:4 as the three most abundant species s. Regarding PS, both techniques also agreed in the existence of an upregulation of PS 36:2, PS 38:4 and PS 38:5 species in cortical samples.
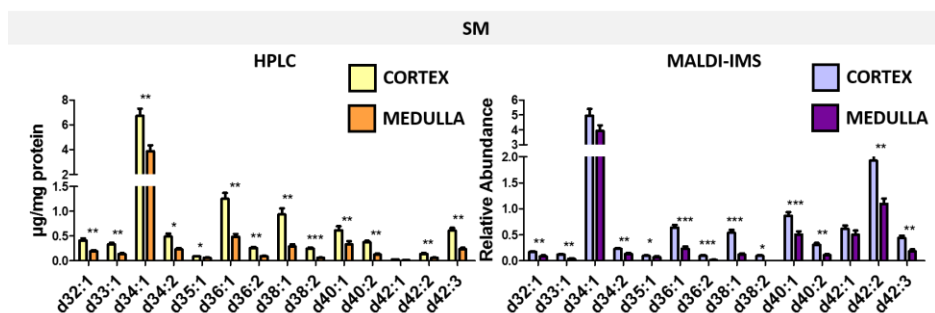
Figure 8.26. *Comparison of individual SM's concentration and relative intensity between cortex and medulla samples studied by uHPLC and MALDI-IMS respectively. uHPLC values are expressed in µg/mg protein while MALDI-IMS data are expressed by relative intensity. Values are expressed as mean ± SEM (n=17 for cortical samples and n=8 for medulla samples). Statistical analysis was assessed using T-test analysis. * = p-value<0.05; **= p-value<0.01; *** =p-value<0.001.*

Following with SM, similar differences between cortex and medulla lipid composition were reported by uHPLC and MALDI-IMS. As can be seen in **Figure 8.26,** a

clear decreasing tendency in medulla was observed for almost all the SM's detected in both techniques. Moreover, SM d34:1 was the most abundant specie in uHPLC and the most intense SM in MALDI-IMS, confirming the comparability of the results.

Finally, the cortical–medullar variations in the lipid classes were analyzed for both techniques. As previously mentioned, lipid abundances can not be compared between methods because each lipid class have its own ionization process and this can interfere in the final ion signal. Thus, lipid classes which are not the most abundant in the tissue can be ionized in a very effective way and provide higher ion signals. Such is the case for PIs, which in MALDI-IMS is the most intense lipid class while in mammal tissues the most abundant lipid classes are PE and PC.

Figure 8.27 displays the variations of lipid abundance between cortex and medulla reported by both techniques. As expected, PE is the most abundant lipid class in uHPLC results, while for MALDI-IMS, PI and PE are the lipid classes with higher total intensity. In good agreement, for both approaches PE and SM lipid classes significantly decreased and PE-O/P's notably increase in medullar sections. Consequently, considering all the information above, it is clear that there is a good correlation between the cortex-medulla lipid modifications obtained by uHPLC and MALDI-IMS techniques.
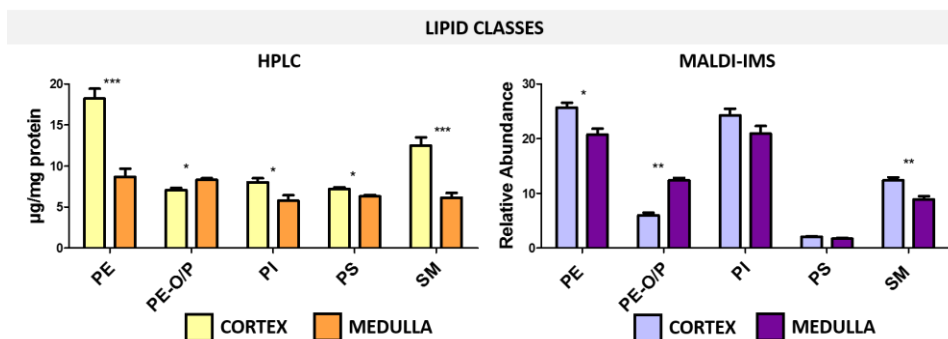
Figure 8.27. Comparison of the main lipid classes concentration and relative intensity between cortex and medulla samples studied by uHPLC and MALDI-IMS respectively. uHPLC values are expressed in µg/mg protein while MALDI-IMS data, they are expressed by relative intensity. Values are expressed as mean ± SEM (n=17 for cortical samples and n=8 for medulla samples). Statistical analysis was assessed using T-test analysis. * = p-value<0.05; **= p-value<0.01; *** =p-value<0.001

Comparison between uHPLC and MALDI-IMS data from ccRCC samples
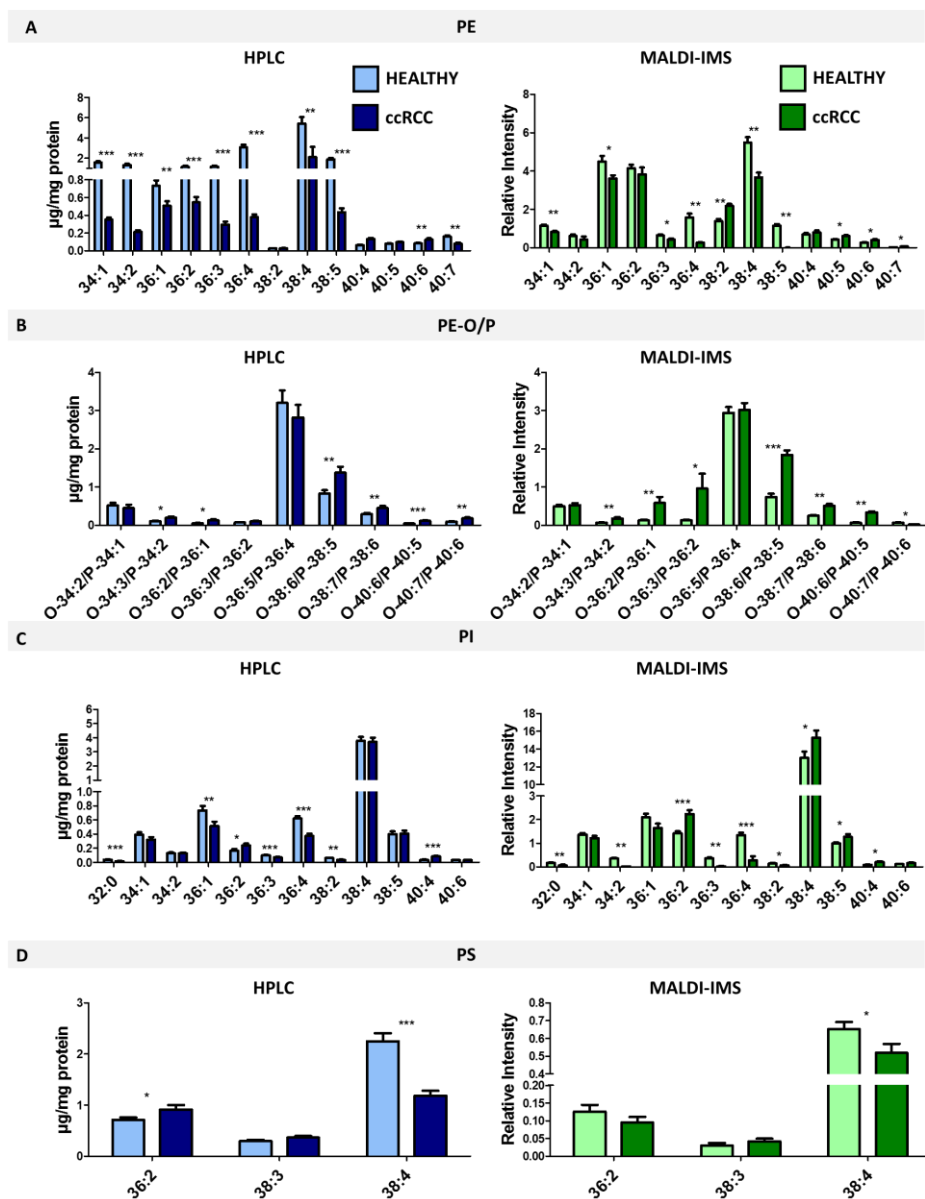
Figure 8.28. *Comparison of individual glycerophospholipids concentration with relative intensity between healthy and ccRCC samples studied by uHPLC and MALDI-IMS respectively. uHPLC values are expressed in µg/mg protein while MALDI-IMS data are given as relative intensity. Values are expressed as mean ± SEM (n=25 for healthy samples and n=40 for ccRCC samples). Statistical analysis was assessed using T-test analysis. * = p-value<0.05; **= p-value<0.01; *** =p-value<0.001*

The same comparison as in the last section was performed over the data from healthy and ccRCC samples. As displayed in **Figure 8.28**, some patterns can also be observed between the results obtained from uHPLC and MALDI-IMS.

uHPLC reported a clear decreasing trend in ccRCC of the PEs containing short length fatty acids, while an upregulation in the C40 fatty acid containing-species was also observed. The same trends were obtained in MALDI-IMS with the exception of PE 36:2 which did not show any variation (**Figure 8.28A**). Overall, both techniques offer slightly different lipid profiles, although the variations in the individual species seem to follow a similar trend. These differences in the lipid profiles could be due in part to the presence of PC species, contributing to the m/z assigned as PE, as some PE and PC species are isobaric. For instance, the m/z of PE 36:1-H⁻ and PC 34:1-CH3⁻ overlap. Therefore, the PE's relative intensity displayed in **Figure 8.28A** probably is a combination of both lipid classes, PE and PC.

Conversely, better agreement exists between the results obtained by both techniques for PE-O/P, PI and PS individual lipid species. In the case of PE-O/Ps, an upregulation in ccRCC was observed for the majority of the species detected by both techniques (**Figure 8.28B**). Similar trends were also reported by both techniques for PIs, which in general decreased in pathological samples, except for the most abundant species, PI 38:4. According to IMS results, this lipid increases in ccRCC, while its concentration does not experience substantial changes in the LC/MS results (**Figure 8.28C**). But the lipid class in which both techniques exhibit more compatible results is PS, for which only three common species were detected. Although LC/MS reports a small increase of PS 36:2 and IMS does not report statistically significant changes, the behavior of the other two species is very similar by both techniques (**Figure 8.28D**).
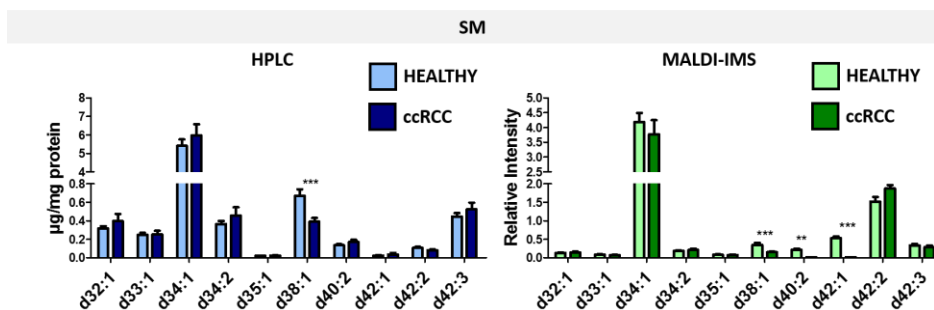
Figure 8.29. *Comparison of individual species of SM between healthy and ccRCC samples studied by uHPLC and MALDI-IMS respectively. uHPLC values are expressed in µg/mg protein while MALDI-IMS data are given in relative intensity. Values are expressed as mean ± SEM ((n=25 for healthy samples and n=40 for ccRCC samples). Statistical analysis was assessed using T-test analysis. * = p-value<0.05; **= p-value<0.01; *** =p-value<0.001.*

Some agreement between the results obtained by both techniques was also reached for SM, as it can be seen in **Figure 8.29.** SM d34:1 is the most abundant species by both techniques and does not experience a significant change. The relative abundance of the rest of the species reported by both techniques strongly varies, and agreement was only reached for the change in SM d38:1, whose concentration reduces in ccRCC.

Interestingly, the variation between healthy and ccRCC lipid classes shows a substantially better agreement between the two methods. While PE and SM are significantly downregulated in ccRCC, PE-O/P lipid class are more abundant in ccRCC samples for both techniques (**Figure 8.30**).
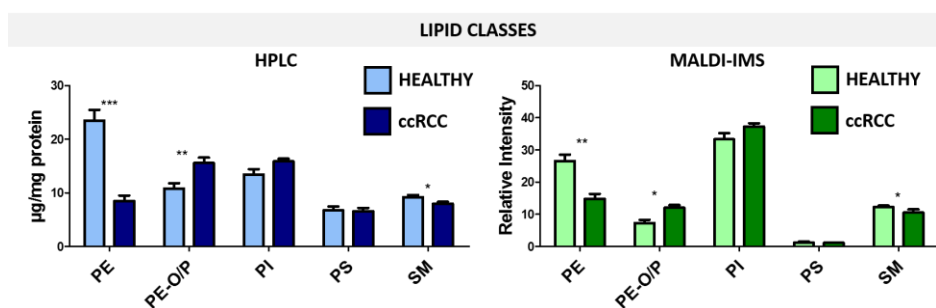
Figure 8.30*. Comparison of the concentration and relative intensity of the common lipid classes between healthy and ccRCC samples studied by uHPLC and MALDI-IMS respectively. uHPLC values are expressed in µg/mg protein while MALDI-IMS data are given in relative intensity. Values are expressed as mean ± SEM ((n=25 for healthy samples and n=40 for ccRCC samples). Statistical analysis was assessed using T-test analysis. * = p-value<0.05; ** = p-value<0.01; *** =p-value<0.001.*

Comparison of the lipid fingerprint of ccRCC classified following Fuhrman grade, obtained by the two techniques, **Figure 8.31**, shows that both sets of data drive to the same conclusions: no substantial changes in the relative abundance of the lipid families was observed, except for a progressive increase the abundance of SM from G2 to G4, especially in the MALDI-IMS dataset. Once more, the comparison also highlights the discrepancies in relative abundance of the families between both datasets, in part due to the lack of a separation stage in MALDI-IMS and the absence of quantification.
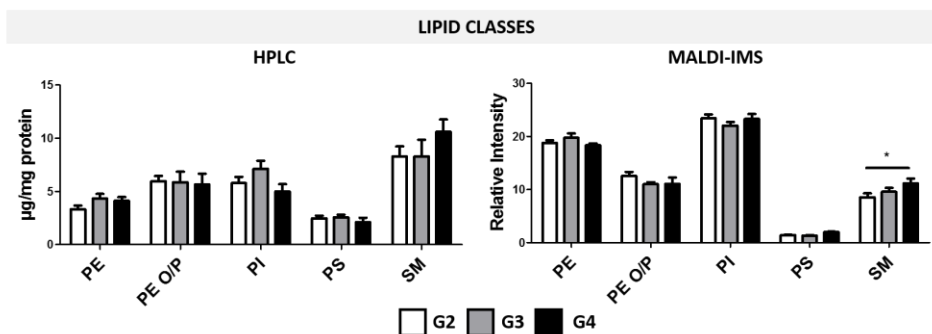
Figure 8.31. *Comparison of the main lipid classes concentration and relative intensity between G2, G3 and G4 Fuhrman grade samples studied by uHPLC and MALDI-IMS. uHPLC values are expressed in µg/mg protein while MALDI-IMS data are given in relative intensity. Values are expressed as mean ± SEM (n=16 for G2, n=21 for G3 and n=3 for G4 samples). Statistical analysis was assessed using T-test analysis. * = p-value<0.05; **= p-value<0.01; *** =p-value<0.001*

8.5 Discussion

The application of metabolomics to cancer studies expands our understanding of the metabolic alterations that are associated with cancer progression. In the present study, we analyzed changes in the lipid profiles in cancerous and adjacent normal renal tissue samples obtained from 49 ccRCC patients studied by two complementary techniques: uHPLC-ESI and MALDI-IMS. The uHPLC results allowed for the identification of 736 different lipid species while 148 were detected by MALDI-IMS. Nevertheless, the spatial resolution provided by MALDI-IMS could unravel histological features, nicely complementing the quantitative character of uHPLC technique.

Comparison between adjacent normal tissue and ccRCC lipid fingerprint

Focusing on uHPLC results and in agreement with previous findings[24-27], our quantitative study clearly showed a neat increase in ChE and TG in ccRCC tumor tissues. Such increase was accompanied by a decrease in the levels of PE, PS, CL and SM and higher levels of Cer, HexCer , PC-O/P, PE-O/P and TG-O/P lipids. As it can be seen, tumor transformation involves a complete remodeling of the lipid metabolism. Among the changes described, the lower PE lipid content represents a significant feature of ccRCC. The underlying mechanism by which PE abundance regulates the proliferation of renal cancer cells remains to be elucidated. However, PE lipids are known to be exposed on the surface of apoptotic cells[28]. In addition, it has been demonstrated that PE 16:1/16:1 induces apoptosis of malignant mesothelioma cells[29]. Thus, one possible mechanism by which the lower PE levels affect cell proliferation in ccRCC might be the inhibition of apoptosis[27].

Apart from PE concentrations, we found that CL levels were notably reduced in the cancerous tissue. CL is a specific mitochondrial phospholipid and perturbations in this lipid have been detected in mouse brain tumors[30]. Because mitochondrial dysfunction is a common feature in cancer cells[31] lower CL levels would be an indication of such dysfunction also in ccRCC.

In contrast to acyl-phospholipids, ether-phospholipids (PC-O/P and PE-O/P) were present in higher concentrations in the cancerous tissue compared to their levels in the normal renal tissue. Because ether-phospholipids are also membrane constituents, higher levels of these phospholipids might compensate for a lower content of other phospholipids, such as PE, PS, and CL. Currently, the functional role of ether/vinyl-ether-phospholipids in ccRCC remains unclear. It has been previously reported that 34:1 and 36:1 PE-O/Ps were more abundant in aggressive metastatic breast cancer cells than in cells with a lower degree of aggressiveness[32]. In addition, higher levels of PC-O/P were also detected in migratory breast cancer cells[33]. Some works have pointed to an anti-oxidant role of these lipids[34] and it is well-known tumor cells change their glucose metabolism producing an increase in oxidative species[35]. Thus, the increase in ether/vinyl-ether lipids could be a mechanism of protection towards lipid oxidation.

Moreover, SM and Cer can be enzymatically converted to each other by the sphingomyelin phosphodiesterase (*SMase*) enzyme. In the present study, the ccRCC tissue samples were characterized by an increased of Cer and a decease of SM compared with healthy tissue. This alteration could be explained by an upregulation of the SM-to-Cer conversion pathway in the cancerous tissue. It has been reported that cells enriched in SM were more sensitive to apoptosis[36]. In addition, it has also been reported that enriched SM levels are associated with the anticancer effect of 2-hydroxyoleate[37]. Thus, the reduced SM levels observed in the ccRCC samples may promote cancer cell survival.

Similar results were obtained by analyzing surrounding normal and ccRCC samples by MALDI-IMS. An excellent classification was observed between groups confirming the clear lipid metabolism differences. The most striking observations were the significant PE, PG and SM decrease and a notably increase in PC-O/P, PE-O/P and HexCer levels in ccRCC. It should be note that an excellent agreement was observed between the results obtained from both techniques, underlying the clear decreasing of PE and SM levels and the increase of ether lipid classes in ccRCC.

CcRCC Furhman grade lipid fingerprint

After analyzing the lipid variation in adjacent healthy renal tissue caused by ccRCC, an additional analysis was performed over tumoral samples. Although our findings of the lipid alterations in ccRCC were analyzed in all grades of ccRCC together, we also

examined the differences in the lipid profiles between G2,G3 and G4 Fuhrman grade ccRCC.

For both techniques, G4 seems to have a characteristic lipid profile, different from those of G2 and G3, which have more similar lipid signature. Specifically, both techniques reported a clear increase in SM from G2 to G4. Moreover, although no significant changes in the whole lipid class were observed, several individual lipid species belonged to PE, PI, PG and PS showed a marked increase in G4.

Interestingly, a recovery effect was observed for the G4 Fuhrman grade samples. As mentioned above, the SM downregulation is a characteristic feature of ccRCC, and from G2 to G4 an increasing trend was appreciated, reducing the gap between SM healthy and G4 ccRCC samples level (**Figure 8.32**).

This reversion effect was also observed in ChE levels, which are clearly upregulated in ccRCC, compared to healthy tissue, while in G4 ccRCC samples they were significantly decreased in comparison with G2 and G3 (**Figure 8.32**).
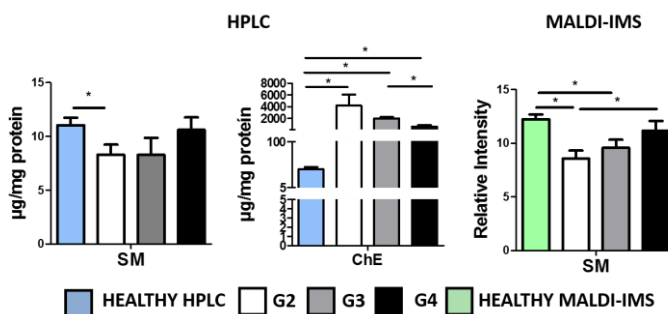
Figure 8.32. SM and ChE variations among healthy and G2, G3 and G4 Fuhrman renal samples studied by uHPLC and MALDI-IMS. uHPLC values are expressed in µg/mg protein while MALDI-IMS data are given in relative intensity. Values are expressed as mean ± SEM (n=16 for G2, n=21 for G3 and n=3 for G4 samples). Statistical analysis was assessed using T-test analysis. * = p-value<0.05; **= p-value<0.01; *** =p-value<0.001.

CcRCC lipid characterization of Necrotic areas by MALDI-IMS

MALDI-IMS is widely used to unravel histological features associated with specific lipid fingerprints observed over a tissue. However, in this study, it was not possible to find correlation between the MALDI-IMS segments ad HE images due to the inherit heterogeneity of ccRCC. Further molecular analysis should be performed such as specific immunohistochemistry protocols in order to elucidate these metabolic heterogeneity.

However, necrotic areas seem to share common lipid features among patients. Non-necrotic areas and necrotic areas of ccRCC was compared and clear classification was obtained in based on lipids. Specifically, HexCer and SM lipid classes showed a clear upregulation while PC, PI and SFT lipid classes are decreased in necrotic areas. This lipid profile is similar to the one obtained from G4 Furhman grade ccRCC samples. As necrotic areas are a poor prognostic indicator[38] , it can be expected similarity between the lipid profile of the higher grade of malignancy samples and necrotic areas.

Comparison between uHPLC and MALDI-IMS lipid profiles in renal samples

uHPLC and MALDI-IMS have been widely used as complementary techniques, mainly to help with the identification of the lipid species detected in the images from MALDI-IMS. However, to the best of our knowledge, this is the first systematic study of the similarities of lipid profiles detected by both techniques, performed in an individual species basis.

Firstly, adjacent normal tissue was analyzed. As MALDI-IMS approach provides images with high spatial resolution, it was possible to determine the region of the kidney from which each sample belonged (**Chapter 6**). Moreover, the same samples were analyzed for both techniques so, uHPLC samples were assigned as cortex or medulla, based on their corresponding MALDI-IMS analysis.

The results were excellent; although lipid abundance from both techniques can not be directly compared, the variations between cortex and medulla samples were in excellent agreement for both techniques; PE and SM levels are higher in cortex while PE-O/P are upregulated in medulla.

This similarity of the results indicates that lipid profile can be used to elucidate the original location of the sample and confirms that uHPLC and MALDI-IMS results are very comparable, reaching similar conclusions.

Likewise, the results from the comparison between normal and ccRCC studied by both techniques were analyzed. As previously mentioned, similar conclusion were reached; PE and SM were reduced, while PE-O/P lipid class was significantly upregulated in ccRCC. However, the differences between the profiles obtained by both techniques were larger than in the case of healthy tissue. One of the reasons can be the high heterogeneity of the tumors: although the same samples were used for both techniques, different cell populations may compose the portions used for each technique. This effect should be mitigated in part by the large number of samples explored, but the high heterogeneity of the tumors may require of even larger cohorts to be measured. Another explanation could be the overlapping in the MALDI-IMS lipid profile of PC and PE isobaric species. Although MS/MS and MS[3] has been performed in order to distinguish between isobaric species, complete separation of the contribution

of several overlapping species requires of sophisticated data treatment, while LC/MS does not face this problem.

8.6   Conclusions

In conclusion, our comprehensive lipidomics study using samples of tumoral and normal renal tissue of ccRCC patients revealed significant changes in the lipid profiles associated with ccRCC. Moreover, uHPLC and MALDI-IMS have proved to reach similar conclusions, although there are large discrepancies in the relative abundance of some of the individual species detected.

Altogether, this study leads to a better understanding of the pathophysiology of this common kidney cancer, which can be used to the development of novel and specific drugs that can be used to improve actual ccRCC treatments.

1. Lucarelli, G. *et al*. Integration of Lipidomics and Transcriptomics Reveals Reprogramming of the Lipid Metabolism and Composition in Clear Cell Renal Cell Carcinoma. *Metabolites* **10**, 509 (2020).

2. Sung, H. *et al*. Global cancer statistics 2020: GLOBOCAN estimates of incidence and mortality worldwide for 36 cancers in 185 countries. *CA: a cancer journal for clinicians* **71**, 209-249 (2021).

3. Cheville, J. C., Lohse, C. M., Zincke, H., Weaver, A. L. & Blute, M. L. Comparisons of outcome and prognostic features among histologic subtypes of renal cell carcinoma. *Am. J. Surg. Pathol.* **27**, 612-624 (2003).

4. Motzer, R. J. & Bukowski, R. M. Targeted therapy for metastatic renal cell carcinoma. *Journal of clinical oncology* **24**, 5601-5608 (2006).

5. Zhang, Y. *et al*. Addressing metabolic heterogeneity in clear cell renal cell carcinoma with quantitative Dixon MRI. *JCI Insight* **2**, 10.1172/jci.insight.94278. eCollection 2017 Aug 3 (2017).

6. Teloken, P. E. *et al*. Prognostic impact of histological subtype on surgically treated localized renal cell carcinoma. *J. Urol.* **182**, 2132-2136 (2009).

7. Davis, C. F. *et al*. The somatic genomic landscape of chromophobe renal cell carcinoma. *Cancer cell* **26**, 319-330 (2014).

8. Durinck, S. *et al*. Spectrum of diverse genomic alterations define non–clear cell renal carcinoma subtypes. *Nat. Genet.* **47**, 13 (2015).

9. Scelo, G. *et al*. Variation in genomic landscape of clear cell renal cell carcinoma across Europe. *Nature communications* **5**, 1-13 (2014).

10. Varela, I. *et al*. Exome sequencing identifies frequent mutation of the SWI/SNF complex gene PBRM1 in renal carcinoma. *Nature* **469**, 539-542 (2011).

11. Burrell, R. A., McGranahan, N., Bartek, J. & Swanton, C. The causes and consequences of genetic heterogeneity in cancer evolution. *Nature* **501**, 338-345 (2013).

12. Jonasch, E. *et al*. State of the science: an update on renal cell carcinoma. *Mol. Cancer. Res.* **10**, 859-880 (2012).

13. Kaelin Jr, W. G. Treatment of kidney cancer: insights provided by the VHL tumor-suppressor protein. *Cancer* **115**, 2262-2272 (2009).

14. Kim, W. & Kaelin Jr, W. G. The von Hippel–Lindau tumor suppressor protein: new insights into oxygen sensing and cancer. *Curr. Opin. Genet. Dev.* **13**, 55-60 (2003).

15. Cancer Genome Atlas Research Network. Comprehensive molecular characterization of clear cell renal cell carcinoma. *Nature* **499**, 43 (2013).

16. Krishnan, B. & Truong, L. D. Renal epithelial neoplasms: the diagnostic implications of electron microscopic study in 55 cases. *Hum. Pathol.* **33**, 68-79 (2002).

17. George, S., Choi, K., Pili, R. & Kazim, A. L. *The lipid metabolome of clear cell renal cell carcinoma (CCRCC).* (2012).

18. Xiang, M. *et al*. Exploring serum metabolic markers for the discrimination of ccRCC from renal angiomyolipoma by metabolomics. *Biomarkers in Medicine* **14**, 675-682 (2020).

19. Jones, E. E. *et al*. MALDI imaging mass spectrometry profiling of proteins and lipids in clear cell renal cell carcinoma. *Proteomics* **14**, 924-935 (2014).

20. Tamura, K., Horikawa, M., Sato, S., Miyake, H. & Setou, M. Discovery of lipid biomarkers correlated with disease progression in clear cell renal cell carcinoma using desorption electrospray ionization imaging mass spectrometry. *Oncotarget* **10**, 1688-1703 (2019).

21. Vijayalakshmi, K. *et al*. Identification of diagnostic metabolic signatures in clear cell renal cell carcinoma using mass spectrometry imaging. *International journal of cancer* **147**, 256-265 (2020).

22. Gerlinger, M. *et al*. Intratumor heterogeneity and branched evolution revealed by multiregion sequencing. *N. Engl. J. Med.* **366**, 883-892 (2012).

23. Keselman, H., Gaines, P. A. & Clinch, J. J. Tests for homogeneity of variance. *Communications in Statistics-Simulation and Computation* **8**, 113-129 (1979).

24. Gebhard, R. L. *et al*. Abnormal cholesterol metabolism in renal clear cell carcinoma. *J. Lipid Res.* **28**, 1177-1184 (1987).

25. Hoffmann, K. *et al*. Lipid class distribution of fatty acids including conjugated linoleic acids in healthy and cancerous parts of human kidneys. *Lipids* **40**, 1057-1062 (2005).

26. Yoshimura, K. *et al*. Analysis of renal cell carcinoma as a first step for developing mass spectrometry-based diagnostics. *J. Am. Soc. Mass Spectrom.* **23**, 1741-1749 (2012).

27. Saito, K. *et al*. Lipidomic signatures and associated transcriptomic profiles of clear cell renal cell carcinoma. *Scientific reports* **6**, 1-12 (2016).

28. Emoto, K., Toyama-Sorimachi, N., Karasuyama, H., Inoue, K. & Umeda, M. Exposure of phosphatidylethanolamine on the surface of apoptotic cells. *Exp. Cell Res.* **232**, 430-434 (1997).

29. Kaku, Y., Tsuchiya, A., Kanno, T., Nakano, T. & Nishizaki, T. Dipalmitoleoyl-phosphatidylethanolamine induces apoptosis of NCI-H28 malignant mesothelioma cells. *Anticancer Res.* **34**, 1759-1764 (2014).

30. Kiebish, M. A., Han, X., Cheng, H., Chuang, J. H. & Seyfried, T. N. Cardiolipin and electron transport chain abnormalities in mouse brain tumor mitochondria: lipidomic evidence supporting the Warburg theory of cancer. *J. Lipid Res.* **49**, 2545-2556 (2008).

31. Koppenol, W. H., Bounds, P. L. & Dang, C. V. Otto Warburg's contributions to current concepts of cancer metabolism. *Nature Reviews Cancer* **11**, 325-337 (2011).

32. Dória, M. L. *et al*. Lipidomic approach to identify patterns in phospholipid profiles and define class differences in mammary epithelial and breast cancer cells. *Breast Cancer Res. Treat.* **133**, 635-648 (2012).

33. Dória, M. L. *et al*. Lipidomic analysis of phospholipids from human mammary epithelial and breast cancer cell lines. *J. Cell. Physiol.* **228**, 457-468 (2013).

34. Zhuo, R., Rong, P., Wang, J., Parvin, R. & Deng, Y. The potential role of bioactive plasmalogens in lung surfactant. *Frontiers in Cell and Developmental Biology* **9**, 79 (2021).

35. Movahed, Z. G., Rastegari-Pouyani, M., hossein Mohammadi, M. & Mansouri, K. Cancer cells change their glucose metabolism to overcome increased ROS: One step from cancer cell to cancer stem cell? *Biomedicine & Pharmacotherapy* **112**, 108690 (2019).

36. Ding, T. *et al*. SMS overexpression and knockdown: impact on cellular sphingomyelin and diacylglycerol metabolism, and cell apoptosis. *J. Lipid Res.* **49**, 376-385 (2008).

37. Barcelo-Coblijn, G. *et al*. Sphingomyelin and sphingomyelin synthase (SMS) in the malignant transformation of glioma cells and in 2-hydroxyoleic acid therapy. *Proc. Natl. Acad. Sci. U. S. A.* **108**, 19569-19574 (2011).

38. Ling, Y. *et al*. Tumor necrosis as a poor prognostic predictor on postoperative survival of patients with solitary small hepatocellular carcinoma. *BMC Cancer* **20**, 1-9 (2020).

Chapter 9

Changes in lipid molecular species for aggressive astrocytoma and its evolution after temozolomide treatment revealed by MALDI-IMS

IMS is not only able to characterize the lipidome of cells in a given metabolic stage and the changes in the context of a disease, but also alterations due to treatments. As a demonstration, we present here the first IMS study of the effects of temozolomide, the most commonly used chemotherapy treatment for glioblastoma, in the lipid fingerprint of tumoral and healthy human brain samples.

9.1   Introduction

Glioblastomas (GBM), the most aggressive type of astrocytomas, are the most frequent malignant primary brain tumor, representing approx. 15 % of all brain tumors[1]. The worldwide incidence of GBM is between 3-4 per 100000 persons (National Cancer Institute), and diagnosis is typically made by a combination of a computed tomography scan, magnetic resonance imaging scan, and tissue biopsy[1]. The standard treatment is a combination of surgery followed by chemotherapy and radiotherapy[2]. Unfortunately, this treatment renders a low median survival of approximately 15 months[3]. In addition, the reference chemotherapeutic agent is the temozolomide (TMZ), a DNA alkylating agent with severe side effects that includes dizziness and blurred vision. In fact, around 20% of patients treated with TMZ discontinue the treatment due to side effects[4]. The high-rate discontinuity of the treatment together with the poor improvement in the overall survival of the TMZ classifies this treatment as a palliative and as a non-curative therapy[4]. In this context, the study of glioblastoma, as in many other cancers, is hindered due to the lack of good models to mimic its genetic heterogeneity and tumor microenviroment[5]. However, great advances in genomics have provided new evidences regarding the development of GMB. For instance, *TP53, ATRX, TERT, NF1, PTEN* and *EGFR* have been identified as common GBM gene drivers [6,7]. Besides, mutations on *IDH1* or *IDH2* genes are related to a better patient outcome[8]. Moreover, three transcriptomic molecular subtypes were defined based on intratumoral variability the different genomic alterations: proneural, classical, and mesenchymal, which was an important step for the development of more accurate treatment strategies[9]. This classification also allowed the identification of specific epigenetic alterations as well as molecular subtype-dependent interactions with the immune microenvironment[9].

Second to the adipose tissue, the brain is the most lipid enriched organ in the body, particularly, in membrane lipids, phospholipid and sphingolipids. Cell membrane lipid composition, or membrane lipidome, includes hundreds of molecular species, each of them with specific roles, which remains most unknown. Hence, the lipidome has proven to be highly sensitive to pathophysiological processes, and alterations in cell lipid profile are associated with multiple pathophysiological processes like differentiation [10–13], proliferation [14–16], and cancer development [17–19]. In fact, membrane lipids are sensitive enough to be used as biomarkers for different cancer types [20–22]. In the last years, the systematic use of MS-based techniques to describe lipidomes allows strengthen the use lipid profiles as a tool to stratify patients[23]. The irruption of IMS techniques into the lipidomic field have clearly demonstrated how specific and sensitive the lipidome is to both physiological changes and pathological insults. Brain tissue has been one of the most analyzed tissues by different IMS techniques, showing different lipid species distribution among grey and white matter in human samples[24–

[26]. Thus, some studies showed the potential of lipidomics to study GBM. In human xenografts models, differences in glycosphingolipid and triglyceride were revealed, sustaining the critical role of some lipids in tumor growth[27]. The application of machine learning protocols coupled to imaging lipidomic techniques showed that gliomas can be rapidly classified based on their histological sections lipid profiles, offering a potential tool for intraoperative examination and rapid classification[23].

Interestingly, lipid-related genes present altered regulation in this disease, such as *SCD1*[28], *ELOVL6*[29], *15-HPGD*[30] and ELOVL2[31]. In this sense, and in the context of a disease with ineffective therapies, the study of GBM lipidome could reveal new targets to treat either the disease or the TMZ side effects.

9.2   Objectives

In this section, we characterized the lipid changes occurring in a GBM by using MALDI-IMS. This technique, allowed characterizing the lipid changes occurring at the proliferative zones of GBM tissue. Moreover, we analyzed how the TMZ treatment affects the GBM and healthy tissue lipidome. Our results showed changes in various lipid species like the PI, sulfatides, and PE plasmalogen in the GBM tissue. Thus, the PE plasmalogen species were the most affected by the tumor transformation, showing a general increase in PUFA-containing species. On the other hand, the treatment by TMZ of the healthy and tumor brain tissue revealed that, at short-term treatments, this compound barely affects the GBM tissue. However, this compound induced multiple changes in the healthy brain, being the PE plasmalogen species the most affected. In addition, the analysis and interrogation of different genomic databases allowed a better understanding of the lipid-related genes with a potential implication in the observed lipid changes. This genomic analysis revealed several genes with different expression depending on the molecular classification of the GBM. Globally, the results showed newly described coordinated lipid-genetic changes that could set the base for other approaches for the GBM treatment.

9.3   Experimental section

Sample collection

Sample collection for this study was specifically approved by the Ethics Research Committee of the Balearic Islands (nº IB 3626/18 PI). Informed consent in writing from was obtained for each patient enrolled in the study. Four patients harboring brain tumors suggestive of GBM, newly diagnosed after neurological symptoms, in which

surgical resection or open biopsy were indicated were included. The anatomopathological analysis confirmed the diagnosis of glioblastoma in the four patients recruited. The patients received the pharmacy-compounded solution of 5-aminolaevulinic acid 1 h before anesthetic induction. Total dose was according to patient weight (20 mg/kg). The Pentero® (Zeiss®, Oberkochen, Germany) surgical microscope with BLUE 400TM integrated fluorescence module was used for surgical resections. Between 3 and 4 h after administration of 5-aminolevulinic acid, positive tumor samples and healthy samples were obtained during surgical resection from the security region and immediately incubated in DMEM-F12 in the presence or absence of TMZ (10 mg/ml) for 4 h at 37 °C and 5% O_2. Then were collected and stored at − 80 °C until processing.

Sections of 10 µm thick were obtained with a cryostat (Leica CM3050S) at −20 °C without using cryoprotective substances and embedding material. Sections were placed on plain-glass microscope slides for MALDI-IMS analysis and consecutive sections for IF analysis were placed on positive charged adherent plain glass microscope slides. Samples were stored at − 80 °C until posterior MALDI-IMS or immunofluorescence analysis.

MALDI-IMS analysis

A total of 40 histological sections obtained from 5 different patients were prepared and analyzed by MALDI-IMS as described in **Chapter 3**. Briefly, MBT or DAN were used as matrix for positive or negative-ion detection, respectively, and deposited with the aid of our in-house designed sublimator device, which allows to perfectly control all the parameters involved in the sublimation process[79]. Sections of brain biopsies from different individuals were scanned in positive and negative ion mode, a MALDI-LTQ-Orbitrap XL (Thermo Fisher, San Jose, CA, USA).

Data were acquired with a mass resolution of 60,000 in the scanning range of 550-1000 for negative-ion mode and 480-100 Da for positive ion mode. Two microscans of 10 laser shots were recorded for each pixel and the raster size used was 50 microns. Spectra were aligned and analyzed using in-house programs in developed in Matlab (MathWorks, Natick, USA). Lipid assignment was based on the comparison between the experimental m/z and the species in the software's database (< 33,000 lipid species plus adducts) and in the lipid maps database (www. lipidmaps.org). Mass accuracy was always better than 6 ppm. For m/z channels with several lipid assignment, "On-tissue" MS/MS and MS[3] was carried out in order to unequivocally assign them. Although phospholipids ether (-O) and vinyl-ether (-P) linkage can not be distinguish by mass spectrometry, PE plasmalogens (PE-P) are more abundant than PE-O subgroup in brain [40]. Consequently, in this chapter, we named all the ether bonds-contained PE as plasmalogens or PE-P. Nevertheless, we can not discard the presence of PE-O.

For the sake of clarity, only species present in at least 80% of the analyzed samples were considered for further statistical analysis

Interrogation of GBM gene expression and methylation datasets

Human TCGA GBM Affymetrix U133a and Methylation27k datasets were interrogated using Xena Browser. The data relative to the selected genes showed in **Figure 9.** were downloaded and statistical differences were measured independently.

Co-Expression Modules identification Tool (CemiTool)

CEMiTool was used to identify co-expression of lipid related genes associated with the GBM molecular subtypes, according to Verhaak et al[43]. For this, the TCGA-GBM[41] AffyU133a dataset and associated clinical data were downloaded and analyzed. The CEMiTool analysis returned seven modules with a different gene number and composition. Six of the modules were positively correlated, according to the normalized enrichment score (NES), with some of the four molecular subtypes applied as phenotype labels (**Figure 9.9**). The parameters used in CEMiTool were the following: value of Beta chosen = 9; Pearson correlation coefficient, dissimilarity threshold used as cutoff on hierarchical clustering = 0.8; similar modules were merged, the number of module returned = 8; area under curve / total area in the Beta vs R squared graph = 0.802; determination coefficient ("scale-freeness" of the resulting network) = 0.939.

Gene ontology (GO) analysis

The GO was made using the DAVID bioinformatic resources 6.8[80].

Data analysis

To establish the tissue clusters, data from each section were analyzed using our own segmentation algorithm (HD-RCA), which groups the pixels according to the similarity of their spectra. The number of clusters was varied from 2 to 8 in an attempt to find the best correlation between immunohistochemically-stained histological section and the MALDI-IMS images. To statistically evaluate the differences in the lipid fingerprints among the identified areas, T-test, ANOVA and Post-Hoc analysis was computed using SPSS Statistics 25.0 for Windows (IBM, Armonk, NY, USA). PCA analysis and separation models were carried out by Orange Biolab 2.7.8 (Ljubljana, Slovenia)[81]. For TCGA GBM gene expression and methylation, multiple comparison ordinary one-way ANOVA with Tuckey adjustment was computed using GraphPad Prim (version 8.0).

9.4   Results

Lipid fingerprint discriminates between the healthy and tumor brain

In attempt to best characterize the lipidome of GBM, we focused on comparing the lipid levels of five different human grade IV glioblastoma samples and its surrounding healthy tissue.

Previous studies from our group has shown the high correlation between IMS lipid clusters resolved by *K-means* and HD-RCA algorithms, and histological tissue structures, cellular types and states[13,17,32,33]. In this study, one of the challenges was to correlate the lipid distribution with their anatomical counterpart. On one hand, the fine architecture is compromised during the incubation in cell culture medium. On the other hand, the malignization process implies a loss of tissular architecture. Taking this into account, we focused on distinguishing those cells exhibiting a high proliferative rate. Different studies has shown the important role of highly proliferative cells in tissue maintenance and cancer progression, particularly the marker of cell proliferation Ki-67 (MKI67), which is involved in the perichromosomal layer during the mitosis[34], and has been reported as a prognostic marker in GBM[35–37]. We used the MKI67+ staining to define regions of interest by immunofluorescence. These MKI67+ regions were used to identify the lipid cluster overlapping with the highly proliferative region in both healthy and GBM biopsies. Hence, the MKI67 staining revealed different intensity regions in tumor tissue, while in the healthy tissue the staining intensity was homogenous and rather low **Figure 9.1.**

A representative portion of the lipidome has been assessed by measuring in positive- and negative-ion modes, leding to the detection of 124 different lipid species divided in 16 lipid families. As appears in some examples in **Figure 9.1**, these species are not uniformly distributed in either healthy or in tumoral samples. For example, it is well known that SFT d42:2 is found at higher concentration in white matter[25, 26] while concentration of PI 38:4 correlates with neuron cell bodies. Therefore, as can be appreciated in **Figure 9.1** grey and white matter can be distinguished using PI 38:4 and SFT d42:2 distribution. Interestingly, the complementary of PI/SFT distributions is no longer observed in the tumor samples.

Moreover, with aiming at establish a comparison between IF and IMS images, a clustering algorithm (HD-RCA in **Figure 9.1**) was applied which group the pixels with similar lipid profile. Thus, IMS data from clusters which correlate with the proliferation zone in their consecutive IF stained sample were selected for further analysis (see MKI67+ cluster in **Figure 9.1**). In the case of some samples of healthy tissue, as the MKI67 marker is homogeneously distributed over the sample, the average spectrum of the whole section was used.
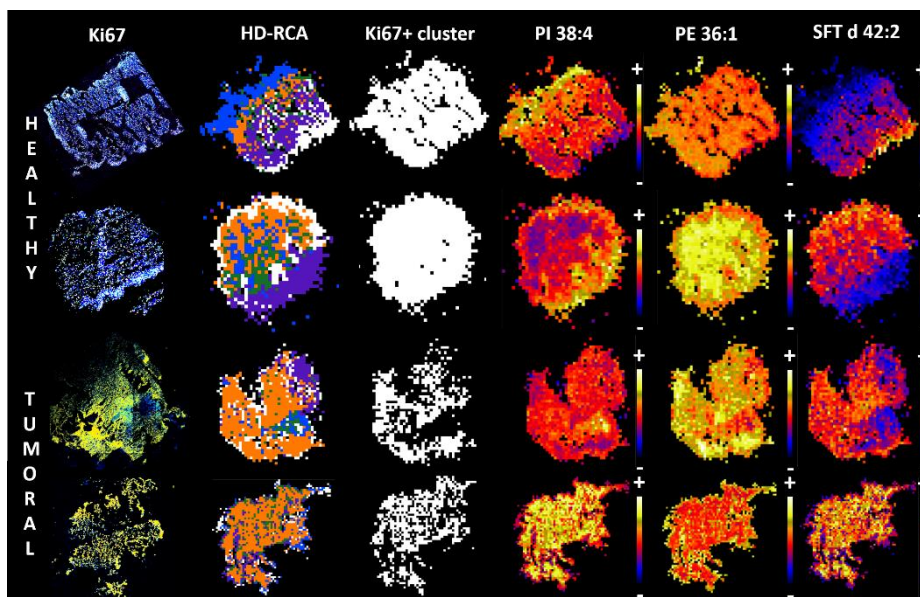
Figure 9.1. *IF and MALDI-IMS images of healthy and tumoral human brain tissue. From left to right MKI67 proliferation marker, HD-RCA clustering algorithm, cluster selected as MKI67+ and three representative lipid distributions are displayed. Orange signal corresponds to proliferation regions (MKI67+) and blue staining correlates with the DAPI marker.*

Comparison of the glioblastoma clusters selected as MKI67+ proliferation zones with the healthy tissue showed clear differences. An initial unsupervised PCA of the dataset of each group revealed a specific lipid fingerprint concomitant to each study group (**Figure 9.2A**). In addition, molecular classification and confusion matrix was generated using four different models resulting in an overall sensibility and specificity of 100% (**Figure 9.2B and C**). Moreover, a broad analysis of the summation of the relative intensity of the lipid species grouped into families was performed (**Figure 9.2D**). While PE's, PI's and SM's showed a significant increase, SFT were decreased in tumor tissue. These results confirm the high influence GMB transformation has over brain lipid metabolism.
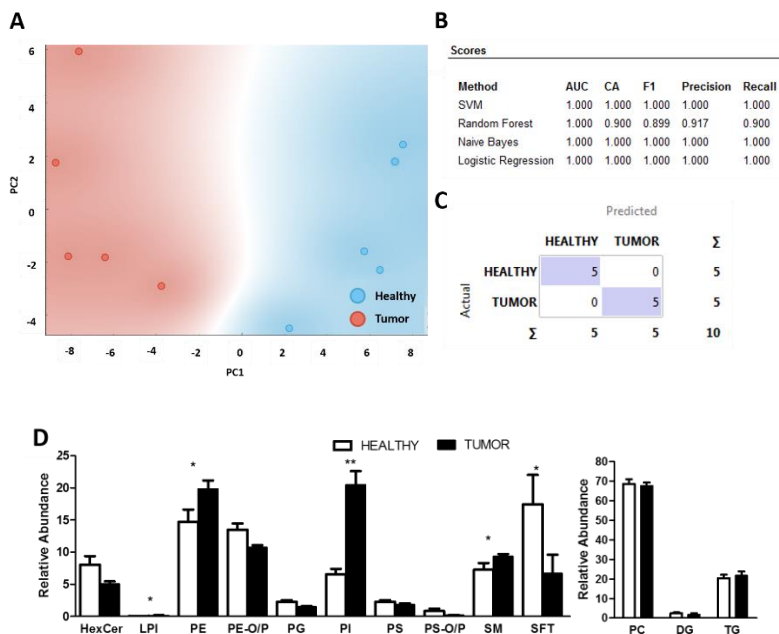
Figure 9.2. (A) *PCA analysis of the proliferation clusters (MKI67+ areas) selected as healthy and glioblastoma tissue. There was a clear separation between healthy brain (blue), and glioblastoma (red) implying distinct lipid fingerprints. Variance explained by the two components: 80,4%.* *(B)* *Summary of the performance of several classification models.* *(C)* *Confusion matrix showing classification results by Logistic Regression.* *(D)* *Bar charts of the variation of the relative abundance of the lipid families in healthy brain and Glioblastoma. Relative abundances of PC, DG and TG lipid families were obtained in positive-ion mode. Values are expressed as mean ± S.E.M (n=5 in both groups). Statistical analysis was assessed using T-test analysis. * = p-value<0.05, **= p-value<0.01.*

In order to better appreciate the changes which occur within the lipid classes, data from each lipid family were normalized and analyzed independently (**Figure 9.3**).

Of special interest is the difference in the impact on the diacyl PE and the PE plasmalogen (PE O/P) species. Thus, while total diacyl PE levels were greatly increased in GBM tissues, this change is not significative for any individual PE specie, except for PE 34:0 and 36:4 (**Figure 9.2, Figure 9.3A**). The most abundant PE diacyl species were the 36:1, the 40:6, and the 38:4 (35.6, 13.9, and 11.3%, respectively) in the healthy brain. In GBM tissue, the most abundant species were the 36:1, the 38:4, and 36:2 (30.0, 13.4, and 10.1%, respectively).

Conversely, while PE plasmalogens total levels were similar in both study groups, the disease affected profoundly PE plasmalogens molecular species. Thus, in healthy tissue, the most abundant PE plasmalogen species was PE P-36:2 and 38:4 followed by 34:1 and 40:6 species (20.8, 14.7, 13.7, and 10.2% of total PE plasmalogen, respectively). Conversely, the most abundant PE plasmalogen species were 38:4, 36:4, 40:6 and 38:6 in the MKI67+ GBM cluster (22.0, 14.8, 10.4, and 10.3% of total PE plasmalogen, respectively). Interestingly, when comparing GBM to healthy tissue, there was a solid tendency in increasing in 36C- and 38C- PUFA-containing species in detriment to 40C-PUFA- and MUFA/DUFA-containing species. This shift was statistically significant for 36:2 (20.8 vs. 3.6 %), 36:4 (1.9 vs. 14.8%), 38:4 (14.7 vs. 22.0%), 38:6 (2.8 vs. 10.3%), and 40:5 (7.1 vs. 4.3%) (**Figure 9.3B, Figure A.9.1**).

Concerning PC's, little changes were observed whose relevant changes are only the significant increase in PC 36:2 and the marked downregulation of 36:4 and 38:4 PC species during glioblastoma (**Figure 9.3C**).

Regarding PI species, PI 38:4 presented the highest relative abundance in healthy tissue (47,5%) followed by 38:6 and 34:1 species (11,7% and 11,3% respectively). Glioblastoma showed a similar profile, but with a reduced proportion of PI 38:4 (76,2%) followed by the 38:5 and 36:2 species (5'6% and 5'5% respectively). Thus, comparing healthy and tumoral samples, the significant statistical differences caused by glioblastoma in PI lipid families were the upregulation of PI 38:4 (47,5% vs. 76,2%) and the marked decreasing of PI 34:1 (11,3% vs. 3,9%) (**Figure 9.3D**).

In the case of SM lipid family (**Figure 9.3E**), the main sphingomyelin species for healthy brain were SM d36:1, SM d42:2 and SM t32:2 species (27.8, 17.7, and 15.1% respectively) while SM d34:1, SM d36:1 and SM t32:2 (27.1, 20.1, and 16.3% respectively) had the higher relative intensity in glioblastoma. The most striking changes were the highlighted increase in 34:1 and the decrease in d42 and t34:2 species when glioblastoma occurs.

Sulfatides, as **Figure 9.3F** shows, presented multiple perturbations in tumor tissue. While the major species in healthy brain were SFT d42:2, SFT t42:1 and SFT d42:1 (50.8, 15,9, and 11,3% respectively), in tumor samples SFT d42:2, SFT d36:3 and SFT d36:4 (23,9, 21,0, and 11,4% respectively) were the prevailing species. Interestingly, a downregulation of all the detected sulfatides with number of carbons higher than 40 and an upregulation of the sulfatides with 34 and 36 number of carbons was observed in the tumor samples.

Finally, regarding DG and TG (**Figure 9.3G, H**), DG 34:2 and TG 40:5 were the most abundant species in both healthy and glioblastoma samples. However, DG and TG levels

remained practically unchanged in glioblastoma. Only TG 40:7 showed a significant
increase in tumoral tissue in comparison with control brain.
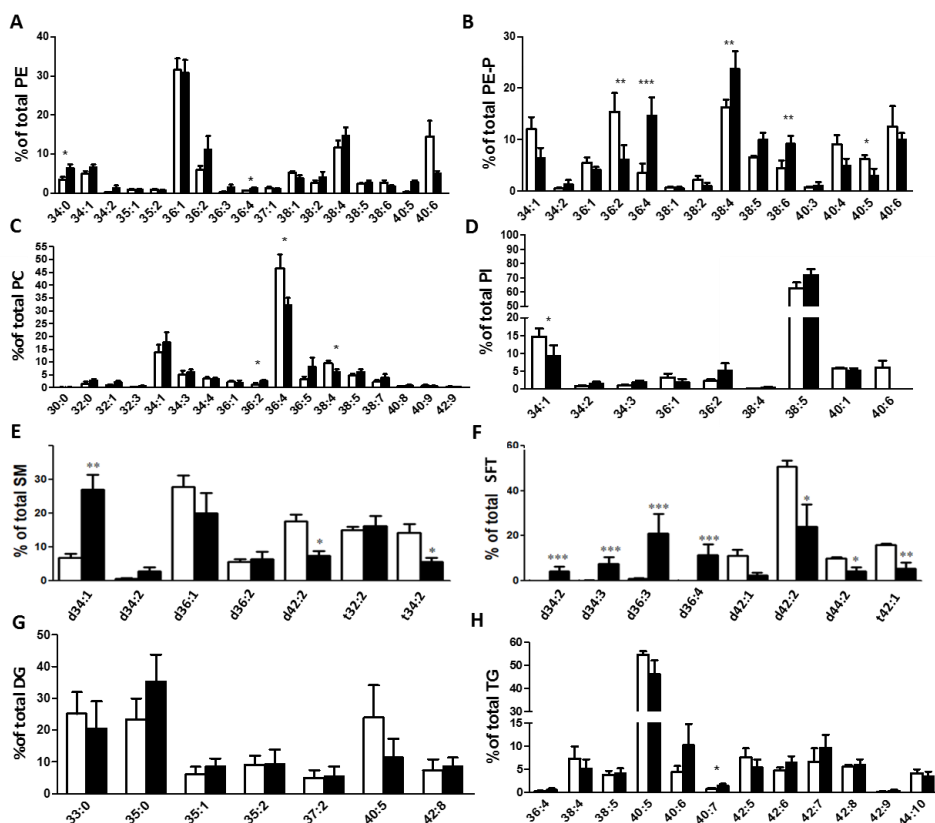
Figure 9.3. *Lipid fingerprint of healthy and tumor brain. Each graph represents the
percentage of each molecular specie belonging to (A) PE, (B) PE-O/P, (C) PC, (D) PI, (E)
SM, (F) SFT, (G) DG, and (H) TG lipid classes. Values are expressed as mean ± S.E.M (n=5
in both groups). Statistical analysis was assessed using T-test analysis. * = p-value<0.05;
**= p-value<0.01; *** =p-value<0.001.*

Temozolomide effects over glioblastoma lipidome

GBM samples with and without TMZ treatment were analyzed by MALDI-IMS of lipids.
As in the previous section, correlating IMS clusters with MKI67 positively-stained tissue
regions were selected and analyzed (**Figure 9.4**).
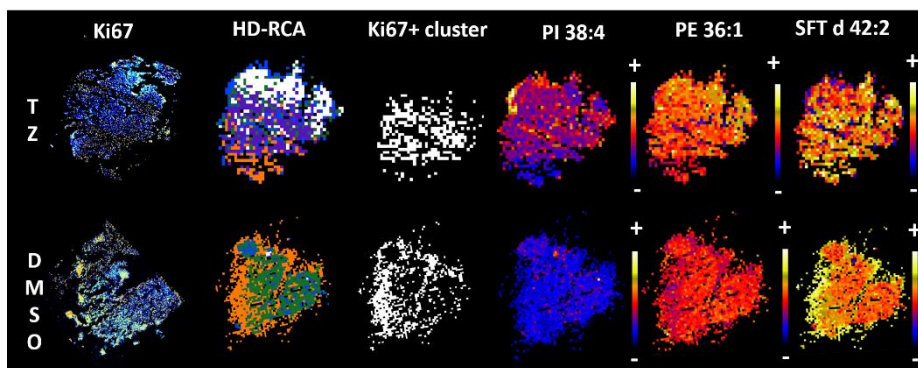
Figure 9.4. *IF and MALDI-IMS images of tumoral human brain tissue. From left to right MKI67 proliferation marker, HD-RCA clustering algorithm, cluster selected as MKI67+ and three representative lipid distributions. Orange signal corresponds to proliferation regions (MKI67+) and blue staining corresponds to the DAPI marker (non-tumor areas).*

PCA from Figure 9.5A revealed differences in the lipid signature between TMZ-treated and non-treated glioblastoma. Thus, the two groups were successfully differentiated based on their lipid profile. In good agreement, the classification models also showed an excellent sensibility and specificity (**Figure 9.5B**). In fact, the classification power and the confusion matrix of the logistic regression model revealed that a perfect classification was achieved (**Figure 9.5B,C**). However, the analysis of the variation in the relative abundance of the lipid families show no significant differences between the two groups, pointing to a multi-variable classification (**Figure 9.5D**).

In addition, as in the last section, the changes in the expression of individual lipid species were analyzed independently. Thus, in the case of PE-O/Ps, the most abundant species in the non-treated glioblastoma were PE P-38:4, PE-P 36:4, and PE-P 40:6 (25,4%, 15,0%, and 12,7% respectively) while PE-P 38:4, 36:4 and 34:1 (22,2%, 23.4% and 12,1% respectively) were the predominant species in TMZ-treated glioblastoma. Moreover, T-test analysis revealed the significant upregulation of PE-P 36:4 and the downregulation of PE-P 40:4 caused by TMZ treatment (**Figure 9.6A**).
Regarding PE subclass, the temozolomide treatment just induced minor changes regarding the molecular species. Only PE 38:1 shows a marked downregulation compensated by an increase in 34:2, 36:4 and 38:5 molecular species (**Figure 9.6B**).

Focusing on PC species (**Figure 9.6C**), the most intense species are PC 36:4, PC 34:1 and PC 38:4 in both DMSO and TMZ treated glioblastoma. However, only PC 38:4 shows a significant upregulation in glioblastoma samples.

Finally, it is worthy of mention the case of PI's, SM's, DG's and TG's, whose abundance was not affected by the treatment. As can be seen in **Figure 9.6D-H**, no significant changes associated to the administration of temozolomide were detected in the species of those families.
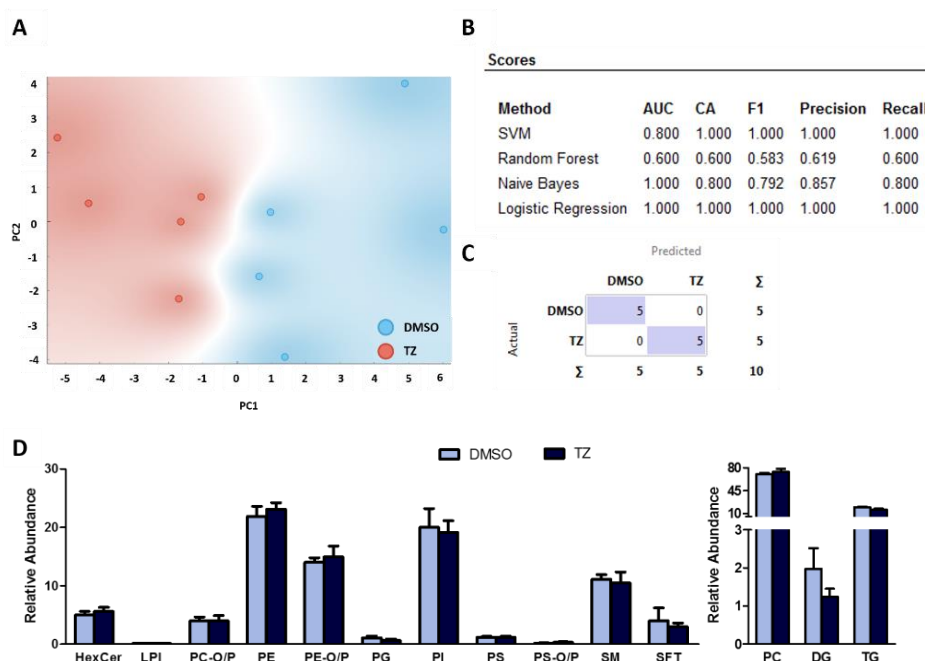
Figure 9.5. (A) PCA analysis of the IMS data from proliferation clusters selected as *temozolomide treated (TMZ) and non-treated (DMSO) glioblastoma. There was a clear separation between the two groups implying distinct lipid fingerprints. Variance explained by the two components: 78,4%.* ***(B)*** *Summary of the models' performance classifications.* ***(C)*** *Confusion matrix showing classification results by Logistic Regression.* ***(D)*** *Bar charts of the relative abundance variation of the lipid families in DMSO treated and TMZ treated glioblastoma. DG and TG lipid families were obtained from positive ion mode detection. Values are expressed as mean ± S.E.M (n= 5 in both groups). Statistical analysis was assessed using T-test analysis. * = p-value<0.05; **= p-value<0.01; *** =p-value<0.001.*
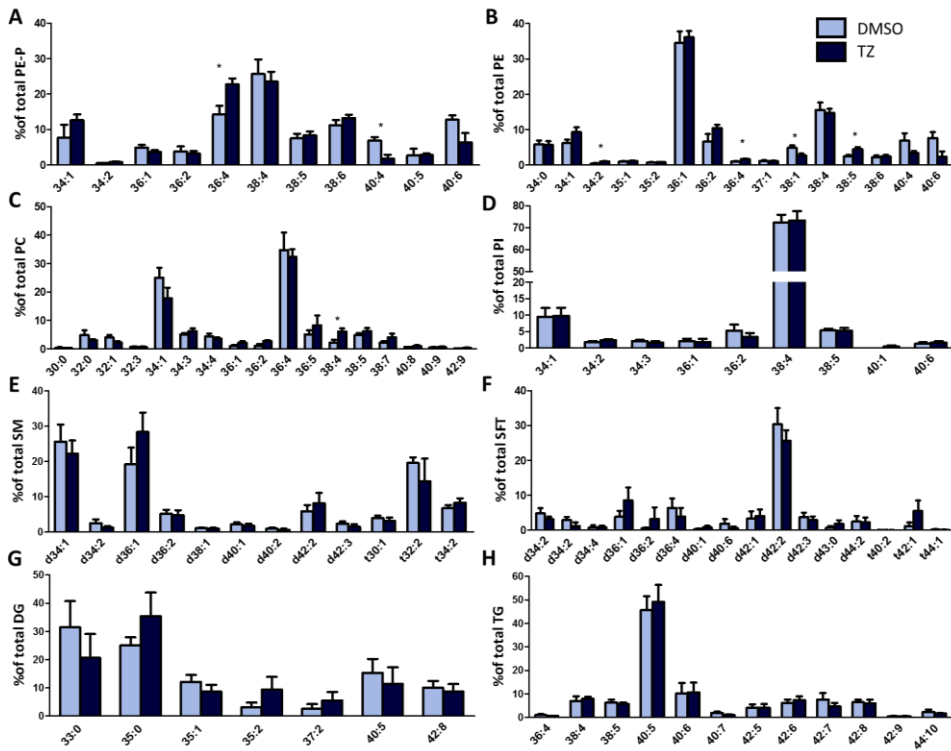
Figure 9.6. *Lipid fingerprint of non-treated glioblastoma (DMSO) and temozolomide treated glioblastoma (TMZ). Each graph represents the percentage of each molecular specie belonging to (A) PE-P, (B) PE, (C) PC (D) PI, (E) SM, (F) SFT, (G) DG, and (H) TG lipid classes. Values are expressed as mean ± S.E.M (n=5 in both groups). Statistical analysis was assessed using T-test analysis. * = p-value<0.05; **= p-value<0.01; *** =p-value<0.001.*

Temozolomide exerts multiple effects over the healthy brain lipidome

One of the most relevant issues addressing glioblastoma treatment is the need to discontinue chemotherapy due to the treatment side effects. Thus, unraveling the effects of TMZ in non-tumoral tissue could be of keen interest. For that, four healthy biopsies were treated with TMZ for 4h, while four additional brain biopsies were incubated in DMSO, acting as control group.

Interestingly, temozolomide treatment induced several lipid changes on heathy brain tissue. As can been appreciated in **Figure 9.7A,** the PCA revealed a clear separation between lipid fingerprints of the two study groups. The best classifier was Logistic regression with an agreement of 100% (**Figure 9.7B**) as indicated also by its confusion matrix (**Figure 9.7C**). Furthermore, as regards of the changes in lipid classes,

T-test analysis of the summation of intensities of each lipid specie grouped into families shows a significant increase in LPI and PI relative abundance and a marked downregulation in HexCer's and SFT's caused by temozolomide treatment (**Figure 9.7D**).
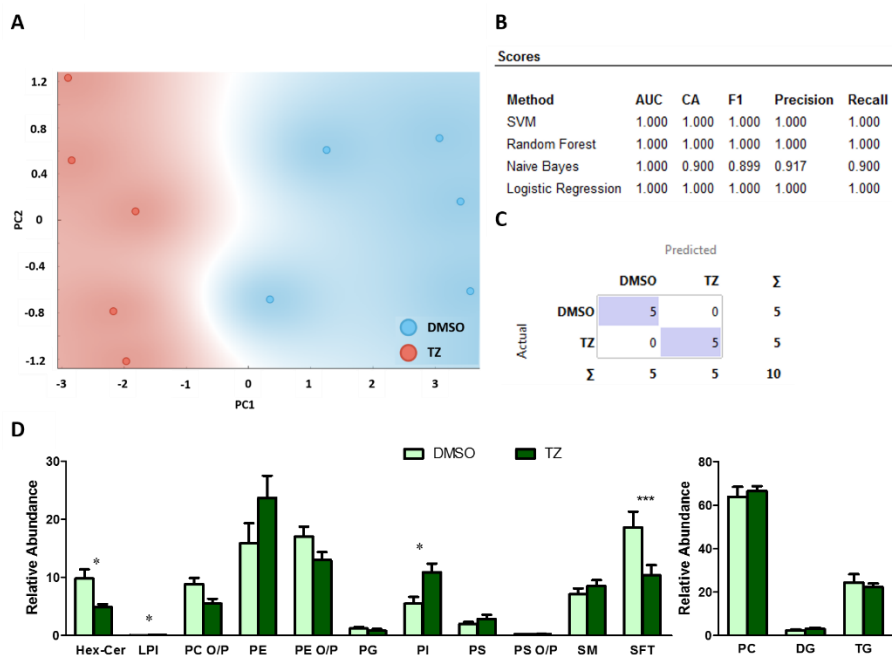
Figure 9.7. ***(A)*** *PCA analysis of the IMS data from temozolomide treated (TMZ) and non-treated (DMSO) healthy brain. There was a clear separation between the two groups implying distinct lipid fingerprints. Variance explained by the two components: 87,8%.* ***(B)*** *Summary of the performance of the classifications.* ***(C)*** *Confusion matrix showing classification results by Logistic Regression.* ***(D)*** *Bar charts of the variations in the relative abundance of the lipid families detected in DMSO- and TMZ-treated samples. PC, DG and TG lipid families were obtained from the experiments recorded in positive-ion mode. Values are expressed as mean ± S.E.M (n= 5 in both groups). Statistical analysis was assessed using T-test analysis. * = p-value<0.05; **= p-value<0.01; *** =p-value<0.001.*

The analysis of the lipid species in each family also reveals changes in the lipidome. The most abundant PE plasmalogen species in healthy tissue treated with TMZ were 40:6, 38:4 and 40:4 (22.0%, 20.0% and 9.6% respectively) while 38:4, 36:2 and 34:1 were the predominant species in DMSO-treated healthy brain samples (16,2%, 15,5% and 12,3% respectively). In addition, comparing the vehicle and TMZ treatment most of the MUFA and DUFA-containing PE plasmalogen species were downregulated by

temozolomide. Specifically, 34:1, 35:1, 36:1 and 36:2 shows a significant variation (**Figure 9.8A**).

However, this decrease in MUFA- and DUFA-containing species was compensated by a clear increase in the PUFA-containing ones, being significant the upregulation of 40:6 and 40:7 species (**Figure 9.8A, Figure A.9.3**).
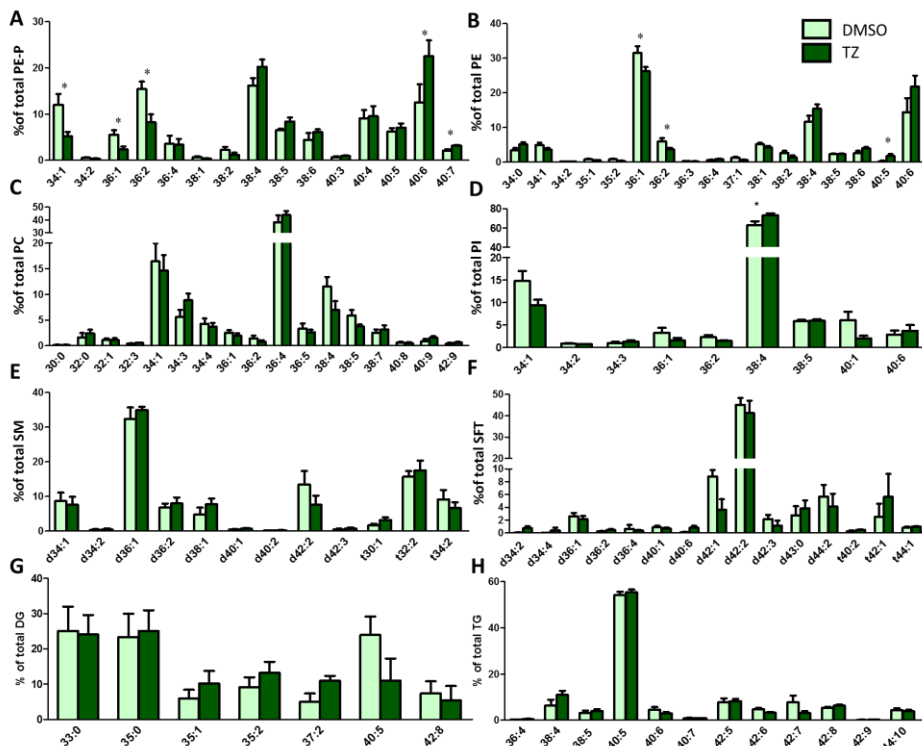
*Figure 9.8. Lipid fingerprint of non-treated (DMSO) and temozolomide treated (TMZ) healthy brain. Each graph represents the percentage of each molecular specie belonging to **(A)** ether/vinyl-ether phosphatidylethanolamine (PE-O/P), **(B)** phosphatidylethanolamine (PE), **(C)** phosphatidylcholine (PC) **(D)** phosphatidylinositol (PI), **(E)** sphingomyelin (SM), **(F)** sulfatide (SFT), **(G)** diacylglicerol (DG), and **(H)** triacylglicerol (TG) lipid families. Values are expressed as mean ± S.E.M (n=5 in both groups). Statistical analysis was assessed using T-test analysis. * = p-value<0.05.*

It is worthy of mention that the same pattern can be seen in PE species which confirms the TMZ effect over healthy tissue of decreasing the MUFA and DUFA containing species and increasing PUFA-containing ones (**Figure A.9.3**). The decrease is significative in PE 36:1 and PE 36:2 and the upregulation is highlighted in PE 40:5 (**Figure**

9.8B). However, as regards PI's, TMZ only significantly induces the increase of PI 38:4, the major lipid species within this class (62.5% vs 78.1%).

On the other hand, the treatment with TMZ did not change drastically the lipid composition of PC's (**Figure 9.8C**), sphingolipids (**Figure 9.8E,F**) nor glycerolipids (**Figure 9.8G,H**) in healthy brain tissue.

Impact of GBM on lipid enzymes at the transcriptional level

This section was developed in the "Lipids in Human Pathology" research group at the IdISBa (Palma, Balearic Island) lidered by Dr, Gwendolyn Barceló Coblijn.

The brain is one of the tissues showing the most singular lipid profile and, as expected, a complex process as tumorigenesis had a profound impact on it. In order to outline the mechanisms accounting for the altered lipid phenotypes observed in GBM and delve into the regulatory mechanisms, we interrogated a transcriptome database publicly accessible, in particular, the TCGA-GBM transcriptome database[41]. We performed a co-expression modular analysis (CEMiTool)[42] applying the molecular subtypes labels described by Verhaak et al.[43] on the TCGA-GBM AffyU133a dataset and associated clinical data (**Figure 9.9**).

The CEMiTool analysis returned seven modules wherein it was possible to distinguish several hub genes. Using the normalized enrichment score (NES), we identified six of the modules correlating positively with some of the four molecular subtypes applied as phenotype labels: Classical, Mesenchymal, Proneural, and Neural subtypes (**Figure 9.9**). Thus, the M1 module showed a high correlation with the Classical molecular subtype module, the M2 and M4 modules correlated with Mesenchymal subtype, the M5 and M6 modules did with Proneural subtype, and the M3 modules with Neural subtype and Normal samples.
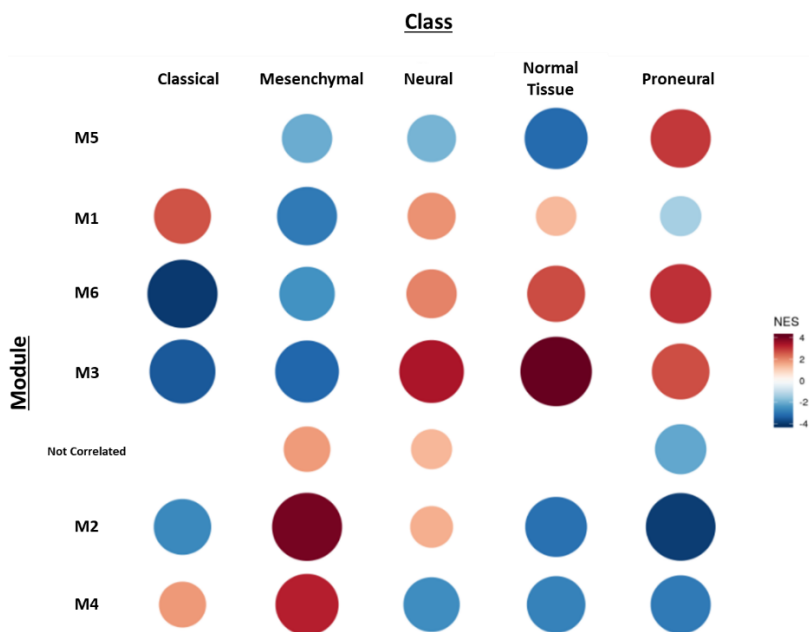
Figure 9.9. *TCGA-GBM transcriptome data (AffyU133a) co-expression modular analysis of the four molecular subtypes described by Verhaak et al.* [41,43] *including the normal tissue samples. Modules M1 presented a high normalized enrichment score (NES) with the Classical molecular subtype, module M2 and M4 with Mesenchymal subtype, M5 and M6 with Proneural subtype, and M3 with Neural subtype and Normal samples.*

Based on the differences observed in the Healthy vs. GBM comparison of the lipidomic results obtained by MALDI-IMS (**Figure 9.2**), we decided to interrogate the genes coding for enzymes involved in PUFA- and sphingolipid metabolism (**Table 9.1**). Among them, genes corresponding to *FABPs, ELOVL*, inositol polyphosphate-5-phosphatase F (INPP5F), secreted *PLA2s*, *PTGS2* (*COX2*), *ALOXs*, diacylglycerol kinase B (*DGKB*), and UDP-galactose-ceramide galactosyltransferase (*UGT8*) were identified (**Table 9.1**).

The Classical and Mesenchymal subtype modules contained several enzymes involved in the fatty acid uptake and intracellular signaling (*FABPs*), fatty acid hydrolysis (*PLA2s*), PUFA synthesis (*ELOVL2*), and eicosanoid synthesis (*PTGS2, ALOXs*), which would go in line with the increase in PUFA in PE P- and PI. On the other hand, the Neural subtype was positively correlated with *INPP5F* and *DGKB* both involved in phospholipid metabolism homeostasis and intracellular signaling. Finally, the module correlating the most with Proneural subtype contained *UGT8*, a sphingolipid related enzyme.

Table 9.1. *Lipid-related enzymes identified in each subtype correlated module*.

		Membrane lipid-related enzymes				
Classical	M1	PLA2G5	FABP7	ELOVL2		
Mesenchymal	M2	PLA2G2A	FABP5	PTGS2	ALOX15B	ALOX5AP
	M4	-				
Neural	M3	INPP5F	DGKB			
Proneural	M5	-				
	M6	UGT8				

Abbreviations: ALOX5, arachidonate 5-lipoxygenase activating protein; ALOX15B, arachidonate 15-lipoxygenase type B; DGKB, diacylglycerol kinase B; ELOVL2, fatty acid elongase 2; FABP7, fatty acid binding protein 7; FABP5, fatty acid binding protein 5; INPP5F, inositol polyphosphate-5-phosphatase F; PLA2G5, phospholipase A2 group V; PLA2G2A, phospholipase A2 groups IIA; PTGS2, prostaglandin-endoperoxide synthase 2; UGT8, UDP-galactose-ceramide galactosyltransferase.

To further understand the implication of these enzymes in the GBM progression, we analyzed the patient survival data associated with the expression levels of the genes included in **Table 9.1** (**Figure 9.10**)
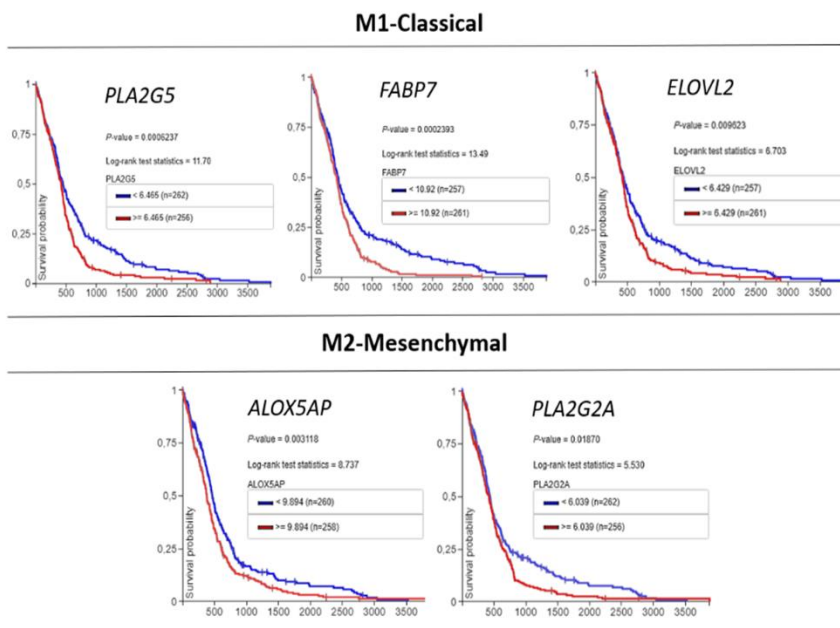
Figure 9.10. *Kaplan-Meier survival analysis in GBM patients based upon PLA2G5, FABP7, ELOVL2, ALOX5P, and PLA2G2A expression in primary GBM tumors. Overall survival rates based on Xena Browser[44] two groups Log-rank test for transcriptome data (AffyU133a) of primary tumor samples from TCGA-GBM database[41]. Only the gene levels included in modules M1 (Classical subtype) PLA2G5, FABP7, ELOVL2, and the M2 (Mesenchymal subtype) PLA2G2A and ALOX5AP, were statistically associated with the poor overall survival are represented.*

The survival analysis revealed an association for elevated gene expression of lipid-related enzymes belonging to modules correlated with Classical and Mesenchymal subtypes (**Figure 9.9**). *PLA2G5, FABP7, ELOVL2, PLA2G2A, and ALOX5AP* genes are tightly involved in fatty acid metabolism, phospholipid synthesis and remodeling, and eicosanoid synthesis according to GO biological process enrichment. Moreover, these genes also were statistically significant in the disease-specific survival tests, where also *ALOX15B* (M2-Mesenchymal) and *UGT8* (M6-Proneural) genes showed statistical significance. However, the rest of the genes included in **Table 9.1** (*FABP5, PTGS2, INPP5F, and DGKB*) did not show any statistical association with survival outcome.

Furthermore, the analysis of the gene methylation status significantly associated with worst overall survival, revealed that for three of them, the molecular subtype dependent gene expression levels may respond to the methylation degree of gene-specific regions (**Figure 9.11**). The *PLA2G5* expression was lower in the Proneural subtype compared to the rest of the subtypes (**Figure 9.11A**). The cg2433549 methylation probe for *PLA2G5* showed higher methylation levels for the Proneural subtype and lower levels for the other subtypes, especially in the classical subtypes (**Figure 9.11B**). Similarly, *FABP7* showed a lower gene expression levels and a higher cg18555555 methylation levels in the Proneural subtype, while the Classical subtype showed a high gene expression and a lower methylation levels compared to the rest of subtype (**Figure 9.11A,B**). Finally, *ALOX5AP* showed a lower expression level in the Proneural and Classical subtypes and higher cg08529529 methylation levels (**Figure 9.11A,B**). Conversely, the Mesenchymal subtype showed high gene expression of *ALOX5AP* and the lower methylation level of the cg08529529 (**Figure 9.11A,B**).
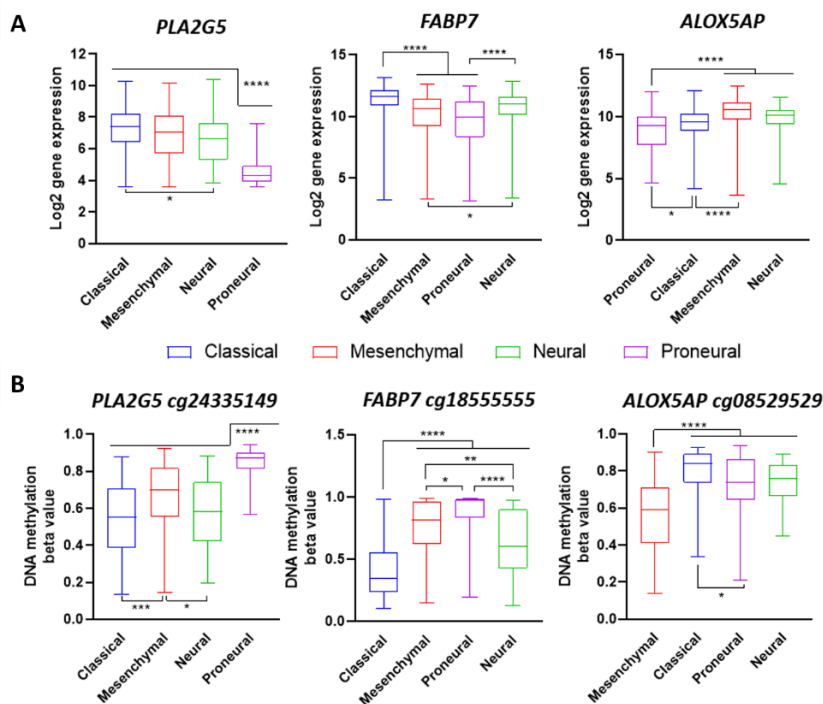
Figure 9.11. *DNA methylation status and gene expression comparison of PLA2G5, FABP7, and ALOX5AP for each molecular subtype. TCGA-GBM molecular subtype dependent gene expression (A) and methylation levels (B) of PLA2G5, FABP7, and ALOX5AP genes. Affymetrix U133a and Methylation27k data sets from TCGA-GBM were used for data representation and statistical analysis. Statistical significance was assessed using multiple comparison ordinary one-way ANOVA with Tuckey adjustment. * P < 0.05, ** P < 0.005, *** P = 0.001, **** P < 0.0001.*

The results of this section identified several lipid-related enzymes that were contained in specific co-expression modules correlated with the different molecular subtypes. Some of these lipid-related enzymes showed statistical association with poor overall and disease-specific survival. Moreover, the PLA2G5, FABP7, and ALOX5AP subtype dependent gene expression were in concordance with their methylation status, being less expressed those genes with higher methylation levels.

9.5   Discussion

The data generated herein by MALDI-IMS analysis demonstrated that the lipidome is able to identify the high proliferation zones of the GBM tissue and that these zones possess an altered lipid fingerprint when compared to healthy brain. Furthermore, the results showed that the lipid composition is sensitive enough to suffer multiple changes when healthy tissue is subdued to TMZ treatment. Interestingly, the current knowledge

of mechanism of action of this drug implies the preferable induction of mutations in tumor tissue through the methylation of adenines and guanines[45]. To our knowledge, this is the first study providing insights into the side effects of chemotherapy treatments on the brain lipidome. Importantly, the short-time treatment of this study excludes the possibility of an effect of the TMZ over the expression of lipid enzymes that could explain the drastic changes observed in healthy brain.

In the field of lipidomics, some studies showed the potential of its application to study GBM. The application of DESI-IMS, showed that gliomas can be rapidly classified based on their histological sections lipid profiles, offering a potential tool for intraoperative examination and rapid classification[23]. In ectopic and orthotopic human xenografts models, differences in glycosphingolipid and triglyceride, sustaining the critical role of some lipids in tumor growth[27]. Recent studies have reinforced the role of lipid metabolism in GBM progression. *ELOVL2*, an important enzyme in PUFAs synthesis, is implicated in the maintenance of *EGFR* signaling and GBM proliferation, through its contribution to membrane composition[31]. In patient-derived neurospheres, LXRβ up-regulates cholesterol biosynthesis, enabling glioma cells to proliferate and survive at high cell densities even when cholesterol is high[46,47].

Our results showed that each phospholipid class in GBM tissues responded differently, being the PE plasmalogens the class changing the most. Interestingly, PE diacyl species barely changed, reinforcing the existing evidence showing that the presence of vinyl-ether linkage implies different biological roles and regulatory mechanisms compared to the diacyl phospholipids[17,48]. Compared to PE-diacyl, PE-vinyl-ether species are highly enriched in PUFA, mainly in arachidonic and docosahexaenoic acid (20:4n-6 and 22:6n-3)[17,48]. In general, the tumors analyzed showed a clear increase in PE P- PUFA at the sn2 position, respectively, which is consistent with previous studies[49,50]. Therefore, the increase in PUFA-containing species but not in the total PE P- described in our GBM samples is in line with these premises. While the healthy tissue contains relatively low levels of PUFA-containing PE P- with 16 and 18 carbon chain length at sn1 position, the tumor tissue requires higher levels of this esterified fatty acid regardless of the fatty acid at sn1 position.

Previous studies of our group in the context of colon cancer, demonstrate a differential PE P- composition in cancer tissue accompanied by the disrupted expression of their rate-limiting proteins[17]. This condition could reflect a need of the tumor of synthesizing bioactive molecules derived from the arachidonic acid like the eicosanoids as plasmalogens are considered a hub of bioactive molecules[51,52]. In this context, despite the free arachidonic acid have antiproliferative capacities[53], is more usually related to the synthesis of pro-proliferative prostanoids. Consistently, cPLA2α,

the main enzyme releasing arachidonic acid from phospholipids, is upregulated in GBM and TMZ-resistant GBM cells[54]. In fact, the interrogation of transcriptomic databases showed the altered expression of different phospholipases A2 is a common feature in different molecular subtypes of GBM (**Table 9.1**, **Figure 9.11**). Finally, a lower expression of prostaglandin synthesis enzymes, particularly PGE2S, as well as , a lower concentration of PGE_2 and $PGF_{2\alpha}$ have been related to better patient outcomes and lower tumor grade[30].

Interestingly, another bioactive precursor hub, the PI 38:4 species was also significantly increased in the GBM compared to the healthy tissue. PI 18:0/20:4, the main PI species, is considered to be a source for arachidonic acid-derived molecules in inflammation. Several studies have shown a an increase of AA after therapeutic treatment[55–57]. Furthermore, the PI species are the precursors of phosphoinositides, important signaling molecules. In fact, the PI3K-AKT signaling pathway is necessary for the development of GBM in mouse model tissue[58] and is upregulated in GBM[59]. Despite little is known regarding the specificity of PI hydrolyzing enzymes and kinases for PI lipid species, some studies have proved the specificity of some PI kinases towards arachidonic acid-containing PI[60]. Therefore, the increase in PI 38:4 in the GBM tissue could correspond to a necessity from the tumor tissue of phosphoinositides-triggered signaling.

The sulfatide class composition, a phospholipid class particularly abundant in the brain, was also altered at the level of lipid species in GMB. Interestingly, Eberlin et. al. showed that grade IV astrocytomas contained undetectable sulfatides levels, while they were detected in lower grade astrocytomas[23]. The latter is in agreement with the results showed herein as we detected lower levels in sulfatide species in tumors compared to healthy tissue. Interestingly, the sulfatide species with 18C fatty acids length tended to increase in the tumor tissue in detriment of fatty acids with longer chains. Interestingly, neurons and astrocytes are enriched in sulfatides containing shorter fatty acids than the oligodendrocytes (C18 vs C22/C24)[61], although the biological significance remains to be elucidated. Part of this decrease could be explained by a higher presence of white mater in the healthy tissue due to the higher number of neurons and axons compared with a tumor where most cells would come from the glia. In any case, this study is in line with the literature that describes the high sensitivity of this lipid class to the tumorigenesis process[62], placing this relatively understudied lipid as, at least, a useful biomarker.

In this *ex-vivo* study, the short treatment of a GBM biopsy with TMZ did not induce relevant changes at the level of lipid composition. Unexpectedly, more changes were detected in healthy tissue. PE plasmalogens species were again the most sensitive showing a general and solid tendency in increasing PUFA-containing species. Similarly,

the PUFA-containing PI molecular species were increased. Interestingly, the TMZ treatment of glioma cells[63] increases the phosphorylation, and consequently activation, of the cytosolic *PLA2*[64], one of the enzymes accounting for the arachidonic acid releasing. This would be in line with other cancers that also present higher levels of AA and *PLA2* like the prostate cancer, breast cancer, or colorectal cancer, among others[49,65,66].

The general increase in PUFA-containing species in all phospholipid classes analyzed could reflect the intact mechanisms of the healthy tissue to respond at the administration of the alkylating agent. In this context, the study addressing the reasons underlying the increase in PUFA levels could help in understanding the side effects induced by the TMZ and counteract them. Despite the lack of major changes in SM and sulfatides species after the treatment, other studies proved the increase in short-chain fatty acids sphingolipids in glioma cells transfected with p53 and treated with a chemotherapeutic agent (SN-38)[67]. The shorter treatment times and the use of a different chemotherapy agent could explain this divergence in the results.

The application of -omics techniques provided useful information to classify patients according to their molecular signature[68]. This approach has revealed interesting genomic, epigenomic, and transcriptomic characteristics commonly shared between different GBM samples which enable a greater stratification[69]. For example, the Proneural molecular subtype, which presents better survival data, frequently presents IDH-mutation, a well-established prognostic marker. Moreover, IDH-mutants commonly manifest the G-CIMP phenotype[70], correlative analyses associated this phenotype of Proneural subtype as a survival advantage[71]. A more detailed analysis showed that the G-CIMP-high subtype was the greater contributor to the enhanced survival[72]. On the other hand, the Mesenchymal subtype presents poor survival, extensive necrosis, inflammation, angiogenesis, highly cell enriched tumor micro-environment, and resistance to different therapies[73]. With this in mind, the genomic and metagenomic analysis of lipid-related enzymes could help in understanding how the lipid changes that we showed are regulated at gene level.

In this context, this study used the molecular subtypes classification established by Verhaak et al.[43] to delve into the subtype co-expressed genes coding for lipid enzymes potentially associated with the described lipidomic phenotype of GBM tissues. The analysis on the TCGA-GBM databases identified nine lipid-related genes that could account for the described alterations in GBM lipidome. Thus, their gene expression levels were regulated in GBM in a molecular subtype-dependent manner. Furthermore, five of these genes, namely *PLA2G5, PLA2G2A, FAPB5, FABP7, ELOVL2*, and *ALOX5AP,* were significantly associated with poor overall and disease-specific survival, in concordance with their expression level. Furthermore, the *PLA2G5, FABP7*, and

ALOX5AP gene expression levels showed an obvious epigenetic regulation according to the specific gene region methylation levels. Particularly remarkable was the high methylation of *FABP7* and *PLA2G5* in the Proneural subtype, which was accompanied by a lower gene expression; and the low methylation and higher gene expression of these genes in the Classical subtype, when compared to the other subtypes. Also, the *ALOX5AP* gene showed lower methylation and higher gene expression in the Mesenchymal subtype compared to the other subtypes.

The Classical subtype gene signature is characterized, among others, by the elevated *EGFR* and *NOTCH3* expression. Recent studies have strengthened the implication of ELOVL2, an important enzyme in PUFAs synthesis, in the maintenance of EGFR signaling and GBM proliferation, through its contribution to membrane composition[31]. Thus, in addition, to describe an increase of PUFAs in GBM samples, they found that *ELOVL2* expression was associated with a decrease in survival. FABP7, a protein involved in the mobilization and transport of fatty acids, is involved in brain development and has been described to improve cell migration and infiltration in malignant glioma cells[74]. FABP7 has a high affinity for AA and DHA being able to regulate the AA metabolism[75] and, in GBM patient-derived neurospheres and cell lines, it appears to modulate the activity of PKC under AA and DHA supplementation[76]. These studies support the role of FABP7 in the increase in PUFA-containing phospholipids, as well as their implication in GBM progression, especially in the classical subtype. Finally, the activity of PLA2G5, a secreted PLA2 with a high affinity for unsaturated fatty acids, may be implicated in the PUFA metabolism as well. Unsaturated fatty acid release from the membrane outer monolayer may increase fatty acid uptake, intracellular signaling, and increase in PUFA containing phospholipids. Finally, the elevated methylation of *ALOX5AP* in the Proneural subtype and its lower methylation in the Mesenchymal may be indicative of the eicosanoid metabolism implication in stromal cells and could account for the tumor microenvironment enrichment in AA. Proneural to Mesenchymal transition has been described as a resistance mechanism to chemotherapy in GMB relapse. Under radiotherapeutic treatment, mesenchymal differentiation is observed, where tumor stem cells switch from Proneural to mesenchymal phenotype or the already present mesenchymal type is selected[77,78]. In this scenario, the pivotal expression and methylation levels of *ALOX5AP* strongly indicate an interesting role of AA-containing phospholipids and the derived metabolism in the tumor microenvironment and GBM progression.

9.6   Conclusions

Altogether, this study provides solid evidence regarding the sensitivity of membrane lipids in the development of GBM and describes some of the multiple

effects occurring in the brain tissue after TMZ treatment. The results suggest a scenario where, at short times, the tumor tissue is initially resistant to the treatment, while the healthy brain is highly sensitive to it. There is no doubt that the knowledge of the side effects of GBM treatment will help in reducing the discontinuity rates, which currently affect 20% of the patients, and could increase the effectiveness of future treatments. The results also highlight the role of PUFAs in GBM progression, especially in the Classical and Mesenchymal subtypes and less remarked in the Proneural subtype. The results encourage the study and exploration of the PUFA metabolism in each specific molecular subtype of GBM to improve the survival and the quality of life of those patients.

1. Young, R. M., Jamshidi, A., Davis, G. & Sherman, J. H. Current trends in the surgical management and treatment of adult glioblastoma. *Annals of Translational Medicine* (2015) doi:10.3978/j.issn.2305-5839.2015.05.10.

2. Gallego, O. Nonsurgical treatment of recurrent glioblastoma. *Current Oncology* (2015) doi:10.3747/co.22.2436.

3. Oike, T. *et al.* Radiotherapy plus concomitant adjuvant temozolomide for glioblastoma: Japanese mono-institutional results. *PLoS One* (2013) doi:10.1371/journal.pone.0078943.

4. Chamberlain, M. C. Temozolomide: Therapeutic limitations in the treatment of adult high-grade gliomas. *Expert Review of Neurotherapeutics* (2010) doi:10.1586/ern.10.32.

5. Broekman, M. L. *et al.* Multidimensional communication in the microenvirons of glioblastoma. *Nat. Rev. Neurol.* (2018) doi:10.1038/s41582-018-0025-8.

6. Patel, A. P. *et al.* Single-cell RNA-seq highlights intratumoral heterogeneity in primary glioblastoma. *Science (80-.).* (2014) doi:10.1126/science.1254257.

7. Parsons, D. W. *et al.* An integrated genomic analysis of human glioblastoma multiforme. *Science (80-.).* (2008) doi:10.1126/science.1164382.

8. Louis, D. N. *et al.* The 2016 World Health Organization Classification of Tumors of the Central Nervous System: a summary. *Acta Neuropathologica* (2016) doi:10.1007/s00401-016-1545-1.

9. Wang, Q. *et al.* Tumor Evolution of Glioma-Intrinsic Gene Expression Subtypes Associates with Immunological Changes in the Microenvironment. *Cancer Cell* (2017) doi:10.1016/j.ccell.2017.06.003.

10. Nikolopoulou, E. *et al.* Arachidonic acid-dependent gene regulation during preadipocyte differentiation controls adipocyte potential. *J Lipid Res* **55**, 2479–2490 (2014).

11. Ponec, M., Weerheim, A., Kempenaar, J., Mommaas, A. M. & Nugteren, D. H. Lipid composition of cultured human keratinocytes in relation to their differentiation. *J. Lipid Res.* (1988) doi:10.1016/S0022-2275(20)38476-5.

12. Yoshida, K., Shinohara, H., Suryono, Haneji, T. & Nagata, T. Arachidonic acid inhibits osteoblast differentiation through cytosolic phospholipase A2-dependent pathway. *Oral Dis.* (2007) doi:10.1111/j.1601-0825.2006.01239.x.

13. Bestard-Escalas, J. *et al.* Lipid fingerprint image accurately conveys human colon cell pathophysiologic state: A solid candidate as biomarker. *Biochim. Biophys. Acta - Mol. Cell Biol. Lipids* **1861**, (2016).

14. Atilla-Gokcumen, G. E. *et al.* Dividing cells regulate their lipid composition and localization. *Cell* **156**, 428–439 (2014).

15. Sagona, A. P. *et al.* PtdIns(3)P controls cytokinesis through KIF13A-mediated recruitment of FYVE-CENT to the midbody. *Nat. Cell Biol.* (2010) doi:10.1038/ncb2036.

16. Echard, A. Phosphoinositides and cytokinesis: The 'PIP' of the iceberg. *Cytoskeleton* (2012) doi:10.1002/cm.21067.

17. Lopez, D. H. *et al.* Tissue-selective alteration of ethanolamine plasmalogen metabolism in dedifferentiated colon mucosa. *Biochim. Biophys. Acta - Mol. Cell Biol. Lipids* **1863**, 928–938 (2018).

18. Lee, S. T. *et al.* Global Changes in Lipid Profiles of Mouse Cortex, Hippocampus, and Hypothalamus Upon p53 Knockout. *Sci Rep* **6**, 36510 (2016).

19. Baenke, F., Peck, B., Miess, H. & Schulze, A. Hooked on fat: the role of lipid synthesis in cancer metabolism and tumour development. *Dis Model Mech* **6**, 1353–1363 (2013).

20. Sutphen, R. *et al.* Lysophospholipids are potential biomarkers of ovarian cancer. *Cancer Epidemiol. Biomarkers Prev.* (2004).

21. Zhou, X. *et al.* Identification of Plasma Lipid Biomarkers for Prostate Cancer by Lipidomics and Bioinformatics. *PLoS One* (2012) doi:10.1371/journal.pone.0048889.

22. Chen, X. *et al.* Plasma lipidomics profiling identified lipid biomarkers in distinguishing early-stage breast cancer from benign lesions. *Oncotarget* (2016) doi:10.18632/oncotarget.9124.

23. Eberlin, L. S. *et al.* Classifying human brain tumors by lipid imaging with mass spectrometry. *Cancer Res.* **72**, 645–654 (2012).

24. Astigarraga, E. *et al.* Profiling and imaging of lipids on brain and liver tissue by matrix-assisted laser desorption/ ionization mass spectrometry using 2-mercaptobenzothiazole as a matrix. *Anal. Chem.* **80**, 9105–9114 (2008).

25. Veloso, A. *et al.* Distribution of lipids in human brain. *Anal. Bioanal. Chem.* **401**, 89–101 (2011).

26. Veloso, A. *et al.* Anatomical distribution of lipids in human brain cortex by imaging mass spectrometry. *J. Am. Soc. Mass Spectrom.* **22**, 329–338 (2011).

27. Ha, S. *et al.* Lipidomic Analysis of Glioblastoma Multiforme Using Mass Spectrometry. *Curr. Metabolomics* (2014) doi:10.2174/2213235x02666141107215357.

28. Pinkham, K. *et al.* Stearoyl CoA Desaturase Is Essential for Regulation of Endoplasmic Reticulum Homeostasis and Tumor Growth in Glioblastoma Cancer Stem Cells. *Stem Cell Reports* (2019) doi:10.1016/j.stemcr.2019.02.012.

29. Shergalis, A., Bankhead, A. 3rd, Luesakul, U., Muangsin, N. & Neamati, N. Current Challenges and Opportunities in Treating Glioblastoma. *Pharmacol. Rev.* **70**, 412–445 (2018).

30. Panagopoulos, A. T. *et al.* The prostanoid pathway contains potential prognostic markers for glioblastoma. *Prostaglandins Other Lipid Mediat.* (2018) doi:10.1016/j.prostaglandins.2018.06.003.

31. Gimple, R. C. *et al.* Glioma stem cell–specific superenhancer promotes polyunsaturated fatty-acid synthesis to support EGFR signaling. *Cancer Discov.* (2019) doi:10.1158/2159-8290.CD-19-0061.

32. Garate, J. *et al.* Imaging mass spectrometry increased resolution using 2-mercaptobenzothiazole and 2,5-diaminonaphtalene matrices: application to lipid distribution in human colon. *Anal. Bioanal. Chem.* **407**, 4697–4708 (2015).

33. Maimó-Barceló, A. *et al.* Confirmation of sub-cellular resolution using oversampling imaging mass spectrometry. *Anal. Bioanal. Chem.* **411**, 7935–7941 (2019).

34. Sun, X. & Kaufman, P. D. Ki-67: more than a proliferation marker. *Chromosoma* **127**, 175–186 (2018).

35. Zeng, A. *et al.* IDH1/2 mutation status combined with Ki-67 labeling index defines distinct prognostic groups in glioma. *Oncotarget* **6**, 30232–30238 (2015).

36. Ma, J. *et al.* Inhibition of Nuclear PTEN Tyrosine Phosphorylation Enhances Glioma Radiation Sensitivity through Attenuated DNA Repair. *Cancer Cell* **35**, 504-518.e7 (2019).

37. Stoyanov, G. S., Dzhenkov, D. L., Kitanova, M., Donev, I. S. & Ghenev, P. Correlation Between Ki-67 Index, World Health Organization Grade and Patient Survival in Glial Tumors With Astrocytic Differentiation. *Cureus* **9**, e1396 (2017).

38. Garate, J. *et al.* Influence of Lipid Fragmentation in the Data Analysis of Imaging Mass Spectrometry Experiments. *J. Am. Soc. Mass Spectrom.* **31**, 517–526 (2020).

39. Ishizuka, I. Chemistry and functional distribution of sulfoglycolipids. *Progress in Lipid Research* (1997) doi:10.1016/S0163-7827(97)00011-8.

40. Snyder, F. & Snyder, F. *Ether Lipids: Chemistry and Biology*. (Academic Press, 1972).

41. McLendon, R. *et al.* Comprehensive genomic characterization defines human glioblastoma genes and core pathways. *Nature* **455**, 1061–1068 (2008).

42. Russo, P. S. T. *et al.* CEMiTool: A Bioconductor package for performing comprehensive modular co-expression analyses. *BMC Bioinformatics* **19**, (2018).

43. Verhaak, R. G. W. *et al.* Integrated Genomic Analysis Identifies Clinically Relevant Subtypes of Glioblastoma Characterized by Abnormalities in PDGFRA, IDH1, EGFR, and NF1. *Cancer Cell* (2010) doi:10.1016/j.ccr.2009.12.020.

44. Goldman, M. J. *et al.* Visualizing and interpreting cancer genomics data via the Xena platform. *Nature Biotchnology* (2020) doi:10.1038/s41587-020-0546-8.

45. Lee, S. Y. Temozolomide resistance in glioblastoma multiforme. *Genes Dis.* **3**, 198–210 (2016).

46. Kambach, D. M. *et al.* Disabled cell density sensing leads to dysregulated cholesterol synthesis in glioblastoma. *Oncotarget* (2017) doi:10.18632/oncotarget.14740.

47. Patel, D. *et al.* LXRβ controls glioblastoma cell growth, lipid balance, and immune modulation independently of ABCA1. *Sci. Rep.* (2019) doi:10.1038/s41598-019-51865-8.

48. Lebrero, P. *et al.* Cellular Plasmalogen Content Does Not Influence Arachidonic Acid Levels or Distribution in Macrophages: A Role for Cytosolic Phospholipase A2γ in Phospholipid Remodeling. *Cells* (2019) doi:10.3390/cells8080799.

49. Pender-Cudlip, M. C. *et al.* Delta-6-desaturase activity and arachidonic acid synthesis are increased in human breast cancer tissue. *Cancer Sci.* (2013) doi:10.1111/cas.12129.

50. Bestard-Escalas, J. *et al.* Lipid fingerprint image accurately conveys human colon cell pathophysiologic state: A solid candidate as biomarker. *Biochim. Biophys. Acta - Mol. Cell Biol. Lipids* **1861**, 1942–1950 (2016).

51. Chilton, F. H. Potential phospholipid source(s) of arachidonate used for the synthesis of leukotrienes by the human neutrophil. *Biochem. J.* (1989) doi:10.1042/bj2580327.

52. Gil-de-Gómez, L. *et al.* Cytosolic Group IVA and Calcium-Independent Group VIA Phospholipase A 2 s Act on Distinct Phospholipid Pools in Zymosan-Stimulated Mouse Peritoneal Macrophages . *J. Immunol.* (2014) doi:10.4049/jimmunol.1302267.

53. Comba, A. *et al.* Nuclear factor of activated T cells-dependent downregulation of the transcription factor glioma-associated protein 1 (GLI1) underlies the growth inhibitory properties of arachidonic acid. *J. Biol. Chem.* (2016) doi:10.1074/jbc.M115.691972.

54. Yang, L. & Zhang, H. Expression of Cytosolic Phospholipase A2 Alpha in Glioblastoma Is Associated With Resistance to Chemotherapy. *Am. J. Med. Sci.* (2018) doi:10.1016/j.amjms.2018.06.019.

55. Dahan, P. *et al.* Ionizing radiations sustain glioblastoma cell dedifferentiation to a stem-like phenotype through survivin: possible involvement in radioresistance. *Cell Death Dis.* **5**, e1543–e1543 (2014).

56. Caragher, S. *et al.* Temozolomide Treatment Increases Fatty Acid Uptake in Glioblastoma Stem Cells. *Cancers (Basel).* **12**, (2020).

57. Lee, G. *et al.* Dedifferentiation of Glioma Cells to Glioma Stem-like Cells By Therapeutic Stress-induced HIF Signaling in the Recurrent GBM Model. *Mol. Cancer Ther.* **15**, 3064–3076 (2016).

58. Holland, E. C. *et al.* Combined activation of Ras and Akt in neural progenitors induces glioblastoma formation in mice. *Nat. Genet.* (2000) doi:10.1038/75596.

59. Höland, K. *et al.* Targeting class Ia PI3K isoforms selectively impairs cell growth, survival, and migration in glioblastoma. *PLoS One* (2014) doi:10.1371/journal.pone.0094132.

60. Shulga, Y. V., Anderson, R. A., Topham, M. K. & Epand, R. M. Phosphatidylinositol-4-phosphate 5-kinase isoforms exhibit acyl chain selectivity for both substrate and lipid activator. *J. Biol. Chem.* (2012) doi:10.1074/jbc.M112.370155.

61. Eckhardt, M. The role and metabolism of sulfatide in the nervous system. *Mol. Neurobiol.* **37**, 93–103 (2008).

62. Liu, Y. *et al.* Elevation of sulfatides in ovarian cancer: An integrated transcriptomic and lipidomic analysis including tissue-imaging mass spectrometry. *Mol. Cancer* **9**, 1–13 (2010).

63. Tsuji, S. *et al.* Temozolomide has anti-tumor effects through the phosphorylation of cPLA2 on glioblastoma cells. *Brain Res.* (2019) doi:10.1016/j.brainres.2019.146396.

64. Pavicevic, Z., Leslie, C. C. & Malik, K. U. CPLA 2 phosphorylation at serine-515 and serine-505 is required for arachidonic acid release in vascular smooth muscle cells. *J. Lipid Res.* (2008) doi:10.1194/jlr.M700419-JLR200.

65. Cummings, B. S. Phospholipase A2 as targets for anti-cancer drugs. *Biochem. Pharmacol.* **74**, 949–959 (2007).

66. Patel, M. I., Kurek, C. & Dong, Q. The arachidonic acid pathway and its role in prostate cancer development and progression. *J. Urol.* **179**, 1668–1675 (2008).

67. He, H. *et al.* Polar lipid remodeling and increased sulfatide expression are associated with the glioma therapeutic candidates, wild type p53 elevation and the topoisomerase-1 inhibitor, Irinotecan. *Glycoconj. J.* **27**, 27–38 (2010).

68. Lee, E., Yong, R. L., Paddison, P. & Zhu, J. Comparison of glioblastoma (GBM) molecular classification methods. *Seminars in Cancer Biology* (2018) doi:10.1016/j.semcancer.2018.07.006.

69. Zhang, P., Xia, Q., Liu, L., Li, S. & Dong, L. Current Opinion on Molecular Characterization for GBM Classification in Guiding Clinical Diagnosis, Prognosis, and Therapy. *Frontiers in Molecular Biosciences* (2020) doi:10.3389/fmolb.2020.562798.

70. Turcan, S. *et al.* IDH1 mutation is sufficient to establish the glioma hypermethylator phenotype. *Nature* (2012) doi:10.1038/nature10866.

71. Brennan, C. W. *et al.* The somatic genomic landscape of glioblastoma. *Cell* (2013) doi:10.1016/j.cell.2013.09.034.

72. Ceccarelli, M. *et al.* Molecular Profiling Reveals Biologically Discrete Subsets and Pathways of Progression in Diffuse Glioma. *Cell* (2016) doi:10.1016/j.cell.2015.12.028.

73. Behnan, J., Finocchiaro, G. & Hanna, G. The landscape of the mesenchymal signature in brain tumours. *Brain* (2019) doi:10.1093/brain/awz044.

74. Brun, M. *et al.* Nuclear Factor I Regulates Brain Fatty Acid-Binding Protein and Glial Fibrillary Acidic Protein Gene Expression in Malignant Glioma Cell Lines. *J. Mol. Biol.* (2009) doi:10.1016/j.jmb.2009.06.041.

75. Elsherbiny, M. E., Emara, M. & Godbout, R. Interaction of brain fatty acid-binding protein with the polyunsaturated fatty acid environment as a potential determinant of poor prognosis in malignant glioma. *Progress in Lipid Research* (2013) doi:10.1016/j.plipres.2013.08.004.

76. Elsherbiny, M. E., Chen, H., Emara, M. & Godbout, R. ω-3 and ω-6 fatty acids modulate conventional and atypical protein kinase C activities in a brain fatty acid binding protein dependent manner in glioblastoma multiforme. *Nutrients* (2018) doi:10.3390/nu10040454.

77. Bhat, K. P. L. *et al.* Mesenchymal Differentiation Mediated by NF-κB Promotes Radiation Resistance in Glioblastoma. *Cancer Cell* **24**, 331–346 (2013).

78. Garnier, D., Renoult, O., Alves-Guerra, M.-C., Paris, F. & Pecqueur, C. Glioblastoma Stem-Like Cells, Metabolic Strategy to Kill a Challenging Target. *Front. Oncol.* **9**, (2019).

79. Fernández, R., Garate, J., Martín-Saiz, L., Galetich, I. & Fernández, J. A. Matrix Sublimation Device for MALDI Mass Spectrometry Imaging. *Anal. Chem.* **91**, 803–807 (2019).

80. Huang, D. W., Sherman, B. T. & Lempicki, R. A. Bioinformatics enrichment tools: Paths toward the comprehensive functional analysis of large gene lists. *Nucleic Acids Res.* **37**, 1–13 (2009).

81. Demšar, J. *et al. Orange: Data Mining Toolbox in Python Tomaž Curk Matija Polajnar Laň Zagar*. *Journal of Machine Learning Research* vol. 14 (2013).

Chapter 10

Ongoing projects and future perspectives.

10.1   Ongoing projects

Characterization of the lipid fingerprint of Crohn disease and ulcerative colitis. Preliminary results

Ulcerative colitis and Crohn's disease are chronic, relapsing, immune-mediated disorders that are collectively referred to as inflammatory bowel diseases (IBD). The prevalence of IBD rapidly increased in Europe and North America in the second half of the twentieth century, and is becoming more common in the rest of the world as different countries adopt a Western lifestyle[1, 2].

Moreover, accurate diagnosis of predominantly colonic IBD is not possible in 30% of patients. For decades, scientists have worked to find a solution to improve diagnostic accuracy for IBD, encompassing Crohn's disease and Ulcerative colitis[1]. Thus, evaluating lipid patterns by MALDI-IMS in surgical pathology colectomy specimens could help in the development and improvement of diagnostic tools complementing traditional histomorphological approaches.
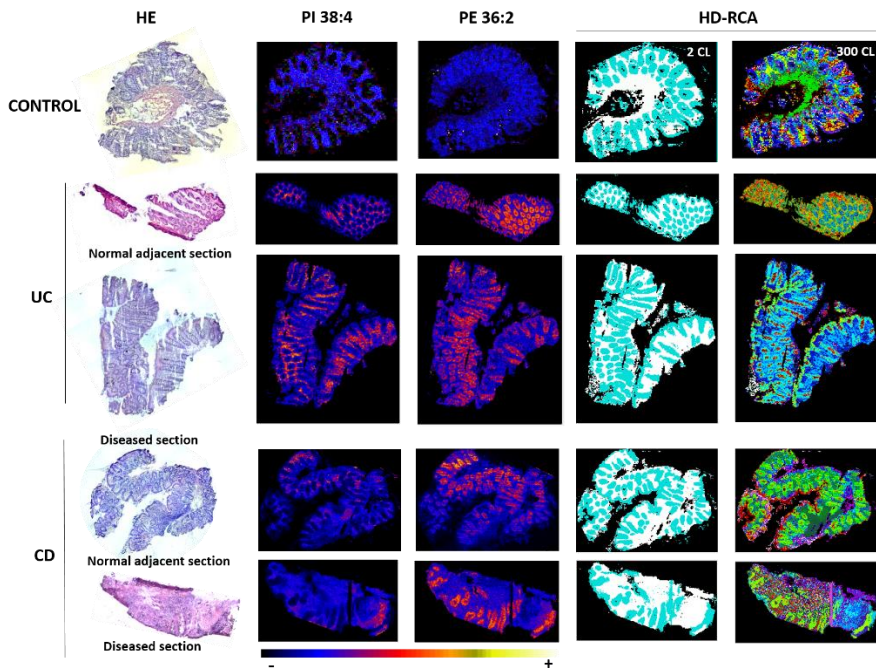
Figure 10.1. *Eosin hematoxylin staining of colonoscopy biopsies of Ulcerative colitis (UC) and Crohn disease (CD) compared with the PI 38:4 and PE 36:2 distributions and the segmentation analysis (HD-RCA) over the same tissue. 2 and 300 clusters proposed by the algorithm are displayed.*

Samples from 11 patients of Crohn disease (CD), 8 patients of Ulcerative Colitis (UC) and 3 healthy (Control) volunteers were used in this project. The sample collection was approved by the Ethics Research committee of the Balearic Island. From each patient, colon endoscopic biopsies from the diseased and the normal adjacent (NA) area were selected. Sections of 10 μm of thickness were obtained using a cryostat and placed on ITO glass slides. A total of 42 sections were analyzed by MALDI-IMS by at Kratos LTD, using a 7090 MALDI-TOF-TOF.

As can be appreciated in **Figure 10.1** and in agreement with previous publications[3, 4], lamina propria (LP) and epithelium (E) present different lipid profiles, not only in control tissue but also in NA, UC and CD sections. As an example, PI 38:4 is mainly found in LP while PE 36:2 in E. Thus, a segmentation analysis (HD-RCA) was applied to the MALDI-IMS images in order to obtain the specific segments and consequently, the lipid fingerprint characteristic of these two histological regions (LP colored in white and E colored in blue in **Figure 10.1** third column).

In control samples, the lipid fingerprint is well stablished, obtaining a specific and invariant lipid profile of LP and E for the three samples, as displayed in the PCA plot (**Figure 10.2A**). Comparison between the relative abundances of the main lipid classes shows significant differences were observed between E and LP; there is higher relative abundance of PE's in the epithelium while PI's and SFT's are more abundant in LP (**Figure 10.2B**).
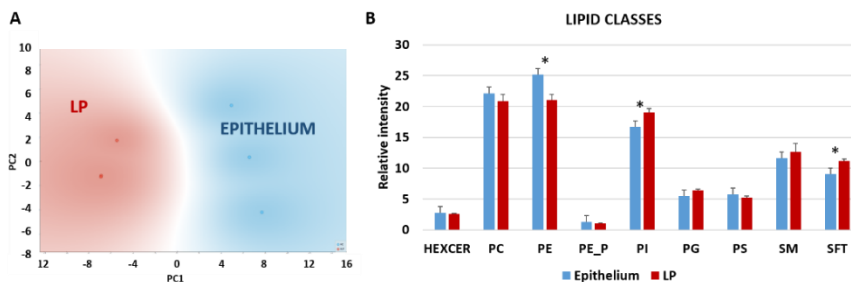
Figure 10.2. (A) *Unsupervised PCA scatter plot separating lamina propria (LP) and Epithelium (E) lipid profile in control samples.* ***(B)*** *Comparison of the relative abundance of the main lipid classes in E and LP.*

In normal UC-adjacent (NA-UC) and UC sections, also clear separation was obtained in the PCA scatter plot among the lipid fingerprint of the four groups: NA E, NA LP, UC E and UC LP (**Figure 10.3A**). Excellent classification results were obtained with the four classification models applied **(Figure 10.3B),** being Logistic

Regression the best classifier. Additionally, data sets are grouped according to their disease condition (UC or NA, **Figure 10.3D**) and into epithelium and lamina propria (**Figure 10.3E**) indicating notably differences between the lipid profile of each region. In fact, an overall comparison of the variation of the main lipid classes including control samples showed significant differences in PE, PI, PS, SM and SFT lipid classes (**Figure 10.3F**). Although NA-UC and UC show similar profiles than control sections, several distinctions enable the classification of the different study groups. For example, in control sections, the higher presence of PE's in the epithelium is clear while in NA-UC samples, this is not observed. Also, PI's present higher intentisty in healthy LP but such difference between LP and E was lost in NA-UC and UC samples (**Figure 10.3F**).
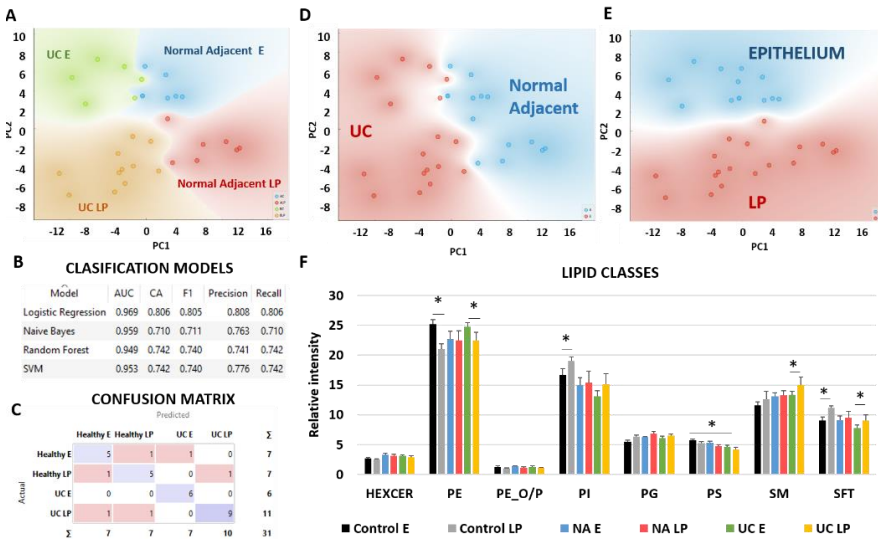
Figure 10.3. *Lipid classification of Ulcerative colitis (UC) samples and normal adjacent sections (NA).* **(A)** *PCA scatter plot of the four UC tissue types analyzed: Ulcerative colitis epithelium (UC E), Ulcerative colitis lamina propria (UC LP), Normal adjacent epithelium (NA E) and Normal adjacent lamina propria (NA LP).* **(B)** *Summary of the classification model results.* **(C)** *Logistic Regression classification model.* **(D)** *PCA scatter plot of the same analysis performed in panel A but colored by the type of sample (healthy or UC).* **(E)** *Same analysis but colored by the type of histological feature (epithelium or LP),* **(F)** *Bar charts of the main lipid classes' variations including control patients data (Control E and Control LP), NA E, NA LP, UC E and UC LP groups.*

The same analysis was performed over normal CD-adjacent (NA-CD) and CD samples. As in the case of UC samples, clusters from each tissue type tend to group together, indicating distinct and characteristic lipid signatures (**Figure**

10.4A-C). Moreover, the analysis revealed Crohn disease –specific differences. As it can be see, all clusters from CD samples were grouped on one side of the graphics, and normal adjacent tissue specific clusters on the other (**Figure 10.4D).** In addition, the same lipid profile is able to distinguish between LP and E indicating common and invariant molecular features among CD patients (**Figure 10.4E**).
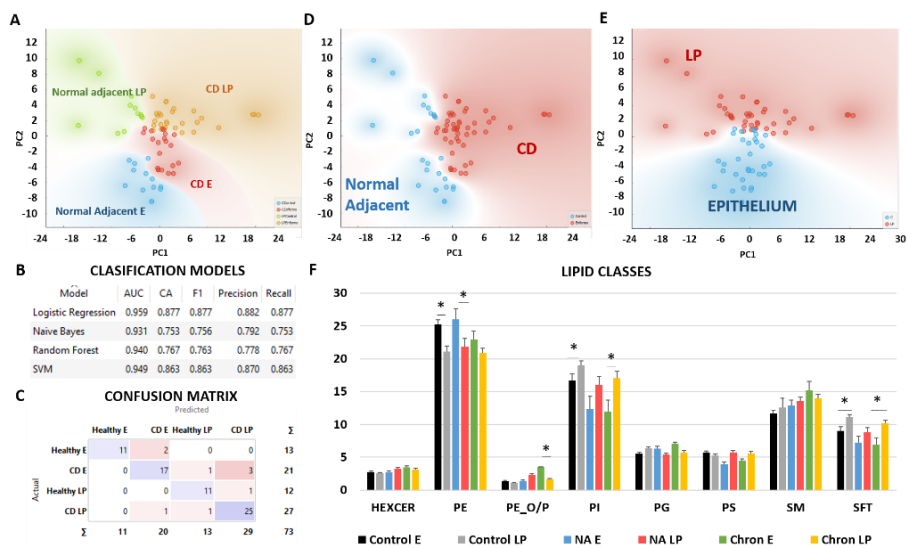
Figure 10.4. *Lipid classification of Crohn disease (CD) samples and normal adjacent sections.* **(A)** *PCA scatter plot of the four tissue types analyzed: Crohn disease epithelium (CD E), Crohn disease lamina propria CD LP), normal adjacent epithelium (NA E) and Normal adjacent lamina propria (NA LP).* **(B)** *Summary of the classification model performance.* **(C)** *Confusion matrix for the Logistic Regression classification model.* **(D)** *PCA plot of the same analysis performed in panel A but colored by the type of sample (healthy or CD).* **(E)** *Same analysis but colored by the type of histological feature (epithelium or LP),* **(F)** *Bar charts of the main lipid classes including controlsamples (Control E and Control LP), NA E, NA LP, Crohn E and Crohn LP groups.*

When control samples were included, interesting variations were also observed in the relative abundance of the main lipid classes contained in CD and NA-CD sections (**Figure 10.4F**). For example, there is clearly a higher relative intensity of PEs in the epithelium in both control and NA-CD samples but this was not observed for CD samples. Additionally, while there is a clear higher abundance of PI in LP in control and CD sections, such difference is somehow diluted in NA samples.

Next, the lipid fingerprint of normal adjacent (NA-CD and NA-UC) and diseased samples (CD and UC) were analyzed independently. In theory, as all the samples correspond to healthy tissue, they should not present large differences in lipid composition. Interestingly, preliminary results showed that normal disease-adjacent samples were not only perfectly classified into LP and epithelium but also each type of tissue seems to present a characteristic and different lipid fingerprint (**Figure 10.5A**,**B**), indicating that larger than expected sections of tissue are affected by the disease and that the type of disease can be identified even using "control" tissue. Specifically, some normal UC clusters seem to have an invariant lipid profile which can be clearly distinguished from control and normal Crohn samples. The latter two types of samples appear to have more similar lipid fingerprints (**Figure 10.5B**). Moreover, if we compare the lipid profile of the histological regions from each group, we observed that NA-UC LP (purple colored in **Figure 10.5C**) is very well separated from control LP and NA-CD LP(red and orange colored), which are not evidently classified. On the other hand, epithelium from control, NA-UC and NA-CD samples (green, yellow and blue colored) seem to have comparable lipid fingerprints. This seems to indicate that at early stage, the disease affects mainly the LP.

Analysis of pathological samples, on the other hand, shows that the separation between LP and E is not as clear as in previous analysis. This result is in agreement with the histology of the samples: visual inspection of the sections shows a loss of structure and in some of them, it is very difficult or even impossible to identify the epithelium. Nevertheless, UC and CD lipids seem to have some common features which enable their reasonably good classification not in the analysis of the whole tissue (**Figure 10.5E**) but also of the epithelium and LP independently (**Figure 10.5F**).

Taking all the above information into consideration, it is clear that the lipid fingerprints revealed by MALDI-IMS can serve to identify and classify not only CD and UC pathologic samples, but also normal adjacent areas. This points to IMS as a powerful complementary tool to improve the IBD diagnosis. Still, more thorough analysis is necessary in order to best understand and solve complex metabolism questions concerning IBD diseases.
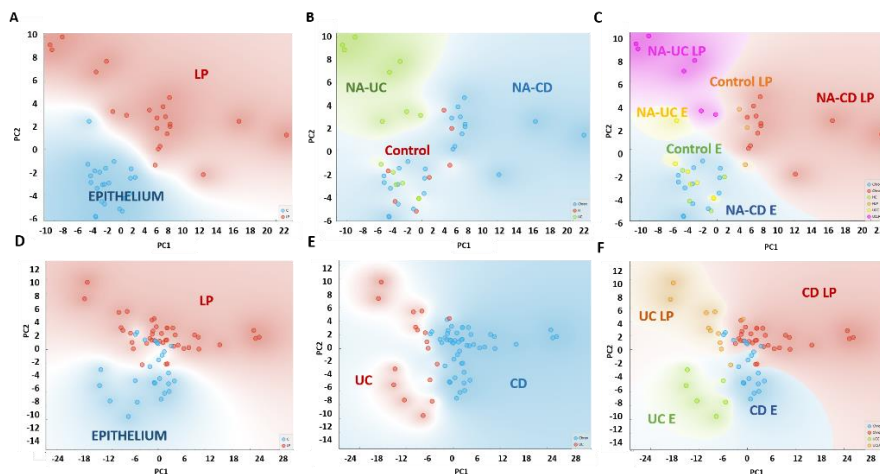
Figure 10.5. *Unsupervised independent lipid analysis of normal adjacent samples and diseased samples.* **(A).** *PCA scatter plot of control and NA samples showing a good separation between LP and epithelium clusters.* **(B)** *Same analysis but samples colored by each tissue origin: NA-UC, NA-CD or control patients.* **(C)** *Same analysis but samples colored by the six different study groups: NA-UC E, NA-UC LP, NA-CD E, NA-CD LP, Control E and Control LP.* **(D)** *PCA scatter plot of diseased samples showing the separation between LP and epithelium clusters.* **(E)** *Same analysis but samples colored by each IBD disease: UC or CD.* **(F)** *Same analysis but samples colored by the four different study groups, combining the pathology and the histological region: UC LP, UC E, CD LP and CD E.*

10.2   Future perspectives

Current improvements in imaging mass spectrometry have sparked a renewed interest in describing the entire lipidome of various clinical conditions, as well as the effects of different drug treatments. However, the approach still faces a number of challenges that are keeping it from becoming widely used in clinics. In the previous chapters, we have dealt with some of these obstacles, improving the IMS workflow and combining IMS results with orthogonal techniques to answer complex biological questions.

The optimization of sample preparation was the first obstacle investigated in **Chapter 4**. This point is crucial to ensure repeatability among various samples to bring IMS up to the level of other well-established optical techniques used in clinical research. We showed that using our in-house designed sublimator, it was possible to achieve higher reproducibility between experiments. Still, this methodology requires of a careful sample handling and the optimal instrument conditions in order to get high spatial resolution.

In this context and thanks to Dr. Raul Montero from the Laser Facility of SGIKER, it was possible to face in **Chapter 4** another challenge: the improvement of spatial resolution in an MALDI LTQ-Orbitrap XL system. Using a set of lenses and a ceramic pinhole, it was possible to spatially filter the beam, to achieve a more gaussian-like profile and to it into a smaller spot. With this simple modification, it was possible to obtain 10 μm laser diameter, improving the overall quality of the images.

Both, the new sublimator and the new optical arrangement in the MALDI LTQ-Orbitrap XL system have been used along this thesis focused on lipid analysis. However, exploring the detection of other important biomolecules and combine all the obtained information can increase the impact of the research. In this context, our lab is currently working on the implementation of the protocol stablished in **Chapter 4** to analyze proteins and lipids on the same tissue by MALDI-IMS**.** The idea is to correlate lipid and trypsin-digested protein information from the same region of ccRCC samples to improve our understanding of different biological processes involved in this common renal cancer.

Technology advancements are required to take research to the next level, particularly in IMS, in order to reach greater spatial resolution that can compete with traditional optic technologies. Nonetheless, advancement without a biological context makes IMS less useful. It is critical to place the results in a biological framework in order to first comprehend and then gain knowledge with the final aim. Thus, integrating orthogonal techniques is what we have developed in **Chapter 5,** combining transcriptomic and lipidomic analysis achieving supportive conclusions. Also in **Chapter 8**, uHPLC and MALDI-IMS of lipids were used complementary in the same samples in order to exploit the synergy between the two techniques.

Moreover, we have demonstrated in **Chapter 6** that it is feasible to link lipid signatures with certain histological features in healthy renal tissue by immunohistochemically staining the same post-MALDI experiment. Hence, our lab is currently engaged in applying this post-MALDI IHC staining protocol in several samples, such as human *Locus coeruleus*, human melanoma metastases, human ccRCC sections and isolated renal tubules. The combination of these techniques can be of tremendous help in the interpretation of MALDI-IMS images, especially in cancer context. Tumoral heterogeneity is an unsettle issue and the correlation between specific lipid variations and changes in macromolecules detected by IHC can provide valuable information.

Apart from the developments presented in this work, several other side projects are ongoing. For example, in collaboration with Dr. Barecelo's group, we

are developing a methodology to characterize the immune cells isolated from peripheral blood, belonging to healthy volunteers and colorectal cancer patients. The hypothesis is that the circulating immune cells from patients with colorectal cancer will exhibit a characteristic lipidoma that would allow us to develop clinical tests for early detection of this deadly disease. The immune cells were sorted by flow cytometry (FACS) and the preliminary results are promising, suggesting it is possible to establish a good classification between immune cells lipid fingerprint of healthy and diseased patients.

Another promising application of MALDI-IMS is prediction of the response of patients to specific treatments or the exploration of the metabolic basis of the impact of a given treatment. We presented in **Chapters 5** and **9** the changes occasioned by Fer-1 in AKI kidney and Temozolomide in astrocytoma samples respectively. The experience gained in those studies will help the research group to tackle more difficult projects, such as prediction of the response of melanoma to biological treatments.

However, several biological questions remain unresolved in the context of normal physiopathological conditions, specially focusing on normal diseased-adjacent samples. In fact, in **Chapter 9,** interesting information was obtained concerning the changes occasioned by a well stablished chemotherapy agent over normal glioblastoma-adjacent tissue sections. The results indicated that the drugs also have an important impact in lipid expression in normal tissue, very likely connected with the side effects associated to the treatment. Moreover, the first part of **this chapter** addressed another appealing question concerning normal IBD diseased-adjacent samples, suggesting IMS of lipids can help in achieving better diagnosis of these pathologies by extracting information from apparently normal tissue areas.

In general, IMS is an excellent, powerful, high-throughput technique for biomedical research, but it is important to associate it with other completing techniques not only to gain more information but also to best interpret the results, aiming at earning adepts in clinical applications. However, another issue that IMS should address is the procedure's complexity. Despite the simplicity of sample preparation and experimental setup, data analysis, particularly pre-processing for the final statistical analysis, remains complex, as demonstrated by this thesis. Accordingly, new software is currently being developed by our group, which automates the entire data processing, analysis, and interpretation, trying to foster its jump into clinics as a useful diagnostic tool.

1. Loftus Jr, E. V. Clinical epidemiology of inflammatory bowel disease: incidence, prevalence, and environmental influences. *Gastroenterology* **126**, 1504-1517 (2004).

2. Sartor, R. B. Mechanisms of disease: pathogenesis of Crohn's disease and ulcerative colitis. *Nature clinical practice Gastroenterology & hepatology* **3**, 390-407 (2006).

3. Bestard-Escalas, J. *et al*. Lipid fingerprint image accurately conveys human colon cell pathophysiologic state: A solid candidate as biomarker. *Biochimica et Biophysica Acta (BBA)-Molecular and Cell Biology of Lipids* **1861**, 1942-1950 (2016).

4. Garate, J. *et al*. Imaging mass spectrometry increased resolution using 2-mercaptobenzothiazole and 2, 5-diaminonaphtalene matrices: application to lipid distribution in human colon. *Analytical and bioanalytical chemistry* **407**, 4697-4708 (2015).

Appendix Chapter 4

Novel matrix Sublimation Device for MALDI Mass Spectrometry Imaging

Stainless steel sublimation prototype

Detailed schematics of the stainless steel sublimator developed may be found in **Figure A.4.1**. The main body (the sublimator chamber) is made of a stainless steel cylinder of 162 mm, ending in ISO K 160 nipples. The upper flange has two ports. The largest one, of ISO KF 25 size, is centered in the flange and is used for a copper arm where the Peltier cell is attached. The cell is clamped between two flat, square copper sheets that enables efficient heat transmission between the sample and the cell's cold face and the heat dissipater and the cell's hot face. The arm also serves dissipate the heat generated at the hot side of the Peltier cell and it is refrigerated by a set of heat dissipater and fan. The second and smaller port in the upper flange, ISO KF16, is used for a four-wire feedthrough, where the (K-type) thermocouple and the Peltier cell are connected. Temperature at the sample holder is controlled with this thermocouple and with a programmable controller (Watlow EZ-ZONE Controller) that regulates the Peltier cell performance, allowing us to maintain the sample at 5 ºC during the whole matrix deposition process.

Four ports, 2 ISO KF 16 and 2 ISO KF 25, were attached to the vertical side of the chamber: one is used for connection to the vacuum system, a second one holds a four-wire feedthrough for the matrix heating system. A third one is used for a digital vacuum controller (Thyracont Vacuum Smart Line) and the fourth one is a multipurpose port for future applications. Vacuum is achieved with a small mechanical pump (Pfeiffer Vacuum, model DUO 2.5, Germany), connected to the chamber by a rubber tube.

The bottom side of the chamber is a flat flange, attached with ISO KF 63-250 double clamps. Attached to the inside of this flange is a holder for the heater and the matrix tray. The heating system consists of an aluminum cylinder on which a heater (DBK Enclosures, mod. FG800006, 200 W, 100-240 v ac/dc, purchased on-line through RS, ref: 381-0119) is placed in a special groove in a fixed position. On top of the heating element, a tray for the matrix is placed. Several geometries for this tray were tested (see **Figure A.4.2** for two examples). The one that gave best results is 5 mm high, with a small sample compartment in the center of 1 mm depth and 10 mm diameter, where the matrix is deposited. The tray position relative to the heater and the holder is fixed thanks to four pins (studs) and fastening with nuts and washers. To control the heating temperature, in the bottom of the matrix tray, on its side adjacent to the heating element, a narrow groove was made for a (K-type) thermocouple that is connected to a controller (Osaka QB48) that regulates the voltage of the heater. This set up enables a fine (± 1 ºC) control of the sublimation temperature.
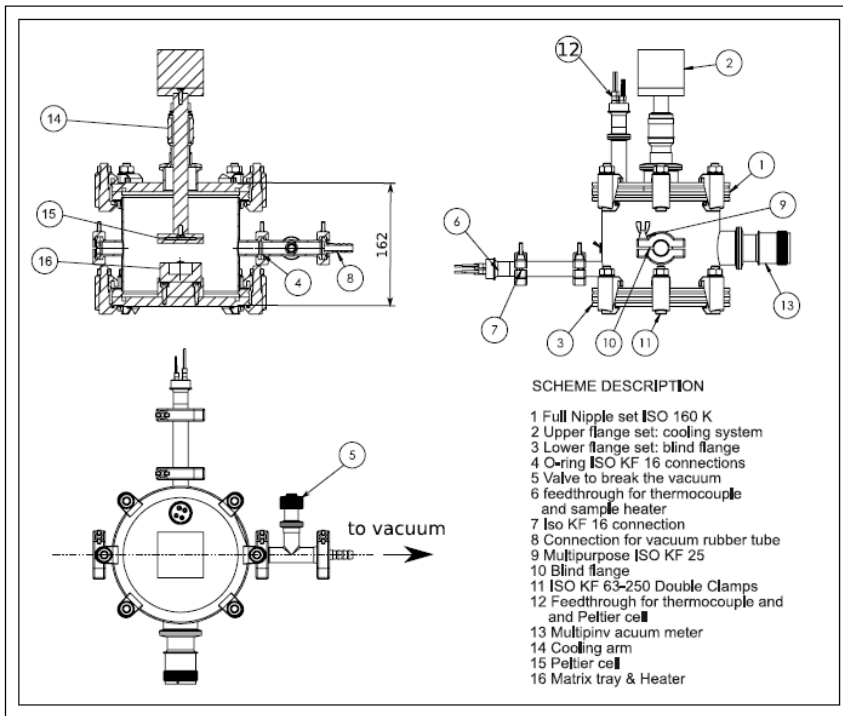
Figure A.4.1. Schematics of the inner (upper left), outer (upper right) and (bottom left) views of the developed stainless steel sublimator.
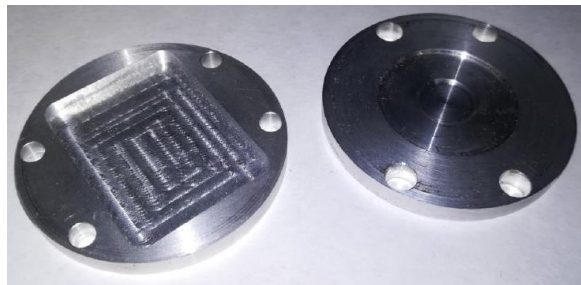
Figure A.4.2. Some of the designs of the matrix holder tested. The one on the right offered the best results.

The heating element is in close contact with the matrix holder to provide maximum thermal contact, and to facilitate temperature control. In the presented version of the sublimator, the total height of the heating system and, consequently, the distance from the matrix powder to the sample surface, is maintained constant, although the design

enables the modification of such distance and it may also influence the sublimation process.

The glass slides (75 mm x 25 mm) carrying the tissue sections, are attached to the sample holder by means of metal holders (snaps), and are always in the same position relative to the matrix holder. This is also important to achieve the best reproducibility of the process.

Matrix deposition using the homemade stainless steel sublimation apparatus

About 300 sublimation experiments were performed for DAN and MBT matrices, always using 30 mg of matrix powder. In order to control and ensure reproducibility of the sublimation process, the experiments were repeated five times for each set of heating temperature and sublimation time values. Between the experiments, the system was cooled down to room temperature (in the initial experiments), or to a maximum 55°C (in later experiments), before starting the next heating cycle. The full series (5 repetitions) for a given heating temperature was not necessarily conducted on the same day, and the starting temperature also varied from experiment to experiment.

The amount of sublimed matrix was determined weighting the glass sample slides before and after sublimation on an analytical balance (Mettler Toledo XP105DR, Switzerland). Due to the small ammount of matrix deposited per area unit (below 1 mg/cm2), and the precision of the balance (0.01 mg in this weight range) the values are given with an ~10% uncertainty. Thus, part of the variability observed in the ammount of matrix deposited may be actually due to the balance.

The cooling temperature and initial vacuum conditions inside the sublimation chamber for all sublimation experiments remained constant. Cooling temperature was maintained at 5°C, and initial vacuum pressure was 0.4 mbar. Sublimation times of 6, 8, 10, 12 and 14 min were explored, while heating temperature of 110, 115, 120, 125, 130°C were used both for DAN and MBT.
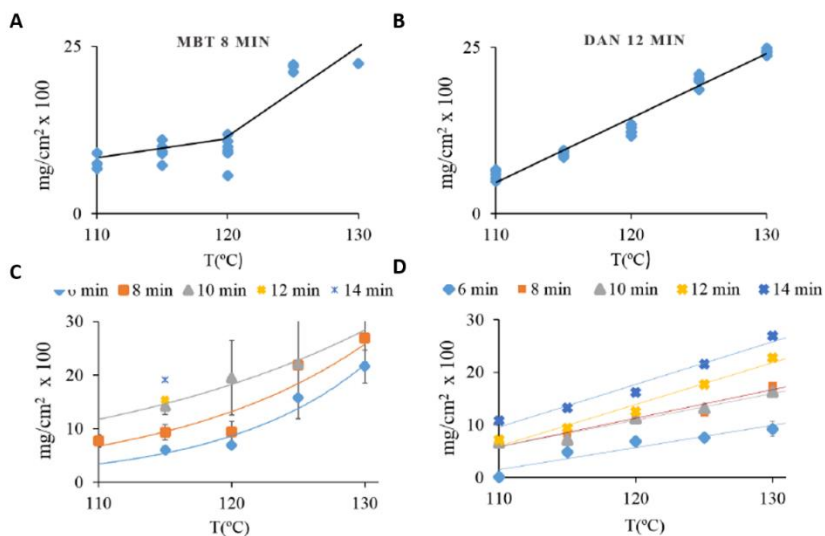
Figure A.4.3. (A) Variation with the temperature of the ammount of MBT deposited with the new sublimator, setting the sublimation time to 8 min; *(B)* Variation with the temperature of the ammount of DAN deposited with the new sublimator, setting the sublimation time to 12 min; *(C)* variation with the temperature of the ammount of MBT deposited, using different deposition times; *(D)* similar experiment for DAN.
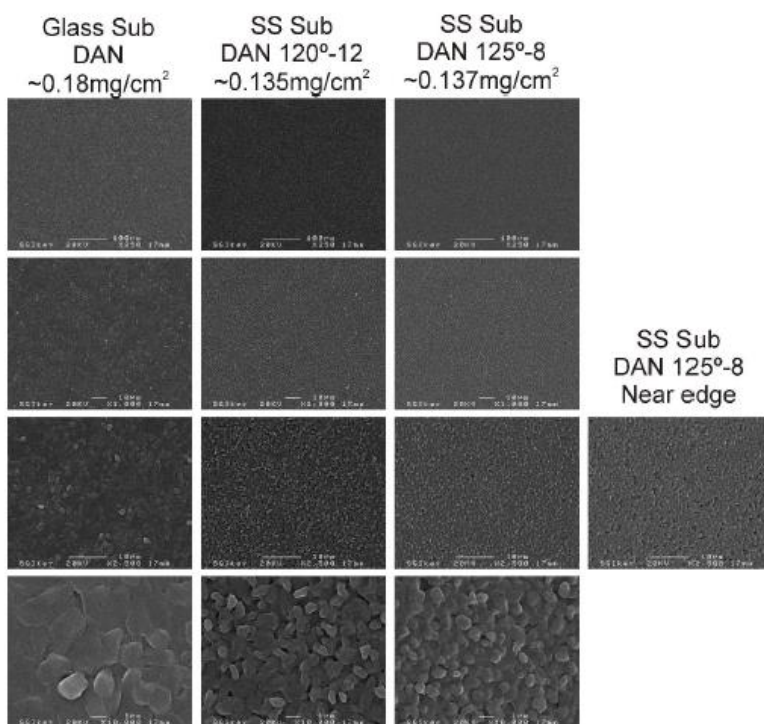
Figure A.4.5. *S.E.M images of 1,5-diaminonapthalene (DAN), deposited on glass slides using the glass sublimator (Glass Sub) and the new stainless steel sublimator (SS Sub). The matrix density and sublimation conditions (temperature in celsius and deposition time) are also included for the SS Sub.*
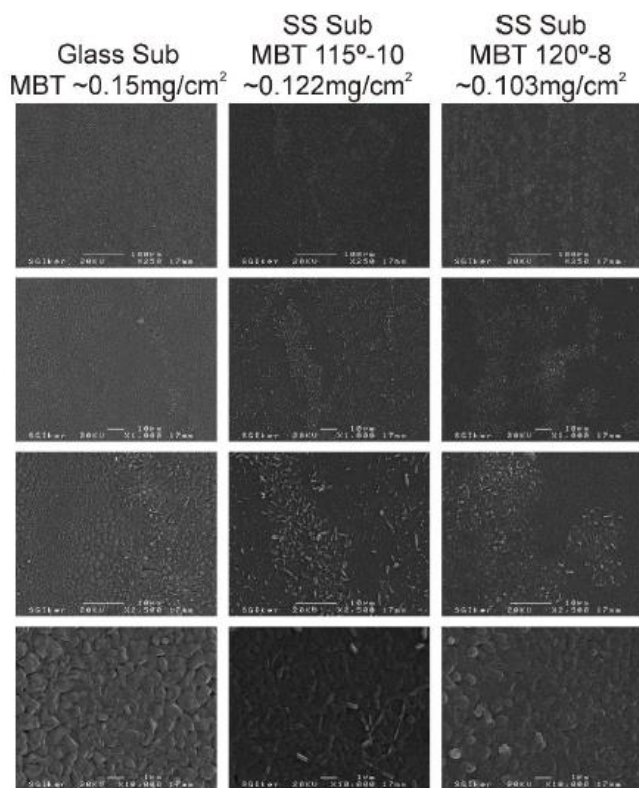
Figure A.4.6. *S.E.M images of 2-mercaptobenzothiazole (MBT), deposited on glass slides using the glass sublimator (Glass Sub) and the new stainless steel sublimator (SS Sub). The matrix density and sublimation conditions (temperature in celsius and deposition time) are also included for the SS Sub.*
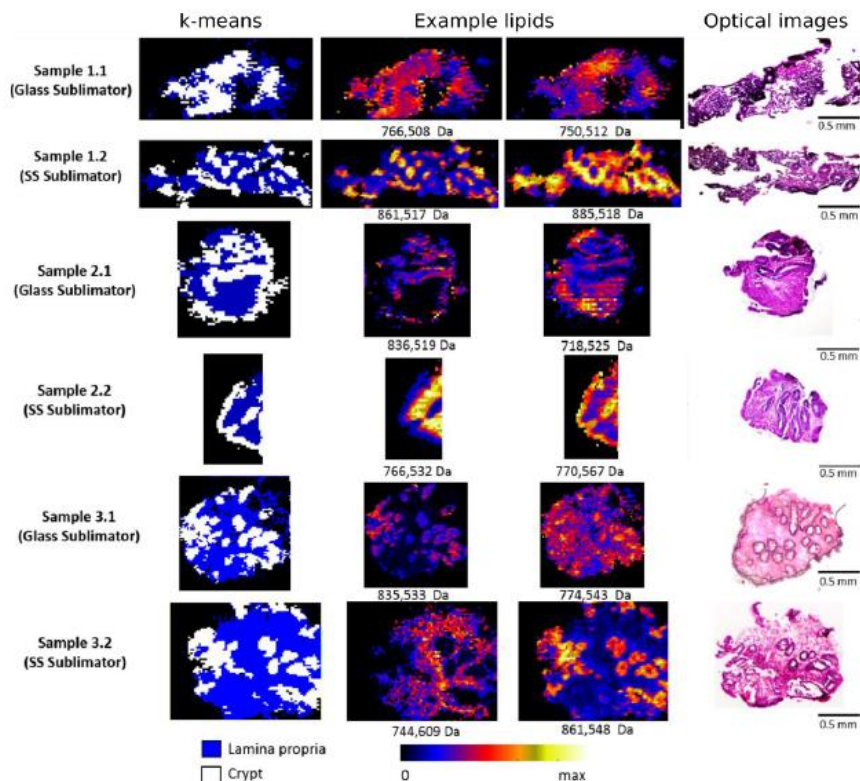
Figure A.4.7. Comparison between the optical images of colon tissue sections (right column) with the distribution of some lipid species along consecutive sections obtained in negative-ion mode using DAN and the segmentation analysis using k-means and setting the number of clusters to 3. The white cluster corresponds to the lamina propria and the blue cluster to the crypts. The cluster outside the tissue and that contains only matrix peaks was omitted.

Improving spatial resolution of a LTQ Orbitrap MALDI source

Table A.4.5 Part list for system upgrade

- **Lenox Laser** (12530 Manor Rd. Glen Arm MD 21057 Tel (410) 592-3106 Fax (410) 592-3362 www.lenoxlaser.com / email - sales@lenoxlaser.com)

H/P Ceramic Aperture, 20 Micron – Pinhole 1u

- **Thorlabs GmbH** (Hans-Böckler-Strasse 6 Dachau, BY 85221, DE. Tel+49 8131 5956 0 Fax +49 8131 5956 99 Email sales.de@thorlabs.com)

LA4380-UV - f = 100 mm, Ø1" UV Fused Silica Plano-Convex Lens, UV AR Coating **2u**

NB1-K07 - Ø1" Mirror, 333 - 364 nm, 0° to 45° AOI	2u
C45P - Right-Angle Kinematic Mount for Ø1" Optics	**2u**
SP30 - 30 mm to 16 mm Cage System Right-Angle Adapter	2u
SR05-P4 - Compact Cage Assembly Rod, 1/2" Long, Ø4 mm, 4 Pack	**1u**
SR1-P4 - Compact Cage Assembly Rod, 1" Long, Ø4 mm, 4 Pack	1u
SP05/M -30 mm to 16 mm Cage Adapter Plate, Metric	**2u**
ER2-P4 - Cage Assembly Rod, 2" Long, Ø6 mm, 4 Pack	1u
ER3-P4 - Cage Assembly Rod, 3" Long, Ø6 mm, 4 Pack	1u
KCB1C/M -Right-Angle Kinematic Mirror Mount	2u
CXY1Q - XY Translating Mount for Ø1" Optics with Quick Release Plate	**2u**
CXY1QF - Quick-Release Plate for the CXY1Q Translation Mount	1u
PF175 -Clamping Fork for Ø1.5" Pedestal Post	**1u**
ER1-P4 - Cage Assembly Rod, 1" Long, Ø6 mm, 4 Pack	1u
SM1Z - Z-Axis Translation Mount, 30 mm Cage Compatible	**2u**
C1515/M - Ø1.5" Mounting Post Bracket, M6 Taps	1u
P350/M - Ø1.5" Mounting Post, M6 Taps, L = 350 mm	**1u**
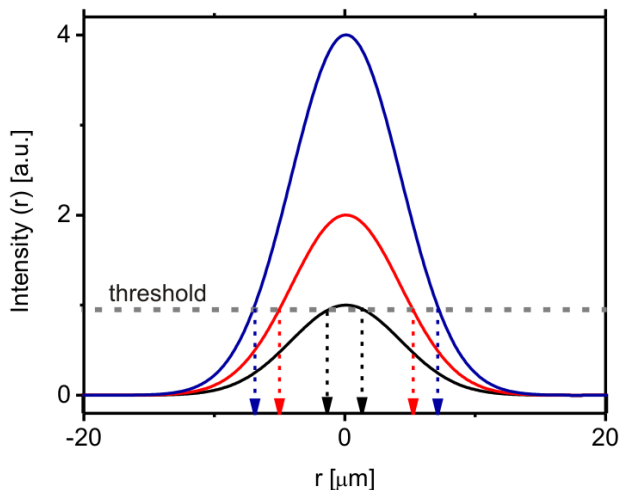
Figure A.4.8. *Dependence of the spot size with the laser intensity. If we consider the matrix evaporation threshold (grey dashed line) as the minimal intensity required to produce matrix ionization and ablation, in the case of gaussian-like intensity distributions, those pulses close to the threshold (black line) will only produce sample removal in regions close to the maximum intensity (between the black arrows). If the intensity is doubled (red line), the spot left will have a diameter equivalent to the FWHM of the intensity curve (I(r)). Likewise, a four times increase in the pulse intensity (blue curve) will produce a print equivalent to the width of the intensity curve at ~ ¼ of its height (blue arrows). Therefore, a systematic study of the spot size on the matrix permits the retrieval of the intensity curve simply by plotting the quantity threshold/energy versus size of the crater as presented in* **Figure 4.21B.**

Appendix Chapter 5
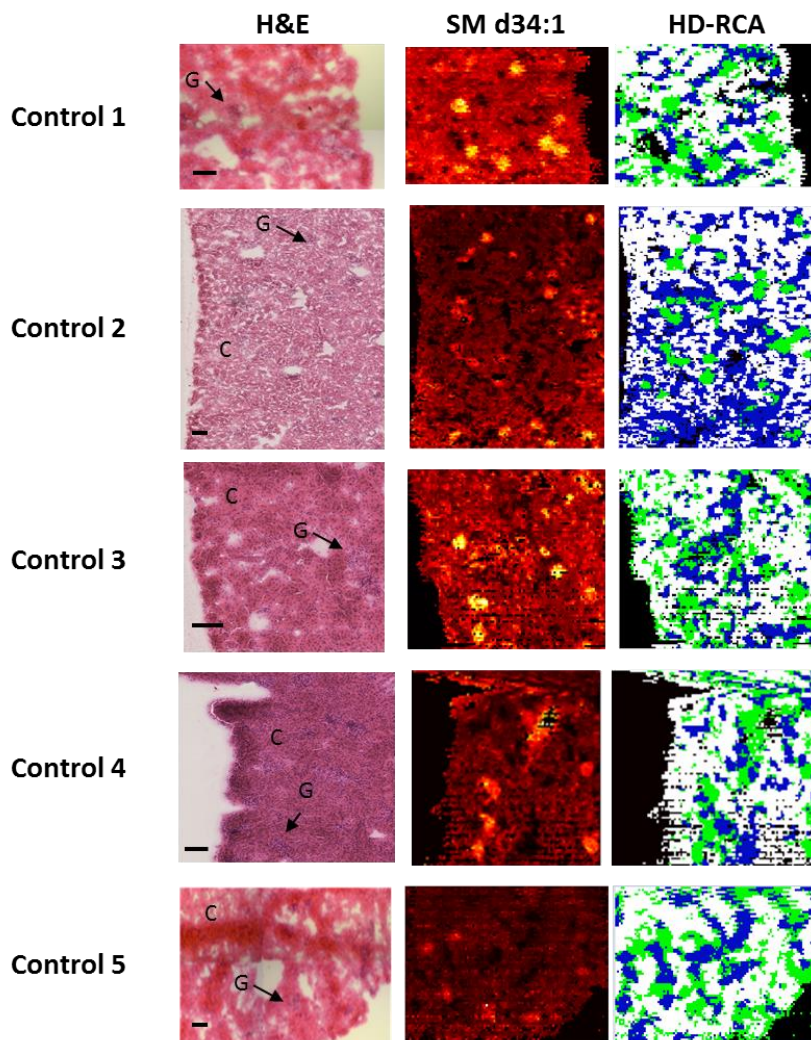
Figure A.5.1. *H&E staining of five control kidney samples compared with SM d34:1 IMS distribution and with the HD-RCA clustering segmentation. Experiments were carried ot at 10 µm of spatial resolution and in negative ion mode. Cortical tubules are colored in white and blue and glomeruli in green. Scale bar=150 µm.*
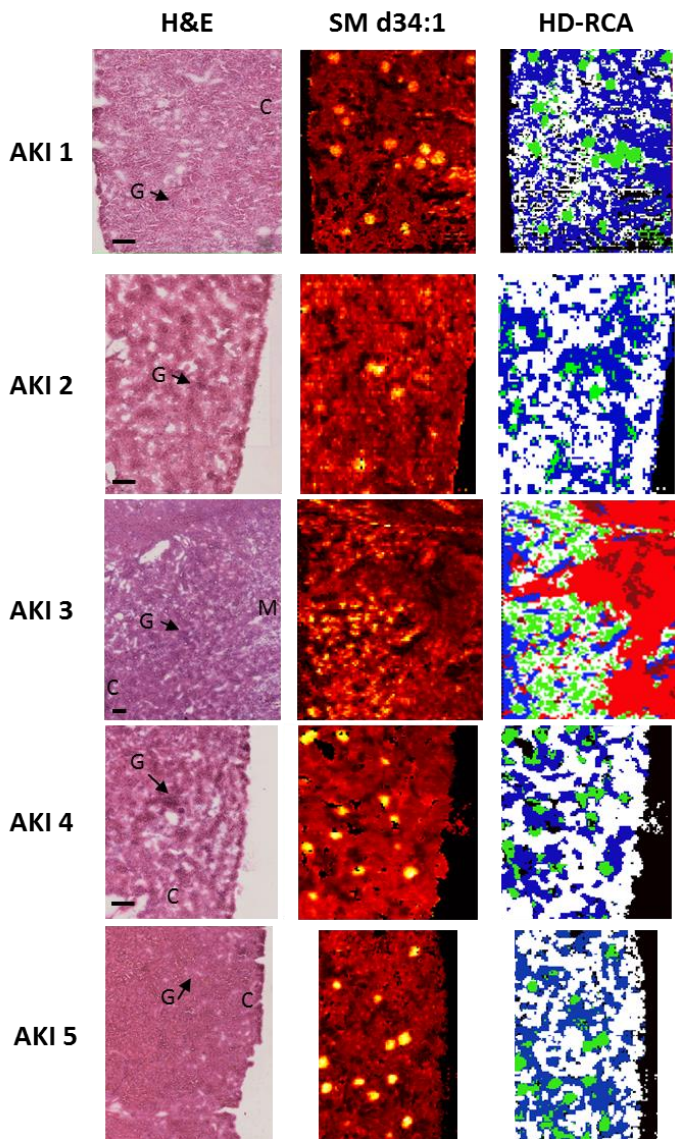
Figure A.5.2. *H&E staining of five AKI kidney samples compared with SM d34:1 IMS distribution and with the HD-RCA clustering segmentation. Experiments were carried ot at 10 µm of spatial resolution and in negative ion mode. Cortical tubules are colored in white and blue and glomerulli in green. Scale bar=150 µm.*
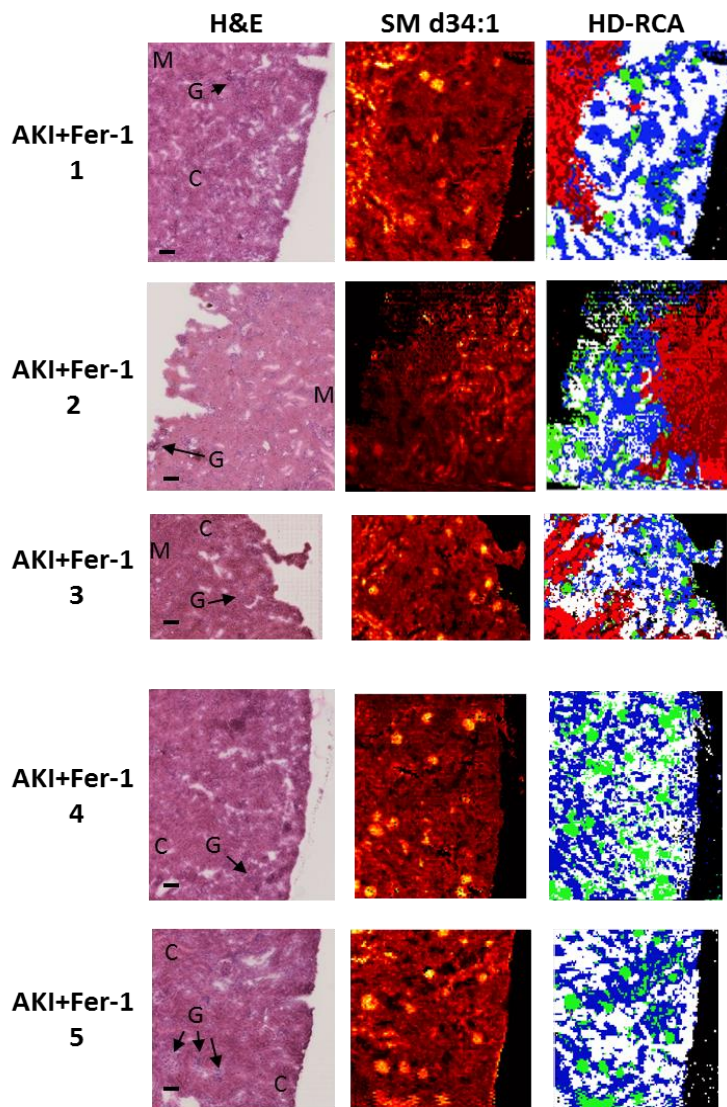
Figure A.5.3 *H&E staining of five AKI+Fer-1 kidney samples compared with SM d34:1 IMS distribution and with the HD-RCA clustering segmentation. Experiments were carried out at 10 µm of spatial resolution and in negative ion mode. Cortical tubules are colored in white and blue and glomeruli in green. Scale bar=150 µm.*

Table A.5.1.Significative differences in lipid species among cortex (C), glomeruli (G) and medulla (M) in healthy kidney.

Lipid	Levene test	ANOVA	p-value post-hoc			post-hoc
			C vs G	C vs M	G vs M	
HexCer d30:0 -H-	0.012	0.022	0.060	0.781	0.143	Games- Howell
HexCer d30:1 -H-	0.136	0.049	0.046	0.730	0.167	Tukey
HexCer t39:4 -H-	0.088	0.050	0.046	0.716	0.175	Tukey
Lyso-PI 20:4-H-	0.410	0.035	0.453	0.232	0.029	Tukey
PC 38:4-CH3-	0.198	0.010	0.021	0.994	0.017	Tukey
PC-O 38:7/PC-P 38:6-CH3-	0.796	0.048	0.042	0.646	0.042	Tukey
PE 38:3-H-	0.657	0.043	0.002	0.830	0.002	Tukey
PE 38:4-H-	0.886	0.045	0.001	0.830	0.001	Tukey
PE 38:6-H-	0.313	0.043	0.001	0.229	0.001	Tukey
PE 40:6-H-	0.404	0.033	0.461	0.213	0.027	Tukey
PE 40:7-H-	0.802	0.043	0.048	0.022	0.048	Tukey
PE-O 38:5/PE-P 38:4-H-	0.168	0.043	0.008	0.943	0.008	Tukey
PE O-40:5/PE-P 38:3-H-	0.088	0.050	0.046	0.716	0.175	Tukey
PG 36:0-H-	0.000	0.006	0.387	0.073	0.107	Games- Howell
PG 36:1-H-	0.051	0.047	0.033	0.993	0.033	Tukey
PG 36:2-H-	0.000	0.010	0.035	0.993	0.035	Games- Howell
PG 36:3-H-	0.001	0.018	0.619	0.014	0.619	Games- Howell
PG 38:1-H-	0.000	0.014	0.017	0.014	0.017	Games- Howell
PI 36:1-H-	0.141	0.041	0.017	0.016	0.017	Tukey
PI 38:3-H-	0.294	0.048	0.176	0.045	0.701	Tukey
PI 38:4-H-	0.865	0.042	0.005	0.943	0.005	Tukey
PI 38:6-H-	0.261	0.022	0.790	0.076	0.024	Tukey
PI-O 38:5/ PI-P 38:4-H-	0.032	0.014	0.022	0.028	0.992	Tukey
PS 36:1-H-	0.792	0.009	0.012	0.914	0.025	Tukey
PS 36:2-H-	0.323	0.041	0.028	0.990	0.028	Tukey
PS 36:4-H-	0.661	0.042	0.022	0.990	0.022	Tukey
PS 40:4-H-	0.003	0.001	0.029	0.404	0.015	Games- Howell
PS-O 38:2/PS-P 38:1-H-	0.228	0.008	0.007	0.507	0.053	Tukey
SM d36:1-CH3-	0.013	0.032	0.091	0.840	0.034	Tukey
SM d38:1-CH3-	0.297	0.041	0.002	0.830	0.002	Tukey
SM d40:1-CH3-	0.373	0.004	0.001	0.830	0.001	Tukey
SM d41:1-CH3-	0.026	0.040	0.029	0.958	0.131	Games- Howell
SM d42:2-CH3-	0.477	0.049	0.048	0.022	0.048	Tukey
SFT t42:0-H-	0.072	0.022	0.002	0.159	0.959	Tukey
SFT t40:0-H-	0.062	0.032	0.032	0.404	0.215	Tukey
SFT t40:2-H-	0.022	0.049	0.086	0.049	0.135	Games- Howell

Table A.5.2.*Significative differences in lipid species among cortex (C), glomeruli (G) and medulla (M) in AKI kidney.*

Lipid	Levene test	ANOVA	p-value post-hoc			Post-hoc
			C vs G	C vs M	G vs M	
HexCer d28:1 -H-	0.0764	0.0159	0.9991	0.0272	0.0292	Tukey
HexCer d30:1 -H-	0.3219	0.0222	0.0174	0.3151	0.2322	Tukey
HexCer t39:4 -H-	0.0943	0.0125	0.0237	0.9986	0.0217	Tukey
PC 38:5-CH3-	0.7477	0.0005	0.0158	0.1141	0.0004	Tukey
PC 38:8-CH3-	0.0580	0.0011	0.0077	0.0011	0.5174	Tukey
PC-O 36:6/PC-P 36:5-CH3-	0.0004	0.0424	0.6179	0.0106	0.0584	Games-Howell
PC-O 40:7/PC-P 40:6-CH3-	0.0296	0.0051	0.0142	0.0502	0.0649	Games-Howell
PE 34:2-H-	0.8741	0.0061	0.0880	0.0047	0.2627	Tukey
PE 36:1-H-	0.8505	0.0148	0.0457	0.8503	0.0172	Tukey
PE 36:4-H-	0.4516	0.0030	0.0029	0.0219	0.5135	Tukey
PE 38:6-H-	0.3859	0.0014	0.0021	0.0050	0.8779	Tukey
PE 40:7-H-	0.8536	0.0028	0.0021	0.0998	0.1114	Tukey
PE 40:8-H-	0.0645	0.0018	0.0081	0.0022	0.7466	Tukey
PE-O 36:5/PE-P 36:4-H-	0.7654	0.0000	0.0000	0.0015	0.0000	Tukey
PE-O 40:5/PE P-40:4-H-	0.0903	0.0135	0.0204	0.9776	0.0294	Tukey
PE-O 40:8/PE P-40:7-H-	0.0124	0.0023	0.0142	0.0582	0.0750	Games-Howell
PG 36:2-H-	0.0258	0.0000	0.7390	0.0008	0.0009	Games-Howell
PG 36:3-H-	0.1737	0.0002	0.6073	0.0013	0.0003	Tukey
PG 36:4-H-	0.6529	0.0062	0.5907	0.0060	0.0361	Tukey
PG 38:1-H-	0.0398	0.0004	0.6280	0.0326	0.0341	Games-Howell
PG 38:6-H-	0.0686	0.0406	0.3006	0.0327	0.3958	Tukey
PG 40:7-H-	0.1044	0.0344	0.0484	0.0655	0.9836	Tukey
PG 40:8-H-	0.1552	0.0070	0.0224	0.0089	0.8655	Tukey
PI-O 38:5/PI-P 38:4-H-	0.0358	0.0438	0.0209	0.4016	0.5106	Games-Howell
PS 31:0-H-	0.1002	0.0210	0.0308	0.9807	0.0430	Tukey
PS 36:2-H-	0.0078	0.0056	0.0702	0.8378	0.0496	Games-Howell
PS 36:4-H-	0.0075	0.0128	0.0531	0.8769	0.0418	Games-Howell
SM d34:1-CH3-	0.2114	0.0105	0.0081	0.2758	0.1384	Tukey
SM d36:1-CH3-	0.1639	0.0000	0.0000	0.7236	0.0000	Tukey
SM t34:2-CH3-	0.5418	0.0000	0.0002	0.0481	0.0000	Tukey
SFT t40:0 -H-	0.6218	0.0085	0.0008	0.0008	0.4314	Tukey
SFT t40:2 -H-	0.2077	0.0022	0.0292	0.0290	0.0837	Tukey
SFT t41:1 -H-	0.3785	0.0453	0.0462	0.0436	0.3525	Tukey
SFT t42:0 -H-	0.6244	0.0283	0.0222	0.0294	0.4770	Tukey

*Table A.5.3.*Significative differences in lipid species among cortex (C), glomeruli (G) and medulla (M) in AKI+Fer-1 kidney.

Lipid	Levene test	ANOVA	p-value pos-hoc			post-hoc
			C vs G	C vs M	G vs M	
HexCer d30:0 -H-	0.178	0.023	0.019	0.427	0.175	Tukey
HexCer d30:1 -H-	0.081	0.044	0.041	0.153	0.729	Tukey
HexCer d36:0 -H-	0.129	0.012	0.010	0.474	0.088	Tukey
HexCer t33:1 -H-	0.734	0.007	0.612	0.007	0.037	Tukey
HexCer t35:1 -H-	0.153	0.000	0.993	0.001	0.001	Tukey
HexCer t39:4 -H-	0.352	0.000	0.000	0.514	0.001	Tukey
PC 34:0-CH3-	0.030	0.032	0.345	0.008	0.615	Games-Howell
PC 38:5-CH3-	0.143	0.042	0.237	0.504	0.035	Tukey
PC-O 34:2/PC-P 34:1-CH3-	0.307	0.011	0.070	0.024	0.824	Tukey
PC-O 36:6/PC-P 36:5-CH3-	0.000	0.042				Games-Howell
PC-O 40:7/PC-P 40:6-CH3-	0.030	0.005	0.014	0.050	0.065	Games-Howell
PE 34:2-H-	0.278	0.001	0.002	0.001	0.929	Tukey
PE 36:3-H-	0.037	0.037	0.036	0.115	0.967	Games-Howell
PE 36:4-H-	0.612	0.001	0.002	0.003	0.929	Tukey
PE 38:3-H-	0.521	0.006	0.006	0.046	0.488	Tukey
PE 38:4-H-	0.806	0.019	0.030	0.036	0.993	Tukey
PE 38:6-H-	0.720	0.004	0.011	0.005	0.916	Tukey
PE 40:7-H-	0.750	0.008	0.020	0.011	0.945	Tukey
PE-O 34:2/PE-P 34:1-H-	0.734	0.007	0.612	0.007	0.037	Tukey
PE-O 36:2/PE-P 36:1-H-	0.153	0.000	0.993	0.001	0.001	Tukey
PE-O 40:5/PE-P 40:4-H-	0.352	0.000	0.000	0.514	0.001	Tukey
PG 36:3-H-	0.068	0.000	0.489	0.001	0.000	Tukey
PG 38:1-H-	0.008	0.001	0.914	0.046	0.045	Games-Howell
PG 40:7-H-	0.153	0.009	0.011	0.035	0.792	Tukey
PG 40:8-H-	0.090	0.004	0.004	0.045	0.374	Tukey
PI 35:6-H-	0.030		0.024	0.890	0.672	Games-Howell
PI O-38:5-H-	0.263	0.012	0.035	0.337	0.376	Tukey
PS 31:0-H-	0.185	0.028	0.031	0.981	0.043	Tukey
PS 36:2-H-	0.002	0.002	0.070	0.838	0.050	Games-Howell
PS 36:4-H-	0.075	0.013	0.015	0.823	0.043	Tukey
SM d34:1-CH3-	0.082	0.010	0.008	0.276	0.138	Tukey
SM d36:1-CH3-	0.006	0.002	0.002	0.484	0.002	Games-Howell

Appendix Chapter 6

Cortex samples
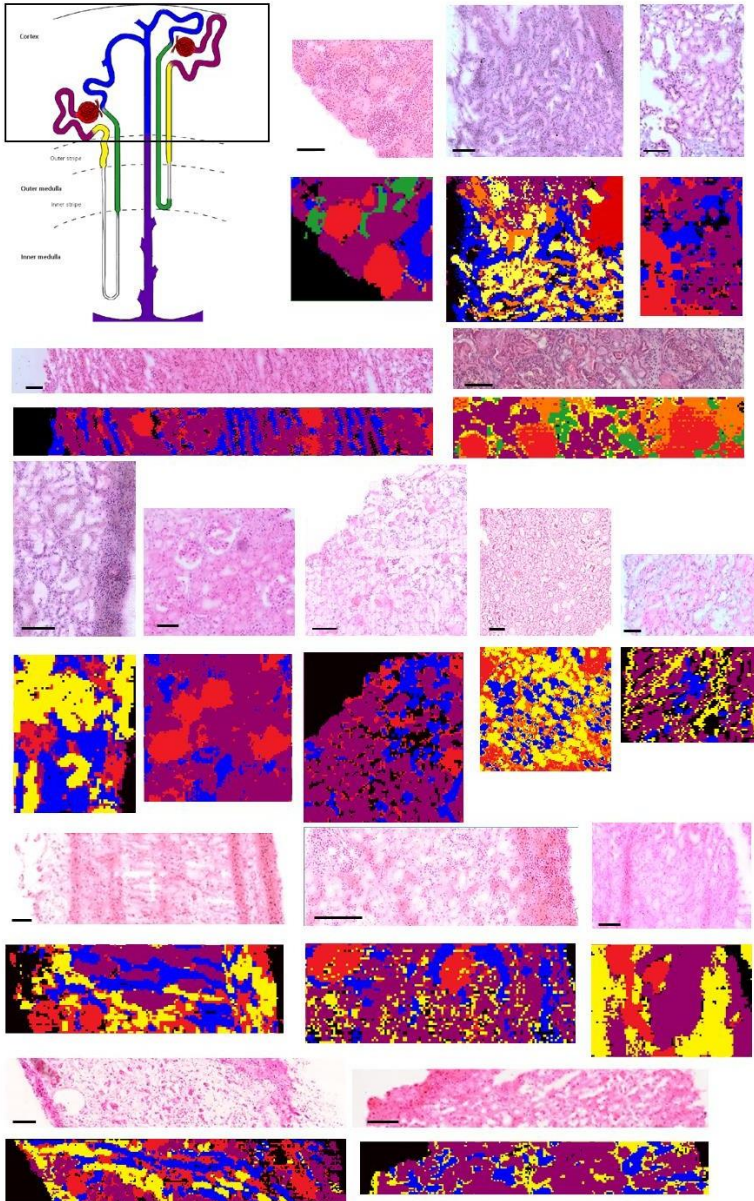
Figure A.6.1. *Comparison between H&E optical images of 15 human cortical renal samples and their corresponding image of the segmentation analysis based on their lipid fingerprint obtained by IMS. The colored nephron scheme clarify the renal area which the samples belong. The Images were recorded in negative-ion mode at a pixel size of 10μm. Scale bar=150 μm.*
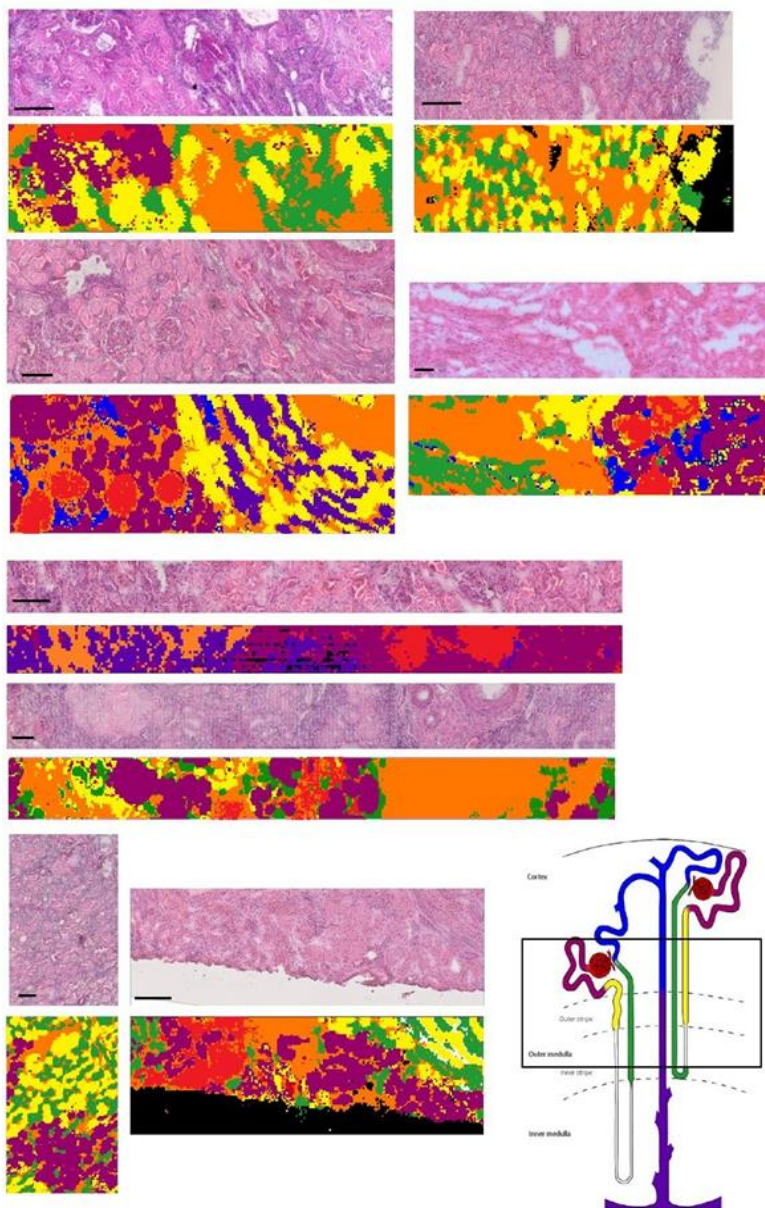
Figure A.6.2. *Comparison between H&E optical images of 8 human corticomedullary renal samples and their corresponding image of the segmentation analysis based on their lipid fingerprint obtained by IMS. The colored nephron scheme clarify the renal area which the samples belong. The Images were recorded in negative-ion mode at a pixel size of 10μm. Scale bar=150 μm.*

Medullary samples
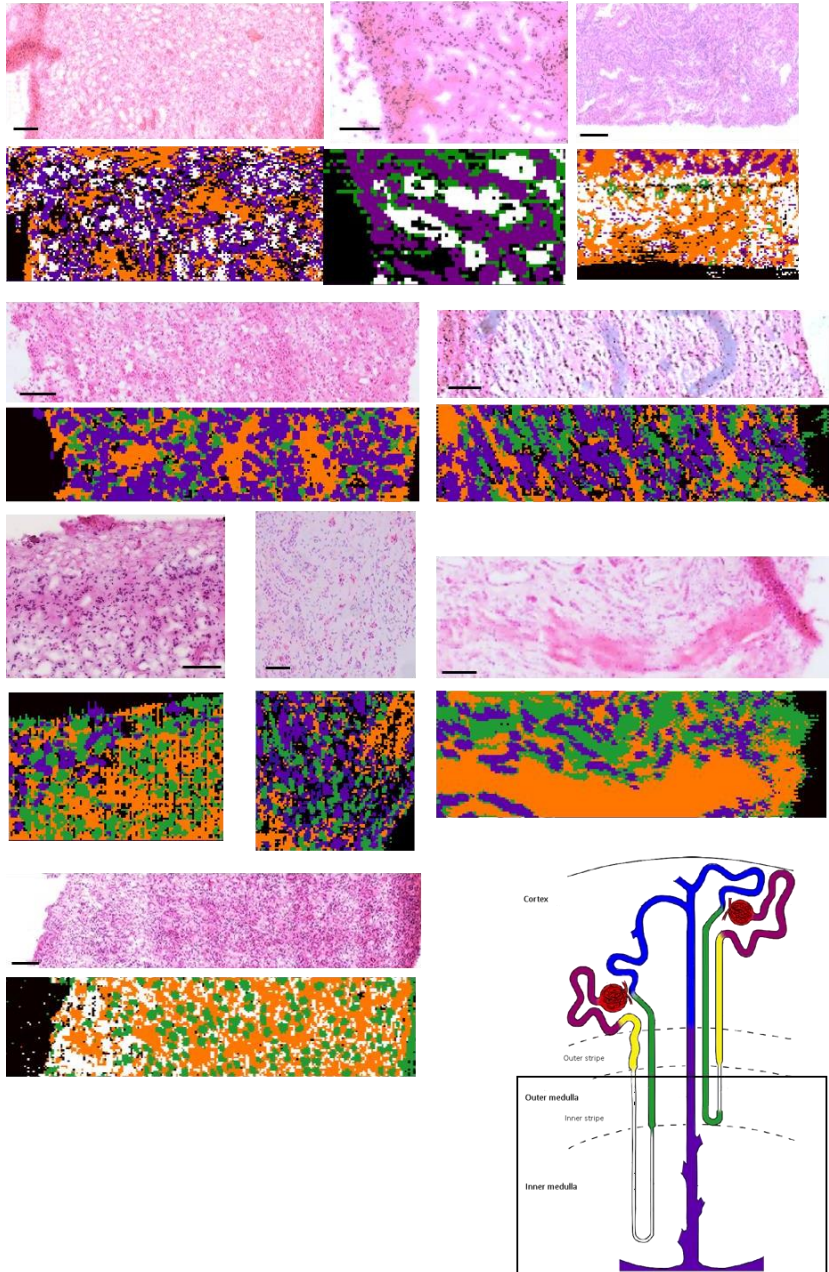
Figure A.6.3. Comparison between H&E optical images of 9 human medullary renal samples and their corresponding image of the segmentation analysis based on their lipid fingerprint obtained by IMS. The colored nephron scheme clarify the renal area which the samples belong. The Images were recorded in negative-ion mode at a pixel size of 10μm. Scale bar=150 μm.
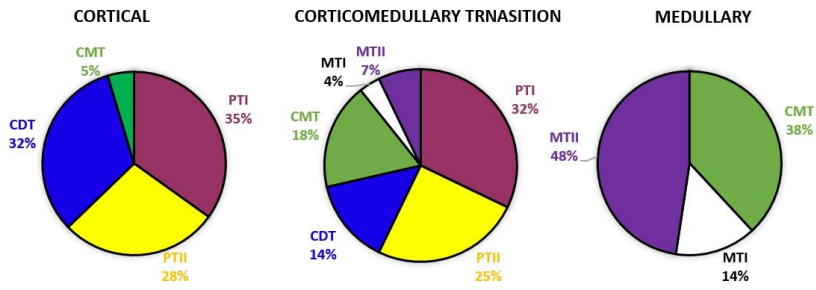
Figure A.6.4. *Percentage of the total area covered by each histologic structure in cortex, corticomedullary and medullary samples, excluding the vascular structures (G and ITS).*
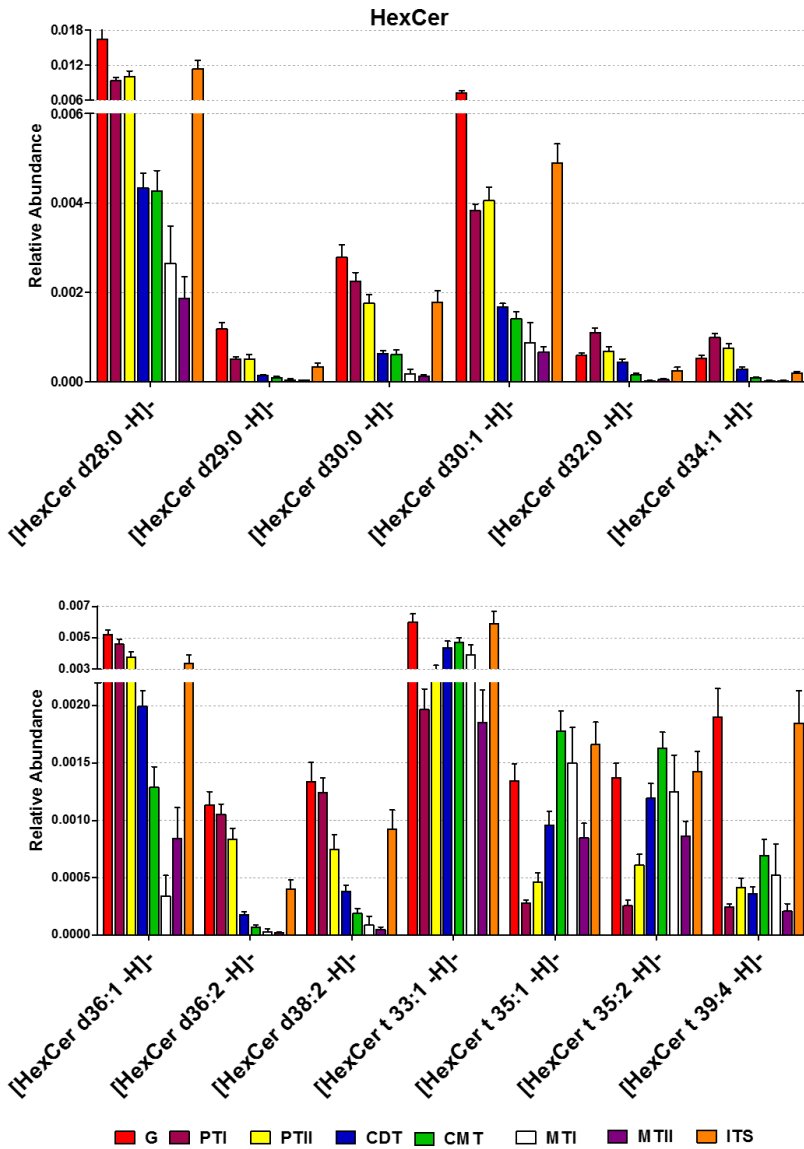
Figure A.6.5. *Bar charts of the relative abundance variation of the Hexo Ceramides lipid species in the eight histological found regions. Abbreviations; G, Glomeruli; PTI, Proximal tubule I; PTII, Proximal tubule II; CDT, Cortical distal tubule; CMT, Corticomedullary tubule; MTI, Medullary distal tubule I; MTII, Medullary distal tubule II; ITS, interstitial structure. Values are expressed as mean ± SEM. Statistical analysis reported in* **Table A.6.1.**
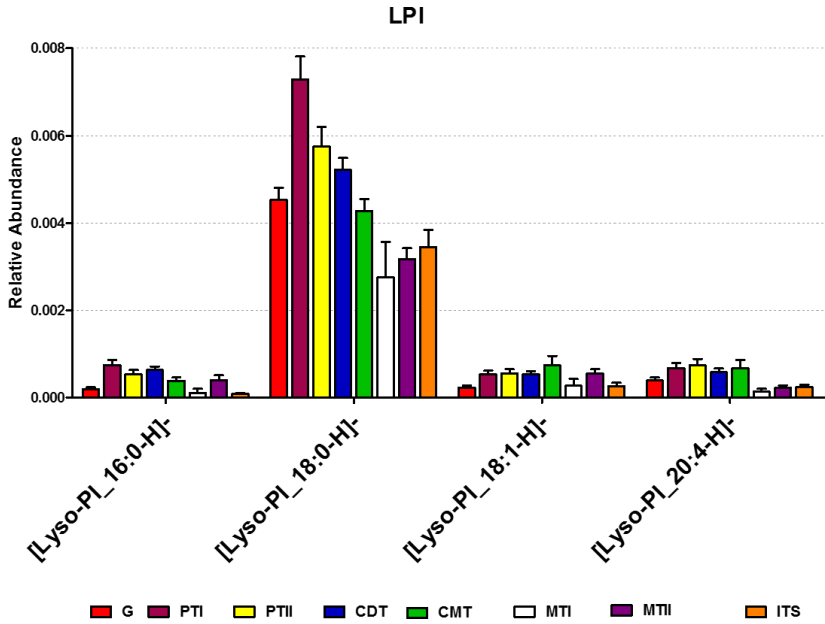
Figure A.6.6. *Bar charts of the relative abundance variation of the Lyso-Phosphatidylinositol lipid species in the eight histological found regions. Abbreviations; G, Glomeruli; PTI, Proximal tubule I; PTII, Proximal tubule II; CDT, Cortical distal tubule; CMT, Corticomedullary tubule; MTI, Medullary distal tubule I; MTII, Medullary distal tubule II; ITS, interstitial structure. Values are expressed as mean ± SEM. Statistical analysis reported in **Table A.6.1.***
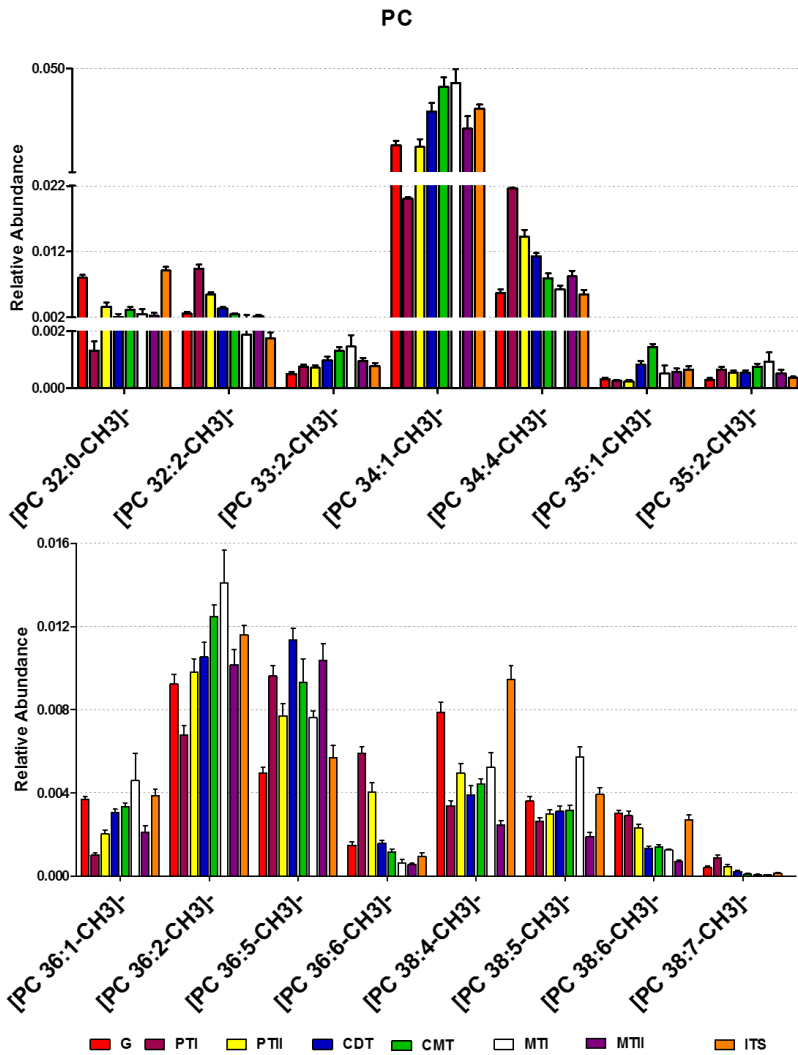
Figure A.6.7. Bar charts of the relative abundance variation of the Phosphatidylcholine lipid species in the eight histological found regions. Abbreviations; G, Glomeruli; PTI, Proximal tubule I; PTII, Proximal tubule II; CDT, Cortical distal tubule; CMT, Corticomedullary tubule; MTI, Medullary distal tubule I; MTII, Medullary distal tubule II; ITS, interstitial structure. Values are expressed as mean ± SEM. Statistical analysis reported in **Table A.6.1.**
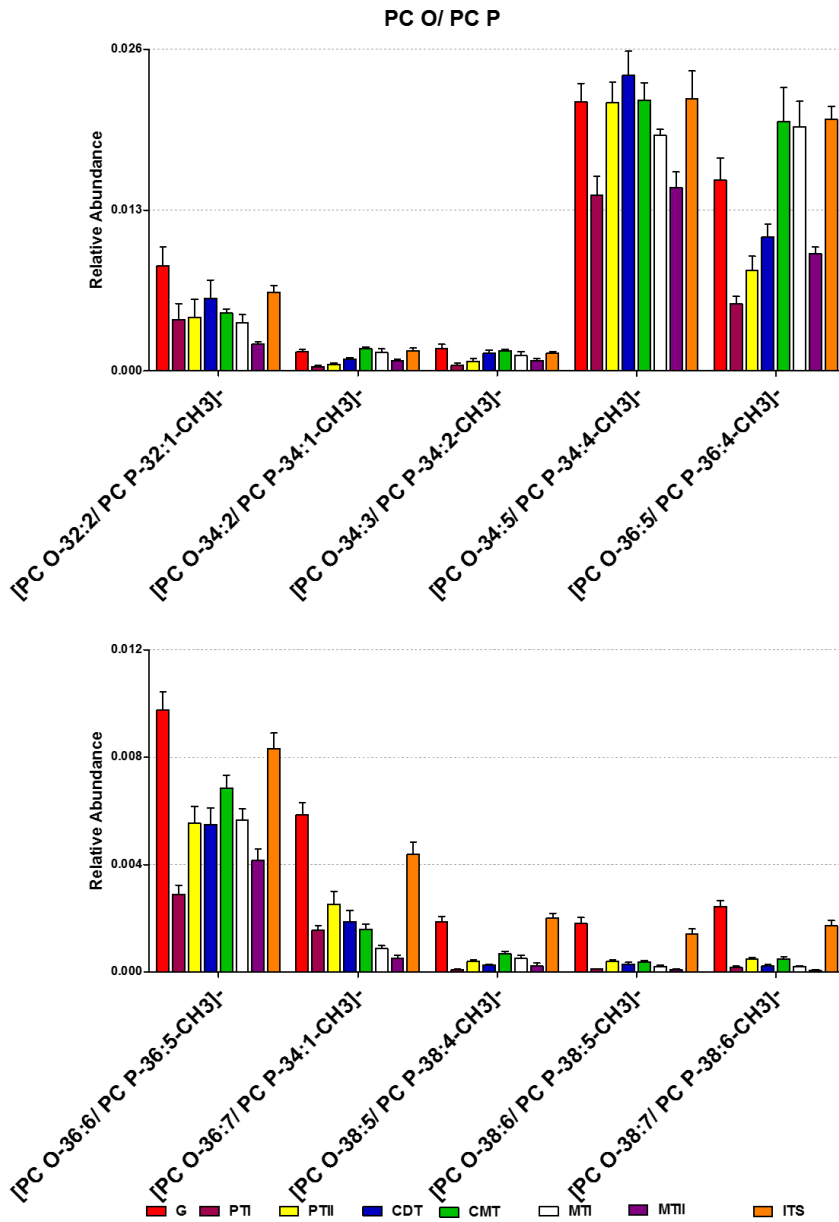
Figure A.6.8. Bar charts of the relative abundance variation of the Phosphatidylcholine plasmalogen lipid species in the eight histological found regions. Abbreviations; G, Glomeruli; PTI, Proximal tubule I; PTII, Proximal tubule II; CDT, Cortical distal tubule; CMT, Corticomedullary tubule; MTI, Medullary distal tubule I; MTII, Medullary distal tubule II; ITS, interstitial structure. Values are expressed as mean ± SEM. Statistical analysis reported in *Table A.6.1.*
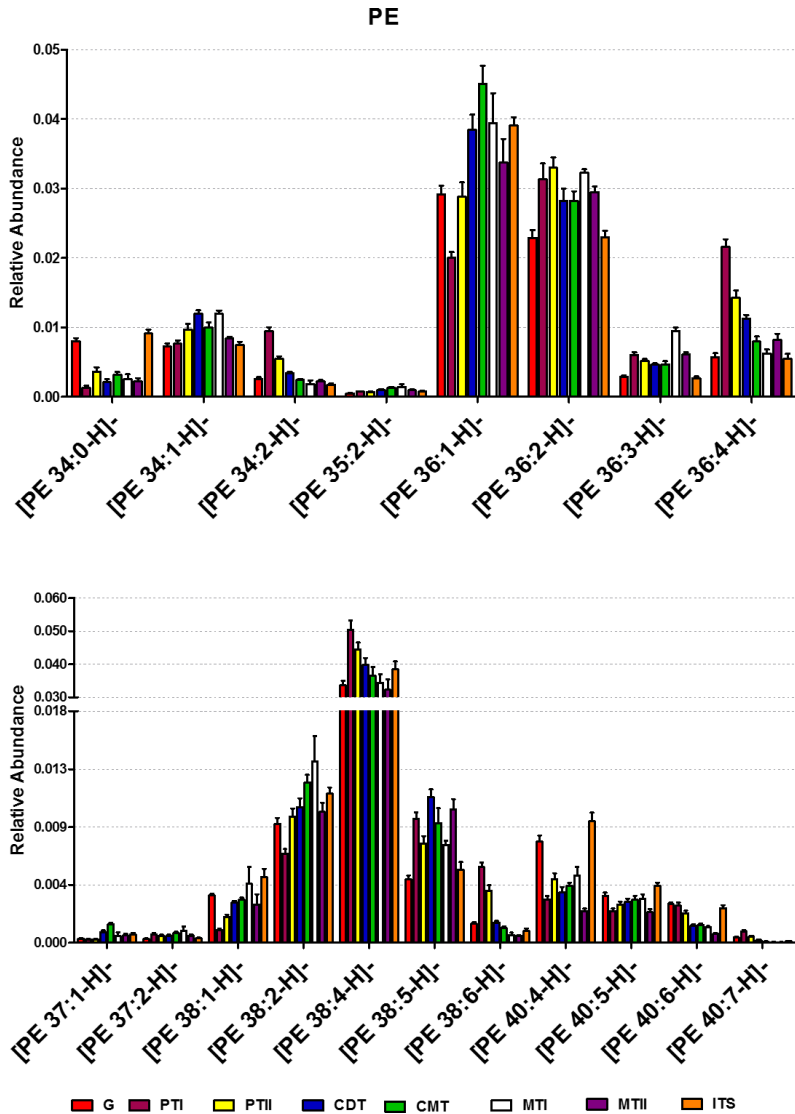
Figure A.6.9*. Bar charts of the relative abundance variation of the Phosphatidylethanoamine lipid species in the eight histological found regions. Abbreviations; G, Glomeruli; PTI, Proximal tubule I; PTII, Proximal tubule II; CDT, Cortical distal tubule; CMT, Corticomedullary tubule; MTI, Medullary distal tubule I; MTII, Medullary distal tubule II; ITS, interstitial structure. Values are expressed as mean ± SEM. Statistical analysis reported in **Table A.6.1.***
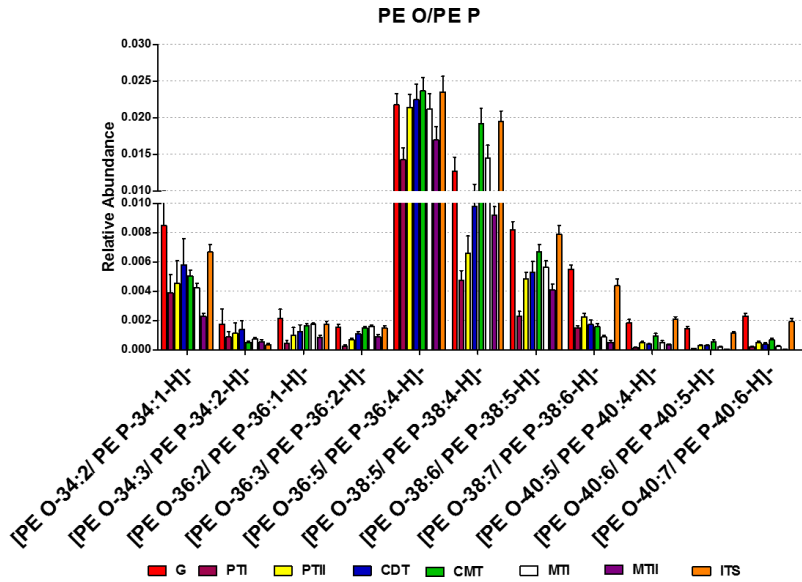
Figure A.6.10. *Bar charts of the relative abundance variation of the Phosphatidyletholamine plasmalogen lipid species in the eight histological found regions. Abbreviations; CPTI, Cortical proximal tubule I,; CPTII, cortical proximal tubule II; CDT, cortical distal tubule; G, Glomeruli; ITS, interstitial structure; MTI, Medullary distal tubule I; MTII, Medullary distal tubule II. Values are expressed as mean ± SEM. Statistical analysis reported in **Table A.6.1.***
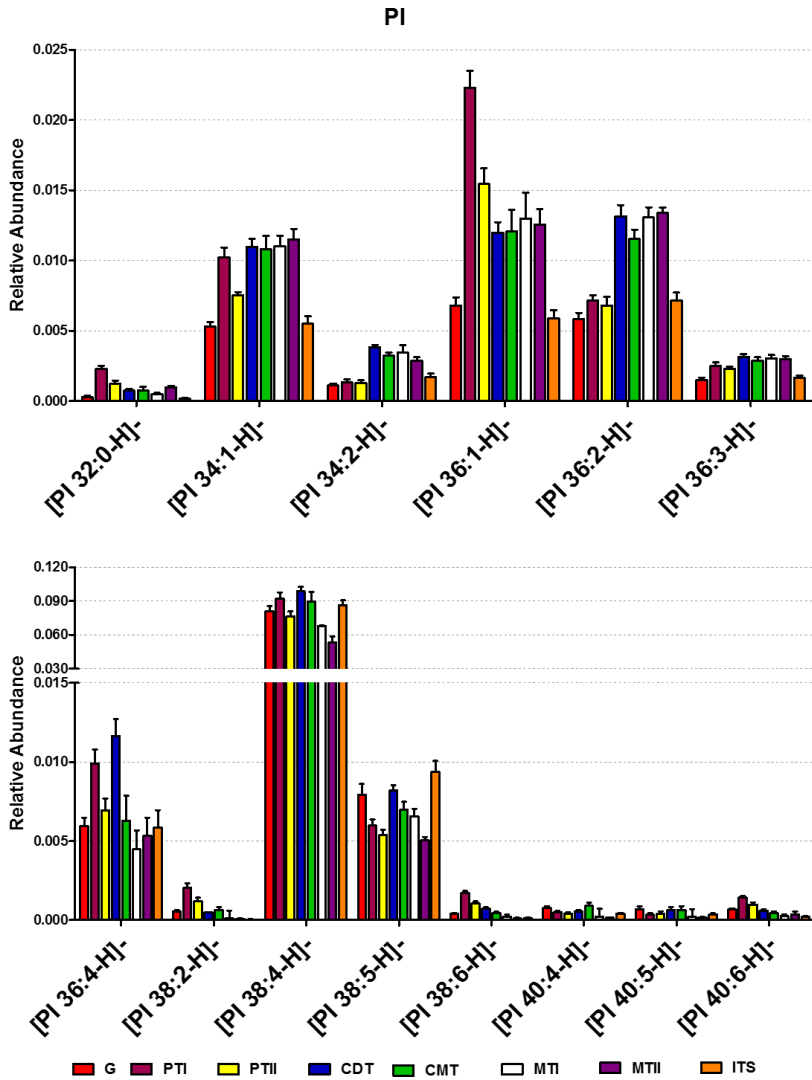
Figure A.6.11. *Bar charts of the relative abundance variation of the Lyso-Phosphatidylinositol and Phosphatidylinositol lipid species in the eight histological found regionsAbbreviations; G, Glomeruli; PTI, Proximal tubule I; PTII, Proximal tubule II; CDT, Cortical distal tubule; CMT, Corticomedullary tubule; MTI, Medullary distal tubule I; MTII, Medullary distal tubule II; ITS, interstitial structure. Values are expressed as mean ± SEM. Statistical analysis reported in Table A.6.1.*
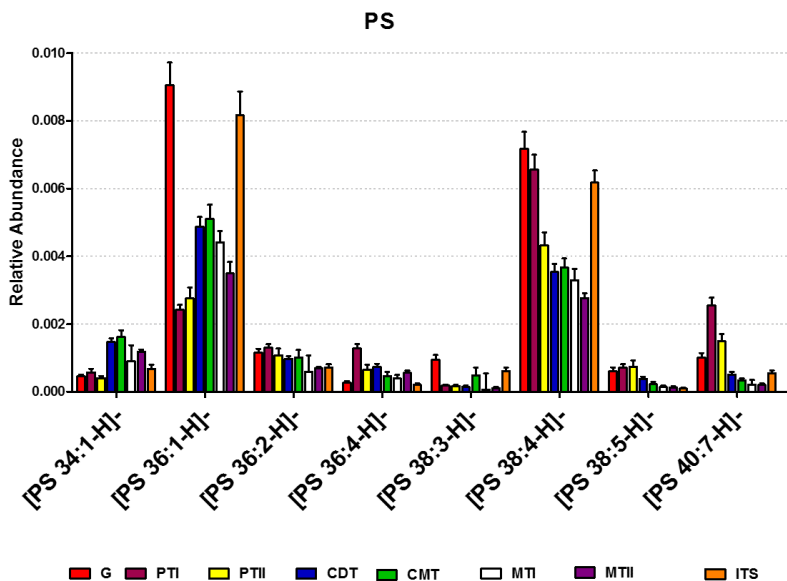
Figure A.6.12. *Bar charts of the relative abundance variation of the Phosphatidylserine lipid species in the eight histological found regions. Abbreviations; G, Glomeruli; PTI, Proximal tubule I; PTII, Proximal tubule II; CDT, Cortical distal tubule; CMT, Corticomedullary tubule; MTI, Medullary distal tubule I; MTII, Medullary distal tubule II; ITS, interstitial structure. Values are expressed as mean ± SEM. Statistical analysis reported in* **Table A.6.1**
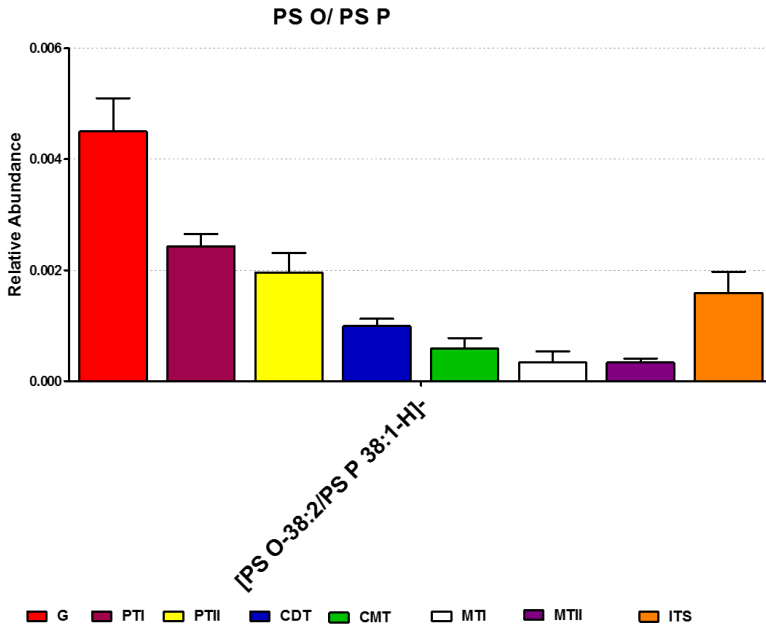
Figure A.6.13. Bar charts of the relative abundance variation of the Phosphatidylserine plasmalogen lipid species in the eight histological found regions. Abbreviations; G, Glomeruli; PTI, Proximal tubule I; PTII, Proximal tubule II; CDT, Cortical distal tubule; CMT, Corticomedullary tubule; MTI, Medullary distal tubule I; MTII, Medullary distal tubule II; ITS, interstitial structure. Values are expressed as mean ± SEM. Statistical analysis reported in **Table A.6.1.**
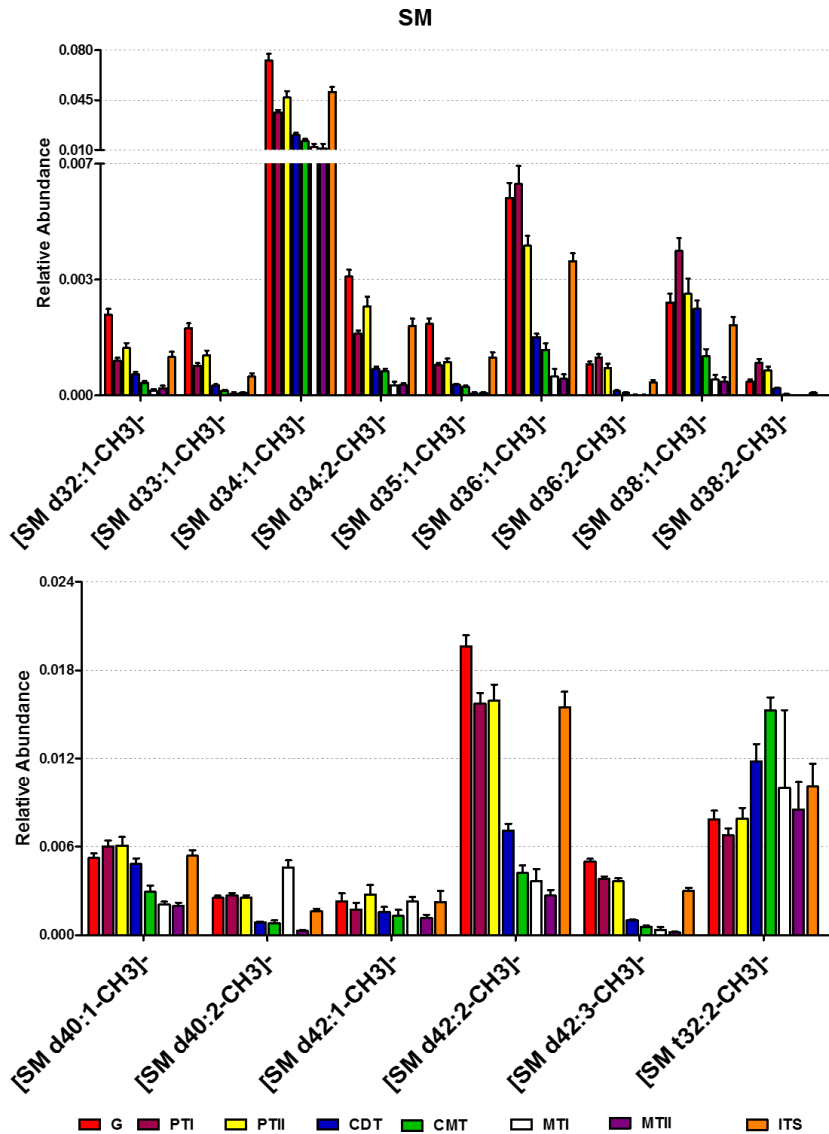
Figure A.6.14. *Bar charts of the relative abundance variation of the Sphingomieline lipid species in the eight histological found regions. Abbreviations; G, Glomeruli; PTI, Proximal tubule I; PTII, Proximal tubule II; CDT, Cortical distal tubule; CMT, Corticomedullary tubule; MTI, Medullary distal tubule I; MTII, Medullary distal tubule II; ITS, interstitial structure. Values are expressed as mean ± SEM. Statistical analysis reported in* ***Table A.6.1***
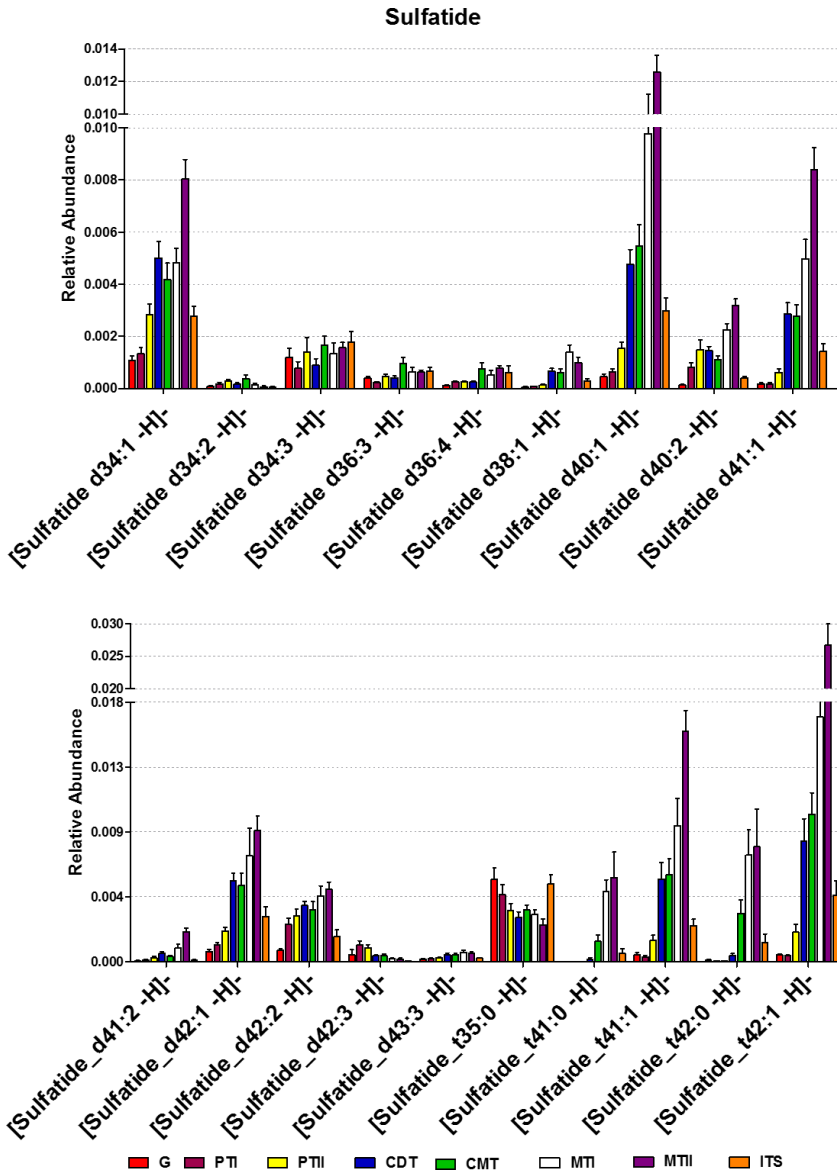
Figure A.6.15. *Bar charts of the relative abundance variation of the Sulfatide lipid species in the eight histological found regions. Abbreviations; G, Glomeruli; PTI, Proximal tubule I; PTII, Proximal tubule II; CDT, Cortical distal tubule; CMT, Corticomedullary tubule; MTI, Medullary distal tubule I; MTII, Medullary distal tubule II; ITS, interstitial structure. Values are expressed as mean ± SEM. Statistical analysis reported in* **Table A.6.1.**
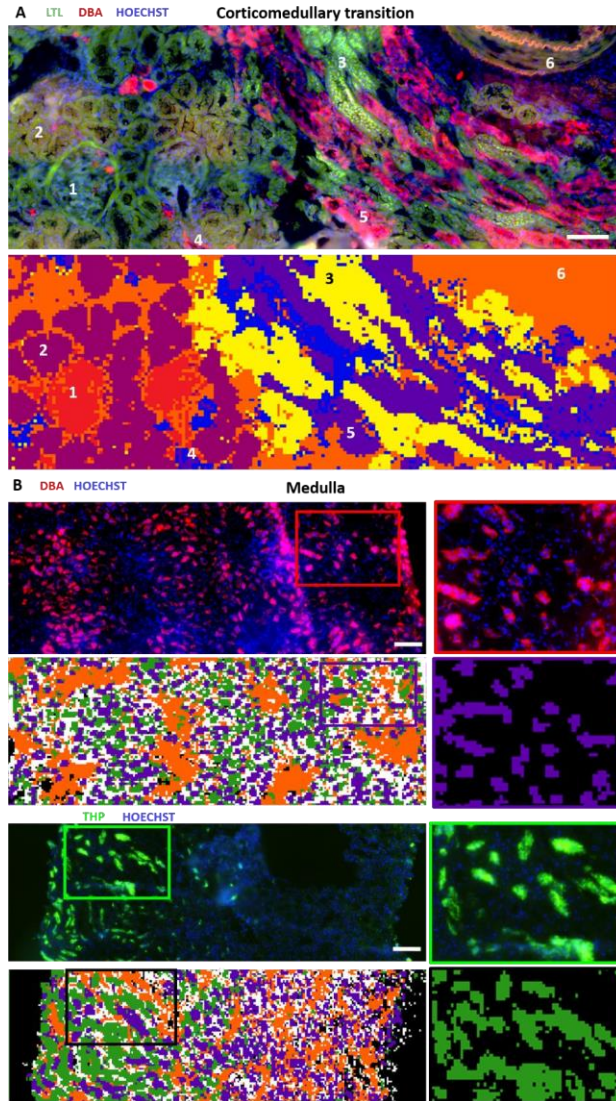
Figure A.6.16. *Comparison between the IF staining and the segmentation analysis of the IMS experiment carried out over the same histological section. A) Section of a cortical-medullary transition. Segment-specific tubular markers used the following: proximal tubule, Lotus tetragonolobus lectin (LTL), distal convoluted tubules and collecting ducts, Dolichos biflorus agglutinin (DBA). Numbers indicate: 1: glomerulus; 2: proximal tubule I (PTI), 3: proximal tubule II (PTII), 4: Cortical distal tubule (CDT), 5: Collecting duct (MTII) and 6: capillary; B) Section of a medullary biopsy. DBA- positive collecting ducts correlate with the purple segment, attributed to MT II based on its lipid signature. Scale bar= 150 µm.*

Table A.6.1. *One-way ANOVA and multiple testing correction of the lipid individual species detected in human renal samples. The table shows the p-values for Levene-test to determine the homogeneity (H0 = groups have equivalent variance) to choose the post hoc method (Tukey or Games-Howell); one-way ANOVA p-values for the seven pair-wise (p-value < 0.05 appears in green shadow); Tukey or Games-Howell P-values for the seven pair-wise.*

Lipid specie	Levene p-value	ANOVA p-value	GvsPTI	GvsPTII	GvsCdN	GvsCMT	GvsMTI	GvsMTII	GvsITS
HexCer d28:0	1.50E-04	1.45E-17	5.00E-03	3.70E-02	0.00E+00	0.00E+00	0.00E+00	0.00E+00	2.43E-01
HexCer d29:0	3.73E-09	5.55E-18	1.00E-03	5.00E-03	0.00E+00	0.00E+00	0.00E+00	0.00E+00	0.00E+00
HexCer d30:0	3.35E-06	1.50E-16	6.22E-01	9.10E-02	0.00E+00	0.00E+00	0.00E+00	0.00E+00	1.39E-01
HexCer d30:1	1.91E-06	1.10E-33	0.00E+00	0.00E+00	0.00E+00	0.00E+00	0.00E+00	0.00E+00	5.00E-03
HexCer d32:0	1.56E-04	3.18E-15	3.00E-03	9.90E-01	8.06E-01	0.00E+00	0.00E+00	0.00E+00	2.60E-02
HexCer d34:1	1.82E-07	6.92E-19	3.00E-03	5.74E-01	6.40E-02	0.00E+00	0.00E+00	0.00E+00	2.00E-03
HexCer d36:1	9.49E-03	1.14E-19	6.40E-01	3.10E-02	0.00E+00	0.00E+00	0.00E+00	0.00E+00	4.20E-02
HexCer d36:2	3.44E-06	1.95E-21	9.95E-01	4.91E-01	0.00E+00	0.00E+00	0.00E+00	0.00E+00	0.00E+00
HexCer d38:2	4.89E-06	1.23E-11	9.98E-01	1.38E-01	1.00E-03	0.00E+00	0.00E+00	0.00E+00	6.00E-01
HexCer t33:1	4.02E-04	1.63E-13	0.00E+00	1.00E-03	2.41E-01	3.97E-01	3.34E-01	0.00E+00	1.00E+00
HexCer t35:1	9.14E-03	1.65E-18	0.00E+00	0.00E+00	4.76E-01	5.55E-01	9.99E-01	2.09E-01	8.56E-01
HexCer t35:2	1.22E-01	9.12E-17	0.00E+00	0.00E+00	9.49E-01	8.12E-01	1.00E+00	1.73E-01	1.00E+00
HexCer t39:4	2.02E-10	4.12E-19	0.00E+00	0.00E+00	0.00E+00	5.00E-03	9.00E-02	0.00E+00	1.00E+00
Lyso-PI16:0	2.43E-06	4.39E-07	1.00E-03	8.80E-02	6.00E-03	9.00E-02	7.44E-01	8.66E-01	3.95E-01
Lyso-PI18:0	1.27E-01	4.66E-11	0.00E+00	1.98E-01	9.94E-01	9.97E-01	1.00E+00	3.41E-01	7.80E-01
Lyso-PI18:1	2.64E-08	3.07E-27	2.70E-02	9.70E-02	2.64E-01	5.04E-01	4.30E-02	1.12E-01	9.06E-01
Lyso-PI20:4	9.69E-06	7.71E-23	2.45E-01	3.40E-01	9.04E-01	8.80E-01	4.90E-02	9.99E-01	9.78E-01
PC32:0	2.63E-01	2.03E-27	0.00E+00	0.00E+00	0.00E+00	0.00E+00	1.00E-03	0.00E+00	7.32E-01
PC32:2	5.49E-11	2.47E-33	0.00E+00	0.00E+00	1.73E-01	1.00E+00	8.81E-01	9.43E-01	2.05E-01
PC33:2	6.19E-01	8.92E-06	4.85E-01	7.65E-01	1.40E-02	0.00E+00	1.00E-02	1.71E-01	5.76E-01
PC34:1	9.45E-05	8.43E-18	0.00E+00	1.00E+00	2.00E-02	1.00E-03	1.63E-01	8.96E-01	0.00E+00
PC34:4	1.21E-03	1.31E-31	0.00E+00	0.00E+00	0.00E+00	2.52E-01	9.97E-01	2.86E-01	1.00E+00
PC35:1	3.97E-03	1.15E-15	9.84E-01	9.84E-01	3.90E-02	0.00E+00	9.88E-01	6.56E-01	1.45E-01
PC35:2	1.67E-02	1.94E-03	2.00E-02	3.60E-01	3.27E-01	1.20E-02	6.12E-01	7.10E-01	9.95E-01
PC36:1	2.07E-03	5.43E-25	0.00E+00	0.00E+00	9.20E-02	8.04E-01	9.87E-01	7.00E-03	9.99E-01
PC36:2	3.91E-01	2.16E-10	2.20E-02	9.95E-01	7.09E-01	7.00E-03	3.20E-02	9.80E-01	7.40E-02
PC36:5	3.93E-04	5.71E-13	0.00E+00	5.00E-03	0.00E+00	3.70E-02	1.20E-02	1.00E-03	8.85E-01
PC36:6	5.83E-06	1.11E-32	0.00E+00	0.00E+00	1.00E+00	7.49E-01	1.08E-01	0.00E+00	2.21E-01
PC38:4	6.67E-02	8.09E-23	0.00E+00	0.00E+00	0.00E+00	0.00E+00	2.71E-01	0.00E+00	1.37E-01
PC38:5	5.02E-01	2.89E-08	2.10E-02	4.49E-01	7.83E-01	9.17E-01	1.60E-02	1.00E-03	9.80E-01
PC38:6	4.97E-04	1.26E-15	1.00E+00	1.02E-01	0.00E+00	0.00E+00	0.00E+00	0.00E+00	9.11E-01
PC38:7	1.72E-10	1.54E-10	4.50E-02	1.00E+00	4.13E-01	1.00E-02	6.00E-03	2.00E-03	3.80E-02
PC O-32:2/ PC P-32:1	2.82E-01	8.17E-02	1.28E-01	2.32E-01	8.07E-01	5.14E-01	8.70E-01	8.40E-02	9.37E-01
PC O-34:2/ PC P-34:1	3.13E-02	2.74E-13	0.00E+00	6.00E-03	3.08E-01	9.86E-01	1.00E+00	1.35E-01	1.00E+00
PC O-34:3/ PC P-34:2	3.81E-01	4.18E-04	1.00E-03	4.60E-02	9.54E-01	1.00E+00	9.90E-01	3.41E-01	9.64E-01
PC O-34:5/ PC P-34:4	2.37E-01	1.15E-04	1.00E-02	1.00E+00	9.82E-01	1.00E+00	9.99E-01	2.53E-01	1.00E+00
PC O-36:5/ PC P-36:4	6.38E-05	3.28E-16	0.00E+00	3.20E-02	3.77E-01	8.26E-01	7.40E-01	6.90E-02	2.65E-01
PC O-36:6/ PC P-36:5	4.30E-01	3.34E-15	0.00E+00	0.00E+00	0.00E+00	4.00E-03	6.60E-02	0.00E+00	3.16E-01
PC O-36:7/ PC P-34:1	4.67E-02	4.82E-20	0.00E+00	0.00E+00	0.00E+00	0.00E+00	9.98E-01	0.00E+00	6.09E-01
PC O-38:5/ PC P-38:4	5.58E-10	2.79E-25	0.00E+00	0.00E+00	0.00E+00	2.00E-03	0.00E+00	0.00E+00	1.00E+00
PC O-38:6/ PC P-38:5	4.72E-13	3.75E-24	0.00E+00	0.00E+00	0.00E+00	0.00E+00	1.18E-01	0.00E+00	1.00E+00
PC O-38:7/ PC P-38:6	4.64E-17	4.61E-33	0.00E+00	0.00E+00	0.00E+00	0.00E+00	0.00E+00	0.00E+00	8.40E-02

PE34:0	2.63E-01	2.03E-27	0.00E+00	0.00E+00	0.00E+00	0.00E+00	1.00E-03	0.00E+00	7.32E-01
PE34:1	4.58E-04	1.81E-08	9.94E-01	1.73E-01	0.00E+00	8.90E-02	3.00E-03	3.95E-01	1.00E+00
PE34:2	5.49E-11	2.47E-33	0.00E+00	0.00E+00	1.73E-01	1.00E+00	8.81E-01	9.43E-01	2.05E-01
PE35:2	6.19E-01	8.92E-06	4.85E-01	7.65E-01	1.40E-02	0.00E+00	1.00E-02	1.71E-01	5.76E-01
PE36:1	1.06E-04	4.57E-17	0.00E+00	1.00E+00	2.00E-02	1.00E-03	4.97E-01	8.96E-01	0.00E+00
PE36:2	8.35E-05	1.72E-05	2.30E-02	0.00E+00	2.05E-01	8.70E-02	0.00E+00	2.00E-03	1.00E+00
PE36:3	3.99E-02	3.54E-20	0.00E+00	0.00E+00	0.00E+00	3.00E-03	1.00E-02	0.00E+00	9.98E-01
PE36:4	1.21E-03	1.31E-31	0.00E+00	0.00E+00	0.00E+00	2.52E-01	9.97E-01	2.86E-01	1.00E+00
PE37:1	3.97E-03	1.15E-15	9.84E-01	9.84E-01	3.90E-02	0.00E+00	9.88E-01	6.56E-01	1.45E-01
PE37:2	1.67E-02	1.94E-03	2.00E-02	3.60E-01	3.27E-01	1.20E-02	6.12E-01	7.10E-01	9.95E-01
PE38:1	2.14E-07	1.38E-17	0.00E+00	0.00E+00	1.61E-01	8.04E-01	9.87E-01	9.83E-01	2.40E-01
PE38:2	2.58E-01	2.14E-10	3.30E-02	9.94E-01	6.78E-01	5.00E-03	2.40E-02	9.77E-01	5.90E-02
PE38:4	6.24E-02	2.60E-07	0.00E+00	1.20E-02	5.01E-01	9.89E-01	1.00E+00	1.00E+00	7.82E-01
PE38:5	3.93E-04	5.71E-13	0.00E+00	5.00E-03	0.00E+00	3.70E-02	1.20E-02	1.00E-03	8.85E-01
PE38:6	5.83E-06	1.11E-32	0.00E+00	0.00E+00	1.00E+00	7.49E-01	1.08E-01	0.00E+00	2.21E-01
PE40:4	6.67E-02	8.09E-23	0.00E+00	0.00E+00	0.00E+00	0.00E+00	2.71E-01	0.00E+00	1.37E-01
PE40:5	7.85E-01	4.49E-07	3.00E-03	3.97E-01	8.20E-01	9.90E-01	1.00E+00	4.10E-02	3.55E-01
PE40:6	4.97E-04	1.26E-15	1.00E+00	1.02E-01	0.00E+00	0.00E+00	0.00E+00	0.00E+00	9.11E-01
PE40:7	1.70E-10	1.56E-10	4.50E-02	1.00E+00	4.13E-01	1.00E-02	6.00E-03	2.00E-03	3.80E-02
PE O-34:2/ PE P-34:1	2.82E-01	8.17E-02	1.28E-01	2.32E-01	8.07E-01	5.14E-01	8.70E-01	8.40E-02	9.37E-01
PE O-34:3/ PE P-34:2	3.26E-02	7.73E-01	9.92E-01	9.99E-01	1.00E+00	9.53E-01	9.21E-01	9.11E-01	8.75E-01
PE O-36:2/ PE P-36:1	2.09E-01	5.17E-02	2.90E-02	2.67E-01	7.73E-01	9.98E-01	9.98E-01	5.20E-01	9.85E-01
PE O-36:3/ PE P-36:2	1.87E-01	7.54E-12	0.00E+00	0.00E+00	5.82E-01	1.00E+00	9.94E-01	9.80E-02	9.99E-01
PE O-36:5/ PE P-36:4	2.35E-01	1.21E-04	1.00E-02	1.00E+00	9.86E-01	1.00E+00	9.99E-01	2.49E-01	1.00E+00
PE O-38:5/ PE P-38:4	2.56E-07	6.00E-12	1.30E-02	1.17E-01	9.97E-01	5.36E-01	9.98E-01	4.08E-01	3.56E-01
PE O-38:6/ PE P-38:5	4.95E-02	7.47E-15	0.00E+00	1.00E-03	9.50E-02	2.78E-01	1.00E+00	0.00E+00	9.74E-01
PE O-38:7/ PE P-38:6	4.60E-03	1.51E-29	0.00E+00	0.00E+00	0.00E+00	0.00E+00	1.00E+00	0.00E+00	8.02E-01
PE O-40:5/ PE P-40:4	3.99E-08	7.02E-32	0.00E+00	0.00E+00	0.00E+00	2.33E-01	8.20E-02	0.00E+00	9.79E-01
PE O-40:6/ PE P-40:5	2.26E-07	4.56E-33	0.00E+00	0.00E+00	0.00E+00	7.10E-02	9.50E-02	0.00E+00	9.85E-01
PE O-40:7/ PE P-40:6	5.51E-10	4.78E-36	0.00E+00	0.00E+00	0.00E+00	0.00E+00	2.18E-01	0.00E+00	9.91E-01
PG40:7	2.16E-16	1.32E-40	4.35E-01	8.59E-01	9.99E-01	3.53E-01	5.10E-02	7.90E-01	9.98E-01
PI32:0	4.91E-09	3.24E-14	0.00E+00	2.60E-02	6.10E-02	6.20E-01	7.66E-01	4.00E-03	9.03E-01
PI34:1	2.68E-04	3.14E-16	0.00E+00	0.00E+00	0.00E+00	1.00E-03	4.20E-02	0.00E+00	1.00E+00
PI34:2	1.52E-02	1.14E-19	9.94E-01	9.99E-01	0.00E+00	0.00E+00	1.85E-01	0.00E+00	4.07E-01
PI36:1	1.63E-03	1.52E-24	0.00E+00	0.00E+00	0.00E+00	8.60E-02	2.94E-01	8.00E-03	9.24E-01
PI36:2	1.20E-02	5.45E-21	2.67E-01	8.87E-01	0.00E+00	0.00E+00	1.00E-02	0.00E+00	5.10E-01
PI36:3	3.27E-01	3.19E-17	5.80E-02	2.00E-02	0.00E+00	0.00E+00	0.00E+00	3.30E-02	9.79E-01
PI36:4	6.80E-02	8.36E-06	2.70E-02	9.94E-01	1.00E-03	1.00E+00	4.64E-01	1.00E+00	1.00E+00
PI38:2	9.31E-07	1.02E-17	0.00E+00	2.05E-01	9.95E-01	1.00E+00	6.60E-02	2.00E-03	1.00E-03
PI38:4	1.73E-02	3.44E-05	8.30E-01	9.96E-01	1.05E-01	9.85E-01	3.50E-02	1.80E-02	9.85E-01
PI38:5	3.19E-03	8.92E-10	1.77E-01	3.50E-02	1.00E+00	9.40E-01	6.08E-01	9.00E-03	7.33E-01
PI38:6	1.86E-06	1.95E-22	0.00E+00	5.00E-03	4.50E-02	1.00E+00	9.19E-01	2.00E-03	3.00E-03
PI40:4	1.57E-03	8.14E-27	5.74E-01	2.49E-01	7.38E-01	9.99E-01	5.70E-02	1.00E-03	1.24E-01
PI40:5	2.93E-01	1.80E-15	5.49E-01	8.29E-01	1.00E+00	1.00E+00	0.00E+00	5.03E-01	7.84E-01
PI40:6	2.07E-04	5.27E-15	0.00E+00	3.95E-01	9.97E-01	7.30E-01	3.15E-01	6.29E-01	0.00E+00
PS34:1	5.56E-05	7.60E-36	9.56E-01	9.96E-01	0.00E+00	1.00E-03	4.30E-02	0.00E+00	5.93E-01
PS36:1	2.68E-08	1.38E-26	0.00E+00	0.00E+00	0.00E+00	1.00E-03	0.00E+00	0.00E+00	9.77E-01
PS36:2	1.72E-08	1.33E-16	9.85E-01	1.00E+00	8.97E-01	9.99E-01	6.20E-02	2.40E-02	6.70E-02
PS36:4	2.09E-07	9.41E-12	0.00E+00	2.11E-01	4.00E-03	7.70E-01	4.79E-01	4.40E-02	9.62E-01
PS38:3	1.44E-13	6.68E-31	1.00E-03	2.00E-03	1.00E-03	7.08E-01	6.30E-02	1.00E-03	6.26E-01
PS38:4	4.74E-04	7.22E-14	9.39E-01	2.00E-03	0.00E+00	0.00E+00	1.30E-02	0.00E+00	7.09E-01
PS38:5	1.63E-07	4.14E-05	9.93E-01	9.98E-01	7.10E-01	1.11E-01	3.80E-02	1.20E-02	6.00E-03
PS40:7	1.56E-06	2.22E-20	0.00E+00	5.46E-01	4.20E-02	2.00E-03	9.60E-02	0.00E+00	6.80E-02
PS O-38:2/ PS P-38:1	4.92E-09	6.29E-13	3.90E-02	1.90E-02	0.00E+00	0.00E+00	0.00E+00	0.00E+00	5.00E-03

SM d32:1	4.13E-05	4.87E-24	1.41E-06	1.63E-03	1.71E-08	2.06E-09	8.01E-10	3.54E-10	2.69E-05
SM d33:1	4.88E-06	2.68E-27	4.85E-06	6.04E-03	7.52E-09	1.35E-09	9.60E-10	7.63E-10	4.87E-08
SM d34:1	4.20E-05	8.68E-26	3.39E-06	7.19E-03	1.07E-08	2.69E-09	3.01E-08	9.44E-10	1.00E-02
SM d34:2	3.32E-06	6.55E-25	5.95E-07	2.32E-01	2.27E-10	8.40E-11	1.40E-09	2.12E-11	1.49E-04
SM d35:1	3.09E-07	1.35E-26	6.95E-06	7.30E-05	3.30E-08	1.36E-08	4.18E-09	5.16E-09	1.50E-03
SM d36:1	5.66E-10	1.19E-23	1.00E+00	1.72E-01	4.10E-07	4.62E-08	1.18E-07	3.76E-09	1.48E-02
SM d36:2	1.19E-07	5.22E-19	8.92E-01	9.97E-01	4.20E-07	1.40E-07	5.91E-08	7.41E-08	4.09E-04
SM d38:1	1.57E-03	3.35E-11	3.85E-02	1.00E+00	9.99E-01	1.25E-03	2.00E-05	6.83E-07	5.09E-01
SM d38:2	1.55E-11	6.86E-17	8.90E-04	3.51E-01	1.71E-01	6.34E-04	2.17E-04	2.41E-04	2.51E-03
SM d40:1	4.00E-01	1.89E-09	8.10E-01	7.97E-01	9.97E-01	1.25E-02	9.42E-02	4.42E-04	1.00E+00
SM d40:2	2.79E-02	6.81E-26	9.94E-01	1.00E+00	6.67E-09	2.26E-05	1.86E-01	3.75E-11	2.73E-03
SM d42:1	2.82E-09	4.98E-01							
SM d42:2	1.93E-02	1.28E-32	8.40E-03	1.38E-01	1.25E-12	9.37E-13	5.95E-05	1.09E-12	2.84E-02
SM d42:3	6.21E-04	5.36E-45	7.12E-04	6.30E-04	1.06E-12	1.03E-12	1.59E-06	1.08E-12	3.78E-07
SM t32:2	1.64E-03	5.23E-07	7.54E-01	1.00E+00	9.11E-02	1.34E-05	9.99E-01	1.00E+00	7.92E-01
SFT d34:1	3.79E-04	5.95E-14	1.00E+00	1.66E-02	1.37E-04	2.47E-02	4.11E-01	1.98E-04	1.63E-03
SFT d34:2	1.69E-10	1.01E-37	9.50E-01	6.21E-02	6.32E-01	5.51E-01	5.77E-02	1.00E+00	5.98E-01
SFT d34:3	2.78E-02	3.66E-07	9.79E-01	1.00E+00	9.87E-01	8.10E-01	3.06E-03	4.22E-01	6.30E-01
SFT d36:3	4.82E-09	1.67E-29	6.24E-01	1.00E+00	1.00E+00	3.04E-01	3.69E-02	9.86E-03	2.31E-01
SFT d36:4	3.03E-10	5.59E-27	4.26E-02	1.24E-01	5.57E-01	2.10E-01	3.61E-02	4.40E-08	1.78E-01
SFT d38:1	5.18E-13	5.17E-11	9.97E-01	7.79E-01	1.50E-03	6.27E-02	6.79E-01	3.64E-02	3.40E-01
SFT d40:1	8.88E-09	1.22E-31	9.91E-01	4.71E-03	8.14E-06	3.69E-03	5.27E-03	4.75E-05	4.86E-04
SFT d40:2	3.14E-07	1.59E-10	1.94E-02	3.53E-02	3.93E-06	1.10E-03	2.11E-03	9.80E-06	3.26E-02
SFT d41:1	1.16E-13	2.66E-32	9.98E-01	6.52E-02	1.64E-04	2.94E-03	8.84E-03	2.03E-04	2.63E-03
SFT d41:2	1.82E-09	7.86E-11	9.63E-01	6.77E-01	1.65E-02	3.98E-01	9.93E-01	4.05E-02	1.00E+00
SFT d42:1	1.01E-11	7.90E-22	4.83E-01	5.96E-04	1.69E-06	3.12E-02	3.50E-01	1.15E-04	2.23E-02
SFT d42:2	3.30E-06	1.49E-13	1.45E-02	6.54E-04	4.91E-08	1.38E-02	8.83E-03	2.98E-06	5.84E-01
SFT d42:3	8.44E-04	2.28E-08	8.61E-01	7.44E-01	1.00E+00	1.00E+00	1.92E-02	9.63E-01	9.08E-01
SFT d43:3	7.17E-09	9.56E-05	9.99E-01	9.84E-01	6.81E-02	1.82E-01	6.40E-01	8.04E-02	9.73E-01
SFT t35:0	1.67E-04	4.97E-03	9.59E-01	2.17E-01	8.15E-02	1.36E-01	8.59E-01	1.42E-02	9.99E-01
SFT t41:0	3.29E-23	3.35E-19	7.79E-01	1.00E+00	7.91E-01	1.66E-01	2.38E-01	7.09E-02	6.82E-01
SFT t41:1	1.56E-16	1.96E-23	9.54E-01	3.20E-01	3.28E-03	2.97E-02	4.28E-05	2.13E-04	9.09E-03
SFT t42:0	1.39E-17	6.69E-19	9.14E-01	9.21E-01	7.10E-01	4.51E-02	3.40E-01	1.13E-01	4.35E-01
SFT t42:1	1.16E-14	4.92E-27	1.00E+00	2.30E-01	6.64E-04	1.40E-02	5.65E-02	6.75E-04	2.50E-02

Lipid specie	Levene p-value	ANOVA p-value	PTIvsPTII	PTIvsCdN	PTIvsCMT	PTIvsMTI	PTIvsMTII	PTIvsITS	PTIIvsCdN
HexCer d28:0	1.50E-04	1.45E-17	9.77E-01	0.00E+00	0.00E+00	2.40E-02	0.00E+00	6.37E-01	0.00E+00
HexCer d29:0	3.73E-09	5.55E-18	1.00E+00	0.00E+00	0.00E+00	0.00E+00	0.00E+00	7.88E-01	1.30E-02
HexCer d30:0	3.35E-06	1.50E-16	8.10E-01	0.00E+00	0.00E+00	0.00E+00	0.00E+00	8.95E-01	0.00E+00
HexCer d30:1	1.91E-06	1.10E-33	9.73E-01	0.00E+00	0.00E+00	8.30E-02	0.00E+00	1.05E-01	0.00E+00
HexCer d32:0	1.56E-04	3.18E-15	9.20E-02	0.00E+00	0.00E+00	0.00E+00	0.00E+00	0.00E+00	4.90E-01
HexCer d34:1	1.82E-07	6.92E-19	5.67E-01	0.00E+00	0.00E+00	0.00E+00	0.00E+00	0.00E+00	3.00E-03
HexCer d36:1	9.49E-03	1.14E-19	7.42E-01	0.00E+00	0.00E+00	0.00E+00	0.00E+00	5.06E-01	0.00E+00
HexCer d36:2	3.44E-06	1.95E-21	8.16E-01	0.00E+00	0.00E+00	0.00E+00	0.00E+00	0.00E+00	0.00E+00
HexCer d38:2	4.89E-06	1.23E-11	2.27E-01	0.00E+00	0.00E+00	0.00E+00	0.00E+00	8.41E-01	1.63E-01
HexCer t33:1	4.02E-04	1.63E-13	1.38E-01	0.00E+00	0.00E+00	2.76E-01	9.99E-01	0.00E+00	1.82E-01
HexCer t35:1	9.14E-03	1.65E-18	8.10E-02	0.00E+00	0.00E+00	2.05E-01	9.00E-03	0.00E+00	4.30E-02
HexCer t35:2	1.22E-01	9.12E-17	5.10E-02	0.00E+00	0.00E+00	9.00E-03	8.00E-03	0.00E+00	5.00E-03
HexCer t39:4	2.02E-10	4.12E-19	2.60E-02	2.00E-02	2.40E-02	7.96E-01	9.03E-01	0.00E+00	9.99E-01
Lyso-PI16:0	2.43E-06	4.39E-07	7.78E-01	8.02E-01	7.40E-02	7.14E-01	1.30E-02	0.00E+00	1.00E+00
Lyso-PI18:0	1.27E-01	4.66E-11	6.20E-02	0.00E+00	0.00E+00	1.70E-01	0.00E+00	0.00E+00	6.70E-01
Lyso-PI18:1	2.64E-08	3.07E-27	1.00E+00	9.80E-01	9.87E-01	4.60E-02	1.00E+00	5.97E-01	9.87E-01
Lyso-PI20:4	9.69E-06	7.71E-23	1.00E+00	8.87E-01	1.00E+00	5.20E-02	9.90E-02	4.50E-02	8.63E-01
PC32:0	2.63E-01	2.03E-27	1.00E-03	6.50E-01	4.90E-02	9.13E-01	7.50E-01	0.00E+00	2.19E-01
PC32:2	5.49E-11	2.47E-33	0.00E+00	0.00E+00	0.00E+00	0.00E+00	0.00E+00	0.00E+00	2.00E-03
PC33:2	6.19E-01	8.92E-06	1.00E+00	7.00E-01	7.00E-03	1.47E-01	9.59E-01	1.00E+00	4.66E-01
PC34:1	9.45E-05	8.43E-18	1.00E-02	0.00E+00	0.00E+00	7.10E-02	4.10E-02	0.00E+00	5.60E-02
PC34:4	1.21E-03	1.31E-31	0.00E+00	0.00E+00	0.00E+00	0.00E+00	0.00E+00	0.00E+00	2.36E-01
PC35:1	3.97E-03	1.15E-15	1.00E+00	1.00E-02	0.00E+00	9.52E-01	3.50E-01	3.00E-02	1.10E-02
PC35:2	1.67E-02	1.94E-03	9.62E-01	9.57E-01	9.98E-01	9.77E-01	9.76E-01	6.00E-02	1.00E+00
PC36:1	2.07E-03	5.43E-25	0.00E+00	0.00E+00	0.00E+00	3.95E-01	3.30E-02	0.00E+00	2.00E-03
PC36:2	3.91E-01	2.16E-10	1.00E-03	0.00E+00	0.00E+00	0.00E+00	1.00E+00	0.00E+00	9.80E-01
PC36:5	3.93E-04	5.71E-13	1.30E-01	5.54E-01	1.00E+00	3.70E-02	9.99E-01	0.00E+00	2.00E-03
PC36:6	5.83E-06	1.11E-32	1.20E-02	0.00E+00	0.00E+00	0.00E+00	0.00E+00	0.00E+00	0.00E+00
PC38:4	6.67E-02	8.09E-23	2.00E-02	8.48E-01	4.38E-01	5.35E-01	9.80E-01	0.00E+00	5.80E-01
PC38:5	5.02E-01	2.89E-08	8.91E-01	6.44E-01	6.66E-01	0.00E+00	6.25E-01	1.00E-03	1.00E+00
PC38:6	4.97E-04	1.26E-15	6.22E-01	0.00E+00	0.00E+00	0.00E+00	0.00E+00	9.99E-01	2.00E-03
PC38:7	1.72E-10	1.54E-10	1.48E-01	1.00E-03	0.00E+00	0.00E+00	0.00E+00	0.00E+00	3.61E-01
PC O-32:2/ PC P-32:1	2.82E-01	8.17E-02							
PC O-34:2/ PC P-34:1	3.13E-02	2.74E-13	6.83E-01	1.00E-03	0.00E+00	2.26E-01	2.50E-02	0.00E+00	2.44E-01
PC O-34:3/ PC P-34:2	3.81E-01	4.18E-04	9.10E-01	3.10E-02	1.50E-02	8.68E-01	9.36E-01	4.00E-02	5.00E-01
PC O-34:5/ PC P-34:4	2.37E-01	1.15E-04	8.00E-03	0.00E+00	2.70E-02	9.27E-01	1.00E+00	1.00E-02	9.78E-01
PC O-36:5/ PC P-36:4	6.38E-05	3.28E-16	1.61E-01	1.00E-03	2.00E-03	5.90E-02	0.00E+00	0.00E+00	6.79E-01
PC O-36:6/ PC P-36:5	4.30E-01	3.34E-15	9.00E-03	1.00E-03	0.00E+00	5.44E-01	8.77E-01	0.00E+00	9.98E-01
PC O-36:7/ PC P-34:1	4.67E-02	4.82E-20	5.54E-01	9.83E-01	1.00E+00	4.10E-02	1.00E-03	0.00E+00	9.71E-01
PC O-38:5/ PC P-38:4	5.58E-10	2.79E-25	5.70E-02	1.10E-02	2.10E-02	8.23E-01	1.00E+00	0.00E+00	1.00E+00
PC O-38:6/ PC P-38:5	4.72E-13	3.75E-24	4.60E-02	6.00E-02	8.00E-03	7.88E-01	9.04E-01	0.00E+00	9.99E-01
PC O-38:7/ PC P-38:6	4.64E-17	4.61E-33	4.80E-02	6.50E-01	5.20E-02	1.00E+00	2.52E-01	0.00E+00	7.33E-01
PE34:0	2.63E-01	2.03E-27	1.00E-03	6.50E-01	4.90E-02	9.13E-01	7.50E-01	0.00E+00	2.19E-01
PE34:1	4.58E-04	1.81E-08	4.57E-01	0.00E+00	2.73E-01	5.00E-03	9.41E-01	1.00E+00	2.46E-01
PE34:2	5.49E-11	2.47E-33	0.00E+00	0.00E+00	0.00E+00	0.00E+00	0.00E+00	0.00E+00	2.00E-03
PE35:2	6.19E-01	8.92E-06	1.00E+00	7.00E-01	7.00E-03	1.47E-01	9.59E-01	1.00E+00	4.66E-01
PE36:1	1.06E-04	4.57E-17	1.00E-02	0.00E+00	0.00E+00	1.71E-01	4.10E-02	0.00E+00	5.60E-02
PE36:2	8.35E-05	1.72E-05	1.00E+00	8.94E-01	8.51E-01	1.00E+00	9.66E-01	1.90E-02	4.57E-01
PE36:3	3.99E-02	3.54E-20	2.69E-01	7.00E-03	1.39E-01	3.40E-02	1.00E+00	0.00E+00	9.06E-01
PE36:4	1.21E-03	1.31E-31	0.00E+00	0.00E+00	0.00E+00	0.00E+00	0.00E+00	0.00E+00	2.36E-01
PE37:1	3.97E-03	1.15E-15	1.00E+00	1.00E-02	0.00E+00	9.52E-01	3.50E-01	3.00E-02	1.10E-02
PE37:2	1.67E-02	1.94E-03	9.62E-01	9.57E-01	9.98E-01	9.77E-01	9.76E-01	6.00E-02	1.00E+00
PE38:1	2.14E-07	1.38E-17	0.00E+00	0.00E+00	0.00E+00	3.95E-01	2.85E-01	0.00E+00	1.00E-03
PE38:2	2.58E-01	2.14E-10	2.00E-03	0.00E+00	0.00E+00	0.00E+00	1.20E-02	0.00E+00	9.77E-01
PE38:4	6.24E-02	2.60E-07	3.25E-01	6.00E-03	1.00E-03	1.03E-01	0.00E+00	2.00E-03	7.83E-01
PE38:5	3.93E-04	5.71E-13	1.30E-01	5.54E-01	1.00E+00	3.70E-02	9.99E-01	0.00E+00	2.00E-03
PE38:6	5.83E-06	1.11E-32	1.20E-02	0.00E+00	0.00E+00	0.00E+00	0.00E+00	0.00E+00	0.00E+00
PE40:4	6.67E-02	8.09E-23	2.00E-02	8.48E-01	4.38E-01	5.35E-01	9.80E-01	0.00E+00	5.80E-01
PE40:5	7.85E-01	4.49E-07	5.79E-01	2.25E-01	1.33E-01	7.14E-01	1.00E+00	0.00E+00	9.98E-01
PE40:6	4.97E-04	1.26E-15	6.22E-01	0.00E+00	0.00E+00	0.00E+00	0.00E+00	9.99E-01	2.00E-03
PE40:7	1.70E-10	1.56E-10	1.48E-01	1.00E-03	0.00E+00	0.00E+00	0.00E+00	0.00E+00	3.61E-01

PE O-34:2/ PE P-34:1	2.82E-01	8.17E-02							
PE O-34:3/ PE P-34:2	3.26E-02	7.73E-01							
PE O-36:2/ PE P-36:1	2.09E-01	5.17E-02							
PE O-36:3/ PE P-36:2	1.87E-01	7.54E-12	3.20E-01	0.00E+00	0.00E+00	1.10E-01	1.44E-01	0.00E+00	9.10E-02
PE O-36:5/ PE P-36:4	2.35E-01	1.21E-04	8.00E-03	0.00E+00	2.70E-02	9.27E-01	1.00E+00	1.00E-02	9.79E-01
PE O-38:5/ PE P-38:4	2.56E-07	6.00E-12	9.33E-01	1.00E-03	4.00E-03	0.00E+00	3.00E-03	0.00E+00	7.50E-02
PE O-38:6/ PE P-38:5	4.95E-02	7.47E-15	1.00E-03	1.00E-03	0.00E+00	4.00E-03	4.40E-02	0.00E+00	9.36E-01
PE O-38:7/ PE P-38:6	4.60E-03	1.51E-29	2.79E-01	9.73E-01	9.98E-01	4.20E-02	1.00E-03	0.00E+00	9.29E-01
PE O-40:5/ PE P-40:4	3.99E-08	7.02E-32	4.50E-02	3.10E-02	1.70E-02	4.80E-02	2.58E-01	0.00E+00	9.99E-01
PE O-40:6/ PE P-40:5	2.26E-07	4.56E-33	2.88E-01	6.10E-02	1.18E-01	5.80E-02	1.00E+00	0.00E+00	1.00E+00
PE O-40:7/ PE P-40:6	5.51E-10	4.78E-36	3.89E-01	3.07E-01	7.50E-02	6.10E-02	1.05E-01	0.00E+00	1.00E+00
PG40:7	2.16E-16	1.32E-40	9.42E-01	7.83E-01	6.58E-01	5.20E-02	9.79E-01	2.90E-01	9.99E-01
PI32:0	4.91E-09	3.24E-14	3.50E-02	0.00E+00	2.00E-03	0.00E+00	0.00E+00	0.00E+00	6.49E-01
PI34:1	2.68E-04	3.14E-16	9.00E-03	1.00E+00	1.00E+00	9.99E-01	9.75E-01	0.00E+00	0.00E+00
PI34:2	1.52E-02	1.14E-19	1.00E+00	0.00E+00	0.00E+00	2.07E-01	2.00E-03	9.59E-01	0.00E+00
PI36:1	1.63E-03	1.52E-24	1.00E-03	0.00E+00	0.00E+00	7.40E-01	0.00E+00	0.00E+00	2.01E-01
PI36:2	1.20E-02	5.45E-21	9.98E-01	0.00E+00	1.00E-03	2.90E-02	0.00E+00	1.00E+00	0.00E+00
PI36:3	3.27E-01	3.19E-17	1.00E+00	2.56E-01	4.00E-02	0.00E+00	9.81E-01	5.26E-01	5.44E-01
PI36:4	6.80E-02	8.36E-06	1.75E-01	9.11E-01	1.33E-01	1.00E+00	6.50E-02	2.80E-02	8.00E-03
PI38:2	9.31E-07	1.02E-17	2.18E-01	0.00E+00	3.00E-03	1.60E-01	0.00E+00	0.00E+00	9.50E-02
PI38:4	1.73E-02	3.44E-05	4.20E-01	9.69E-01	1.00E+00	2.00E-03	1.00E-03	9.93E-01	1.10E-02
PI38:5	3.19E-03	8.92E-10	9.73E-01	2.00E-03	6.76E-01	1.80E-02	5.72E-01	1.00E-03	0.00E+00
PI38:6	1.86E-06	1.95E-22	1.60E-02	0.00E+00	0.00E+00	0.00E+00	0.00E+00	0.00E+00	5.56E-01
PI40:4	1.57E-03	8.14E-27	9.98E-01	1.00E+00	5.98E-01	5.20E-02	2.60E-02	9.91E-01	9.26E-01
PI40:5	2.93E-01	1.80E-15	1.00E+00	7.69E-01	7.96E-01	0.00E+00	9.99E-01	1.00E+00	9.51E-01
PI40:6	2.07E-04	5.27E-15	1.48E-01	0.00E+00	0.00E+00	4.00E-03	0.00E+00	0.00E+00	2.09E-01
PS34:1	5.56E-05	7.60E-36	7.79E-01	0.00E+00	4.00E-03	4.10E-02	0.00E+00	9.97E-01	0.00E+00
PS36:1	2.68E-08	1.38E-26	2.43E-01	0.00E+00	0.00E+00	1.11E-01	1.70E-02	0.00E+00	0.00E+00
PS36:2	1.72E-08	1.33E-16	9.79E-01	2.91E-01	9.36E-01	6.80E-02	1.00E-03	4.00E-03	1.00E+00
PS36:4	2.09E-07	9.41E-12	2.00E-02	1.10E-02	1.00E-03	6.00E-03	0.00E+00	0.00E+00	1.00E+00
PS38:3	1.44E-13	6.68E-31	9.72E-01	9.99E-01	7.28E-01	5.30E-02	1.00E+00	1.00E-03	1.00E+00
PS38:4	4.74E-04	7.22E-14	1.80E-02	0.00E+00	0.00E+00	8.20E-02	0.00E+00	1.00E+00	6.47E-01
PS38:5	1.63E-07	4.14E-05	1.00E+00	1.19E-01	4.00E-03	1.00E-03	0.00E+00	0.00E+00	6.03E-01
PS40:7	1.56E-06	2.22E-20	2.10E-02	0.00E+00	0.00E+00	0.00E+00	0.00E+00	0.00E+00	5.00E-03
PS O-38:2/ PS P-38:1	4.92E-09	6.29E-13	9.88E-01	0.00E+00	0.00E+00	1.00E-03	0.00E+00	6.14E-01	2.20E-01
SM d32:1	4.13E-05	4.87E-24	3.57E-01	1.32E-02	3.83E-06	1.94E-06	1.47E-06	9.94E-01	1.30E-03
SM d33:1	4.88E-06	2.68E-27	5.28E-01	1.81E-06	1.38E-08	4.36E-08	3.16E-09	1.31E-01	7.41E-05
SM d34:1	4.20E-05	8.68E-26	3.11E-01	3.39E-05	3.36E-07	5.11E-03	2.12E-04	3.53E-03	2.56E-04
SM d34:2	3.32E-06	6.55E-25	1.46E-01	1.36E-06	2.74E-08	4.03E-04	3.62E-12	8.58E-01	7.87E-05
SM d35:1	3.09E-07	1.35E-26	9.46E-01	8.55E-08	6.00E-08	1.79E-06	2.45E-11	6.19E-01	1.08E-04
SM d36:1	5.66E-10	1.19E-23	1.35E-01	8.08E-07	1.35E-07	6.02E-08	7.40E-09	1.62E-02	9.55E-08
SM d36:2	1.19E-07	5.22E-19	6.72E-01	1.87E-07	6.80E-08	2.64E-08	2.99E-08	5.85E-05	2.51E-04
SM d38:1	1.57E-03	3.35E-11	3.78E-01	1.18E-02	1.30E-06	7.16E-08	1.46E-08	4.17E-04	9.86E-01
SM d38:2	1.55E-11	6.86E-17	7.65E-01	2.05E-06	9.40E-08	5.32E-08	5.65E-08	1.41E-07	9.47E-03
SM d40:1	4.00E-01	1.89E-09	1.00E+00	3.47E-01	5.08E-05	9.65E-03	1.64E-06	9.33E-01	3.42E-01
SM d40:2	2.79E-02	6.81E-26	9.98E-01	1.61E-08	6.18E-06	2.15E-01	6.97E-11	1.13E-03	8.99E-08
SM d42:1	2.82E-09	4.98E-01							
SM d42:2	1.93E-02	1.28E-32	1.00E+00	3.62E-10	1.53E-12	4.43E-04	9.66E-13	1.00E+00	1.37E-06
SM d42:3	6.21E-04	5.36E-45	1.00E+00	1.04E-12	9.41E-13	3.79E-05	1.06E-12	8.13E-02	1.55E-10
SM t32:2	1.64E-03	5.23E-07	8.47E-01	9.60E-03	1.69E-06	9.92E-01	9.70E-01	3.03E-01	1.30E-01

SFT d34:1	3.79E-04	5.95E-14	3.73E-02	2.31E-04	3.33E-02	4.45E-01	1.80E-04	6.21E-03	3.97E-01
SFT d34:2	1.69E-10	1.01E-37	4.66E-01	1.00E+00	7.54E-01	5.73E-02	9.84E-01	6.06E-01	5.09E-01
SFT d34:3	2.78E-02	3.66E-07	9.97E-01	1.00E+00	2.65E-01	6.71E-03	3.53E-03	6.10E-02	9.98E-01
SFT d36:3	4.82E-09	1.67E-29	8.16E-01	8.41E-01	1.23E-01	3.69E-02	1.29E-05	1.41E-02	1.00E+00
SFT d36:4	3.03E-10	5.59E-27	1.00E+00	9.81E-01	4.06E-01	3.78E-02	4.25E-08	4.38E-01	9.98E-01
SFT d38:1	5.18E-13	5.17E-11	9.30E-01	2.31E-03	7.55E-02	6.92E-01	4.19E-02	4.68E-01	1.08E-02
SFT d40:1	8.88E-09	1.22E-31	1.48E-02	1.24E-05	4.39E-03	5.07E-03	5.07E-05	8.82E-04	8.37E-04
SFT d40:2	3.14E-07	1.59E-10	5.25E-01	2.54E-01	3.93E-01	1.04E-01	2.35E-06	3.87E-01	9.90E-01
SFT d41:1	1.16E-13	2.66E-32	3.40E-02	1.35E-04	2.63E-03	9.36E-03	1.97E-04	1.93E-03	1.93E-03
SFT d41:2	1.82E-09	7.86E-11	8.72E-01	5.37E-02	6.76E-01	1.00E+00	4.81E-02	9.96E-01	9.79E-01
SFT d42:1	1.01E-11	7.90E-22	2.45E-02	6.44E-06	4.83E-02	2.78E-03	1.55E-04	8.95E-02	8.34E-04
SFT d42:2	3.30E-06	1.49E-13	6.71E-01	3.05E-01	5.36E-01	4.62E-04	2.96E-03	7.31E-01	1.00E+00
SFT d42:3	8.44E-04	2.28E-08	1.00E+00	2.26E-01	6.68E-01	4.86E-02	4.66E-02	2.67E-02	3.26E-02
SFT d43:3	7.17E-09	9.56E-05	1.00E+00	1.36E-01	2.67E-01	7.02E-01	1.36E-01	1.00E+00	2.53E-01
SFT t35:0	1.67E-04	4.97E-03	8.43E-01	5.71E-01	7.10E-01	1.00E+00	1.48E-01	9.98E-01	1.00E+00
SFT t41:0	3.29E-23	3.35E-19	7.26E-01	7.31E-01	1.60E-01	2.37E-01	7.04E-02	6.64E-01	7.95E-01
SFT t41:1	1.56E-16	1.96E-23	8.08E-02	2.14E-03	2.42E-02	5.27E-03	2.11E-04	2.65E-03	2.53E-02
SFT t42:0	1.39E-17	6.69E-19	1.00E+00	3.15E-01	3.85E-02	3.37E-01	1.09E-01	3.62E-01	3.20E-01
SFT t42:1	1.16E-14	4.92E-27	2.06E-01	6.27E-04	1.36E-02	5.62E-02	6.68E-04	2.33E-02	8.59E-03

Table A.6.1 continued

Lipid specie	Levene p-value	ANOVA p-value	PTIIvsCMT	PTIIvsMTI	PTIIvsMTII	PTIIvsITS	CdNvsCMT	CdNvsMTI	CdNvsMTII
HexCer d28:0	1.50E-04	1.45E-17	0.00E+00	4.00E-03	0.00E+00	9.88E-01	1.00E+00	6.38E-01	1.10E-02
HexCer d29:0	3.73E-09	5.55E-18	4.00E-03	1.00E-03	1.00E-03	8.15E-01	8.40E-01	2.45E-01	3.00E-03
HexCer d30:0	3.35E-06	1.50E-16	0.00E+00	0.00E+00	0.00E+00	1.00E+00	1.00E+00	1.43E-01	0.00E+00
HexCer d30:1	1.91E-06	1.10E-33	0.00E+00	3.20E-02	0.00E+00	6.45E-01	8.35E-01	6.98E-01	0.00E+00
HexCer d32:0	1.56E-04	3.18E-15	1.00E-03	0.00E+00	0.00E+00	2.10E-02	1.70E-02	0.00E+00	0.00E+00
HexCer d34:1	1.82E-07	6.92E-19	0.00E+00	0.00E+00	0.00E+00	0.00E+00	1.60E-02	1.00E-03	1.00E-03
HexCer d36:1	9.49E-03	1.14E-19	0.00E+00	0.00E+00	0.00E+00	9.95E-01	7.90E-02	7.00E-03	3.40E-02
HexCer d36:2	3.44E-06	1.95E-21	0.00E+00	0.00E+00	0.00E+00	1.70E-02	8.60E-02	8.50E-02	1.00E-03
HexCer d38:2	4.89E-06	1.23E-11	6.00E-03	6.00E-03	0.00E+00	9.83E-01	1.74E-01	2.13E-01	0.00E+00
HexCer t33:1	4.02E-04	1.63E-13	1.90E-02	8.23E-01	4.26E-01	1.50E-02	9.98E-01	9.97E-01	1.00E-03
HexCer t35:1	9.14E-03	1.65E-18	0.00E+00	2.96E-01	2.37E-01	0.00E+00	1.50E-02	7.28E-01	9.98E-01
HexCer t35:2	1.22E-01	9.12E-17	0.00E+00	3.94E-01	8.91E-01	0.00E+00	2.03E-01	1.00E+00	7.01E-01
HexCer t39:4	2.02E-10	4.12E-19	6.74E-01	1.00E+00	4.75E-01	1.00E-03	4.17E-01	9.96E-01	6.66E-01
Lyso-PI16:0	2.43E-06	4.39E-07	8.06E-01	9.99E-01	4.90E-01	7.00E-03	5.26E-01	9.93E-01	1.48E-01
Lyso-PI18:0	1.27E-01	4.66E-11	6.60E-02	9.54E-01	1.00E-03	2.00E-03	8.52E-01	1.00E+00	9.20E-02
Lyso-PI18:1	2.64E-08	3.07E-27	9.90E-01	4.30E-02	1.00E+00	7.07E-01	9.14E-01	4.40E-02	9.33E-01
Lyso-PI20:4	9.69E-06	7.71E-23	1.00E+00	4.70E-02	1.85E-01	1.15E-01	9.93E-01	5.10E-02	6.13E-01
PC32:0	2.63E-01	2.03E-27	9.96E-01	9.85E-01	6.54E-01	0.00E+00	8.23E-01	1.00E+00	1.00E+00
PC32:2	5.49E-11	2.47E-33	0.00E+00	2.30E-02	0.00E+00	0.00E+00	6.00E-03	3.54E-01	3.00E-03
PC33:2	6.19E-01	8.92E-06	3.00E-03	9.50E-01	8.66E-01	1.00E+00	3.90E-01	6.31E-01	1.00E+00
PC34:1	9.45E-05	8.43E-18	1.00E-03	1.30E-01	9.08E-01	3.00E-03	5.24E-01	6.62E-01	9.32E-01
PC34:4	1.21E-03	1.31E-31	1.00E-03	0.00E+00	3.00E-03	0.00E+00	2.10E-02	1.10E-02	1.16E-01
PC35:1	3.97E-03	1.15E-15	0.00E+00	9.48E-01	3.54E-01	3.40E-02	1.90E-02	9.55E-01	8.55E-01
PC35:2	1.67E-02	1.94E-03	7.27E-01	8.84E-01	1.00E+00	6.48E-01	7.08E-01	8.83E-01	1.00E+00
PC36:1	2.07E-03	5.43E-25	0.00E+00	6.26E-01	1.00E+00	0.00E+00	9.48E-01	8.95E-01	1.62E-01
PC36:2	3.91E-01	2.16E-10	4.50E-02	8.60E-02	1.00E+00	3.18E-01	3.44E-01	2.62E-01	1.00E+00
PC36:5	3.93E-04	5.71E-13	9.05E-01	1.00E+00	2.13E-01	1.94E-01	7.52E-01	1.00E-03	9.70E-01
PC36:6	5.83E-06	1.11E-32	0.00E+00	0.00E+00	0.00E+00	0.00E+00	3.59E-01	7.80E-02	0.00E+00
PC38:4	6.67E-02	8.09E-23	9.88E-01	1.00E+00	1.40E-02	0.00E+00	9.94E-01	9.31E-01	4.79E-01
PC38:5	5.02E-01	2.89E-08	9.99E-01	0.00E+00	1.14E-01	6.80E-02	1.00E+00	1.00E-03	4.90E-02
PC38:6	4.97E-04	1.26E-15	5.00E-03	0.00E+00	0.00E+00	8.21E-01	1.00E+00	9.99E-01	6.00E-03
PC38:7	1.72E-10	1.54E-10	2.00E-02	1.00E-02	7.00E-03	5.70E-02	3.66E-01	1.69E-01	5.70E-02
PC O-32:2/ PC P-32:1	2.82E-01	8.17E-02							
PC O-34:2/ PC P-34:1	3.13E-02	2.74E-13	0.00E+00	3.29E-01	6.27E-01	0.00E+00	1.70E-02	7.40E-01	9.97E-01
PC O-34:3/ PC P-34:2	3.81E-01	4.18E-04	2.74E-01	9.95E-01	1.00E+00	5.28E-01	9.99E-01	1.00E+00	8.80E-01
PC O-34:5/ PC P-34:4	2.37E-01	1.15E-04	1.00E+00	9.99E-01	2.38E-01	1.00E+00	9.94E-01	9.56E-01	4.30E-02
PC O-36:5/ PC P-36:4	6.38E-05	3.28E-16	1.70E-02	7.60E-02	9.64E-01	0.00E+00	8.90E-02	1.59E-01	9.41E-01
PC O-36:6/ PC P-36:5	4.30E-01	3.34E-15	8.35E-01	1.00E+00	8.37E-01	1.20E-02	9.89E-01	1.00E+00	5.44E-01
PC O-36:7/ PC P-34:1	4.67E-02	4.82E-20	7.70E-01	3.20E-02	1.60E-02	6.00E-03	9.99E-01	2.00E-02	5.00E-02
PC O-38:5/ PC P-38:4	5.58E-10	2.79E-25	4.40E-01	6.27E-01	1.61E-01	0.00E+00	3.09E-01	6.00E-02	8.10E-02
PC O-38:6/ PC P-38:5	4.72E-13	3.75E-24	1.00E+00	9.94E-01	5.98E-01	0.00E+00	9.30E-01	9.76E-01	8.35E-01
PC O-38:7/ PC P-38:6	4.64E-17	4.61E-33	9.99E-01	1.67E-01	1.00E-03	0.00E+00	4.84E-01	7.22E-01	1.90E-02

PE34:0	2.63E-01	2.03E-27	9.96E-01	9.85E-01	6.54E-01	0.00E+00	8.23E-01	1.00E+00	1.00E+00
PE34:1	4.58E-04	1.81E-08	1.00E+00	3.11E-01	7.81E-01	2.52E-01	3.27E-01	1.00E+00	0.00E+00
PE34:2	5.49E-11	2.47E-33	0.00E+00	2.30E-02	0.00E+00	0.00E+00	6.00E-03	3.54E-01	3.00E-03
PE35:2	6.19E-01	8.92E-06	3.00E-03	9.50E-02	8.66E-01	1.00E+00	3.90E-01	6.31E-01	1.00E+00
PE36:1	1.06E-04	4.57E-17	1.00E-03	4.92E-01	9.08E-01	3.00E-03	5.24E-01	1.00E+00	9.32E-01
PE36:2	8.35E-05	1.72E-05	3.08E-01	1.00E+00	4.75E-01	0.00E+00	1.00E+00	3.65E-01	9.98E-01
PE36:3	3.99E-02	3.54E-20	9.92E-01	1.20E-02	4.10E-01	0.00E+00	1.00E+00	1.60E-02	2.70E-02
PE36:4	1.21E-03	1.31E-31	1.00E-03	0.00E+00	3.00E-03	0.00E+00	2.10E-02	1.10E-02	1.16E-01
PE37:1	3.97E-03	1.15E-15	0.00E+00	9.48E-01	3.54E-01	3.40E-02	1.90E-02	9.55E-01	8.55E-01
PE37:2	1.67E-02	1.94E-03	7.27E-01	8.84E-01	1.00E+00	6.48E-01	7.08E-01	8.83E-01	1.00E+00
PE38:1	2.14E-07	1.38E-17	0.00E+00	6.26E-01	9.30E-01	1.00E-03	9.83E-01	9.06E-01	1.00E+00
PE38:2	2.58E-01	2.14E-10	3.50E-02	6.90E-02	1.00E+00	2.82E-01	3.07E-01	2.28E-01	1.00E+00
PE38:4	6.24E-02	2.60E-07	2.88E-01	6.95E-01	4.00E-02	5.64E-01	9.83E-01	9.86E-01	5.46E-01
PE38:5	3.93E-04	5.71E-13	9.05E-01	1.00E+00	2.13E-01	1.94E-01	7.52E-01	1.00E-03	9.70E-01
PE38:6	5.83E-06	1.11E-32	0.00E+00	0.00E+00	0.00E+00	0.00E+00	3.59E-01	7.80E-02	0.00E+00
PE40:4	6.67E-02	8.09E-23	9.88E-01	1.00E+00	1.40E-02	0.00E+00	9.94E-01	9.31E-01	4.79E-01
PE40:5	7.85E-01	4.49E-07	9.64E-01	9.96E-01	8.00E-01	1.00E-03	1.00E+00	1.00E+00	5.00E-01
PE40:6	4.97E-04	1.26E-15	5.00E-03	0.00E+00	0.00E+00	8.21E-01	1.00E+00	9.99E-01	6.00E-03
PE40:7	1.70E-10	1.56E-10	2.00E-02	1.00E+00	7.00E-03	5.80E-02	3.66E-01	1.69E-01	5.70E-02
PE O-34:2/ PE P-34:1	2.82E-01	8.17E-02							
PE O-34:3/ PE P-34:2	3.26E-02	7.73E-01							
PE O-36:2/ PE P-36:1	2.09E-01	5.17E-02							
PE O-36:3/ PE P-36:2	1.87E-01	7.54E-12	0.00E+00	7.14E-01	9.84E-01	2.00E-03	4.05E-01	1.00E+00	8.82E-01
PE O-36:5/ PE P-36:4	2.35E-01	1.21E-04	1.00E+00	9.99E-01	2.45E-01	1.00E+00	9.95E-01	9.59E-01	4.50E-02
PE O-38:5/ PE P-38:4	2.56E-07	6.00E-12	1.10E-02	0.00E+00	7.13E-01	0.00E+00	2.03E-01	3.89E-01	3.50E-01
PE O-38:6/ PE P-38:5	4.95E-02	7.47E-15	3.84E-01	2.80E-02	2.35E-01	1.90E-02	9.94E-01	1.89E-01	6.90E-02
PE O-38:7/ PE P-38:6	4.60E-03	1.51E-29	7.80E-01	4.40E-02	0.00E+00	0.00E+00	1.00E+00	3.20E-02	8.00E-03
PE O-40:5/ PE P-40:4	3.99E-08	7.02E-32	1.87E-01	5.00E-02	7.85E-01	0.00E+00	1.12E-01	5.10E-02	9.37E-01
PE O-40:6/ PE P-40:5	2.26E-07	4.56E-33	4.97E-01	6.00E-02	3.55E-01	0.00E+00	6.08E-01	6.10E-02	8.90E-02
PE O-40:7/ PE P-40:6	5.51E-10	4.78E-36	6.56E-01	6.10E-02	3.10E-02	0.00E+00	5.14E-01	6.30E-02	1.00E-02
PG40:7	2.16E-16	1.32E-40	4.65E-01	5.20E-02	1.00E+00	6.10E-01	4.06E-01	5.10E-02	9.93E-01
PI32:0	4.91E-09	3.24E-14	8.92E-01	1.60E-01	9.87E-01	8.00E-03	1.00E+00	7.29E-01	8.21E-01
PI34:1	2.68E-04	3.14E-16	7.40E-02	1.56E-01	7.00E-03	1.50E-02	1.00E+00	1.00E+00	9.99E-01
PI34:2	1.52E-02	1.14E-19	0.00E+00	1.97E-01	1.00E-03	8.64E-01	4.13E-01	9.90E-01	7.70E-02
PI36:1	1.63E-03	1.52E-24	6.52E-01	9.16E-01	6.04E-01	0.00E+00	1.00E+00	9.98E-01	1.00E+00
PI36:2	1.20E-02	5.45E-21	0.00E+00	9.00E-03	0.00E+00	1.00E+00	7.69E-01	1.00E+00	1.00E+00
PI36:3	3.27E-01	3.19E-17	1.23E-01	0.00E+00	9.99E-01	2.93E-01	9.74E-01	0.00E+00	9.84E-01
PI36:4	6.80E-02	8.36E-06	1.00E+00	7.21E-01	9.74E-01	9.91E-01	8.00E-03	1.00E+00	4.00E-03
PI38:2	9.31E-07	1.02E-17	6.06E-01	6.60E-02	3.00E-03	2.00E-03	9.95E-01	6.80E-02	0.00E+00
PI38:4	1.73E-02	3.44E-05	8.64E-01	1.42E-01	5.60E-02	6.74E-01	9.73E-01	0.00E+00	0.00E+00
PI38:5	3.19E-03	8.92E-10	1.82E-01	1.60E-02	9.86E-01	0.00E+00	5.01E-01	5.10E-01	0.00E+00
PI38:6	1.86E-06	1.95E-22	1.80E-02	3.10E-02	0.00E+00	0.00E+00	2.53E-01	2.13E-01	0.00E+00
PI40:4	1.57E-03	8.14E-27	3.80E-01	5.00E-02	2.00E-01	1.00E+00	7.16E-01	5.60E-02	1.00E-03
PI40:5	2.93E-01	1.80E-15	9.50E-01	0.00E+00	9.90E-01	1.00E+00	1.00E+00	0.00E+00	6.78E-01
PI40:6	2.07E-04	5.27E-15	7.80E-02	5.10E-02	8.60E-02	0.00E+00	9.48E-01	4.46E-01	8.56E-01
PS34:1	5.56E-05	7.60E-36	1.00E-03	4.20E-02	0.00E+00	3.44E-01	9.98E-01	6.30E-02	3.17E-01
PS36:1	2.68E-08	1.38E-26	3.00E-03	5.68E-02	7.57E-01	0.00E+00	1.00E+00	2.71E-01	8.80E-02
PS36:2	1.72E-08	1.33E-16	1.00E+00	4.30E-02	6.05E-01	7.18E-01	1.00E+00	6.30E-02	4.80E-02
PS36:4	2.09E-07	9.41E-12	9.70E-01	9.92E-01	9.98E-01	8.60E-02	6.78E-01	7.78E-01	8.17E-01
PS38:3	1.44E-13	6.68E-31	8.42E-01	5.40E-02	9.26E-01	3.00E-03	7.89E-01	5.40E-02	9.95E-01
PS38:4	4.74E-04	7.22E-14	8.43E-01	9.99E-01	1.50E-02	1.20E-02	1.00E+00	3.54E-01	1.50E-01
PS38:5	1.63E-07	4.14E-05	1.77E-01	9.60E-01	5.20E-02	3.60E-02	7.30E-01	2.88E-01	5.90E-02
PS40:7	1.56E-06	2.22E-20	1.00E-03	7.00E-03	0.00E+00	7.00E-03	6.93E-01	9.22E-01	4.00E-02
PS O-38:2/ PS P-38:1	4.92E-09	6.29E-13	3.60E-02	1.50E-02	4.00E-03	9.94E-01	6.37E-01	2.84E-01	3.00E-03

SM d32:1	4.13E-05	4.87E-24	1.92E-05	1.42E-06	2.52E-06	8.83E-01	8.05E-02	1.83E-03	6.48E-03
SM d33:1	4.88E-06	2.68E-27	5.96E-06	2.31E-06	2.32E-06	1.17E-02	4.47E-02	2.08E-02	2.80E-03
SM d34:1	4.20E-05	8.68E-26	2.74E-05	4.87E-05	1.34E-05	9.95E-01	5.83E-01	2.70E-01	2.39E-01
SM d34:2	3.32E-06	6.55E-25	4.46E-05	4.61E-06	2.76E-06	7.17E-01	9.96E-01	1.38E-01	3.75E-04
SM d35:1	3.09E-07	1.35E-26	3.22E-05	2.07E-06	9.85E-07	9.94E-01	9.55E-01	4.75E-02	3.50E-04
SM d36:1	5.66E-10	1.19E-23	1.65E-08	1.16E-05	4.62E-11	8.93E-01	7.22E-01	1.17E-01	2.09E-05
SM d36:2	1.19E-07	5.22E-19	9.04E-05	2.97E-05	3.08E-05	5.48E-02	5.05E-01	4.25E-03	2.12E-04
SM d38:1	1.57E-03	3.35E-11	1.70E-02	4.39E-04	2.45E-04	5.75E-01	3.63E-03	4.59E-05	1.07E-06
SM d38:2	1.55E-11	6.86E-17	4.08E-04	2.17E-04	2.30E-04	8.30E-04	5.79E-03	6.70E-04	8.15E-04
SM d40:1	4.00E-01	1.89E-09	5.89E-05	9.40E-03	1.90E-06	9.24E-01	7.68E-02	2.14E-01	3.53E-03
SM d40:2	2.79E-02	6.81E-26	2.57E-05	1.83E-01	3.89E-10	6.38E-03	1.00E+00	6.71E-02	9.32E-07
SM d42:1	2.82E-09	4.98E-01							
SM d42:2	1.93E-02	1.28E-32	5.64E-09	2.84E-05	6.92E-10	1.00E+00	7.18E-03	1.75E-02	4.40E-06
SM d42:3	6.21E-04	5.36E-45	5.22E-12	1.03E-05	2.72E-12	3.09E-01	1.20E-02	2.62E-01	2.38E-08
SM t32:2	1.64E-03	5.23E-07	2.06E-05	9.99E-01	1.00E+00	8.40E-01	3.00E-01	1.00E+00	8.05E-01
SFT d34:1	3.79E-04	5.95E-14	7.98E-01	9.97E-01	2.48E-03	1.00E+00	1.00E+00	9.59E-01	1.30E-01
SFT d34:2	1.69E-10	1.01E-37	9.98E-01	6.06E-02	8.65E-02	2.05E-02	7.90E-01	5.87E-02	7.99E-01
SFT d34:3	2.78E-02	3.66E-07	9.04E-02	5.55E-04	7.75E-01	8.33E-01	2.80E-01	9.80E-03	1.81E-03
SFT d36:3	4.82E-09	1.67E-29	3.17E-01	3.44E-02	3.76E-02	3.01E-01	2.33E-01	3.73E-02	9.84E-04
SFT d36:4	3.03E-10	5.59E-27	3.80E-01	3.74E-02	2.57E-08	4.03E-01	3.29E-01	3.66E-02	8.73E-09
SFT d38:1	5.18E-13	5.17E-11	1.34E-01	7.27E-01	6.17E-02	9.39E-01	9.99E-01	9.59E-01	8.49E-01
SFT d40:1	8.88E-09	1.22E-31	2.08E-02	3.71E-04	6.75E-05	2.33E-01	8.53E-01	4.51E-01	3.88E-04
SFT d40:2	3.14E-07	1.59E-10	9.95E-01	9.83E-01	1.10E-01	1.11E-01	1.00E+00	1.00E+00	9.57E-05
SFT d41:1	1.16E-13	2.66E-32	1.17E-02	6.22E-04	2.66E-04	1.41E-01	9.98E-01	9.96E-01	1.56E-03
SFT d41:2	1.82E-09	7.86E-11	1.00E+00	9.95E-01	1.12E-01	7.34E-01	9.60E-01	7.36E-01	1.95E-01
SFT d42:1	1.01E-11	7.90E-22	1.60E-01	6.71E-04	3.58E-04	9.42E-01	9.73E-01	2.43E-05	4.51E-02
SFT d42:2	3.30E-06	1.49E-13	9.99E-01	3.61E-04	6.05E-01	5.24E-02	9.97E-01	5.91E-03	1.96E-01
SFT d42:3	8.44E-04	2.28E-08	3.80E-01	6.67E-02	2.79E-03	1.30E-03	9.94E-01	6.36E-02	2.42E-02
SFT d43:3	7.17E-09	9.56E-05	3.71E-01	7.57E-01	2.21E-01	1.00E+00	1.00E+00	1.00E+00	1.00E+00
SFT t35:0	1.67E-04	4.97E-03	1.00E+00	5.41E-01	8.25E-01	3.38E-01	1.00E+00	1.74E-01	8.58E-01
SFT t41:0	3.29E-23	3.35E-19	1.67E-01	2.38E-01	7.09E-02	6.83E-01	3.12E-01	2.49E-01	7.84E-02
SFT t41:1	1.56E-16	1.96E-23	7.70E-02	1.15E-05	2.66E-04	7.00E-01	9.89E-01	9.87E-01	2.29E-03
SFT t42:0	1.39E-17	6.69E-19	3.87E-02	3.37E-01	1.09E-01	3.63E-01	7.62E-02	3.50E-01	1.29E-01
SFT t42:1	1.16E-14	4.92E-27	4.78E-02	5.03E-02	8.72E-04	4.69E-01	9.96E-01	1.87E-01	5.27E-03

Lipid specie	Levene p-value	ANOVA p-value	CdNvsITS	CMTvsMTI	CMTvsMTII	CMTvsITS	MTIvsMTII	MTIvsITS	MTIIvsITS
HexCer d28:0	1.50E-04	1.45E-17	1.00E-03	7.09E-01	3.40E-02	1.00E-03	9.81E-01	1.00E-03	0.00E+00
HexCer d29:0	3.73E-09	5.55E-18	1.83E-01	8.94E-01	6.35E-01	6.10E-02	1.00E+00	1.70E-02	9.00E-03
HexCer d30:0	3.35E-06	1.50E-16	2.00E-03	1.70E-01	4.00E-03	2.00E-03	9.99E-01	0.00E+00	0.00E+00
HexCer d30:1	1.91E-06	1.10E-33	0.00E+00	9.12E-01	2.50E-02	0.00E+00	9.99E-01	9.00E-03	0.00E+00
HexCer d32:0	1.56E-04	3.18E-15	4.69E-01	1.32E-01	4.49E-01	8.95E-01	9.64E-01	4.00E-02	1.12E-01
HexCer d34:1	1.82E-07	6.92E-19	7.60E-01	3.93E-01	3.98E-01	3.50E-01	1.00E+00	1.70E-02	1.50E-02
HexCer d36:1	9.49E-03	1.14E-19	1.47E-01	7.70E-02	8.57E-01	9.00E-03	7.57E-01	0.00E+00	2.00E-03
HexCer d36:2	3.44E-06	1.95E-21	1.04E-01	9.10E-01	3.26E-01	5.00E-03	1.00E+00	2.00E-03	1.00E-03
HexCer d38:2	4.89E-06	1.23E-11	3.80E-02	9.15E-01	1.57E-01	2.00E-03	9.98E-01	2.00E-03	0.00E+00
HexCer t33:1	4.02E-04	1.63E-13	5.75E-01	9.22E-01	0.00E+00	7.64E-01	3.12E-01	4.82E-01	1.00E-03
HexCer t35:1	9.14E-03	1.65E-18	4.50E-02	9.83E-01	6.00E-03	1.00E+00	6.05E-01	9.99E-01	1.70E-02
HexCer t35:2	1.22E-01	9.12E-17	8.35E-01	9.24E-01	9.00E-03	9.46E-01	9.31E-01	9.99E-01	1.01E-01
HexCer t39:4	2.02E-10	4.12E-19	0.00E+00	9.97E-01	8.90E-02	9.00E-03	9.10E-01	1.05E-01	0.00E+00
Lyso-PI16:0	2.43E-06	4.39E-07	0.00E+00	9.91E-01	1.00E+00	2.82E-01	9.54E-01	5.09E-01	9.50E-02
Lyso-PI18:0	1.27E-01	4.66E-11	3.03E-01	9.99E-01	8.10E-01	9.97E-01	7.91E-01	9.72E-01	9.82E-01
Lyso-PI18:1	2.64E-08	3.07E-27	9.80E-01	2.00E-02	9.97E-01	7.57E-01	4.30E-02	4.20E-02	5.57E-01
Lyso-PI20:4	9.69E-06	7.71E-23	3.68E-01	2.90E-02	7.81E-01	7.07E-01	4.90E-02	4.90E-02	1.00E+00
PC32:0	2.63E-01	2.03E-27	0.00E+00	1.00E+00	9.70E-01	0.00E+00	1.00E+00	0.00E+00	0.00E+00
PC32:2	5.49E-11	2.47E-33	0.00E+00	9.25E-01	9.80E-01	1.43E-01	9.95E-01	1.00E+00	6.86E-01
PC33:2	6.19E-01	8.92E-06	7.78E-01	1.00E+00	4.85E-01	1.40E-02	6.17E-01	1.67E-01	9.69E-01
PC34:1	9.45E-05	8.43E-18	1.00E+00	1.00E+00	2.04E-01	4.17E-01	3.56E-01	6.60E-01	7.85E-01
PC34:4	1.21E-03	1.31E-31	0.00E+00	6.20E-01	1.00E+00	1.94E-01	5.92E-01	9.82E-01	2.27E-01
PC35:1	3.97E-03	1.15E-15	9.73E-01	3.13E-01	1.00E-03	0.00E+00	1.00E+00	9.99E-01	9.99E-01
PC35:2	1.67E-02	1.94E-03	6.14E-01	9.97E-01	8.23E-01	3.10E-02	8.89E-01	6.70E-01	8.89E-01
PC36:1	2.07E-03	5.43E-25	2.33E-01	9.49E-01	5.00E-02	7.54E-01	6.57E-01	9.96E-01	6.00E-03
PC36:2	3.91E-01	2.16E-10	8.90E-01	9.64E-01	3.55E-01	9.77E-01	2.27E-01	7.15E-01	8.33E-01
PC36:5	3.93E-04	5.71E-13	0.00E+00	8.29E-01	9.94E-01	1.35E-01	1.31E-01	1.02E-01	5.00E-03
PC36:6	5.83E-06	1.11E-32	5.40E-02	4.03E-01	1.70E-02	9.65E-01	1.00E+00	8.29E-01	2.79E-01
PC38:4	6.67E-02	8.09E-23	0.00E+00	9.96E-01	1.96E-01	0.00E+00	2.83E-01	6.00E-03	0.00E+00
PC38:5	5.02E-01	2.89E-08	2.26E-01	2.00E-03	6.10E-02	4.34E-01	0.00E+00	7.50E-02	0.00E+00
PC38:6	4.97E-04	1.26E-15	0.00E+00	9.29E-01	2.00E-03	0.00E+00	4.00E-03	0.00E+00	0.00E+00
PC38:7	1.72E-10	1.54E-10	8.22E-01	9.85E-01	9.71E-01	9.85E-01	1.00E+00	7.12E-01	4.91E-01
PC O-32:2/ PC P-32:1	2.82E-01	8.17E-02							
PC O-34:2/ PC P-34:1	3.13E-02	2.74E-13	5.00E-02	9.83E-01	6.00E-03	1.00E+00	6.05E-01	9.99E-01	1.70E-02
PC O-34:3/ PC P-34:2	3.81E-01	4.18E-04	1.00E+00	9.99E-01	6.71E-01	9.99E-01	9.99E-01	1.00E+00	8.85E-01
PC O-34:5/ PC P-34:4	2.37E-01	1.15E-04	9.94E-01	9.98E-01	3.06E-01	1.00E+00	9.87E-01	9.98E-01	2.26E-01
PC O-36:5/ PC P-36:4	6.38E-05	3.28E-16	0.00E+00	1.00E+00	3.30E-02	1.00E+00	1.40E-01	1.00E+00	0.00E+00
PC O-36:6/ PC P-36:5	4.30E-01	3.34E-15	8.50E-02	9.97E-01	2.07E-01	6.35E-01	9.78E-01	6.55E-01	1.00E-03
PC O-36:7/ PC P-34:1	4.67E-02	4.82E-20	0.00E+00	3.00E-02	2.70E-02	0.00E+00	3.80E-02	9.22E-01	0.00E+00
PC O-38:5/ PC P-38:4	5.58E-10	2.79E-25	0.00E+00	7.20E-02	2.80E-02	1.00E-03	9.71E-01	0.00E+00	0.00E+00
PC O-38:6/ PC P-38:5	4.72E-13	3.75E-24	0.00E+00	9.99E-01	2.47E-01	0.00E+00	8.86E-01	1.52E-01	0.00E+00
PC O-38:7/ PC P-38:6	4.64E-17	4.61E-33	0.00E+00	1.06E-01	6.00E-03	0.00E+00	8.65E-01	0.00E+00	0.00E+00
PE34:0	2.63E-01	2.03E-27	0.00E+00	1.00E+00	9.70E-01	0.00E+00	1.00E+00	0.00E+00	0.00E+00
PE34:1	4.58E-04	1.81E-08	0.00E+00	3.95E-01	5.51E-01	1.35E-01	3.60E-02	4.00E-03	6.08E-01
PE34:2	5.49E-11	2.47E-33	0.00E+00	9.25E-01	9.80E-01	1.43E-01	9.95E-01	1.00E+00	6.86E-01
PE35:2	6.19E-01	8.92E-06	7.78E-01	1.00E+00	4.85E-01	1.40E-02	6.17E-01	1.67E-01	9.69E-01
PE36:1	1.06E-04	4.57E-17	1.00E+00	9.16E-01	2.04E-01	4.17E-01	9.44E-01	1.00E+00	7.85E-01
PE36:2	8.35E-05	1.72E-05	1.64E-01	1.68E-01	9.93E-01	5.70E-02	1.58E-01	0.00E+00	0.00E+00
PE36:3	3.99E-02	3.54E-20	0.00E+00	4.00E-03	2.14E-01	1.50E-02	3.40E-02	8.00E-03	0.00E+00
PE36:4	1.21E-03	1.31E-31	0.00E+00	6.20E-01	1.00E+00	1.94E-01	5.92E-01	9.82E-01	2.27E-01
PE37:1	3.97E-03	1.15E-15	9.73E-01	3.13E-01	1.00E-03	0.00E+00	1.00E+00	9.99E-01	9.99E-01
PE37:2	1.67E-02	1.94E-03	6.14E-01	9.97E-01	8.23E-01	3.10E-02	8.89E-01	6.70E-01	8.89E-01
PE38:1	2.14E-07	1.38E-17	4.00E-02	9.49E-01	1.00E+00	9.10E-02	9.38E-01	1.00E+00	4.06E-01
PE38:2	2.58E-01	2.14E-10	8.74E-01	9.58E-01	3.17E-01	9.72E-01	1.96E-01	6.83E-01	8.11E-01
PE38:4	6.24E-02	2.60E-07	1.00E+00	1.00E+00	9.71E-01	9.99E-01	1.00E+00	9.97E-01	7.68E-01
PE38:5	3.93E-04	5.71E-13	0.00E+00	8.29E-01	9.94E-01	1.35E-01	1.31E-01	1.02E-01	5.00E-03
PE38:6	5.83E-06	1.11E-32	5.40E-02	4.03E-01	1.70E-02	9.65E-01	1.00E+00	8.29E-01	2.79E-01
PE40:4	6.67E-02	8.09E-23	0.00E+00	9.96E-01	1.96E-01	0.00E+00	2.83E-01	6.00E-03	0.00E+00
PE40:5	7.85E-01	4.49E-07	9.00E-03	1.00E+00	3.30E-01	1.00E+00	7.58E-01	7.89E-01	0.00E+00
PE40:6	4.97E-04	1.26E-15	0.00E+00	9.29E-01	2.00E-03	0.00E+00	4.00E-03	0.00E+00	0.00E+00
PE40:7	1.70E-10	1.56E-10	8.30E-01	9.85E-01	9.71E-01	9.83E-01	1.00E+00	7.02E-01	4.75E-01

PE O-34:2/ PE P-34:1	2.82E-01	8.17E-02							
PE O-34:3/ PE P-34:2	3.26E-02	7.73E-01							
PE O-36:2/ PE P-36:1	2.09E-01	5.17E-02							
PE O-36:3/ PE P-36:2	1.87E-01	7.54E-12	9.14E-01	9.72E-01	6.10E-02	9.81E-01	9.75E-01	1.00E+00	2.88E-01
PE O-36:5/ PE P-36:4	2.35E-01	1.21E-04	9.94E-01	9.98E-01	3.10E-01	1.00E+00	9.87E-01	9.98E-01	2.29E-01
PE O-38:5/ PE P-38:4	2.56E-07	6.00E-12	1.30E-02	5.79E-01	3.40E-02	1.00E+00	1.00E-03	1.60E-01	0.00E+00
PE O-38:6/ PE P-38:5	4.95E-02	7.47E-15	4.95E-01	4.27E-01	4.00E-03	8.57E-01	2.60E-02	9.95E-01	0.00E+00
PE O-38:7/ PE P-38:6	4.60E-03	1.51E-29	0.00E+00	3.00E-02	2.70E-02	0.00E+00	3.80E-02	9.22E-01	0.00E+00
PE O-40:5/ PE P-40:4	3.99E-08	7.02E-32	0.00E+00	4.40E-02	5.40E-02	1.80E-02	5.00E-02	1.17E-01	0.00E+00
PE O-40:6/ PE P-40:5	2.26E-07	4.56E-33	0.00E+00	5.40E-02	1.23E-01	8.00E-02	5.80E-02	1.04E-01	0.00E+00
PE O-40:7/ PE P-40:6	5.51E-10	4.78E-36	0.00E+00	6.10E-02	2.00E-02	0.00E+00	5.80E-02	1.86E-01	0.00E+00
PG40:7	2.16E-16	1.32E-40	9.71E-01	3.40E-02	4.92E-01	3.23E-01	5.20E-02	5.10E-02	5.70E-01
PI32:0	4.91E-09	3.24E-14	3.00E-03	9.62E-01	9.91E-01	3.46E-01	1.39E-01	3.41E-01	1.00E-03
PI34:1	2.68E-04	3.14E-16	0.00E+00	1.00E+00	9.99E-01	2.00E-03	9.99E-01	3.10E-02	0.00E+00
PI34:2	1.52E-02	1.14E-19	0.00E+00	1.00E+00	9.51E-01	1.00E-03	9.55E-01	3.04E-01	2.50E-02
PI36:1	1.63E-03	1.52E-24	0.00E+00	1.00E+00	1.00E+00	3.00E-02	1.00E+00	2.28E-01	2.00E-03
PI36:2	1.20E-02	5.45E-21	0.00E+00	7.64E-01	3.17E-01	1.00E-03	1.00E+00	1.80E-02	0.00E+00
PI36:3	3.27E-01	3.19E-17	2.00E-03	0.00E+00	6.98E-01	0.00E+00	0.00E+00	0.00E+00	2.50E-01
PI36:4	6.80E-02	8.36E-06	1.00E-03	5.98E-01	9.99E-01	1.00E+00	4.08E-01	4.47E-01	1.00E+00
PI38:2	9.31E-07	1.02E-17	0.00E+00	4.70E-02	2.49E-01	1.85E-01	5.80E-02	5.70E-02	6.34E-01
PI38:4	1.73E-02	3.44E-05	3.40E-01	1.42E-01	3.30E-02	1.00E+00	5.24E-01	0.00E+00	3.00E-03
PI38:5	3.19E-03	8.92E-10	6.69E-01	9.20E-02	4.20E-02	7.40E-02	2.40E-02	1.00E+00	0.00E+00
PI38:6	1.86E-06	1.95E-22	0.00E+00	8.75E-01	3.30E-02	4.50E-02	9.20E-01	9.49E-01	1.00E+00
PI40:4	1.57E-03	8.14E-27	7.67E-01	4.40E-02	4.30E-02	3.21E-01	5.00E-02	5.40E-02	1.00E-02
PI40:5	2.93E-01	1.80E-15	9.23E-01	0.00E+00	6.90E-01	9.24E-01	0.00E+00	0.00E+00	9.97E-01
PI40:6	2.07E-04	5.27E-15	1.00E-03	9.39E-01	1.00E+00	5.66E-01	9.97E-01	1.00E+00	9.41E-01
PS34:1	5.56E-05	7.60E-36	0.00E+00	5.00E-02	4.88E-01	1.00E-02	5.90E-02	4.20E-02	6.00E-03
PS36:1	2.68E-08	1.38E-26	1.00E-03	2.31E-01	1.03E-01	7.00E-03	1.00E+00	0.00E+00	0.00E+00
PS36:2	1.72E-08	1.33E-16	2.46E-01	3.80E-02	8.46E-01	9.08E-01	5.70E-02	5.40E-02	1.00E+00
PS36:4	2.09E-07	9.41E-12	1.00E-03	1.00E+00	9.97E-01	4.52E-01	1.00E+00	3.21E-01	8.00E-03
PS38:3	1.44E-13	6.68E-31	2.00E-03	3.40E-02	7.12E-01	9.99E-01	5.30E-02	6.20E-02	1.00E-03
PS38:4	4.74E-04	7.22E-14	0.00E+00	4.96E-01	1.30E-01	0.00E+00	1.01E-01	1.07E-01	0.00E+00
PS38:5	1.63E-07	4.14E-05	1.90E-02	9.98E-01	8.64E-01	5.90E-01	9.72E-01	7.43E-01	9.97E-01
PS40:7	1.56E-06	2.22E-20	1.00E+00	1.00E+00	6.20E-01	3.42E-01	9.59E-01	8.13E-01	6.00E-03
PS O-38:2/ PS P-38:1	4.92E-09	6.29E-13	7.09E-01	9.70E-01	8.92E-01	2.00E-01	1.00E+00	7.80E-02	3.20E-02
SM d32:1	4.13E-05	4.87E-24	3.44E-02	1.66E-01	6.68E-01	4.60E-04	9.87E-01	2.91E-05	5.79E-05
SM d33:1	4.88E-06	2.68E-27	1.83E-01	7.56E-01	8.94E-01	5.68E-03	1.00E+00	1.29E-03	1.27E-03
SM d34:1	4.20E-05	8.68E-26	7.71E-08	8.28E-01	8.54E-01	8.07E-09	1.00E+00	2.67E-05	2.45E-07
SM d34:2	3.32E-06	6.55E-25	5.28E-05	2.25E-01	1.37E-02	2.43E-05	1.00E+00	1.19E-05	6.54E-07
SM d35:1	3.09E-07	1.35E-26	5.35E-04	1.75E-01	5.73E-02	2.18E-04	1.00E+00	2.31E-05	2.29E-05
SM d36:1	5.66E-10	1.19E-23	1.56E-08	3.21E-01	4.03E-02	2.24E-08	1.00E+00	4.36E-04	8.95E-12
SM d36:2	1.19E-07	5.22E-19	1.26E-02	2.25E-01	1.04E-01	1.96E-03	1.00E+00	2.58E-04	2.66E-04
SM d38:1	1.57E-03	3.35E-11	8.11E-01	2.14E-01	9.77E-02	7.98E-02	1.00E+00	6.87E-04	1.49E-05
SM d38:2	1.55E-11	6.86E-17	1.20E-01	7.80E-02	1.39E-01	8.58E-01	7.86E-01	1.40E-01	1.79E-01
SM d40:1	4.00E-01	1.89E-09	9.84E-01	9.95E-01	9.19E-01	7.94E-03	1.00E+00	7.17E-02	2.81E-04
SM d40:2	2.79E-02	6.81E-26	3.04E-03	3.76E-02	3.97E-01	6.96E-02	5.11E-02	8.68E-02	1.73E-06
SM d42:1	2.82E-09	4.98E-01							
SM d42:2	1.93E-02	1.28E-32	5.19E-07	9.98E-01	3.28E-01	2.28E-09	9.27E-01	1.35E-04	4.52E-10
SM d42:3	6.21E-04	5.36E-45	7.49E-08	9.31E-01	1.44E-02	1.92E-09	9.48E-01	1.36E-04	5.96E-10
SM t32:2	1.64E-03	5.23E-07	9.78E-01	9.42E-01	9.12E-02	6.13E-02	1.00E+00	1.00E+00	9.97E-01

SFT d34:1	3.79E-04	5.95E-14	1.48E-01	9.94E-01	2.32E-01	6.12E-01	2.04E-01	9.79E-01	1.74E-03
SFT d34:2	1.69E-10	1.01E-37	1.60E-01	4.34E-02	5.82E-01	4.44E-01	5.78E-02	5.68E-02	5.17E-01
SFT d34:3	2.78E-02	3.66E-07	5.88E-02	3.73E-03	1.00E+00	1.00E+00	3.71E-02	1.01E-02	1.00E+00
SFT d36:3	4.82E-09	1.67E-29	1.04E-01	1.83E-02	9.38E-01	9.52E-01	4.59E-02	3.67E-02	1.00E+00
SFT d36:4	3.03E-10	5.59E-27	3.33E-01	1.35E-02	1.00E+00	1.00E+00	5.10E-02	1.86E-02	9.86E-01
SFT d38:1	5.18E-13	5.17E-11	1.50E-01	9.89E-01	9.95E-01	3.36E-01	1.00E+00	7.88E-01	1.29E-01
SFT d40:1	8.88E-09	1.22E-31	1.98E-01	1.00E+00	1.05E-02	1.40E-01	2.70E-03	9.82E-04	9.81E-05
SFT d40:2	3.14E-07	1.59E-10	1.04E-04	1.00E+00	2.31E-04	7.59E-03	3.32E-04	7.51E-05	9.07E-06
SFT d41:1	1.16E-13	2.66E-32	2.11E-01	1.00E+00	3.20E-03	1.78E-01	3.67E-03	3.60E-03	4.41E-04
SFT d41:2	1.82E-09	7.86E-11	2.26E-02	9.88E-01	1.08E-01	4.67E-01	7.53E-02	9.97E-01	4.21E-02
SFT d42:1	1.01E-11	7.90E-22	1.27E-01	7.64E-03	9.62E-01	3.58E-01	2.28E-03	1.90E-06	6.58E-04
SFT d42:2	3.30E-06	1.49E-13	2.60E-03	9.44E-04	9.96E-01	9.69E-02	1.03E-02	4.96E-04	2.31E-05
SFT d42:3	8.44E-04	2.28E-08	3.14E-04	4.50E-02	5.46E-01	3.44E-01	5.75E-02	5.67E-02	6.81E-01
SFT d43:3	7.17E-09	9.56E-05	1.92E-01	1.00E+00	1.00E+00	3.30E-01	1.00E+00	7.42E-01	1.81E-01
SFT t35:0	1.67E-04	4.97E-03	1.08E-01	3.36E-01	8.97E-01	2.06E-01	3.85E-02	9.83E-01	1.39E-02
SFT t41:0	3.29E-23	3.35E-19	9.10E-01	3.41E-01	1.54E-01	9.73E-01	9.92E-01	2.81E-01	1.08E-01
SFT t41:1	1.56E-16	1.96E-23	1.50E-01	7.89E-01	3.56E-02	1.86E-01	2.06E-03	2.99E-03	4.13E-04
SFT t42:0	1.39E-17	6.69E-19	7.06E-01	4.93E-01	5.04E-01	6.48E-01	9.65E-01	3.93E-01	2.18E-01
SFT t42:1	1.16E-14	4.92E-27	4.01E-01	6.04E-01	1.39E-02	3.38E-01	1.33E-01	5.29E-02	1.46E-03

Abbreviations: ANOVA, analysis of variance; Hex Cer, Hexocyl Ceramide; LPI, Lyso phosphatidylinositol; PC, phosphatidylcholine; PC O/ PC P; ether/vynil-ether phosphatydilcholine; PE, phosphatidylethanolamine; PE O/ PE P, ether/vynil-ether phosphatidylethanolamine; PG, phosphatydilglyerol; PI, phosphatidylinositol; PS, phosphatidylserine; PSO, ether/vynil-ether phosphatidylserine; SM, sphingomyelin; SULF, Sulfatide; G, Glomerulus; PTI, Proximal tubule I; PTII, Proximal tubule II; CDT, cortical distal tubule; CMT, Corticomedular tubule; MTI, Medullary distal tubule I; MTII, Medullary distal

Table A.6.2. *One-way ANOVA and multiple testing correction of the lipid classes detected in human renal samples. The table shows the p-values for Levene-test to determine the homogeneity (H0 = groups have equivalent variance) to choose the post hoc method (Tukey or Games-Howell); one-way ANOVA p-values; Tukey or Games-Howell P-values for the seven pair-wise (p-value < 0.05 appears in green shadow).*

Lipid class	Levene test	ANOVA	GvsPTI	GvsPTII	GvsCDT	GvsCMT	GvsMTI	GvsMTII	GvsITS
Hex Cer	1.76E-04	0.00E+00	5.83E-05	2.10E-04	1.33E-07	1.71E-07	1.54E-05	2.06E-09	9.37E-02
LPI	1.01E-02	8.33E-12	7.41E-04	1.22E-01	6.23E-01	9.90E-01	8.17E-02	3.54E-01	7.22E-01
PC	2.35E-02	9.43E-03	7.91E-01	8.17E-01	3.61E-01	9.61E-02	1.97E-01	9.92E-01	5.76E-03
PC O/PC P	5.46E-02	3.76E-21	6.47E-13	1.01E-07	3.62E-04	2.96E-01	7.14E-01	2.54E-09	1.00E+00
PE	1.76E-02	2.74E-03	5.55E-03	6.82E-03	5.22E-02	1.14E-01	9.26E-02	9.95E-01	9.06E-02
PE O/PE P	7.02E-03	5.00E-19	4.73E-09	1.95E-04	1.07E-01	8.05E-01	1.00E+00	8.78E-08	1.00E+00
PG	2.16E-16	1.32E-40	4.35E-01	8.59E-01	9.99E-01	3.53E-01	5.11E-02	7.90E-01	9.98E-01
PI	5.18E-02	2.55E-08	1.39E-04	9.76E-01	4.46E-05	9.76E-02	7.56E-01	9.84E-01	9.98E-01
PS	3.28E-04	4.96E-15	5.27E-03	3.60E-01	3.55E-05	2.23E-04	7.80E-01	1.40E-07	2.62E-01
PS O/PS P	4.92E-09	6.29E-13	3.94E-02	1.94E-02	3.04E-04	7.31E-05	4.30E-05	3.52E-05	4.60E-03
SM	1.03E-03	5.28E-33	4.62E-06	3.93E-03	1.39E-10	6.26E-12	3.35E-11	4.05E-12	5.10E-04
SFT	7.56E-11	6.33E-35	9.64E-01	9.28E-04	6.68E-06	6.20E-04	1.91E-02	1.79E-04	4.78E-03

Lipid class	Levene test	ANOVA	PTIvsPTII	PTIvsCDT	PTIvsCMT	PTIvsMTI	PTIvsMTII	PTIvsITS	PTIIvsCDT
Hex Cer	1.76E-04	0.00E+00	9.99E-01	2.78E-04	1.76E-04	4.34E-02	3.77E-11	2.57E-01	8.99E-04
LPI	1.01E-02	8.33E-12	7.32E-01	4.37E-02	2.30E-02	2.36E-01	1.31E-05	2.89E-05	8.60E-01
PC	2.35E-02	9.43E-03	1.00E+00	9.85E-01	6.96E-01	5.71E-01	5.74E-01	5.56E-01	9.93E-01
PC O/PC P	5.46E-02	3.76E-21	1.06E-03	9.24E-07	2.52E-09	7.47E-03	9.61E-01	6.48E-13	6.64E-01
PE	1.76E-02	2.74E-03	1.00E+00	9.97E-01	9.98E-01	9.96E-01	1.62E-01	6.96E-01	1.00E+00
PE O/PE P	7.02E-03	5.00E-19	4.93E-03	1.75E-05	8.95E-07	5.47E-04	6.91E-01	4.16E-07	3.83E-01
PG	2.16E-16	1.32E-40	9.42E-01	7.83E-01	6.58E-01	5.18E-02	9.79E-01	2.90E-01	9.99E-01
PI	5.18E-02	2.55E-08	4.22E-03	1.00E+00	8.85E-01	9.93E-01	1.85E-04	3.26E-03	1.35E-03
PS	3.28E-04	4.96E-15	1.94E-01	2.02E-01	6.24E-01	9.38E-02	1.47E-06	4.42E-01	9.89E-01
PS O/PS P	4.92E-09	6.29E-13	9.88E-01	1.94E-01	2.08E-05	1.07E-03	9.37E-08	6.14E-01	2.20E-01
SM	1.03E-03	5.28E-33	6.40E-01	4.95E-08	7.96E-08	2.37E-11	9.82E-08	4.08E-01	1.30E-06
SFT	7.56E-11	6.33E-35	1.64E-02	1.54E-05	8.80E-04	1.77E-02	1.92E-04	1.53E-02	4.02E-03

Lipid class	Levene test	ANOVA	PTIIvsCMT	PTIIvsMTI	PTIIvsMTII	PTIIvsITS	CDTvsCMT	CDTvsMTI	CDTvsMTII
Hex Cer	1.76E-04	0.00E+00	7.17E-04	2.12E-02	8.48E-09	5.30E-01	1.00E+00	5.17E-01	1.48E-05
LPI	1.01E-02	8.33E-12	6.10E-01	1.24E-01	3.35E-03	8.33E-03	9.97E-01	1.01E-01	9.29E-03
PC	2.35E-02	9.43E-03	7.73E-01	6.37E-01	5.96E-01	7.08E-01	9.95E-01	9.66E-01	2.56E-01
PC O/PC P	5.46E-02	3.76E-21	2.20E-02	7.45E-01	3.79E-01	5.90E-07	6.36E-01	9.96E-01	1.51E-02
PE	1.76E-02	2.74E-03	1.00E+00	1.00E+00	2.48E-01	8.76E-01	1.00E+00	1.00E+00	4.65E-01
PE O/PE P	7.02E-03	5.00E-19	1.15E-02	1.20E-03	7.62E-02	1.24E-03	7.99E-01	9.90E-02	2.92E-04
PG	2.16E-16	1.32E-40	4.65E-01	5.17E-02	1.00E+00	6.10E-01	6.45E-01	5.09E-02	9.93E-01
PI	5.18E-02	2.55E-08	4.82E-01	9.56E-01	6.83E-01	1.00E+00	6.73E-01	9.66E-01	6.45E-05
PS	3.28E-04	4.96E-15	9.79E-01	2.36E-02	3.55E-01	3.75E-03	1.00E+00	6.32E-02	1.91E-04
PS O/PS P	4.92E-09	6.29E-13	3.56E-02	1.47E-02	4.11E-03	9.94E-01	6.37E-01	2.84E-01	3.40E-03
SM	1.03E-03	5.28E-33	9.60E-08	9.24E-09	5.57E-09	1.00E+00	4.72E-01	6.93E-06	4.23E-03
SFT	7.56E-11	6.33E-35	7.40E-03	1.79E-02	3.58E-04	7.96E-01	6.17E-01	1.40E-02	1.61E-03

Lipid class	Levene test	ANOVA	CDTvsITS	CMTvsMTI	CMTvsMTII	CMTvsITS	MTIvsMTII	MTIvsITS	MTIIvsITS
Hex Cer	1.76E-04	0.00E+00	4.61E-04	5.03E-01	1.32E-05	4.65E-04	7.21E-01	1.32E-03	1.42E-06
LPI	1.01E-02	8.33E-12	4.29E-02	7.74E-02	2.65E-01	4.55E-01	7.41E-02	6.75E-02	1.00E+00
PC	2.35E-02	9.43E-03	9.99E-01	1.00E+00	7.90E-02	1.00E+00	1.19E-01	9.94E-01	4.62E-02
PC O/PC P	5.46E-02	3.76E-21	1.18E-03	1.00E+00	1.65E-04	4.22E-01	1.09E-01	7.78E-01	1.01E-08
PE	1.76E-02	2.74E-03	9.85E-01	1.00E+00	5.49E-01	9.91E-01	3.62E-01	9.28E-01	7.80E-01
PE O/PE P	7.02E-03	5.00E-19	1.91E-01	7.85E-01	1.15E-05	8.80E-01	1.91E-03	1.00E+00	3.44E-06
PG	2.16E-16	1.32E-40	9.71E-01	3.44E-02	4.92E-01	3.23E-01	5.17E-02	5.07E-02	5.70E-01
PI	5.18E-02	2.55E-08	1.07E-03	1.00E+00	3.63E-02	3.74E-01	4.63E-01	9.21E-01	8.45E-01
PS	3.28E-04	4.96E-15	1.22E-03	4.64E-02	1.60E-02	2.14E-02	4.34E-02	1.90E-01	1.97E-07
PS O/PS P	4.92E-09	6.29E-13	7.09E-01	9.70E-01	8.92E-01	2.00E-01	1.00E+00	7.77E-02	3.16E-02
SM	1.03E-03	5.28E-33	1.82E-09	3.96E-01	1.27E-01	1.83E-09	5.83E-01	1.38E-10	1.02E-08
SFT	7.56E-11	6.33E-35	3.06E-01	1.37E-02	1.20E-02	4.83E-02	1.00E+00	8.81E-03	4.16E-04

Appendix Chapter 7

Table A.7.1. *One-way ANOVA and multiple testing correction of the lipid fingerprint of human and murine renal samples. The table shows the P-values for Levene-test to determine the homogeneity (H$_0$ = groups have equivalent variance) to choose the post hoc method (Tukey or Games-Howell); one-way ANOVA P-values; Tukey or Games-Howell P-values for the six pair-wise. HC=Human cortex, HG=Human glomerulus, HMe=Human medulla, MC=Murine cortex, MG=Murne glomeruli, MMe=Murine medulla*

	Levene test	ANOVA	HC.vs HG	HC.vs HMe	HC.vs MC	HC.vs MG	post-hoc
Hex Cer	7.17E-01	3.78E-11	1.84E-06	9.93E-01	4.15E-01	9.91E-01	Games Howell
LPI	1.07E-01	8.32E-10	6.41E-04	6.70E-04	2.42E-04	1.32E-05	Games Howell
LPI-O/P	4.30E-01	1.13E-03	4.64E-03	2.53E-01	4.81E-02	1.36E-02	Games Howell
PC	5.91E-01	2.17E-05	5.46E-01	4.89E-01	1.71E-02	2.96E-01	Games Howell
PC-O/P	2.79E-04	4.08E-25	9.83E-09	4.36E-02	4.67E-11	8.82E-08	Tukey
PE	4.07E-01	7.77E-06	1.48E-02	1.00E+00	2.50E-01	1.94E-01	Games Howell
PE-O/P	3.95E-01	2.14E-08	8.18E-05	3.44E-02	7.17E-01	3.15E-02	Games Howell
PG	5.56E-03	9.79E-02	8.80E-02	1.00E+00	9.74E-01	5.37E-01	Tukey
PI	6.24E-01	2.12E-10	1.28E-03	8.06E-02	3.37E-01	9.87E-01	Games Howell
PS	3.73E-02	5.05E-18	1.73E-02	8.92E-01	1.35E-10	6.20E-13	Tukey
SM	1.28E-05	3.01E-14	4.93E-06	1.70E-02	2.27E-01	6.23E-01	Tukey
SFT	1.05E-01	1.30E-11	2.70E-04	6.71E-06	1.83E-04	3.18E-04	Games Howell

	Levene test	ANOVA	HC.vs MMe	HC.vs Hme	HG.vs MC	HG.vs MG	post-hoc
Hex Cer	7.17E-01	3.78E-11	8.19E-01	1.41E-04	3.94E-07	2.64E-03	Games Howell
LPI	1.07E-01	8.32E-10	7.79E-03	9.48E-01	9.70E-01	5.88E-02	Games Howell
LPI-O/P	4.30E-01	1.13E-03	4.32E-01	9.05E-01	8.61E-01	9.99E-01	Games Howell
PC	5.91E-01	2.17E-05	9.99E-01	6.71E-02	3.19E-04	9.33E-03	Games Howell
PC-O/P	2.79E-04	4.08E-25	6.83E-02	7.72E-02	6.11E-13	6.11E-13	Tukey
PE	4.07E-01	7.77E-06	9.65E-01	4.98E-02	1.31E-04	9.90E-01	Games Howell
PE-O/P	3.95E-01	2.14E-08	4.51E-01	4.63E-01	2.59E-07	1.00E+00	Games Howell
PG	5.56E-03	9.79E-02	8.55E-01	3.46E-01	4.20E-01	9.85E-01	Tukey
PI	6.24E-01	2.12E-10	1.46E-01	3.36E-01	6.90E-06	7.37E-04	Games Howell
PS	3.73E-02	5.05E-18	2.65E-06	3.69E-03	3.70E-06	6.19E-11	Tukey
SM	1.28E-05	3.01E-14	2.88E-01	2.56E-08	7.42E-08	2.03E-02	Tukey
SFT	1.05E-01	1.30E-11	8.58E-02	1.21E-12	9.94E-01	4.98E-02	Games Howell

	Levene test	ANOVA	HG.vs MMe	HMe.vs MC	HMe.vs MG	HMe.vs MMe	post-hoc
Hex Cer	7.17E-01	3.78E-11	2.45E-04	8.49E-01	9.34E-01	9.87E-01	Games Howell
LPI	1.07E-01	8.32E-10	9.99E-01	1.00E+00	6.00E-01	9.12E-01	Games Howell
LPI-O/P	4.30E-01	1.13E-03	8.83E-01	1.00E+00	9.71E-01	1.00E+00	Games Howell
PC	5.91E-01	2.17E-05	8.05E-01	7.46E-01	1.00E+00	9.59E-01	Games Howell
PC-O/P	2.79E-04	4.08E-25	6.05E-11	7.02E-13	5.38E-11	6.61E-05	Tukey
PE	4.07E-01	7.77E-06	9.13E-01	3.28E-01	2.46E-01	9.65E-01	Games Howell
PE-O/P	3.95E-01	2.14E-08	6.22E-01	2.06E-03	8.87E-01	9.99E-01	Games Howell
PG	5.56E-03	9.79E-02	9.54E-01	9.98E-01	7.94E-01	9.51E-01	Tukey
PI	6.24E-01	2.12E-10	9.14E-04	7.16E-04	2.90E-02	5.43E-03	Games Howell
PS	3.73E-02	5.05E-18	7.33E-03	4.41E-10	6.95E-13	1.06E-06	Tukey
SM	1.28E-05	3.01E-14	1.54E-05	8.18E-01	4.27E-02	9.72E-01	Tukey
SFT	1.05E-01	1.30E-11	9.82E-01	1.67E-12	4.47E-12	1.70E-08	Games Howell

	Levene test	ANOVA	CM.vs MG	CM.vs MMe	GM.vs MMe	post-hoc
Hex Cer	7.17E-01	3.78E-11	3.94E-01	9.96E-01	7.01E-01	Games Howell
LPI	1.07E-01	8.32E-10	3.05E-01	9.37E-01	1.76E-01	Games Howell
LPI-O/P	4.30E-01	1.13E-03	9.66E-01	1.00E+00	9.53E-01	Games Howell
PC	5.91E-01	2.17E-05	6.55E-01	5.18E-01	9.42E-01	Games Howell
PC-O/P	2.79E-04	4.08E-25	7.77E-01	1.92E-03	7.04E-02	Tukey
PE	4.07E-01	7.77E-06	3.36E-03	4.13E-01	9.87E-01	Games Howell
PE-O/P	3.95E-01	2.14E-08	5.36E-03	1.52E-01	8.49E-01	Games Howell
PG	5.56E-03	9.79E-02	9.17E-01	9.93E-01	1.00E+00	Tukey
PI	6.24E-01	2.12E-10	7.30E-01	9.43E-01	3.44E-01	Games Howell
PS	3.73E-02	5.05E-18	4.23E-02	9.70E-01	2.57E-02	Tukey
SM	1.28E-05	3.01E-14	1.30E-01	1.00E+00	1.16E-01	Tukey
SFT	1.05E-01	1.30E-11	1.00E+00	9.00E-01	8.66E-01	Games Howell

Appendix Chapter 9

Table A.9.1. GBM lipidomic data expressed in mean ± SEM, of the total lipid class % for each sample type. Values are expressed as a percentage of the total membrane lipid intensity and represent the mean ± S.E.M (n=5). a=significative difference in heathy DMSO vs tumor DMSO T-test comparison, b= significative difference in tumor DMSO vs tumor TMZ T-test comparison and c= significative difference in healthy DMSO vs healthy TMZ T-test comparison.

	Healthy DMSO		Healthy TMZ		Tumor DMSO		Tumor TMZ	
	Mean	SEM	Mean	SEM	Mean	SEM	Mean	SEM
PE plasmalogens (PE-O/P)								
PE P-34:0	0.0	0.0	0.0	0.0	1.6	0.9	0.9	0.4
PE P-34:1[c]	13.7	5.7	5.0	2.7	8.5	5.4	10.3	4.6
PE P-34:2	5.0	3.2	0.0	0.0	1.3	1.9	1.3	1.1
PE P-36:0	0.0	0.0	0.0	0.0	0.9	0.2	0.3	0.0
PE P-36:1[c]	8.6	0.0	2.8	1.1	4.3	1.4	3.7	1.0
PE P-36:2[c]	20.8	7.1	7.3	3.9	3.6	2.1	3.6	1.5
PE P-36:3	1.7	0.9	0.9	0.0	1.6	0.7	1.9	0.5
PE P-36:4[a,b]	1.9	0.7	3.8	3.4	14.8	5.4	20.4	3.6
PE P-38:1	1.0	0.4	0.4	0.3	0.7	0.5	0.4	0.0
PE P-38:2	3.9	0.0	1.8	0.0	0.7	0.4	1.0	0.8
PE P-38:4	14.7	2.2	20.4	4.5	22.0	6.4	21.8	3.6
PE P-38:5	7.1	0.6	8.1	2.5	8.0	3.3	8.3	2.0
PE P-38:6[a]	2.8	1.5	6.5	1.3	10.3	2.7	11.1	3.4
PE P-40:3	0.9	0.1	0.9	0.2	1.8	1.5	0.7	0.6
PE P-40:4[b]	8.8	3.1	11.5	2.9	5.6	2.0	3.6	2.3
PE P-40:5	7.1	1.6	6.2	0.9	4.3	2.0	3.3	1.6
PE P-40:6[c]	10.2	10.8	23.5	8.0	10.4	3.6	7.6	2.7
PE P-40:7[c]	1.8	0.8	3.2	0.1	1.8	1.0	1.3	1.1
PE P-42:5	0.6	0.0	0.0	0.0	0.6	0.4	0.4	0.0
PE P-42:6	0.0	0.0	0.0	0.0	0.7	0.5	0.5	0.0
PE								
PE 32:0	0.3	0.1	0.4	0.1	0.5	0.4	0.7	0.3
PE 34:0[a]	3.2	0.9	5.5	1.6	5.4	1.7	5.1	1.3
PE 34:1	5.5	2.1	3.8	1.7	6.2	1.9	6.6	4.5
PE 34:2[b]	0.0	0.0	0.0	0.0	1.2	1.9	1.4	0.8
PE 36:0	1.8	0.0	0.0	0.0	2.0	1.3	2.4	1.6
PE 36:1[c]	35.6	10.4	27.1	5.2	30.0	7.9	31.7	7.4
PE 36:2[c]	7.4	3.3	3.9	1.8	10.1	9.5	13.1	6.8
PE 36:3	0.7	0.0			1.5	1.6	2.1	1.4
PE 36:4[a, b]	0.6	0.2	1.0	0.3	1.1	0.5	1.7	0.3
PE 38:0					0.3	0.1	0.2	0.1
PE 38:1[b]	6.1	1.7	4.0	0.7	3.9	1.8	2.5	0.8
PE 38:2	4.2	1.8	2.3	1.2	5.9	1.6	5.5	2.3
PE 38:3	0.0	0.0	0.0	0.0	1.5	0.0	0.0	0.0
PE 38:4	11.3	3.3	15.8	3.3	13.4	4.1	13.9	3.1
PE 38:5[b]	2.6	0.6	2.4	0.9	2.3	0.6	4.0	1.2
PE 38:6	2.3	1.9	4.3	0.9	1.9	0.9	2.2	0.9
PE 40:1	0.0	0.0	0.0	0.0	0.0	0.0	0.0	0.0
PE 40:3	0.6	0.0	0.0	0.0	0.2	0.0	0.5	0.1
PE 40:4	5.2	2.2	6.6	1.8	5.5	3.8	3.3	1.1
PE 40:5[a, c]	2.3	0.0			2.6	0.5	2.5	0.4
PE 40:6	13.9	11.0	23.2	7.7	6.2	3.3	4.0	1.9
PE 40:7	1.0	0.3	1.4	0.4	1.4	0.6	1.4	0.8
PI								
LPI 18:0	0.5	0.4	0.0	0.0	0.3	0.2	0.0	0.0
LPI 18:1	1.5	2.0	0.2	0.2	0.0	0.0	0.0	0.0
PI 34:0	0.0	0.0	0.0	0.0	0.3	0.0	2.4	3.3
PI 34:1	13.7	4.3	0.0	0.0	4.8	2.7	4.6	4.0
PI 36:1	4.5	2.7	2.1	0.8	2.4	0.8	35.7	0.0
PI 36:2	2.6	1.2	1.7	0.0	5.5	5.5	6.6	5.5
PI 36:4	8.3	1.7	10.9	0.0	5.1	1.4	6.5	5.7
PI 38:2	0.0	0.0	0.0	0.0	0.9	0.4	0.0	0.0
PI 38:4[a, c]	54.9	8.4	80.4	7.2	75.7	11.1	65.0	29.4
PI 38:5	5.1	0.3	6.3	0.5	5.5	1.5	5.5	1.7
PI 38:6	0.8	0.5	0.0	0.0	0.0	0.0	0.0	0.0

PI 40:0	0.0	0.0	0.0	0.0	0.0	0.0	0.0	0.0
PI 40:1	6.0	4.3	2.7	1.4	0.0	0.0	0.0	0.0
PI 40:4	0.0	0.0	0.0	0.0	1.6	0.2	3.0	0.3
PI 40:5	0.0	0.0	0.0	0.0	1.3	0.8	1.5	1.2
PI 40:6[a]	2.8	1.8	5.4	2.1	2.8	1.3	2.7	2.4
PI 40:7	0.1	0.0	0.6	0.4	0.2	0.1	0.0	0.0
PC								
PC 30:0	0.2	0.1	0.2	0.1	0.3	0.1	0.1	0.1
PC 32:0	1.8	1.3	3.0	2.4	3.0	0.4	1.1	0.7
PC 32:1	1.2	0.5	1.1	0.9	2.2	0.5	0.9	0.5
PC 32:3	0.4	0.1	0.2	0.5	0.6	0.2	0.3	0.1
PC 33:0	0.1	0.0	0.1	0.2	0.2	0.1	0.1	0.1
PC 33:1	0.2	0.1	0.3	0.2	0.3	0.0	0.1	0.1
PC 34:1	16.0	5.7	12.8	12.3	17.8	3.8	7.2	4.2
PC 34:3	5.1	1.4	3.2	8.3	6.2	1.0	2.4	1.5
PC 34:4	3.8	1.2	2.7	3.0	3.6	0.4	1.3	0.9
PC 35:1	1.4	0.3	0.6	1.2	1.2	0.2	0.5	0.3
PC 35:4	0.6	0.2	0.5	0.4	0.5	0.1	0.2	0.1
PC 36:1	2.7	1.0	2.2	1.8	2.1	0.7	0.9	0.5
PC 36:2[a]	1.6	0.9	2.0	0.5	2.8	0.3	1.0	0.7
PC 36:4[a]	41.0	10.2	22.8	36.6	32.4	2.7	11.7	8.0
PC 36:5	4.2	1.5	3.3	2.1	8.3	3.5	3.9	1.9
PC 37:4	0.4	0.1	0.3	0.4	0.3	0.1	0.1	0.1
PC 38:4[a, b]	10.1	1.8	4.1	6.5	6.1	1.1	2.4	1.4
PC 38:5	5.3	1.3	2.8	3.0	6.2	1.2	2.5	1.5
PC 38:7	2.4	0.8	1.7	3.3	4.0	1.3	1.8	0.9
PC 40:8	0.6	0.2	0.4	0.6	1.0	0.3	0.4	0.2
PC 40:9	0.8	0.3	0.8	1.4	0.6	0.2	0.3	0.1
PC 42:9	0.3	0.2	0.4	0.6	0.3	0.1	0.2	0.1
DG								
DG 32:0	2,5	1,3	2,0	1,0	7,8	4,9	9,5	7,7
DG 32:1	3,0	3,0	4,1	3,8	4,5	0,9	4,2	3,0
DG 32:2	3,3	1,6	3,1	2,1	2,8	0,9	4,9	3,4
DG 34:0	4,5	1,4	2,9	0,7	5,9	1,2	7,7	4,7
DG 34:2	58,0	11,2	51,6	10,1	33,3	17,8	41,0	18,5
DG 34:3	4,4	2,5	3,3	1,8	10,0	6,9	9,3	6,3
DG 36:2	6,1	5,6	7,2	4,2	5,2	4,6	5,0	1,3
DG 36:3	2,8	2,7	3,8	1,1	7,1	1,6	2,3c	2,6
DG 36:4	1,3	0,8	2,1	0,5	2,9	3,4	3,9	1,6
DG 36:5	4,5	3,3	5,4	3,4	7,1	6,0	5,7	4,4
DG 38:4	1,0	0,4	1,9	1,0	0,8	1,0	0,5	0,4
DG 38:5	4,2	3,4	5,5	3,4	6,9	5,5	3,6	1,3
DG 38:6	1,1	0,7	1,7	0,4	2,4	1,0	1,6	0,5
DG 38:7	1,9	1,8	3,2	1,9	2,1	0,7	0,7	0,7
DG 40:7	1,2	1,3	2,4	1,2	1,2	0,7	0,2	0,3
TG								
TG 36:4	0,4	0,1	0,4	0,3	1,0	0,4	0,9	0,9
TG 38:4	5,1	5,2	10,2	3,9	8,0	5,7	9,0	2,2
TG 38:5	3,3	2,6	3,9	2,0	4,7	1,1	6,6	3,1
TG 40:5	55,1	2,7	56,1	2,3	42,6	15,1	47,4	15,1
TG 40:6	3,6	1,7	3,1	1,3	13,5	9,6	11,0	9,1
TG 40:7	1,0	0,4	0,9	0,3	1,4	0,4	1,7	1,2
TG 42:5	7,7	4,3	8,1	2,5	4,8	3,6	2,7	2,4
TG 42:6	4,6	1,2	3,4	0,5	8,1[b]	2,3	7,0	4,0
TG 42:7	8,8	6,8	3,5	1,8	4,2	3,4	4,8	3,2
TG 42:8	5,4	0,8	6,0	0,5	8,4	5,0	7,0	2,9
TG 42:9	0,2	0,1	0,2	0,1	0,8	0,5	0,5	0,4
TG 44:10	5,0	1,5	4,1	1,3	2,4[a]	0,8	1,2	0,9
SM								
SM d32:2	0.6	0.8	0.0	0.0	1.0	0.7	0.5	0.3
SM d34:0	0.0	0.0	0.0	0.0	2.4	1.1	2.7	1.3
SM d34:1	10.6	4.4	10.7	5.9	37.5	15.5	33.1	8.7
SM d34:2	1.0	0.1	1.1	0.9	3.9	3.9	2.0	1.2
SM d36:0	0.0	0.0	0.0	0.0	2.8	1.1	3.5	1.1
SM d36:1	41.0	8.0	50.1	9.0	26.6	16.2	34.6	19.3
SM d36:2[a]	8.3	2.8	9.7	3.7	8.3	5.2	9.9	3.4
SM d38:1	6.6	6.6	12.4	6.3	1.7	0.7	1.7	0.2

|								
SM d40:1[a]	0.8	0.3	1.2	0.5	3.2	1.7	2.9	1.6
SM d40:2	0.0	0.0	0.0	0.0	1.8	1.4	1.3	1.0
SM d42:1	3.4	1.0	1.3	0.5	5.4	3.9	1.9	0.8
SM d42:2	26.8	7.7	12.2	5.8	9.4	3.5	14.5	8.9
SM d42:3[a]	1.3	0.4	1.1	0.6	3.6	2.0	2.3	2.6
SM d44:2	2.9	1.0	1.2	0.7	0.0	0.0	0.0	0.0
SFT								
SFT d34:2	0.4	0.0	1.7	1.1	5.4	4.2	3.7	3.3
SFT d34:3	0.3	0.2	1.7	1.8	9.6	5.9	11.9	13.5
SFT d36:0	0.0	0.0	0.0	0.0	0.0	0.0	2.5	0.4
SFT d36:1[a]	3.4	0.7	3.0	0.8	3.9	4.4	14.7	8.1
SFT d36:2 [a]	0.4	0.1	0.7	0.3	1.3	0.8	9.3	14.2
SFT d36:3 [a]	1.4	1.2	6.2	4.3	26.2	17.8	14.2	11.3
SFT d36:4 [a]	0.2	0.2	0.7	0.4	11.4	10.9	10.5	15.0
SFT d38:6	0.0	0.0	0.0	0.0	9.1	0.0	5.6	1.9
SFT d40:1	1.3	0.2	1.0	0.2	0.2	0.0	2.3	0.7
SFT d42:1	11.3	5.7	6.6	2.3	3.8	3.5	7.1	5.8
SFT d42:2 [a]	50.8	5.5	49.4	7.0	29.9	20.4	40.6	19.7
SFT d44:2	10.0	1.2	10.2	1.5	5.3	4.1	10.3	1.4
SFT d44:3	1.5	0.5	1.9	0.2	0	0	0	0
SFT t40:1	2.7	0.6	4.0	1.7	1.3	1.5	0.9	1.5
SFT t40:4	0.7	0.0	1.4	0.5	4.8	5.0	5.5	7.5
SFT t42:1	15.9	1.3	15.7	9.4	5.4	6.3	0.0	0.0
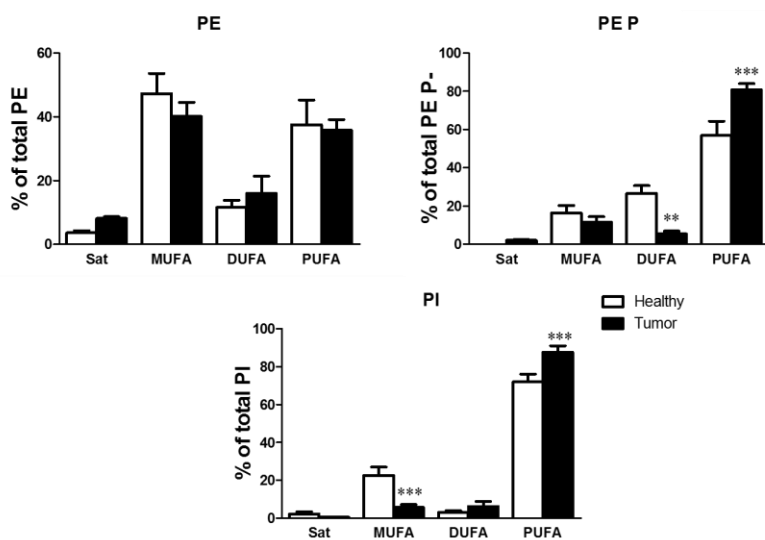
Figure A.9.1. Saturated, MUFA, DUFA, PUFA PE, PE P and PI composition of healthy and tumor tissue.
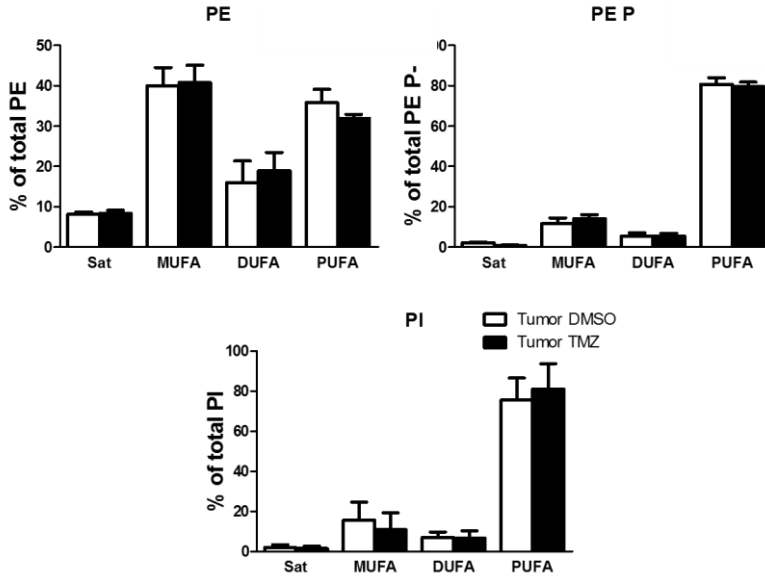
Figure A.9.2. Saturated, MUFA, DUFA, PUFA PE, PE P and PI composition of DMSO and TMZ-treated tumor tissue.
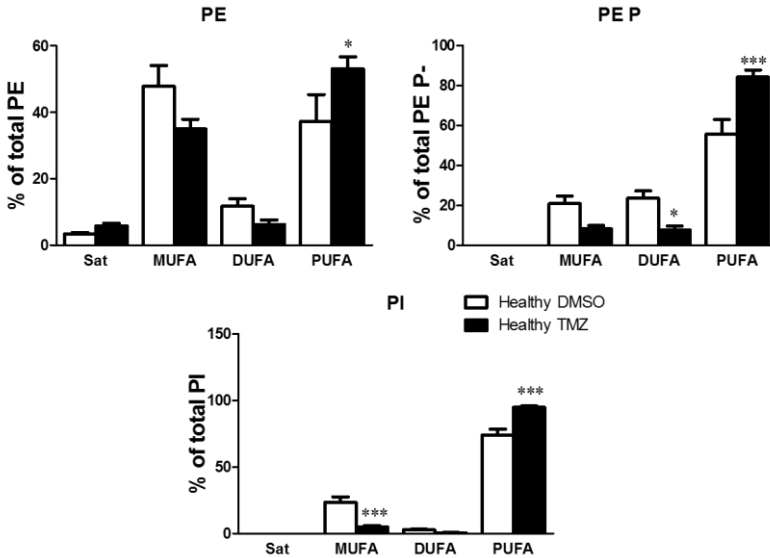

Figure A.9.3. Saturated, MUFA, DUFA, PUFA PE, PE P and PI composition of DMSO and TMZ-treated healthy tissue.

Abbreviations

Abbreviation	Meaning
AA	Arachidonic acid
AA-PE	Arachidonic acid-containing phosphatidylethanolamine
AKI	Acute kidney injury
ALOX15B	Arachidonate 15-lipoxygenase type B
ALOX5	Arachidonate 5-lipoxygenase activating protein
ANOVA	Analysis of variance
API	Atmospheric pressure
BUN	Blood urine nitrogen
ccRCC	Clear cell renal cell carcinoma
CD	Collecting duct
cCD	Clear collecting duct
CDT	Cortical distal tubules
Cer	Ceramide
CerP	Ceramide-1-phosphate
Cer-PE	Ceramide phosphoethanolamine
CHCA	α-cyano-4-hidroxicinamic acid
ChE	Cholesteryl ester
CKD	Chronic kidney disease
CMT	Corticomedullary tubules
CV	Coefficient of variation
DAG	Diacylglicerol
DAN	1,5-diaminonaphthalene
DBA	Dolichos biflorus agglutinin
DESI	Desorption electrospray ionization
DG	Diacylglicerols/diglycerides
DGKB	Diacylglycerol kinase B
DIANA	Divisive Analysis algorithm
DIOS	Desorption ionization on silicon
ECL	Chemiluminescence method
EI	Electron impact ionization
ELOVL	Fatty acid elongase
ESI	Electrospray ionization
ESRD	End-stage renal disease
FA	Fatty acids
FABP	fatty acid binding protein
Fer-1	Ferrostatin-1
FPKM	Fragments per kilo base per million mapped reads

FT-ICR	Fourier transform ion cyclotron resonance
FWHM	Full width at a half maximum
G	Glomerulus/Glomeruli
GBM	Glioblastoma
GL	Glycerolipids
GP	Glycerophospholipids
GPL	Glycerophospholipids
GS	Glycosphingolipids
GSub	Glass sublimator
H&E	Hematoxylin & Eosin
HD-RCA	Hierarchical divisive-RankComplete clustering algorithm
HexCer	Cerebrosides
HPLC	High performance liquid chromatography
i.p.	Intraperitoneal
IBD	Inflammatory bowel desease
ICs	Intercalated cells
IF	Immunofluorescence
IHC	Immunohistochemistry
IMS	Imaging mass spectrometry
INPP5F	Inositol polyphosphate-5-phosphatase F
ITS	Interstitial vascular structures
LAESI	Laser desorption electrospray ionization
LC	Liquid chromatography
LC-ESI-MS	Liquid chromatography-electrospray ionization-mass spectrometry
LC-MS	Liquid chromatography-mass spectrometry
LD	Laser Desorption
LIT-TOF	Linear trap-time of flight
LPC	Lyso glycerophosphocholine
LPC-O/P	Lyso glycerophosphocholine ether/vinyl-ether
LPE	Lyso glycerophosphoethanolamine
LPE-O/P	Lyso glycerophosphoethanolamine ether/vinyl-ether
LPI	Lyso glycerophosphoinositol
LPI-O/P	Lyso glycerophosphoinositol ether/vinyl-ether
LTL	Lotus tetragonolobus lectin
m/z	Mass-to-charge ratio
m/Δm	Mass resolving power
MALDI	Matrix-assisted laser desorption ionization
MBT	2-mercaptobenzothiazole

MS	Mass spectrometry
MTI	Medullary tubule I
MTII	Medullary tubule II
NALDI	Nanotechnology-assisted laser desorption/ionization
NMR	Nuclear magnetic resonance
PC	Glycerophosphocholine
PC-O/P	PC ether/vinyl-ether
PCs	Principal cells
PE	Glycerophosphoethanolamine
PE-Cer	Ceramide phosphoethanolamine
PE-O/P	PE ether/vinyl-ether
PG	Glycerophosphoglycerol
PI	Glycerophosphoinositol
PI-O/P	PI ether/vinyl-ether
PK	Polyketides
PLA2G2A	Phospholipase A2 group IIA
PLA2G5	Phospholipase A2 group V
PR	Prenols
pRCC	Papillary renal cell carcinoma
PS	Glycerophosphoserine
PS-O/P	PS ether/vinyl-ether
PTGS2	Prostaglandin-endoperoxide synthase 2
PTI	Proximal tubule I
PTII	Proximal tubule Ii
PUFA	Polyunsaturated fatty acid
QC	Quality control
Qqof	Quadrupole-time-of-flight
RCC	Renal carcinoma
RF	Radio Frecuency
RT	Retention time
S.E.M	Standar error of the mean
SA	Sinapinic Acid
SFT	Sulfatides
SIMS	Secondary ion mass spectrometry
SL	Saccharolipids
SP	Sphingolipids
SPF	Simple Peak Finding
SSSub	Stainless steel sublimator

ST	Sterols
SVM	Support Vector Machine
TG	Triacylglycerols/ triglycerides
TG-O/P	Triglyceride ether/vinyl-ether
TIC	Total ion current
TMZ	Temozolomide
TOF	Time of flight
UGT8	UDP-galactose-ceramide galactosyltransferase
uHPLC	Ultra high performance liquid chromatography